MODELING, OPTIMIZATION AND ASSESSMENT OF SURFACE TOPOGRAPHY IN EDM BY ADVANCED METHODS

THESIS SUBMITTED BY

USHASTA AICH

DOCTOR OF PHILOSOPHY
(ENGINEERING)

MECHANICAL ENGINEERING DEPARTMENT
FACULTY COUNCIL OF ENGINEERING & TECHNOLOGY
JADAVPUR UNIVERSITY
KOLKATA, INDIA

2018

JADAVPUR UNIVERSITY
KOLKATA - 700032, INDIA

INDEX NO. 37/14/E

Title of the thesis	:	MODELING, OPTIMIZATION AND ASSESSMENT OF SURFACE TOPOGRAPHY IN EDM BY ADVANCED METHODS
Name, designation & institution of the supervisor	:	Dr. Simul Banerjee Professor (Retired) Mechanical Engineering Department Jadavpur University Kolkata 700032, India

LIST OF PUBLICATIONS:

Journal papers (SCIE journal, SCOPUS indexed)

1. U. Aich, S. Banerjee, *Characterizing topography of EDM generated surface by time series and autocorrelation function*, Tribology International, 111 (2017) 73-90 (Impact factor: 2.259).

2. U. Aich, S. Banerjee, *Application of teaching learning based optimization procedure for the development of SVM learned EDM process and its pseudo Pareto optimization*, Applied Soft Computing, 39 (2016) 64-83 (Impact factor: 2.81, Citations in SCOPUS: 5).

3. U. Aich, S. Banerjee, *Modeling of EDM responses by support vector machine regression with parameters selected by particle swarm optimization*, Applied Mathematical Modelling, 38 (2014) 2800-2818 (Impact factor: 1.706, Citations in SCOPUS: 37).

Book chapter

1. U. Aich, S. Banerjee, *Multiobjective optimization of support vector regression parameters by teaching-learning-based optimization for modeling of electric discharge machining responses*, (chapter 7) in: A.P. Markopoulos, J.P. Davim (Eds.), *Advanced Machining Processes: Innovative Modeling Techniques*, CRC Press, December 2017.

Periodical paper (SCOPUS indexed)

1. U. Aich, S. Banerjee, *Evaluation for chaos in EDM generated surface topography*, Key Engineering Materials, 765 (2018) 227-231.

LIST OF PATENT: Nil

LIST OF PRESENTATION:

Conference (presented)

1. U. Aich, S. Banerjee, *Evaluation for chaos in EDM generated surface topography,* presented in the 8th International Conference on Advanced Materials Research (ICAMR 2018), Fukuoka, Japan, January 20-22, 2018.

CERTIFICATE FROM THE SUPERVISOR

This is to certify that the thesis entitled "***Modeling, optimization and assessment of surface topography in EDM by advanced methods*** " submitted by Shri ***Ushasta Aich***, who got his name registered on 20.10.2014 for the award of Ph. D. (Engg.) degree of Jadavpur University is absolutely based upon his own work under the supervision of **Dr. Simul Banerjee** and that neither his thesis nor any part of the thesis has been submitted for any degree/diploma or any other academic award anywhere before.

(Dr. Simul Banerjee)

Professor (Retired)
Mechanical Engineering Department
Jadavpur University
Kolkata 700032, India

ACKNOWLEDGEMENT

It is a great pleasure to express my sincere gratitude and indebtedness to **Prof. Simul Banerjee** for suggesting the problem and providing valuable guidance at every stage of work. I remain very much beholden to him for the orderly and successful completion of this thesis.

I wish to record my thankfulness to **Prof. Sankar Dhar**, **Prof. Dipankar Sanyal**, **Prof. Goutam Sutradhar**, **Prof. Goutam Majumdar**, **Prof. Prasanta Sahoo** for their continuous encouragement and all other teachers of Mechanical Engineering Department, Jadavpur University who have shown a keen interest in the progress of my work.

I particularly acknowledge the help of **Prof. Suddhasatwa Chakraborty** and **Prof. Susanta Ray** of Electrical Engineering Department, Jadavpur University for extending the departmental facilities.

I take this opportunity to thank Council of Scientific and Industrial Research (**CSIR**), Human Resource Development Group, India (File no. 09/096(0833)/2015-EMR-I), for arranging financial assistance during my work.

I express my great appreciation to my father, my wife and my younger brother for understanding, patience and active co-operation throughout the course of my doctoral work.

I thank my beloved friends particularly **Suman Nihar**, **Suswagata Poria**, **Sovan Bhowmick** and **Sandeep Kumar Paral** for their valuable help.

Last but not the least, I express my recognition for the services of **Mr. Subrata Sarkar** and **Mr. Ashim Naskar** and several of my friends who have helped me either directly or indirectly at different stages of my research period.

(USHASTA AICH)

ॐ सह नाववतु ।
सह नौ भुनक्तु ।
सह वीर्यम् करवावहै ।
तेजस्वी नावधीतमस्तु मा विद्विषावहै ।
ॐ शान्तिः शान्तिः शान्तिः ।।

(तैत्तिरीय उपनिषद)

May God protect us both the teacher and the student (during the journey of awakening our knowledge).

May God bestow upon us both with the spring of knowledge (which nourishes life when awakened).

May we work together with energy and vigor for cleansing ourselves with the flow of energy for the knowledge to manifest.

May our study be enlightened through taking us towards the essence of underlying truth of everything. Let there be no animosity between us by constricting the understanding of the essence in a particular manifestation only.

Let there be threefold peace.

(Taittiriya Upanishad)

PREFACE

Impetuous passion of human society compels themselves to invent more sophisticated technology or to amend the existing ones. As, manufacturing industry plays a vital role to meet this ever growing demand, so, research on precision machining is always appreciated. For reduction of effective production cost, working in virtual environment is necessary. Therefore, near-accurate representation of machining process is prerequisite.

For this purpose, researchers are trying to implement different modeling methods, still, complexity of the machining process and drawbacks of modeling methods itself keep them far behind their deemed goal. Therefore, robust modeling techniques and advanced optimization methods, as and when developed, are to be attended. Besides, underlying features of machining phenomena are to be understood.

It is in this context, the present work on modeling, optimization and analysis of surface topography in electric discharge machining (EDM) process, a versatile and widely used non-traditional machining process, assumes significance.

To date, neither the available models on process responses of EDM could absorb the irregular fluctuations in responses nor the adopted optimization procedures could ascertain a trade-off between two conflicting responses namely material removal rate, an index of productivity and surface finish that attributes to quality. Also surface topography, an end result of mechanism of material removal in EDM, has not been qualitatively assessed for its randomness or periodicity or chaos. Addressing each of the three issues quantitatively is the major contribution of the present work.

The text of the thesis is organized in seven chapters and four appendices including introduction, review of literature, experiments, modeling, optimization, assessment of surface topography, conclusions and a list of pertinent references.

ABSTRACT

Electric discharge machining (EDM) is one of the most versatile nontraditional machining processes in modern industries. Though application of EDM covers a wide range of industrial demand still complex mechanism of material removal restricts its maneuverability towards precision manufacturing. Presence of complex thermo-electrical phenomena, material inhomogeneity, transient behavior of dielectric fluid results complicated surface integrity. In the present study, a novel attempt is made towards the development of virtual environment of EDM process through modeling, pseudo Pareto optimization, inverse solution method and the understanding of randomness and chaos in surface topography.

Experiments are conducted with different levels of three most significant machining control parameters namely current, pulse on time and pulse off time. For each experimental run, material removal rate, different surface roughness parameters are measured and scanning electron micrographs are taken. From the obtained results, some irregularities in the behavior of process outcomes are observed. To encompass the irregular fluctuations, support vector machine (SVM) regression is employed for model building purpose. During model building of process outcomes internal structural parameters of SVM regression are tuned using two evolutionary metaheuristic optimization methods namely particles swarm optimization (PSO) and teaching learning based optimization (TLBO). Generalized modifications namely population based termination criterion, weight combining method are improvised for better performance of optimization techniques. It is observed that modified TLBO is computationally cost efficient than modified PSO. Modified TLBO is further employed for developing a unique learning system for two process outcomes. Here combined rank method is proposed for efficient handling of multiple objective functions without affecting their individual impacts.

Further, the representative SVM regression based learning systems for each of the process outcomes are used for optimization of EDM process. Pseudo Parent front is developed and a relation between optimum achievable combination of process outcomes is estimated. An inverse solution methodology is proposed to get the setting of machining control parameters in EDM machine to meet the customer demand based requirement.

Moreover, an attempt is made to correlate the surface generation process with the characteristics of surface topography. Sequence of profile heights measured on each of the machined surfaces is considered as representative time series of that corresponding machined surface. Contributive effects of randomness and periodicity on surface topography is assessed through the formation of autocorrelation function. Predominance of randomness is observed through the evaluation of a non-dimensional index called as PR ratio. Also, presence of chaos in surface topography is checked. Saturation of correlation exponents measured on phase space, reconstructed from representative time series, indicates the presence of chaos. Non-integer value of correlation dimension suggests the fractal nature of machined surface. A different test directly from time series without phase space reconstruction, that is 0-1 test, is performed and presence of chaos for all machined surfaces is substantiated.

However, the proposed methodology for model building of process outcomes, pseudo Pareto front development, inverse solution method to get settings of machining control parameters to meet specific need based requirement, evaluation of contributive effects of randomness and periodicity in surface topography and investigation of the presence of chaos could be implemented to any such process in a generalized way.

KEYWORDS: Electric discharge machining; Support vector machine regression; Particle swarm optimization; Teaching learning based optimization; Autocorrelation function; Randomness; Chaos

LIST OF FIGURES

LIST OF TABLES

NOMENCLATURE

$\boldsymbol{A}$	amplitude of FID
$\boldsymbol{a}$	coefficient of Bezier function
ACF	autocorrelation function
ASR	average surface roughness (µm)
b	bias
BHS	Bezier hyper-surface
$B_{i,m}$, $B_{j,n}$, $B_{k,p}$	Bernstein blending function
C	regularization parameter
c	randomly chosen value for 0-1 test for chaos
$\boldsymbol{CA}$	constant part FID with respect to $\boldsymbol{\tau}$
CD	correlation dimension
CE	correlation exponent
CI	confidence interval
$CM_{iter,d}$	mean of current population along d^{th} dimension in $iter^{th}$ iteration
$cog_{initial}$, cog_{final}	limits of cognitive acceleration coefficient
$\boldsymbol{CS}$	correlation sum
ct	cutting time (min)
$CT_{iter,\,d}$	teacher of current population along d^{th} dimension in $iter^{th}$ iteration
cur	current (A)
d	training input space dimension
$\boldsymbol{d}$	coefficients of backward linear prediction
$\boldsymbol{D_c}$	modified mean square displacement for particular c
$f(\boldsymbol{x})$	target function
FID	freely induced decay
$g_{best,\,d}$	component best position of swarm along d^{th} dimension
$\boldsymbol{H}$	Hankel matrix
$iter_{max}$	maximum number of iterations
K	number of FIDs buried in roughness profile, median of all K_cs obtained from a parent time series
$K(x_i, \boldsymbol{x})$	kernel function
$\boldsymbol{K_c}$	asymptotic growth rate for particular c
L	predictor order of backward linear prediction
m	embedding dimension
M	number of points in phase space
$MATE_1$, $MATE_2$	mean absolute training error in estimation of MRR (for 1) and ASR (for 2)
$\boldsymbol{M_c}$	mean square displacement for particular c
MRR	material removal rate (mm^3/min)

n	number of particles in swarm, number of learners in class, number of profile heights collected from roughness profile, length of time series
N	number of training data, length of ACF
n_{cut}	length of $\boldsymbol{M_c}$, $\boldsymbol{D_c}$, $\boldsymbol{\xi}$, $\boldsymbol{\delta}$
$\boldsymbol{p_c}$, $\boldsymbol{q_c}$	translational vectors for particular c
$p^i_{best,\,d}$	component best position of i^{th} particle along d^{th} dimension
PR ratio	periodicity to randomness ratio
PLM	power law model
PSO	particle swarm optimization
r	radius of hyper-sphere, a pseudorandom integer generated following standard uniform distribution within range [1, n] except k
r^2	coefficient of determination
$\boldsymbol{R}$,$\boldsymbol{R'}$	real coordinate space, roots of polynomial with coefficients $\boldsymbol{d}$
Ra	center line average surface roughness (μm)
rand	a pseudorandom number generated following standard uniform distribution within range (0, 1), Gaussian random vector
RITE	redundance and irrelevance tradeoff exponent
Rku	kurtosis of the distribution of profile heights
RLo	developed length of profile (%)
Rng	span of searching range
Rrms	root mean square of profile heights (μm)
Rsk	skewness of the distribution of profile heights
Rt	maximum peak to valley height over evaluation length (μm)
rw_1, rw_2	random weight factors
RΔq	root mean square of slopes of profile (°)
s	sample standard deviation of ACF
SOAC	second order autocorrelation
$soc_{initial}$, soc_{final}	limits of social acceleration coefficient
$\boldsymbol{SP}$	variable part of FID with respect to $\boldsymbol{\tau}$
std	standard deviation of population
SVD	singular value decomposition
SVM	support vector machine
t_{off}	pulse off time (μs)
t_{on}	pulse on time (μs)
$TF_{iter,\,d}$	teaching factor along d^{th} dimension in $iter^{th}$ iteration
TLBO	teaching learning based optimization
$\boldsymbol{u}$, $\boldsymbol{v}$, $\boldsymbol{w}$	parameters along the dimensions of cur, t_{on} and t_{off} respectively
$\boldsymbol{U^H}$, $\boldsymbol{S^H}$, $\boldsymbol{V^H}$	components of SVD of Hankel matrix $\boldsymbol{H}$
$v^k_{iter,\,d}$	velocity component of k^{th} particle along d^{th} dimension in $iter^{th}$ iteration
$\boldsymbol{w}$	weight vector
W	length of Theiler window

$\boldsymbol{x}$	training input vector, pseudo Pareto optimal vectors, control points on Bezier hyper-surface
$x^{k}_{iter,\, d}$	component of velocity corrected position of kth particle along dth dimension in iterth iteration
$x^{k}_{new,\, d}$	component of kth new learner along dth dimension after teacher phase
$x^{r}_{new,\, d}$	component of randomly selected rth new learner along dth dimension after teacher phase
$\bar{x}$	sample mean of ACF
$\boldsymbol{y}$	training output vector, profile height (µm)
$\boldsymbol{Y}$	phase vector
y_{min}, y_{max}	minimum profile height (µm), maximum profile height (µm)
$\boldsymbol{y_{norm}}$	normalized profile heights
$\bar{y}$	mean of training output set, mean of n profile heights (µm)
z	number of attributes
α	level of significance
$\boldsymbol{\alpha}$	decay rate of FID
α_i, α_i^*, η_i, η_i^*	Lagrange multipliers
$\boldsymbol{\beta}$	characteristic correlation length of FID (mm)
ε	radius of loss insensitive hyper-tube
$\boldsymbol{\lambda}$	period of FID (mm)
v	degrees of freedom
$\boldsymbol{\xi}$, $\boldsymbol{\delta}$	variables used for calculation of $\boldsymbol{K_c}$
ξ_i, ξ_i^*	slack variables
ρ	measured density of workpiece (gm/mm^3)
σ	standard deviation of radial basis function (kernel function), standard deviation of n profile heights (µm)
$\boldsymbol{\tau}$	lag e.g. 1, 2, 3, ... etc, embedding delay
τ_{opt}	optimum embedding delay
$\boldsymbol{\Phi}$	phase angle of FID (in radian)
$\Phi(\boldsymbol{x})$	feature space
$\psi_{initial}$, ψ_{final}	limits of constriction factor
$\boldsymbol{\omega}$	angular frequency of FID
$\omega_{initial}$, ω_{final}	limits of inertia factor

TABLE OF CONTENTS

CHAPTER 1

INTRODUCTION

Modern industries like automobile, aeronautical, nuclear reactor demand materials having combination of diverse properties like higher strength temperature resistance (HSTR), higher hardness, higher toughness and also higher strength to weight ratio concurrently. To meet the demands, different alloys like nimonics, stellites, ceramics, particle and fiber reinforced composites are invented by researchers [1, 2]. Besides, machining of such hard to cut materials creates a challenging task to process engineers. Making of complex intricate shapes like blind holes, non-circular holes, holes with shallow entry angle, holes with large aspect ratio, conformal channels on very hard materials like titanium, tool steel put limitations on productivity. With the aid of material removal by physical contact with wedge shaped tool in the form of chips formed due to plastic deformation in conventional machining processes, high production rate, better surface finish and near zero tolerance could not be achieved simultaneously.

Therefore, different methods of material removal, named under the group of non-traditional machining (NTM) process, are invented. Based on the sources of energy used for machining operation, NTM processes are broadly classified in the four groups namely mechanical processes, electrical processes, thermal processes and chemical etching processes [3]. Material removal may not be due to macroscopic chip formation (AJM, UCM), physical tool might be absent (WJM, LBM), cutting tool need not to be harder than workpiece (EDM) and not necessarily mechanical energy required for machining (ECM, EDM) are some significant advantages of NTM over conventional machining. As a consequence, better surface finish with close tolerance are easily achieved. Each of the non-traditional machining processes is suitable for specific working environment. Selection of the process depends on physical parameters, properties of workpiece material, final geometry, production constraints, process capability, economic considerations etc. [4].

Among all the NTM processes, electric discharge machining (EDM) gains high popularity for its potential to machine complex shapes with high accuracy and precision on almost all conductive materials irrespective of their strength, hardness and toughness. Development of electric discharge machining (EDM) was started in the mid of 1940's. Since the debut of EDM, modifications are still going on. Whatever might be the modifications, presence of uncertainty in the mechanism of material removal still keeps it away from very accurate controlling. As a result, prediction of process outcomes and setting of the optimum levels of machining control parameters become more challenging.

Reported developments on the assessment of EDM process outcomes have been grouped into modeling and optimization. Different analytical, empirical and intelligent procedures are used to build representative model of EDM process. From the theory of material removal mechanism in spark erosion, it is obvious that involvement of transient thermo-electric phenomena, complex behavior of plasma dynamics, material inhomogeneity, flow of dielectric and debris particles cause erratic fluctuations in process outcomes. As, quality of the product should be maintained at predefined specific level without too much sacrificing productivity, so, along with robust modeling and optimization methods, systematic scientific investigation for understanding the underlying features of EDM process is necessary. In machining process, machined surface carries the inherent features of surface generation process, thus, meticulous study of surface topography is inevitable for accurate representation of EDM process.

While highlighting the lacunae in the existing methodologies of modeling, optimization and assessment of surface topography, machining theories, process parameters involved, specific applications and difficulties in EDM and proposed study on modeling, optimization and assessment of surface topography are presented in chapter 2. In light of the discussions, specific objectives for the present work are set forth in the same chapter.

From the review of literature, need of appropriate experimental data for the proposition of robust modeling and efficient optimization is evident. To cover a wide range of applicability of the proposed models, ample experiment should be conducted. Significant machining control parameters are identified from literature namely current, pulse on time and pulse off time and different levels are chosen from the available machine settings. Experiments are designed and performed in keeping with the decided objectives of the present work. Experimental results of the quantitative measurements of process performance like material removal rate, different surface roughness parameters exhibit irregular variations. Therefore, application of an advanced robust modeling technique becomes prerequisite. It is also observed that quality of machined surface reduces with increase of production rate. Thus, a guideline is required to obtain the possible maximum level of surface finish without sacrificing productivity. To deduce this tradeoff, optimization of the process outcomes is necessary. Further, scanning electron micrographs of various machined surfaces are taken. Complex pattern, erratic fluctuations and overall random behavior of surface topography are found. This type of surface topography compels further investigation to reveal the underlying features of surface topography and correlate the surface topography with surface generation in EDM process. Details of experimentation are reported in chapter 3.

In order to improve the prediction capability, the proposed modeling technique must address complex high dimensional interactive behavior of input parameters and irregular variations of process outcomes. In this regard, a supervised batch learning methodology, named as support vector machine (SVM) regression, is suggested for modeling of the two process outcomes, material removal rate (MRR) and average surface roughness (ASR). In SVM regression, experimental data are fitted through minimization of the upper bound of expected risk along with empirical risk. Adverse effects of complex high dimensional interactive patterns of input parameters are reduced by mapping the input space to feature space. Irregular variations in process outcomes are absorbed by introducing a insensitive zone around the estimated model that is points inside the insensitive zone are deemed as zero error in fitting. The insensitive zone allows the engineers to use the model for products obtained in different batches. One of the major contributions of the present work is to frame out the exact procedure for modeling of such process through SVM regression. During model development, internal structural parameters of SVM regression are optimized. For this optimization. two evolutionary metaheuristic techniques, particle swarm optimization (PSO) and teaching learning based optimization (TLBO), are imposed with some relevant modifications. The proposed modifications. namely current population based termination criterion, initial population with high dispersion measured by termination criterion, selection of guide for next iteration in case of multiple particles have same optimum score, are added to the existing algorithm for smoother convergence and could be implemented to other population based optimizations in a generalized way. Apart from the above said modifications, need of tuning of own internal parameters of PSO is eliminated in TLBO. Further, SVM regression based a unified learning system for MRR and ASR is tried to predict both the process outcomes from a single set of internal structural parameters of SVM regression. In this proposed unification process, a novel idea of handling multiple objective functions for solving multiobjective optimization problem is proposed which could be implemented to any multiobjective problem with large number of objective functions. The above said propositions for modeling of EDM process are elaborated in chapter 4.

Rate of material removal from workpiece controls the productivity of the process. Therefore, higher material removal rate (MRR) is always preferred. At the same time, productivity should not be increased at the cost of the quality of product. In EDM, higher MRR results low surface finish. Higher surface roughness of finished product exhibits deleterious effect on its long-term performance. Hence, during machining operation, a compromise between productivity and product quality is always maintained. Process engineers should be aware of the achievable limit of product quality without hampering the productivity schedule. This productivity-quality balancing must be completed at the early stage of product design. A typical weighted combination of MRR and ASR is formulated. With different combinations of weight factors, level of compromise is decided. The objective functions with different weighted combinations are optimized with the aid of modified TLBO. A pseudo Pareto front is found and a relation is developed which will guide the process engineers to select the achievable optimum ASR for a specific need of MRR. Further, an inverse solution methodology is proposed to select the near-optimum settings of machining control parameters in EDM machine to get near-optimum combination of MRR and ASR which is another major contribution of the present work. In chapter 5, the above mentioned optimization process is discussed in detail.

During the model building and optimization of EDM process, it is observed that the representation of the process is greatly affected by the erratic fluctuations in process outcomes. As, quality of machined surface is a consequence of complex material removal phenomena, so, thorough study of the characteristics of surface topography is necessary. In chapter 6, surface topography is analyzed by representing the roughness profile as a time series. Finite sequence of profile heights is considered as representative time series of machined surface. Autocorrelation function of representative time series is calculated and used for an organized analysis of surface topography. Contributive effects of randomness and periodicity in surface topography are assessed using a non-dimensional index, PR ratio. Further, presence of chaos in the surface topography is checked. This test for chaos is done from two different perspectives. In first approach, phase space is reconstructed from representative time series with chosen set of embedding delay and embedding dimension. Correlation exponents are estimated for a selected range of embedding dimensions. In second approach, test for chaos is performed directly on the representative time series. The results from both the approaches suggest similar features of surface topography and thereby correlate surface generation process in EDM.

The salient conclusions are drawn and the recommendations are suggested in chapter 7.

CHAPTER 2

REVIEW OF LITERATURE

2.1 Introduction

Electric discharge machining (EDM) process is widely used in recent-day manufacturing practice. Electric sparks for metal erosion was first used by Joseph Priestly, an English chemist, in 1878 [3]. After several years, Lazarenko [5] of Moscow University did control machining by electric sparks in 1944. Within next 6 to 8 years, machines using spark erosion were developed in USA, Japan and Switzerland. Since the first development of spark erosion machines, modifications are still going on towards nano-scale precision machining.

As the major concern of the present study centers around modeling, optimization and assessment of surface topography in EDM process by advanced methods, the review of literature has been restricted to arriving at the need of the present work vis-a-vis the existing literature and its lacunae. The topics for discussion are arranged as (i) machining theories and mechanism of material removal, (ii) parameters involved, (iii) applications, (iv) modeling of the process for responses, (v) optimization of the process performances and (vi) assessment of surface topography.

2.2 Machining theories and mechanism of material removal

Electric discharge machining is capable of machining any conductive material (resistivity should not exceed 100 ohm-cm) regardless of its hardness, toughness and strength [6]. Material is removed by high frequency, high power density, spatial and sporadic electrical discharges (sparks). In general, both the electrodes - tool and workpiece are immersed in dielectric fluid with a precisely controlled fine gap (figure 2.1) maintained at 10-100 µm [7] depending upon electrode-dielectric combination. The performance of EDM process is primarily dependent on energy release during sparking. There are four theories which try to explain the erosion phenomena in spark machining.

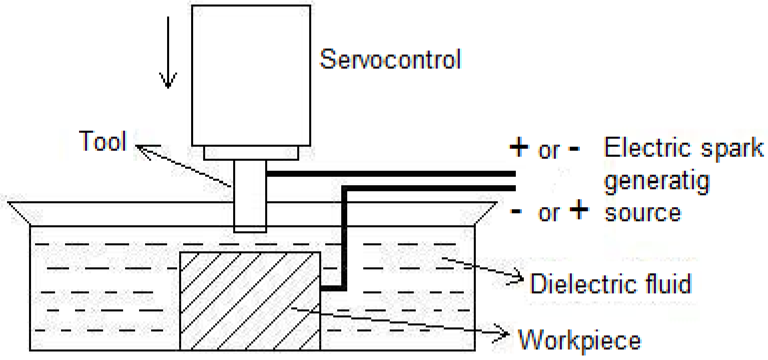

Fig. 2.1 Schematic of electric discharge machining process [1]

2.2.1 High pressure theory [8]

According to high pressure theory [8], high impulsive pressure is released on the electrode surfaces due to sudden stoppage of electro-dynamic waves. This high impulsive pressure is considered to be responsible for the erosion of electrodes.

Pressure of electrical discharge was first measured by Niwa and Fujimoto [9]. Inoue [10] reported that pressure as high as 1000 kg/mm^2 was caused but the expected plastic deformation was not found on the surface. From the energy distribution of discharge spectrum, Motoki and Hashiguchi [11] reported that the pressure in the arc column was 0.1 to 1 kg/mm^2 only. Satio and Kobayashi [12] obtained that the duration during which pressure acts was longer than the discharge period. Fujimoto and Togoshima [13] measured the maximum force about 60 kg and observed that the impulse was proportional to the discharge power. It was concluded [8] that in smaller energy discharges, the discharge pressure alone would not be sufficient to erode the material, but in conjunction with some other facts, such as heat energy, the pressure might blow out molten metal from the electrode surfaces.

2.2.2 Static field theory [14, 15, 16]

Electro-mechanical theory or static field theory states that erosion takes place only because of ripping away of bits of the electrodes by a strong electric field that produces sufficient electrostatic force [14].

For very short discharge duration, less than 2 µs, force required for tensile rupture is generated due to strong electric field gradient caused by extremely high current density under electrode surface. For ferromagnetic materials, current density decreases substantially as current passes inside. Therefore, skin effect comes into play which is unlikely in non-ferromagnetic materials. Due to the assumption of non-involvement of ionic force in material removal, this static field theory is not capable of explaining the material removal for discharge duration longer than 2 µs. In case of stainless steel cathode, Singh and Ghosh [15] observed that for pulse on time less than 5 µs, electrostatic force acting on the surface played dominant role in metal removal and crater depth varied with square root of total current during discharge. As the pulse duration increased, yield strength decreased and electrostatic force became not sufficient for rupture the material. Even the assumption of non-influence of EDM process on material properties of electrode surface was proved to be wrong as metallographic investigations revealed the presence of a thin layer of resolidified and rehardened metal on the electrode surface [16].

2.2.3 High temperature theory [8]

According to the high temperature theory [8], the bombardment of the charged particles on the respective electrodes results in high temperature at those spots. Because of this high temperature, material at the respective spots instantaneously melts and vaporizes leaving a crater on the surface. The ratio between the energy expended at the anode and the total discharged energy are related to various parameters like gap between the electrodes, mean-free-path of electrons, cathode and anode work-functions. There is a large variation among the suggested percentage values of the total energy carried by the electrodes. Singh [17] observed that the fraction of input energy transferred to the anode (workpiece) varied from 6.1% to 26.82% with different settings of current and pulse duration. DiBitonto et al. [18] and Patel et al. [19] found that cathode (workpiece) took away 18% of total input energy. Using water as dielectric, Shankar et al. [20] found that 40-45% of heat input was taken away by anode (workpiece) itself. Zhang et al. [21] suggested that energy transferred to the cathode (workpiece) was almost 50% of the total input energy.

The joule-heating by high density current of the discharge channel was also considered to contribute towards the generation of this high temperature. Marafona and Chousal [22] considered this radius of the conductor (high current density channel) was a function of current intensity and pulse duration with no variation of electrical potential in the radial direction.

2.2.4 Thermo-electric theory [16, 23]

According to thermo-electric theory [16, 23], the discharge occurs in several stages. The charge induced on the two electrodes by the power supply creates an electric field at a location where the electrodes come closest. This is where the discharge takes place. Molecules and ions of the dielectric fluid are polarized and oriented between the two peaks, forming a narrow, low-resistance channel. Actual current flow is initiated, as current ‘streamers’ organize and open the way to the main flow of current. The emitted high velocity electrons collide with dielectric molecules, makes them ionized and secondary electron emission starts. Ionization continues through the next two stages, even though current is already flowing between the two electrodes. In the next stage, resistance of the channel continues to decrease while the current is increased. Supplied electric energy is transformed to thermal energy. At this point, the ionized path consists of plasma [24], formed from positive ions and free electrons, mixed with the gas formed by the chemical decomposition of the dielectric. Current intensity in the plasma channel is very high at this stage, perhaps in the order of 10^7-10^8 A/s. The high current continues to ionize the channel and produces a strong magnetic field, which attracts the ions towards the axis of the discharge channel (pinch effect). The magnetically attracted ions compress the channel of current and increase its temperature in the range of 8000°C to 12000°C [25] or as high as 20000°C [26], which melts a portion of the electrodes and vaporizes some of it.

2.2.4.1 Ejection of molten material and formation of crater

The forces causing the ejection of the molten material from the electrodes are not fully understood [27, 28]. Although it is believed that shock waves and electromagnetic and electrostatic forces are responsible for violent nature of ejection of material [29].

Presence of evaporated conductive electrode material is much higher than dielectric vapor because ionization potential is much smaller for metals (Cu: 7.7 V, Fe: 7.8 V) than non-metallic gases (N_2: 15.9 V) [30]. Generated metal vapor at electrode surface provides some of the forces needed to expel the molten material from the electrodes and the rapidly collapsing ionized channel assists the process. Due to high temperature, dielectric starts to vaporize, plasma channel expands radially and very high pressure inside the plasma channel distributes shock wave in surrounding dielectric medium. Another effect, the mechanical impact of the discharge itself, contributes to the expulsion. Even, electrostatic force from the electrodes pulls apart some amount of molten material [31].

On the contrary, VanDijck et al. [30] proposed a different theory to explain the ejection of molten material, the majority of which takes place at the end of a pulse. Liquid material in the crater is superheated to a temperature corresponding to the boiling point at the increased pressure within the plasma channel. Sudden drop in this pressure at the end of the pulse causes the material in the subsurface layers to boil vigorously. As a result, liquid drops will be ejected from the molten material pool by rapid formation of vapor bubbles. This boiling can take place in a material volume defined by the electrode surface and the boiling point isotherm at ambient pressure. At the end of discharge, temperature at electrode surface suddenly drops and plasma channel collapses, the maximum possible volume of material has been already melted. Due to severe thermal gradient and surface tension, tensile and bonding strength between liquid-solid phases [32], part of molten material is exploded and rest is resolidified forming tiny debris particles. This evacuation process is virtually the only remaining mechanism for displacing any appreciable amount of material.

After the "flare" ejection of material [33], each discharge left craters on electrode surfaces, a large crater in the workpiece (hopefully) and a smaller one in the tool electrode. Molten material removed from the electrode surfaces cools quickly in the dielectric liquid, forming tiny spheres that are flushed away [23]. This ejected part forms a bulge around the crater. The path of expulsion leaves marks on the edge of the crater. Ejection occurs tangentially to the crater lip and the molten layer breaks up into fragments. Based on the analysis of hydrodynamic propagation of shock waves generated due to electrical breakdown in dielectric, an expression for the velocity for the ejected particle is available [29]. The tracks of ejected particles are straight lines. Particles typically travel many crater diameters and resolidify in the dielectric. Some of the ejected particles definitely bombard a nearby electrode surface [27].

Volume % of molten material removed depends on thermal expansion coefficient of electrode material, amount of molten material, plasma channel radius, thermal properties of electrodes, dielectric flushing conditions [32]. Material equivalent to almost 8-10 times of final crater volume melts and 10-15% of the final crater volume vaporizes [34]. Around 10-15% of total molten material is removed at the end of discharge [34]. Though volume of material removal in each discharge is in the range of 10^{-6}-10^{-4} mm^3 [35], still, frequency of discharge is maintained at high level - 10^3-10^6 Hz [7]. For small electrode gap, high pressure results large force on tool and workpiece, but there is a restriction effect of the surrounding medium on expansion in large discharge gap [36]. In case of large discharge gap, plasma channel is longer and as a consequence, amount of heat loss, radial diffusion of ions and amount of recombination occurred between anode and cathode drop region increase. Material removal efficiency decreases on account of the losses. Though to accommodate high discharge energy (above 50 mJ), electrode gap is increased to maintain breakdown strength [37], still, smaller inter-electrode distance yields higher material removal rate. Erden [31] studied the effects of different pulse shapes on material removal rate. Pulse shape having negative slope causes higher material removal rate compared to pulse shape having positive slope. For the pulses having positive slope, wear in tool electrode also reduces. Therefore, to achieve highest material removal rate from workpiece and lowest from tool simultaneously, shape of pulse should be justifiably selected.

During discharge time, normal component of stress at the surface changes from compressive to tensile, whereas, inside the electrode, it remains compressive [38]. High compressive stress is generated (greater than 3 GPa) at the direct heat spot. As the material melts, this stress is relieved.

Then, cooling of this molten and expanded material causes high tensile stress (more than 3GPa) and results in disintegration of material. At the beginning of cooling at around 1100 K, heterogeneous solidification starts and more than 3 GPa residual tensile stress exists at this resolidified layer. When temperature falls down below 700 K, homogeneous solidification starts. White layer is formed where tensile and compressive stress exist alternatively [39]. Therefore, residual stresses at the surface and inside the electrode are conflicting type, which causes more prone area of crack generation [38]. Crack propagates from top surface to almost twice the crater depth [40]. Higher heat flux and longer pulse duration favor more thermal damage in EDM.

Selection of the polarity of electrodes plays crucial role in material removal as rate of material removal from the electrodes are different. The phrase "all parameters yielding a decrease of the current density will reduce the positive electrode wear" [30, 41, 42] is common to the researchers. For higher pulse duration, current density decreases, anode wear decreases. Growth rate of plasma channel are increased for longer pulse duration due to reduction of inertia forces acting upon less denser dielectric flown into electrode gap. Growth rate of plasma are also increased due to reduction of dielectric pressure. All the above said effects cause lower current density and thereby result smaller anode wear. Therefore, in case of pulse generators, negative polarity for workpiece is generally recommended.

Hence, surface generated in EDM is superposition of the craters formed by each of the discrete discharges. As machined surface topography is combined effect of all discharges, the time and space separations between discharges are very important. Though high frequency of discharges is to be maintained to get good productivity, yet, enough time between successive discharges is necessary to recover the breakdown strength of dielectric medium. As, next discharge will occur at the position of minimum resistance between electrode surfaces, so, to avoid localized non-uniform erosion of material, proper flushing of debris particles after each discharge is to be ensured [43]. Otherwise, colloidal suspension of removed particles may form current carrying bridges at electrode gap which cause repeated melting and reunion resulting low productivity and poor surface integrity.

However, materials with melting point below 2800ºC are eroded by the above melting mechanism, while for the materials with higher melting point, such as TiB_2, BN-TiB_2, the mechanism of erosion is thermal spalling [44, 45].

2.2.5 Spalling and oxidation/decomposition

Spalling effect is most often related to the generation of larger micro-cracks perpendicular and parallel to the top surface. The large micro-cracks make the separation of material during successive discharges much easier [46]. Due to lower fracture toughness and mechanical strength of Al_2O_3-TiCN compared to ZrO_2-TiN, severe micro cracks are induced on machined surface [47]. The cracks propagate parallel to the surface and may cause detachment of large flakes during subsequent sparks. Malek et al. [48] investigated the spark machining of transition metal diboride ceramics like $(Nb_xZr_{1-x})B_2$-SiC. They suggested both the thermal shock due to negative thermal expansion coefficient of Nb_2O_5 and concomitant spalling that was material delamination due to high residual stress as the dominant material removal mechanism. Apart from ceramic composites, sub-surface microstructure of electric discharge machined aeronautical alloy (Inconel 718) [49], hard to machine Ti-6Al-4V [50], ceramic/carbon nanostructure composite [51] and diamond polycrystalline super hard material [52] showed mostly the crack formation as their dominant material erosion mechanism.

Material removal of ceramic matrix composite is mostly through cracking, crack expansion and stripping off [53]. Insulating fibers are broken due to thermal expansion/compression by the cracks. During the pulse on time, rise of temperature might be sufficient enough to melt the matrix due to its lower melting temperature than reinforced material [54]. After melting of matrix material, no binding exist, reinforcement could be easily evacuated from the crater without getting melted.

During machining of conductive ceramic composites [46] that is ceramic materials, namely ZrO_2 based, Si_3N_4 based and Al_2O_3 based, with additions of electrical conductive phases like TiN and TiCN, material is removed through oxidation/decomposition along with spalling. In case of short pulse duration that is less than 2 µs (relaxation discharge pulse), dominant mechanism is chemical reactions like decomposition and oxidation. When deionized water is used as dielectric medium, huge amount of nitrogen gas is evolved which becomes responsible for porous structure of the machined surface [46, 55]. When discharge duration is relatively long, the input energy is higher (iso-energetic pulse). In lieu of oxidation/decomposition and spalling, melting/evaporation becomes dominant and forms more regular craters relative to splashed crater in short pulses. It is found that compared to long pulses, tool wear ratio is lower and machining speed is higher [55].

Different variations over standard configuration of EDM are developed to meet the ever-growing demands of modern industries like machining of exotic, high strength and temperature resistive (HSTR) and super hard metal alloys used in aeronautical and aerospace parts. In Wire-cut electric discharge machining (WEDM), a thin continuously fed wire is used to shape workpiece. Fabrication of need-based shape of tool electrode for die-sinking EDM is not required in WEDM. Further, hybridization of standard EDM process is also developed by combining laser beam machining, ultrasonic machining, grinding etc.

2.3 Process parameters involved in EDM process

As discussed above, EDM involves transient thermoelectric phenomena in the dielectric medium present at the gap between electrodes having certain metallurgical features. Therefore, recognition and classification of different electrical and non-electrical parameters provide viable option for close monitoring and control of EDM process. Process parameters involved in EDM [1, 7, 35, 56-58] are listed in figure 2.2.

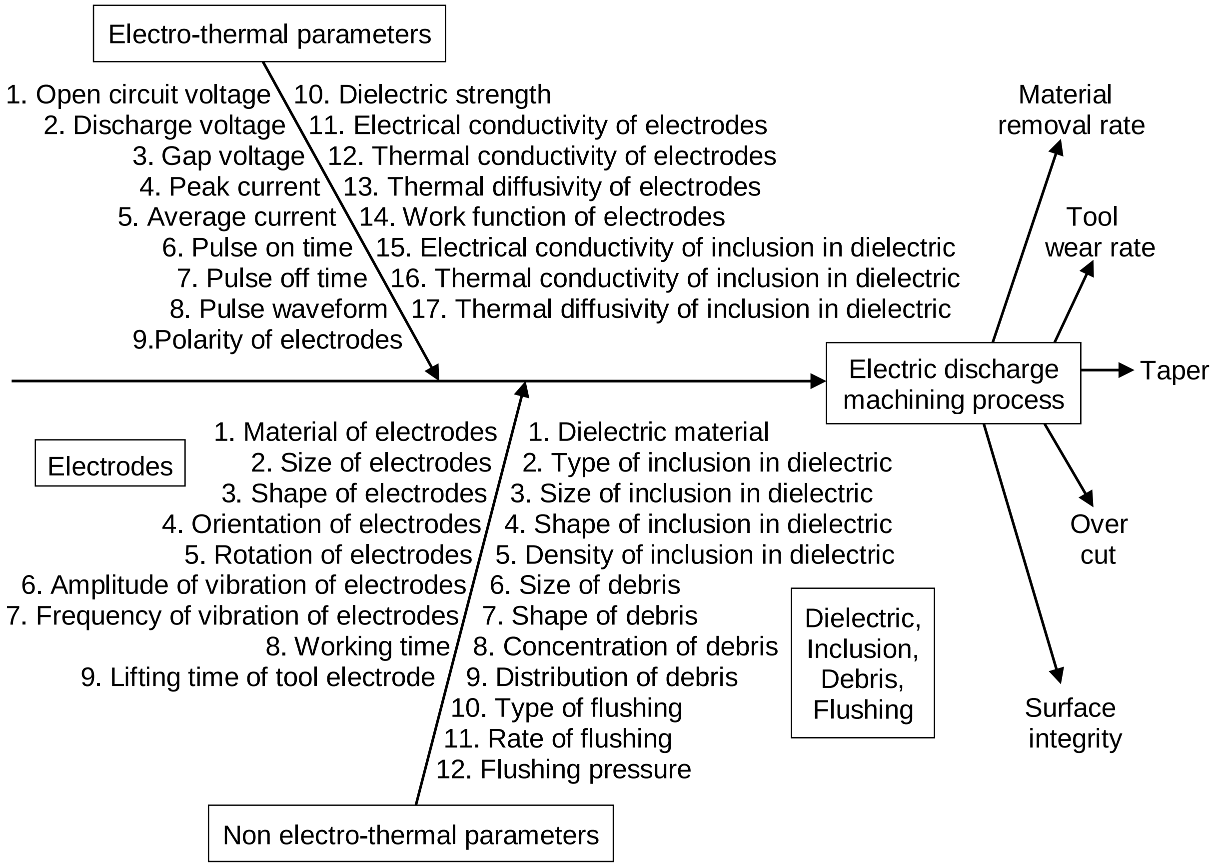

Fig. 2.2 Process parameters involved in EDM process

2.4 Applications

Electric discharge machining process is well known for its wide range of applications in modern industries. Electric discharge machining is a potential process of developing complex surface geometry and integral angles in mould, die, aerospace, surgical components etc. [35] irrepective of hardness, toughness and strength of material. Different hard to machine materials even toxic materials can be machined by EDM. Dies for moulding, casting, forging, stamping, coining, extrusion, wire drawing with intricate features like square, hole, D-shaped holes, narrow spline-shaped slots, conformal channel are also manufactured by EDM operation. Broken tap, drill, stud, reamer, pin could be removed from machine parts by EDM process. With relatively small sub-surface damage, EDM is applicable for machining particle reinforced metal matrix composites. Even WC-Co coated ceramic-metal composite steel plate could be machined by EDM [59]. Now-a-days feasibility of machining ceramics doped with conductive material is tested [46]. As there is no burr formation in EDM operation, post-treatment cost like polishing reduces.

During EDM operation no mechanical force acts except bursting pressure of plasma channel. Thus, very thin and fragile components (in micron level) can be manufactured. Micro-EDM is capable of making micro-holes of diameter 40 µm and micro-shafts of diameter 5 µm with high repeatability.

As EDM generated surface is composed of tiny craters, distribution of lubricants over entire machined surface could be maintained. Even, low fatigue strength could be achieved in components having surface machined by EDM process.

Though different difficult to manufacture parts could be produced by EDM process, still, resistivity of workpiece, crack generation, low material removal rate and emission of aerosols put limitation towards successful utilization of the process in modern industries. Even, performance of EDM for material with both high electrical and thermal conductivity like aluminum is not very good [1]. Emission from EDM process might be a mixture of metallic particles and different hydrocarbons of n-alkanes, branched alkanes, aromatic compounds, alicyclic compounds, hetrocyclic compounds etc. [60]. The emissions can cause adverse health effect to the operators and have direct impact on environment. Paramashivan et al. [60] showed that 70% of the constituents of aerosol generated from EDM process were metallic particles which are caused by the vaporization of workpiece and tool electrode. Remaining 30% consisted of carbon particles and other reaction products attached to aerosol.

The goal of developing and deploying machining techniques, capable of meeting almost all performance requirements, is difficult to achieve till now. Whereas, near exact representation of the process and thus, setting of control parameters to achieve simultaneous optimum responses are necessary to freeze the procedure at the earliest in pre-production stage. Therefore, characterization of EDM process is still persuaded so as to work in virtual world. Manufacturing processes could be well characterized by both the quantitative and the qualitative assessments of their performances. The performance measures are to be modeled and optimization of process performances is to be done. It is to be noted here that due to involvement of complex electrodynamics, electromagnetics, thermodynamics and hydrodynamics in spark erosion, assessment of process performance is very difficult. Different approaches taken by the researchers for model building, optimization of process performances and assessment of surface topography are sequentially reviewed in the next three sections.

2.5 Modeling of EDM process

Modeling of any process plays crucial role for developing a virtual platform of the process. Different researchers considered different approaches to reveal the underlying relationship of EDM process parameters and outcomes. Broadly, three groups are identified namely analytical, empirical and intelligent procedure for model building (refer figure 2.3). Discussion on each of the three groups is made in the following subsections and is restricted to a few relevant literature in each group.

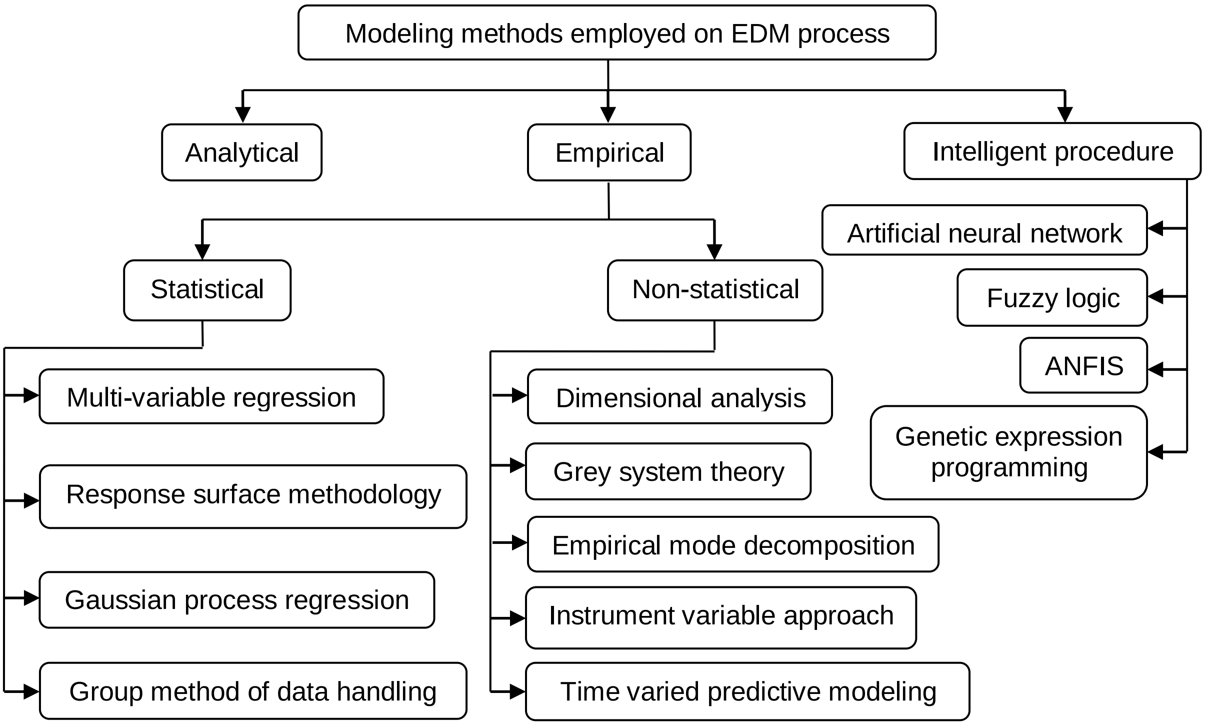

Fig. 2.3 Classification of modeling methods employed on EDM process

2.5.1 Analytical modeling

Analytical method for model developing addresses the fundamental knowledge of the physical phenomena behind the process.

In general, physical phenomena behind the material erosion is tried to be numerically framed in analytical modeling of any machining process. Melting/evaporation, spalling and oxidation/decomposition are the main causes of erosion in EDM process depending on the metallurgical behavior of workpiece material. In section 2.2, it is mentioned that during machining operation, immense heat is generated at electrode surfaces. Plasma formation-growth-collapse and its aftereffects are found to be the main cause of heat generation and material erosion (refer subsection 2.2.4). As, generated surface topography is a superposition of craters with various shape and size formed after removal of material, so, plasma channel remains in the core of analytical modeling through thermal approach. Therefore, understanding of plasma channel geometry and temperature distribution therein are very much essential. The information available in literature [21, 32, 61-75] regarding that is summarized and given in table D.1 in appendix D.

Plasma channel diameter was measured by two experimental methods namely, metallographic method [21, 37, 74-76] and optical spectroscopic [69,77] method. The transient nature of plasma channel in EDM was confirmed by ultra-rapid photographic study [78] and kerr-cell photographs taken for underwater (deionised) plasma [79-81]. Still, due to high temperature and high frequency of sparks, measurement of plasma channel geometry was very difficult in EDM. In general, characterization of plasma channel was done either estimating the growth rate from analytical relationship for a given tool-workpiece combination [78, 82] or through experiments by exploding wires in water [79-81]. While some investigators [30, 41, 42, 78] followed the first method, others [19, 83] followed the second. Even, in the first method, there were three different analytical approaches for the computation of plasma channel growth namely thermodynamic model, crater shape measurement and constant surface temperature approach [78, 82]. The net emission coefficient of plasma channel [84] was estimated using fluid description approach [85] in liquid nitrogen dielectric medium.

However, adapting the plasma channel characteristics, modeling of material removal through estimation of crater geometry was attempted by different researchers. In 1972, Snoey and VanDijck [82] first studied the effects of spark radius on different responses of EDM process. It was observed that spark radius was very sensitive to tool-workpiece electrode material combination. In 1983, Erden [32] considered pulse shape as rectangular and suggested an empirical relationship (refer table D.1) among spark radius, discharge power and discharge duration for specific tool-workpiece electrode pair and dielectric. Padey and Jilani [61] included energy density and material properties like boiling temperature, thermal diffusivity in their proposed model of spark radius in 1986. Still, the suggested model was limited to be applicable for a few pair of electrodes and dielectric. A critical assessment of five important thermal models based on thermo-electric theory was published by Yeo et al. [86] in 2008. Main considerations, assumptions, fraction of discharge energy, radius of the heat flux and limitation of the models [18, 61, 78, 87-91] are listed in table D.2, in appendix D. DiBitonto et al. [18] and Patel et al. [19] introduced point heat source model for cathode erosion and expanding circular heat source model for anode erosion. In cathode erosion model [18], they considered power as a boundary condition instead of conventional temperature conditions. Though, power was supplied at a point, yet, the area, upon which heat flux was working, was growing with time. Melting front and subsequent resolidification boundary were rapidly migrating. Thus, expanding circular heat source model for anode erosion was considered by Patel et al. [19]. They assumed that the erosion took place through melting by one spark per single pulse. Plasma radius at anode was growing with fractional power of time. Plasma flushing efficiency at anode was marginally low compared to cathode model. In microscopic level, the spark characteristics were studied by Shankar et al. [20] through an integrated approach analyzing dielectric and electrodes together. Using finite element method, spark profile was found to be non-cylindrical and at the middle section it was the smallest. Generally, electrode having high thermal diffusivity made larger spark radius but, cross section at the cathode interface was found to be larger than anode-interface. During simulation, spark radius was corrected considering the discharge current at each cross section as constant [20].

Two temperature model (TTM) and molecular dynamics based models were integrated and dynamical behavior of material at the atomic level in electric discharge machining was studied by Guo et al. [92] and Ming et al. [93]. During simulation of material removal, pure thermal condition, pure electric condition and hybrid action by combining both of them were implemented by Guo et al. [92]. When pure thermal condition was applied, it was found that, at the beginning, material was removed in the form of clusters due to thermal shock effect. As time progressed, strength of the shock waves was decreased and material was removed in the form of single atoms or tiny clusters. When, pure electric action was applied, generated high tensile stress caused polycrystalline region at the top part of cathode. Thus, material was removed in the form of single atom or small clusters. Ming et al. [93] observed that material was removed from the harder tungsten surface in the form of clusters, whereas, single atom was removed from comparatively softer copper surface. Yang et al. [94] reported that for low power density, vaporization played the significant role in material removal in the form of single atom and for high power density, material was removed in the form of clusters by bubble explosion. Crater surface morphology for the raised edges were simulated by considering the movement of molten material as incompressible viscous flow [95]. From the molecular dynamics based simulation, it was concluded that crater generated in gas medium was larger in diameter and smaller in depth compared to hydrocarbon oil. High power density resulted large diameter and depth of the molten area, and thereby improved removal efficiency as well as machinability [94]. Whatever may be the material removal mechanism, removal efficiency was very low (e.g. 0.02-0.05), as most of the molten part were resolidified. Stress in the resolidified layer highly fluctuated during the discharge progresses, but at the end, rate of fluctuation fell [38]. The spatiotemporal scale of the molecular dynamics confirmed this theory. Fluctuation of stress level and presence of alternating tensile and compressive stress during solidification were also supported by Zhang et al. [39]. They integrated TTM with molecular dynamics and exclusively suggested the material removal mechanism in four steps namely melting, disintegration, ablation and solidification.

Though EDM process could be applicable to any conductive material irrespective of its hardness, toughness and strength properties, researchers proposed methods to identify the ease of machining of any tool-workpiece combination. Earlier, ease of machinability was determined by λ X θ theory (λ =

thermal conductivity and θ = melting point of workpiece) [96]. That theory only used machining time as the decision parameter to measure the ease of machinability. Later Mahadika et al. [96] pointed out that time of machining might be affected by some complex phenomenon like adhesion, cavitation and short-circuiting. Therefore, they introduced electrical resistivity (ρ) of the workpiece along with the previous theory. Hence, the product of λ, θ and ρ of the workpiece material, was considered and five parameters, namely total energy of discharge pulses, discharge pulse number, average discharge pulse energy, discharge pulse density and tool electrode wear, were chosen for measuring the ease of machining.

Further, semi-implicit CFD algorithm was implemented in the FLUENT software for simulation of the turbulent model of dielectric flow with low Reynolds number [97] considering dielectric with constant density. Using Particle image velocimetry (PIV) [43], trajectory of debris particles inside the dielectric was studied. Wang and Han [98] proposed a three dimensional flow field model with solid, liquid and gas phases for simulation of debris and bubble movement inside the gap between electrode and workpiece.

A plate capacitor model was developed to describe the sparing process during pulse on time in EDM process [99]. The correlative functions of process parameters and energy distribution were deduced with the help of field electron emission theory. Energy analysis showed that the ratio of valid machining time and critical field intensity played crucial role for improvement of the efficiency of EDM process.

Pandit and Rajurkar [100] proposed a data dependent system based mathematical model in the form of stochastic differential equation of surface profile obtained from machining of cemented carbide (grades K-8 and K-701 of Kennametal). Their models were used to predict ejected volume of material and to evaluate thermal stresses which was further extended to estimate length of cracks in terms of material properties and machining parameters.

Analytical models are developed by framing the physical phenomena involved in the process. Yet, applicability of the developed model is limited as chosen assumptions reduces the closeness to actual event. In this regard, empirical modeling based on relevant experimental results is more effective for practical applications.

2.5.2 Empirical modeling – statistical approach

Empirical models are developed from the experimental results. A relationship is fitted among process parameters and outcomes. Unknown coefficients are estimated for the purpose. Under the group of statistical analysis, multivariable regression and response surface methodology are the most common approaches used by the researchers. Some researchers tried Gaussian process regression and group method of data handling for building prediction model of electric discharge machining process outcomes.

2.5.2.1 Modeling based on multivariable regression

Models based on multivariable regression consist of linear models, second order polynomial models, higher order polynomial models, power law models and multivariable regression models of fractional order. A few are briefly discussed here.

Linear models were built by Rajesh and Anand [101], Ugrasen et al. [102] and Mahapatra and Patnaik [103]. Rajesh and Anand [101] considered working current, pulse on time, pulse off time, working voltage, oil pressure and spark gap as input parameters and MRR and surface roughness in EDM as output parameters. They did L32 orthogonal array based experiments. Using molybdenum wire in WEDM of EN 31, Ugrasen et al. [102] developed linear models of accuracy, surface roughness and volumetric MRR. L16 orthogonal array was used to accommodate different levels of current, pulse on time, pulse off time and bed speed. However, no testing of estimated model was done. Mahapatra and Patnaik [103] did experimentation based on L27 orthogonal array. They used zinc coated copper wire and D2 tool steel as workpiece element. They developed linear models of MRR, surface finish and kerf width with input parameters as discharge current, pulse duration, pulse frequency, wire speed, wire tension and dielectric flow rate. Testing of fitted models were not reported there.

Second order polynomial models were built by Boopathi and Sivakumar [104], Liao et al. [105] and Huang et al. [106]. Boopathi and Sivakumar [104] considered discharge current, pulse on time, pulse off time, gap voltage and air mist pressure as input parameters and MRR and surface roughness in near dry WEDM of HSS (M2 grade) by molybdenum wire as output parameters. They did experiments using L18 orthogonal array. Their estimated models were further tested with 12 different data set. Liao et al. [105] did L18 orthogonal array based experiments with different levels of pulse on time, pulse off time, wire speed, wire tension, table feed and flushing pressure for WEDM of SKD11 alloy steel by brass wire. They developed models of MRR, gap width, surface roughness, discharging frequency, gap voltage and normal discharge frequency ratio. With same workpiece and wire material, used by Liao et al. [105], Huang et al. [106] accommodated different levels of input parameters, namely pulse on time, pulse off time, table feed, flushing pressure, machining history distance between wire periphery and workpiece surface, in L18 orthogonal array for experimentation in WEDM. Their estimated models of surface roughness, gap width, white layer depth were fitted with experimental results with high r^2 values. Though testing of fitted models were not reported.

A higher order polynomial model of MRR with current, pulse on time, pulse off time and capacitance as input parameters was estimated by Al-Ghamdi and Aspinwall [107]. They conducted 81 full factorial experiments in EDM of WC-Co by copper electrode. Their model was fitted with the experimental data with r^2 value 0.81. They did testing of their model with 9 sets of intermediated data points.

Power law model of wire wear ratio in WEDM of AISI 4140 steel by brass wire was developed by Tosun and Cogun [108]. Their model includes pulse duration, open circuit voltage, wire speed and dielectric flushing pressure as input parameters. They did testing of their model with 12 different sets of data.

Multivariable regression model of fractional order was developed by Petropoulos et al. [109]. They did experimentation with 12 different combinations of levels of current and pulse on time in EDM of CK60 carbon steel using copper electrode. Different roughness and waviness parameters, namely center line average surface roughness, quadratic mean profile inclination, mean spacing of the asperities, skewness of the profile height distribution and arithmetic average of waviness, were fitted. Testing of fitted models were not reported there.

Thus, it appears that for better fitting of estimated data, large size of data set is necessary for multivariable regression. So, rigorous experimentation is required. Besides, experimental results are fitted with predefined relationship. Along with fitting error, measurement errors further shift the model from accurate representation of the process.

.

2.5.2.2 Modeling based on response surface methodology (RSM)

Modeling based on response surface methodology considers central composite design, face centered central composite design and Box-Behnken design. A few models are briefly discussed here.

Rotatable central composite design was employed by Shashikant et al. [110], Das et al. [111] and Habib [112]. Shashikant et al. [110] and Das et al. [111] considered 31 experiments to accommodate different levels of discharge current, pulse on time, pulse off time and gap voltage. Shashikant et al. [110] correlated surface roughness with input parameters EDM of EN19 by electrolytic copper and found r^2 value 0.77. They did testing of their model with only the result obtained at the combination of mid-levels of each of the four input parameters and found 0.02% prediction error. Das et al. [111] developed models of MRR and surface roughness but no fitting error was reported and testing of estimated models was not done. Habib [112] considered peak current, pulse on time, average gap voltage and volume percentage of SiC as input parameters and accommodated 31 runs in EDM of Al/SiC composite material by copper tool electrode. Their estimated models of gap size, material removal rate, tool wear rate and surface roughness were fitted with r^2 values as 0.96, 0.93, 0.87 and 0.92 respectively. Testing of the fitted models was not reported.

Face centered central composite design was used by Assazadeh and Ghoreishi [113], Gopalakannan et al. [114], Pal et al. [115] and Maji and Pratihar [116]. Both Assarzadeh and Ghoreishi [113] and Gopalakannan et al. [114] measured MRR, tool wear rate and surface roughness as output parameters. Assarzadeh and Ghoreishi [113] considered discharge current, pulse on time, duty cycle and gap voltage as input parameters. They did 31 experiments in EDM of WC-Co by copper electrode and output parameters were correlated with input parameters. Values of fitting error were not given and no testing of estimated model was done. With gap voltage, pulse on time, pulse off time and discharge current as input parameters, Gopalakannan et al. [114] did 30 experimental runs in EDM of Al 7075/B_4C metal matrix composite by copper tool and their experimental results are fitted with r^2 value 0.98, 0.96 and 0.99 respectively. Testing of fitted model was not reported. Pal et al. [115] correlated MRR, surface roughness and fractal dimension of machined surface with current, pulse on time and pulse off time. They did 20 experimental runs in EDM of HSS (M2 grade) by copper tool electrode. They did not report their fitting errors but tested their estimated models with 5 separate runs and found 6.45%, 6.77% and 0.79% prediction errors respectively. Models of MRR and surface roughness with input parameters as peak current, pulse on time and duty factor were developed by Maji and Pratihar [116]. They took mild steel workpiece and copper electrode and did 17 experiments. Confirmatory test was done by six intermediate settings. Both the values of fitting error and testing error were not reported.

Box-Behnken design was implemented by Mohanty et al. [117] and Sahu et al. [118]. Mohanty et al. [117] correlated MRR and surface roughness measured in EDM of Inconel 718 with current, pulse on time, duty factor and type of tool material. Along with MRR and surface roughness, Sahu et al. [118] developed models of tool wear rate and circularity of workpiece. They considered discharge current, pulse on time, duty factor and flushing pressure as control parameters and did 27 experiments in EDM of AISI D2 steel by copper electrode. In both the studies [117, 118], values of fitting error were not given and no testing of estimated models was done.

Confirmatory test of estimated models is necessary before practical application of RSM based models. In most of the above studies, fitting errors and testing of estimated models are not reported. The above models, limited to development of second-order polynomial, could not reflect the effect of complex interactive relations among input parameters.

2.5.2.3 Modeling based on Gaussian process regression

Sufficient sampling is time consuming and expensive, still, large history might be helpful for future prediction. Gaussian process regression (GPR) performs better than neural network based prediction technique for short training data set. This Bayesian approach has the ability to choose hyper-parameters from training set directly and provides a probabilistic measure of uncertainty of the model prediction. In this approach, nonlinear process is treated as multiple-input-single-output (MISO) model [119]. Gaussian process (GP) is a collection of random variables of any finite number which have a joint Gaussian distribution. Gaussian process regression is developed on Bayesian framework. Correlation between two latent variables is defined by a covariance function. Two basic assumptions in this modeling approach are Gaussian noise and smooth response surface of process outcomes. Therefore, GPR model with Laplace or even Student-t distribution might be a good assumption for obtaining better result.

Yuan et al. [119] further developed GPR models of MRR and surface roughness of WEDM process with on time, off time and mean current as input parameters. Estimated models were trained with mean squared error 1.25 and 0.02 for MRR and surface roughness respectively.

Yuan et al. [120] improved the prediction capability and robustness of the model by fusing fuzzy model with GPR approach. Re-sampling algorithm based on GPR was proposed for incorporating prior model. True training data set and re-sampled prior confidence dataset were fused with piecewise relational transfer interpolation method and obtained a pseudo training data set. This fusion model predicted MRR and surface roughness better than direct GPR based model by 28.7% and 20.7% respectively.

Ming et al. [121] developed a hybrid intelligence model for prediction of MRR and surface roughness in EDM process. They implemented finite element method for estimation of process responses with different setting of pulse current, pulse duration and discharge voltage. The estimated responses were correlated by GPR approach. Estimated models of MRR and surface roughness were tested with six separate data sets and average prediction error were found as 14.75% and 20.74% respectively.

As, the random noise are assumed as Gaussian in nature, so, this approach may not work well for the data lies near to the boundary. Though offline training of relatively sparse training data are common in practice, still, this involves highly non-linear interactive optimization process.

2.5.2.4 Modeling based on group method of data handling

Group method of data handling (GMDH) is a family of inductive algorithms for computer-based mathematical modeling of multi-parametric datasets. This algorithm is characterized by inductive procedure that performs sorting-out of gradually complicated polynomial models and selection of the best solution by means of the so-called external criteria. To find best solution of GMDH algorithm, various component subsets of the base function (partial models) are considered. The most popular base function used in GMDH is the gradually complicated Kolmogorov-Gabor polynomial [102].

Ugrasen et al. [102] developed prediction models of surface roughness, volumetric material removal rate and accuracy in WEDM of EN-31 material by this approach. Three different criteria functions, namely regularity, unbiased and combined, were tried with training data of different size. It was reported that regularity criterion function gave better result than other two. For surface roughness, 62.5% data were used as training set and 75% for volumetric material removal rate. Testing result was not reported.

It appears that performance of GMDH depends on base function and criterion function. In real world practice it is very difficult to select the suitable base function and criterion function in earlier.

2.5.3 Empirical modeling - non-statistical approach

Though multivariable regression and response surface methodology are the most common approaches for empirical model building, yet, non-statistical techniques like dimensional analysis, grey system theory, empirical mode decomposition, instrument variable approach, time-varied predictive model are also employed for modeling of EDM process.

2.5.3.1 Modeling based on dimensional analysis

Dimensional analysis based semi-empirical models are able to include more number of process variables in model building than the estimated error based empirical techniques. Dimensional analysis is founded on the concept that variables could be represented in a dimensionally homogeneous equation [122]. Using Buckingham pi theorem all variables appearing in the problem will be connected through number of different dimensionless products. The dimensionless products or groups of variables are raised to unknown indexes and they are estimated through experimentation using different linear and non-linear regression analysis techniques.

Wang and Tsai [123] developed models for MRR and tool wear in EDM with dimensional analysis. Their models included peak current, discharge time, input energy on electrode, boiling point, electrical conductivity, specific heat capacity, thermal conductivity, density and latent heat of vapor per unit mass of electrode material. With the variables, they constructed five dimensionless groups and they were connected through unknown indexes. Different non-linear regression techniques were tested for estimation of the indices. They did number of experiments earlier for screening of significant parameters with different tool-workpiece variations. This screening procedure was done by S/N ratio based noise analysis. Tsai and Wang [124] used the same procedure for model development of average surface roughness value in EDM with same input parameters. In both the papers, models were unable to represent the process efficiently. For average surface roughness, material removal rate and tool wear rate, prediction error varied within 0.92%-46.48%, 8.46%-79.11% and 1.02%-303.5%.

Patil and Brahmankar [125] considered same variables along with melting phenomenon instead of boiling condition. Here, they did experiments on Al/SiC composite with three different levels of ceramic reinforcements namely 10%, 20% and 30%. It was reported that this model [125] was able to capture the MRR with almost 99% accuracy for all three composites. Their model was compared to RSM model. This semi-empirical model slightly overestimated MRR than RSM based model for higher pulse on time. With higher ceramic reinforcements this model showed decrease in MRR value.

It is observed that dimensional analysis is not capable of reflecting either of the additive or subtractive input-output relationship. Even, it could not derive formula containing trigonometric function, exponential function, logarithmic function etc. Correlation with constant is not captured in this approach. It is difficult to handle the physical quantities having same dimensional formula.

2.5.3.2 Modeling based on grey system theory

Grey system theory is more suitable for the system having partially unknown parameters where some information are poor, incomplete and uncertain [126]. To study the discharge state prediction, calamities grey prediction theory [127] and to forecast the process outcomes, grey dynamic model [128] were implemented by the researchers.

Liu et al. [127] implemented calamities grey prediction theory to predict the discharge state of micro-EDM process and tried to reduce the electrode pullback and to improve the processing efficiency and processing quality in both micro-hole and micro-groove EDM. Nonstationarity, nonlinearity and internal coupling characteristics of voltage signal, current signal and spark ratio caused the hysteresis of conventional control method. To reduce this hysteresis effect, output velocity of conventional control system was replaced and a real-time predictive control method with voltage signal, current signal and spark ratio was proposed. They considered negative velocity (electrode pull back) as a calamity value. As, this predictive method exhibited good real-time performance in prediction whether the future processing cycles would be in discharge state or not, so, the proposed discharge state predictive method was coupled with conventional control system.

Chiang and Chang [128] conducted experiment on EDM of electro-conductive ceramic (Al_2O_3+30%TiC) with variation of pulse current and pulse duration and measured the process performances namely material removal rate, electrode wear ratio and maximum surface roughness. Using this experimental data, residual grey dynamic model (1, 3) was developed. Least square method was used to estimate the parameters of grey model and predicted values of the original discrete data were obtained by using inverse accumulation generating operation (IAGO). Though it was reported that, residual error of proposed forecasting model was less than 4%, still, some lacunae of this approach were identified.

As, the prediction is dependent on primitive sequence, if the historical data sequence is altered, prediction could be affected. Interaction effects of parameters are not revealed clearly. Time series data should be independently and identically distributed. Therefore, some confusion is still present as to whether this type of historical data set could be considered as time series or not.

2.5.3.3 Modeling by empirical mode decomposition

High frequency discharge, complex interference and frequent discharge signal distortion are common in micro-EDM. Thus, method for detection of discharge state should be faster, have less operations and good real-time performance.

For the same prediction length, discharge state prediction of EDM using empirical mode decomposition was proved as better than conventional methods [129]. The decomposition technique was developed by combining autoregressive model identification and linear prediction. Complex discharge state signals were divided into several linear, smooth and mutually orthogonal intrinsic mode function (IMF) components. Autoregressive identification model of each IMF was built and thus, linear prediction was employed for each IMF component. This method showed good real-time performance with less operational time by reducing the lag of conventional model.

Performance of empirical mode decomposition is affected by the selection of IMF. It is difficult to set number of IMF prior to modeling. Linear prediction of IMF component may not be appropriate for all practical problems.

2.5.3.4 Modeling based on instrumental variable approach

Online modeling of EDM process by instrumental variable approach with Kalman filters was developed by Zhou et al. [130, 131]. They used two Kalman filters for this purpose. One was used for estimation of gap states from gap state identifications and the other for the estimation of autoregressive model parameters [130]. Gap state identification and the other were defined as an average of states identified based on pulse discriminating criteria from sample voltage and current in a time interval. Spark pulses, transient arc pulses, stable arc pulses and short pulses were classified by their different voltage threshold value. Compared to the four pulses, very high voltage during open pulses and almost zero voltage during pulse off time were used as the criteria for state identification. Multi-performance optimization of noise variances, namely identification of noise variance and parameter of noise variances, were done by grey correlation approach. Filter parameters were upgraded [131]. Prediction errors of the developed model of gap state were found within theoretical bounds which showed the confidence of two Kalman filters for online modeling of gap state in EDM process.

Classification of different pulses depends on pulse discriminating criteria and therefore, efficiency of instrumental variable approach will be affected by selection of Kalman filters. Efficiency of instrumental variable approach is also suffered by the quality of the instruments and associated errors.

2.5.3.5 Time-varied predictive model

Classification technique for discriminating different discharge pulses in EDM based on gap states was developed by Zhou et al. [132]. They mentioned five discharging pulses in gap according to waveforms of voltage and current, namely machining pulses like spark and transient arc pulses, non-machining open pulse and deleterious pulses like stable arc and short pulses. Sum of spark ratio and transient arc ratio was considered as gap state. Time series of gap state was analyzed with spectral analysis. Their time-varied predictive model was found to work with on-step-ahead mean prediction error less than 2%.

It appears that performance of time varied predictive modeling is affected by chosen sampling rate of time varying signal and discriminating criteria of gap state. However, it is to be noted here that gap state status, as described in grey prediction theory, instrumental variable approach and time varied predictive modeling, attributes to material removal rate and surface topography in EDM.

2.5.4 Modeling by intelligent procedure

Researchers also use intelligent procedures to build a representative architecture of the EDM process from experimental results and physical experiences. With the aid of different learning theories, some soft and some hard computing based methods like artificial neural network, fuzzy logic, ANFIS, genetic expression programming are used by the researchers.

2.5.4.1 Modeling based on artificial neural network (ANN)

Variants in modeling by artificial neural network of EDM process are method of learning, selection of activation function, values of learning and momentum coefficients, number of hidden layers and number of neurons in each of the hidden layers.

In feed forward neural network (FFNN), information is passed into forward direction without forming any cycle or loop. Two typical architectures namely, multi-layer FFNN and radial basis function networks (RBFN) were used for modeling of EDM process. For the purpose of getting optimum multi-layer FFNN architecture with optimum internal parameters, gradient descent search based back propagation algorithm were used by Pal et al. [115] and Mandal et al. [133]. Pal et al. [115] trained experimental results of MRR, surface roughness and fractal dimension in EDM obtained at different combinations of levels of current, pulse on time and pulse off time. Learning rate and momentum coefficient were chosen as 0.9 and 0.8. For both hidden layer and output layer, tansigmoidal function was chosen as activation function and weights were updated by gradient descent search based back propagation algorithm. With 5000 iterations and training error 0.0001, they finally selected 3-14-3 architecture for their study. Their network was tested and found as better compared to RSM based model [115]. With same input parameters [115], models of MRR and tool wear rate were developed by Mandal et al. [133]. They considered 3-2-2 architecture and 10 neurons for each of the two hidden layers. For selection of optimum learning rate and momentum coefficient, gradient descent search based back propagation algorithm was employed and optimum values of both the learning rate and momentum coefficient were found as 0.6. It is observed that first order derivative based gradient descent search method is quite slow and chance of trapping in local optimum is very high.

Therefore, Al-Ghamdi and Aspinwall [107] employed second order derivative based Levenberg-Marquardt algorithm for searching optimum architecture for prediction of MRR in EDM of WC-Co by copper tool with current, on time, off time and capacitance as input parameters. One hidden layer was decided and different schemes of choosing number of neurons were tried. Finally, 9 neurons for hidden layer were set. Activation functions for hidden layer and output layer were chosen as sigmoid function and linear function respectively. With dynamic damping factor of Levenberg-Marquardt algorithm, termination criterion was set by 1300 epochs and obtained MSE in training is 0.01. Their network could predict better compared to RSM based model [107].

To avoid the uni-directional search in Levenberg-Marquardt approach, Joshi and Pande [134] used scaled conjugate gradient (SCG) based searching method for developing models of MRR, crater depth, crater radius and tool wear rate in EDM. They generated data set from thermo-physical FEM based model with discharge current, discharge duration, duty cycle and breakdown voltage as input parameters. With two hidden layers, interconnected weight factors were optimized by SCG. At the end of simulation, 4-5-28-4 architecture was finalized with 7% mean prediction error. Testing result with 16 separate data set showed that 90% of testing data set could predict within 15% absolute error. They compared their multi-layer FFNN with RBFN.

Derivative based searching algorithm are suffering from large memory and poor convergence rate. Trapping inside local optimum is also high. For better searching operation, evolutionary optimization method like genetic algorithm (GA) was implemented by Rao et al. [135] and Wang et al. [136]. Rao et al. [135] developed model of surface roughness in EDM of different workpieces like Ti-6Al-4V, HE15, 15CDV6 and M250. They considered current, average voltage and machining time as input parameters. Number of hidden layer was chosen as one. For both the hidden layer and output layer, hyperbolic tangent function was chosen as activation function. At the end of 30000 epochs, MSE was obtained as 0.00063369. Architecture and interconnected weights of the network were found through optimization by GA. Root mean square error in prediction was considered as objective function for GA. Wang et al. [136] developed models for MRR and surface roughness, obtained from EDM of Ni base alloy by graphite tool, with six control parameters namely peak current, on time, off time, voltage, dielectric fluid and electrode material. Sigmoid transfer function was used as activation function for both hidden layer and output layer. For optimization by GA, they considered same objective function as mentioned by Rao et al. [135]. Testing error for MRR and surface roughness were found as 5.6% and 4.98% respectively.

Instead of using multiple hidden layers in multi-layer FFNN, Joshi and Pande [134] considered RBFN with single hidden layer and Gaussian radial basis function was used as transfer function in the hidden layer. They employed RBFN to correlate MRR, crater depth, crater radius and tool wear rate in EDM with discharge current, discharge duration, duty cycle and breakdown voltage as input parameters. Thermo-physical FEM based model was used for data generation. Number of hidden neurons, centers of RBF neurons and interconnected weights between hidden and output layers were optimized by orthogonal least square approach. Optimum spread factor of Gaussian function was selected by trial and error method. With optimum spread factor 0.12, 4-250-4 RBFN architecture was found as best fitted and absolute mean error was found as 19%. Using 16 separate data set for testing purpose, it was found that 80% of testing data set could predict each of MRR, crater depth and crater radius within 15% absolute error. Mean prediction error was 10%. In case of tool wear rate, mean prediction error was 46% and 25% of testing data set were within 15% absolute error. They concluded that in spite of the simplicity and fast convergence rate of RBFN, it was not suitable for global fitting. Further, it was claimed that SCG based multi-layer FFNN was more accurate and had more potential to model complex machining process like EDM.

Thus, it appears that training time is high due to poor convergence rate of derivative based search methods. Large memory is required for derivative calculation. Internal parameters of optimization method, namely learning rate and momentum coefficient of gradient descent method, damping factor of Levenberg-Marquardt algorithm and crossover and mutation probability of genetic algorithm, affect the training schedule and thereby final architecture. Final architecture of ANN might not be optimum and might have low repeatability due to size of training data set and initial setting of weight factors. Besides, ANN based models are suffering from efficiency of training, efficiency of testing, over-fitting.

2.5.4.2 Modeling based on fuzzy logic

Researchers also used fuzzy logic for prediction of outcomes of EDM process. Formulation of membership function for fuzzification, definition of the expert rules and selection of defuzzification method are three main criteria to be decided prior to the application of fuzzy logic based intelligent modeling.

Shabgard et al. [137] developed models of MRR, tool wear rate and different roughness parameters with current and pulse on time as input parameters. Shabgard et al. [137] did EDM of WC-Co by commercial copper. By trial and error, triangular and trapezoidal membership functions were found better and used for fuzzification. Fuzzy sets for input and output parameters were 5, 3, 5, 5, 5, 5. Number of fuzzy rules used was 15. Their models were tested with five different test sets and accuracy in prediction was found above 91% in each case.

Sengottuvel et al. [138] conducted EDM on Inconel 718 using copper electrode with different combinations of levels of current, pulse on time, pulse off time, flushing pressure and tool geometry and measured MRR, tool wear rate and surface roughness. By trial and error, they found Gaussian membership function was better and used for fuzzufication. They used 16 fuzzy rules and center of area method for defuzzification. Their models were tested with one separate data set and predicted within 5% absolute error in each case.

Lin et al. [139] predicted models of MRR, electrode wear ratio and surface roughness in EDM of SKD11 alloy steel by copper electrode with discharge current, pulse on time and duty factor as input parameters. Number of fuzzy rules used here was 27. No results of testing were reported.

For combining multiple responses, Lin and Lin [140] used grey-fuzzy approach and Tzeng and Chang [141] used multiple performance characteristics indices (MPCI). Using grey-fuzzy approach Lin and Lin [140] developed combined model of MRR, electrode wear ratio and surface roughness in EDM of SKD11 alloy steel by copper electrode with discharge current, pulse on time and duty factor as input parameters. Nine fuzzy rules were used for this purpose. Values of prediction error was not reported but it was concluded that grey-fuzzy approach [140] performed better than direct data based single response fuzzy model [139]. Dimensional precision and accuracy of slope were combined to multiple performance characteristics indices (MPCI) for fuzzy modeling by Tzeng and Cheng [141]. They did experimentation on EDM of SKD11 tool steel by electrolytic copper with aluminum powder added to dielectric fluid. Along the variation of powder size and concentration, they considered pulse peak current, pulsed duration, duty cycle, open circuit voltage, regular distance for electrode lift and time interval for electrode lift as input parameters. Number of fuzzy rules used was 27 and defuzzification was done by center of gravity method. Result of confirmatory test was not reported.

Modeling by fuzzy logic suffers from uncertainty of the modeling process itself. Methods of fuzzification and defuzzification and selection of fuzzy rules affect the performance of fuzzy logic based prediction. Allocation of same importance to all input parameters is not appropriate.

2.5.4.3 Modeling based on adaptive neuro-fuzzy inference system (ANFIS)

In adaptive neuro-fuzzy inference system (ANFIS) based modeling, mapping from input and hidden layers to corresponding hidden and output layers of neural network is replaced by fuzzification and defuzzification of fuzzy logic based approach.

Models of MRR and surface roughness in magnetic field assisted EDM process were developed by Teimouri and Baseri [142] using ANFIS. Magnetic field intensity, rotational speed and product of average current and pulse on time were considered as input parameters. Using trial and error method, different architectures were tested with 0.01 root mean squared error or 500 epochs as termination criteria. Among 39 experimental results, 25, 7, 7 results were used for training, validation and testing purposes respectively. First order Sugeno-fuzzy rules were implemented and 27 Gaussian membership functions were selected for the architecture. Average RMSE of testing of MRR and surface roughness with four separate data set were found as 46.28 and 49.76 respectively but confirmatory test gave lower values like 1.16 and 0.85 respectively.

Maji and Pratihar [116] employed ANFIS for developing models of MRR and surface roughness in EDM with input parameters as peak current, pulse on time and duty factor. They took mild steel workpiece and copper electrode. Linear and non-linear membership functions were tried for forward and reverse mapping of MRR and Ra with input parameters. Based on developed RSM model [116], they generated almost thousand data sets and used for training purpose for this approach. Genetic algorithm was implemented to find optimum distribution of membership function and coefficients of fuzzy rules. It was found that bell shaped membership function performed better than any other membership functions. Confirmatory test was done with six different data set.

As, ANFIS approach combined neural network and fuzzy logic, so, uncertainty and less repeatability in prediction are common problem. Complex architecture, lack of training efficiency and chance of over-fitting restrict the use of ANFIS in practical field.

2.5.4.4 Modeling based on genetic expression programming

Genetic expression programming (GEP) algorithm gives a solution in searching of global function, developed from genetic algorithm and genetic programming [143].

Salman and Kayacan [143] developed GEP based modeling of surface roughness with variation of discharge current, pulse on time, pulse off time, gap voltage and various electrodes. No significant difference was found in EDM generated surface for different electrodes.

Need of internal parameter tuning of genetic expression programming makes it difficult for implementation in real world problems.

The above mentioned procedures of model development are rigorously used for modeling empirical data. Suffering from generalization of model estimation, over-fitting might have occurred in ANN. Besides, random variations in process outcomes are obvious in stochastic type machining process. The random fluctuations in experimental results are required to be absorbed with specified tolerance value for intelligent predictions. Advanced learning based systems being devoid of four problems, namely efficiency in training, efficiency in testing, over-fitting and algorithm parameter tuning, would be effective in such situation. Structural risk minimization based [144] supervised batch learning system, support vector machine regression, could be a smart way of handling the situation and makes a trade-off between flatness and complexity of the unknown underlying fixed function.

2.5.5 Support vector machine (SVM) regression

Support vector machine regression, a supervised batch learning system, is firmly grounded in the framework of statistical learning theory. Vapnik [144] introduced structural risk minimization (SRM) principle instead of empirical risk minimization (ERM) implemented by most of the traditional artificial intelligence based modeling technologies. Neural network approaches may have suffered with generalization, producing over fitted models but SRM minimizes upper bound on the expected risk, as opposed to ERM, that minimizes error on the training data. This difference equips SVM regression with a greater ability to generalize [145]. Detailed discussion on SVM regression [144-150] is given in appendix A.1. Only a few applications of SVM regression learning system for development of predictive models of different machining processes are found and reported as follows.

Zhang et al. [151] developed separate hybrid models of processing time and electrode wear in micro-EDM through SVM regression. They also employed discrete level leave-one-out cross-validation for choosing C and ε. Though they used Gaussian kernel function but no such choice of σ was reported.

Surface roughness in CNC turning of AISI 304 austenitic stainless steel was modeled with high correlation coefficient through three SVM regression learning systems namely least square SVM (LS-SVM) regression, Spider SVM regression and SVM-KM based on clustering by k-means and ANN [152]. Internal parameters of SVM regression (C and σ) were set by grid search method. Though it was reported that for model development, SVM regression learning systems consumed less time than

ANN but no clear explanation about the specific choice of searching regions of SVM regression parameters was stated. Also, the values of SVM regression parameters obtained through grid search method depended on the choice of jumping interval.

Ramesh et al. [153] conducted CNC end milling operation on 6061 aluminum varying feed rate, spindle speed and depth of cut. They employed SVM regression for modeling of surface finish in milling operation. Though their estimated model could predict with 8.34 % error which is better compared to 9.71% in prediction through multivariable regression model, but the procedure of their iterative choice of internal parameters of SVM regression, namely error, width and upper bound of global basis function, was not reported anywhere.

Models of surface finish in face milling of steel were also developed using multivariable regression analysis, SVM regression learning system and Bayesian neural network by Lela et al. [154]. It was reported that SVM regression learned model estimated better than multivariable regression model. All three internal parameters of SVM regression were chosen by leave-one-out cross validation procedure keeping two parameters fixed at particular values and other one was searched by minimizing the mean square error. A continuous optimization technique which simultaneously searches the three parameters should be used to get better result for a newly developed system.

Three prediction models of milling operation were developed by Dong et al. [155] using LS-SVM regression, standard SVM regression and ANN. They considered spindle speed, feed rate, depth of cut and number of milling blades as input parameters and surface roughness was considered as output parameter. With their training set of 54 samples, testing set of 8 samples and radial basis function as kernel function, LS-SVM regression performed better than standard SVM regression and ANN in terms of computational time and prediction accuracy. Internal parameters of SVM regression like C, ε and parameter of kernel function were set by their own choice. No guidelines were reported.

Further, LS-SVM regression was used for modeling of surface roughness with more input parameters namely spindle speed, feed rate, axial depth of cut, radial depth of cut, rake angle and tool diameter [156]. Jiang [156] selected radial basis function (RBF) as kernel function and estimated C, ε and parameter of kernel function by 5-fold cross validation procedure. With training set of 16 experiments (following L16 orthogonal array), testing results over 8 separate sets of data were within average 8% prediction error.

Different parameters of vibration signal in worm wheel and gear grinding in CNC machine were predicted using LS-SVM regression [157]. Wang et al. [157] considered RBF as kernel function and selected the values of C, ε and parameter of kernel function by grid search method. Their developed model predicted with more accuracy than auto-regressive model and neural network.

From the above discussion, it is observed that in EDM, irregular fluctuations in process outcomes like MRR, surface roughness could be captured by insensitive zone of support vector machine regression and use of kernel function reduces the curse of dimensionality in model development process. This robust way of modeling would be helpful to machine within an allowable tolerance limit.

2.6 Optimization related to EDM process

To sustain in the competitive industrial market, manufacturing processes should be implemented in economically viable way. Both the quantity and quality of the process outputs are to be balanced. Thus, from early days of industrial revolution, optimum results are rigorously searched by researchers. Recent applications of evolutionary techniques for optimization of machining processes are listed by Yusup et al. [158]. They reported very few publications regarding EDM process parameter optimization. Though the evolutionary methods were proposed in recent time and already gained the popularity due to its stable performances, yet, different hard computing methods are more common to the researchers. Most popular hard computing based discrete techniques are S/N ratio based method, grey relation analysis, principal component analysis etc. and continuous methods are feasible direction, Newton's steepest descent method etc. Soft computing techniques include probabilistic approaches namely trajectory based simulated annealing (SA), heuristic method like genetic algorithm (GA) and metaheuristic techniques like ant colony optimization (ACO), particle swarm optimization (PSO), sheep flock (SF) algorithm, artificial bee colony (ABC) algorithm, biography based optimization (BBO), etc. The above said methods are employed for single and multiobjective optimization of machining processes. Classification of the optimization methods employed on EDM process is shown in figure 2.3. In each group, discussion is kept limited to a few typical literature.

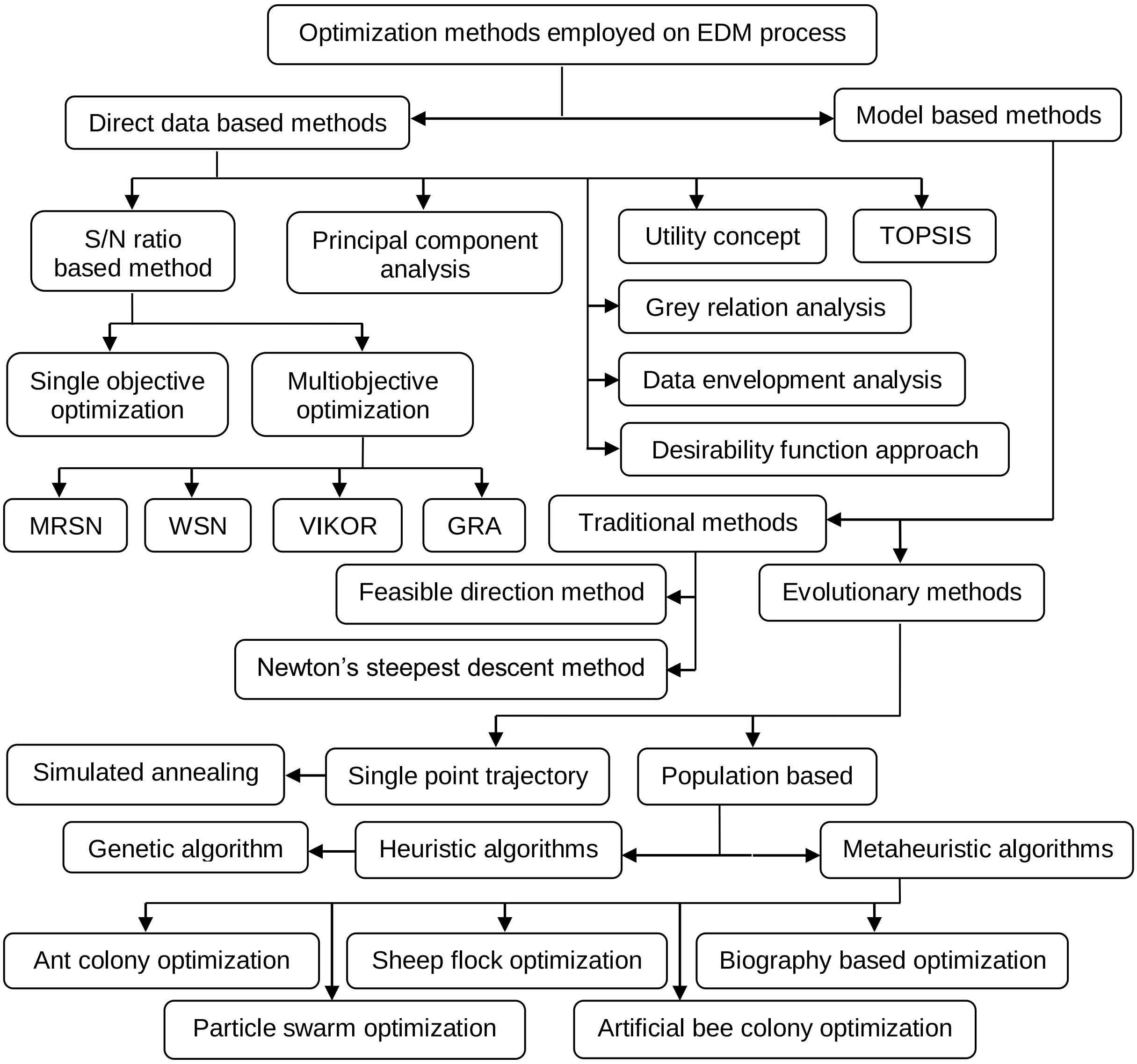

Fig. 2.3 Classification of optimization methods employed on EDM process

2.6.1 Optimization based on direct data based methods

Deterministic approaches for searching optimum result that is hard computing methods are classified into two groups namely discrete methods and continuous methods. Optimum result obtained from discrete methods is limited within the preselected levels of parameters but continuous methods are capable to reach any point within the specified boundary.

2.6.1.1 Single objective optimization based on S/N ratio

Among, discrete methods, S/N ratio based method is generally restricted to implement for single objective optimization. Depending on the type of optimization, either of the three types of S/N ratio, namely larger the better, nominal the better and smaller the better, is calculated.

Rajmohan et al. [159] performed EDM of 304 stainless steel with process parameters as current, pulse on time, pulse off time and voltage. They used L9 orthogonal array and measured MRR for each run. Based on S/N ratio calculation, they obtained optimum set of input parameters for maximum MRR. Bergaley and Sharma [160] also performed L9 orthogonal array based experiment on EDM of high-carbon-high-chromium steel using copper electrode with same process parameters as [159] except copper powder concentration in dielectric instead of voltage. They did maximization of MRR and minimization of tool wear rate. Both Rajmohan et al. [159] and Bergaley and Sharma [160] did not conduct any validation test. Boopathi and Sivakumar [104] did experimentation on near dry WEDM of M2 grade HSS using molybdenum wire and measured MRR and surface roughness in each run. L18 orthogonal array was used to accommodate different levels of discharge current, pulse on time, pulse off time, gap voltage and air mist pressure. They reported that discharge current, pulse on time and gap voltage had significant contributions on MRR and surface roughness. They estimated the optimum setting separately for maximum MRR and minimum surface roughness.

It is noted that optimum results obtained from S/N ratio based method are restricted within the discrete combination of the levels of input parameters.

2.6.1.2 Multiobjective optimization based on S/N ratio

To implement the S/N ratio method for simultaneous optimization of multiple responses, concept of weighted average is introduced. Combining the number of process performances using different scheme of weight vectors, it makes a way out for multiobjective optimization.

Ramakrishnan and Karunamoorthy [161] conducted WEDM of Inconel 718 by brass wire and measured MRR and surface roughness. They considered ignition current, pulse on time, delay time and wire feed speed as input parameters and did experimentation using L9 orthogonal array. Assigning equal weight vectors (each of 0.5), normalized MRR and normalized surface roughness were combined and multi-response S/N ratio (MRSN) was evaluated. Optimum results were validated. Confirmation test showed that MRSN ratio was improved by 0.783. Along with multi-response S/N ratio (MRSN) method, Gauri and Chakrabarty [162] compared WSN and VIKOR method for multiobjective optimization of both the combinations namely MRR-surface roughness-kerf width and SR-cutting removal rate. Among the three techniques, WSN method gave better result than other methods but no confirmation test was reported. Searching of Non-dominated solution in optimization of MRR and surface finish of WEDM was done by Scott et al. [163] using S/N ratio based calculations. Discharge current, pulse duration and pulse frequency were found as significant control factors compared to wire speed, wire tension and dielectric flow rate. They concluded that dynamic programming approach was more efficient than complementary approach in case of searching non-dominated solution through S/N ratio based multiobjective optimization.

It appears that result of multiobjective optimization by S/N based method depends on the scheme of weight vector employed for combining multiple responses.

2.6.1.3 Optimization based on principal component analysis (PCA)

Principal component analysis (PCA) is a method to transform the multiple normalized process outcomes into uncorrelated linear combinations. Two shortcomings of standard PCA are, in case of eigen value greater than unity, feasible solution becomes unknown and multiresponse performance index (MPI) could not be replaced by multiresponse solution. To overcome this, weighted PCA is generally used where assigned weights are used to combine all principal components to obtain a multiresponse performance index (MPI). Using this MPI, optimum levels of control parameters are identified.

Das et al. [164] conducted L27 orthogonal array based experiment on EDM of EN31 tool steel by electrolytic copper. With variation of discharge current, pulse on time, pulse off time and voltage, they measured MRR and five different surface roughness parameters, namely center line average surface roughness, root mean square of profile heights, skewness of the profile height distribution, kurtosis of profile height distribution and mean width of profile elements. At first they checked the correlation between process outcomes and it was reported that all responses are correlated in pair. Principal component of each trial is computed by eigen vectors of each response. Next, accountability proportion is estimated and multiresponse performance index is calculated from principal components. From the level average of MPI, optimum settings were found and compared to experimental results. Confirmation test showed that S/N ratio was improved by 1.6554 dB.

It is observed that estimation of eigen value increases computation time and assignment of weight vectors demands prior information about input-output relationship. If output parameters have higher order relationships, then, correlation coefficients and principal components are not capable of capturing them. Also, optimum results are limited within discrete levels of experimentation.

2.6.1.4 Optimization based on grey relation analysis (GRA)

Grey relational analysis (GRA), one of the widely used multiresponse discrete optimization methods, is consisted of four steps, namely grey relational normalization, grey relational gathering, calculation of grey relational coefficient and evaluation of grey relational grade. Normalization technique absorbs the differences between maximization and minimization problem. Grey relational grade is calculated by averaging the grey relational coefficients which are generated by gathering multiple responses using distinguishing coefficients. In general distinguishing coefficient is chosen as 0.5. Parameter settings corresponding to highest grey relational grade indicates the optimum settings of input parameters.

Jegan et al. [165] conducted EDM of AISI 202 stainless steel with electrolytic copper and measured MRR and surface roughness. They considered discharge current, pulse on time and pulse off time as process parameters and did full factorial experimentation. Based on grey relational grade, optimum setting was reported but value of distinguishng coefficient was not mentioned. Rajesh and Anand [101] measured the same responses as [165] in EDM with copper electrode, but to further incorporate working voltage, oil pressure and spark gap as the control parameters, they used L32 orthogonal array. Optimum results were not validated. Along with MRR and surface roughness, Lin et al. [139] minimized electrode wear ratio. They did EDM of SKD11 alloy steel by copper electrode and used L9 orthogonal array to accommodate different levels of discharge current, pulse on time and duty factor. Their confirmation test showed that at the optimum condition, grey relational grade was improved by 0.092. Vikas et al. [166] conducted EDM of EN41 by copper electrode and measured different surface roughness parameters, namely center line average surface roughness, root mean square of profile heights, skewness of profile height distribution, kurtosis of profile height distribution and mean width of profile elements, of machined surface. They used L27 orthogonal array for experimentation to accommodate different levels of discharge current, pulse on time, pulse off time and gap voltage. Using GRA, they found the optimum setting of input parameters and conformation test showed that grey relational grade was improved by 0.18137.

In optimization using GRA method, optimum setting depends on selection of distinguishing coefficient and is limited within discrete combinations input parameters.

2.6.1.5 Optimization based on data envelopment analysis (DEA)

In data envelopment analysis (DEA) each experimental run is considered as a decision making unit (DMU). Fractional mathematical linear programming technique is employed to calculate the relative efficiency, a ratio of weighted sum of DMU of outputs and that of inputs. Best among the calculated relative efficiency values is selected for the optimum solution. In case of multiple DMUs having same relative efficiency value, average ranked value method is adopted to find out the best solution.

Sahu et al. [118] did Box-Behnken based 27 experiments with different levels of discharge current, pulse on time, duty factor and flushing pressure in EDM. For each experimental run, MRR, tool wear rate, surface roughness and circularity of workpiece were measured. For tool wear rate and surface roughness, responses are set as inputs for calculating DMU but for larger-the-better type performances, namely material removal rate and circularity, responses are set as outputs for DMU. Average ranked values were calculated and optimum combination was identified. Effect of variation of duty factor on relative efficiency is the highest among all input parameters. Validation test showed that optimum results of MRR, tool wear rate, surface roughness and circularity of workpiece were differed from experimental values by 5.45%, 18.90%, 17.86% and 0.23% respectively.

It is observed that implementation of linear programming is time consuming and selection of weight factors for calculation of DMU affects the optimum setting.

2.6.1.6 Optimization based on desirability function approach (DFA)

Desirability function is a dimensionless measure of performance calculated by combining multiple responses. In this approach, each response is transformed to a desirability value between zero and one, where higher value indicates better preference of that response. This desirability may be nonlinear function depending on the assigned weight factor between one and ten. Overall desirability is estimated by taking the geometric mean of individual desirability of each response raised to an importance value (least important as 1 to most important as 5). Highest desirability value is declared as the optimum result.

Sengottuvel et al. [138] conducted experiment on EDM of Inconel 718 with copper tool. They incorporated peak current, pulse on time, pulse off time, flushing pressure and electrode geometry as input parameters in L16 orthogonal array. Assigning 0.33 weight factor to each of MRR, tool wear rate and surface roughness, optimum setting was found by desirability function approach. No validation test was done. Assarzadeh and Ghoreishi [113] measured same process outcomes in EDM of WC-Co by commercial copper electrode. They conducted face centered CCD based 31 experiments with different combination of levels of discharge current, pulse on time, duty cycle and gap voltage. Optimum values of MRR, tool wear rate and surface roughness were validated with 8.56%, 9.45% and 6.45% error respectively. Gopalakannan et al. [114] did experiment on EDM of Al 7075/B4C using electrolytic copper as tool electrode. With the help of desirability function approach, they simultaneously maximized MRR, minimized electrode wear rate and minimized surface roughness. Using the optimum setting of input parameters, namely pulse current, pulse on time, pulse off time, gap voltage, they conducted confirmatory test and reported average error of 3.21%, 6.19% and 4.63% for MRR, tool wear rate and surface roughness respectively.

It appears that performance of desirability function approach is affected by nature of desirability function and chosen weight factors.

2.6.1.7 Optimization based on utility concept

Products based on different quality characteristics are assessed by prospective buyer. Different characteristics are combined and composite index is evaluated [167]. This composite index represents the utility of the product. At first, preference scale is set based on experimental observation. This preference scale of each response multiplied by weight factors are added to get overall utility function. Therefore, multiple responses could be optimized simultaneously using this method.

Goswami and Kumar [167] performed WEDM of Nimonic 80A using brass wire. L27 orthogonal array was used to accommodate different levels of peak current, pulse on time, pulse off time, wire feed, wire tension and gap voltage. They measured MRR and surface roughness value in each experimental run. Assigning equal weight factor as 0.5 to each response, multiresponse optimization was done by implementing utility concept and single optimum set of input parameters was obtained. No confirmatory test was reported.

It is noted that construction of preference scale depends on both experimental observations and users. Besides, assignment of weight factors affects the results of optimization.

2.6.1.8 Optimization based on technique for order of preference by similarity to ideal solution (TOPSIS)

For optimization of multiple responses, TOPSIS method is implemented in fuzzy environments. Decision makers give their decisions on responses for each attribute weight factor. Normalized responses are multiplied by the fuzzy weights. Based on the characteristics of the responses, positive and negative ideal solutions are identified. Using the weighted performances and ideal solutions, distance between two fuzzy numbers is estimated. With the distance value, closeness coefficient (CC) is calculated for each experimental run. The highest CC value indicates optimum setting of input parameters.

Dewangan et al. [168] simultaneously minimized white layer thickness, surface crack density, surface roughness and overcut in EDM of AISI P20 tool steel using copper electrode by Fuzzy-TOPSIS-based multi-criteria decision making approach (MCDM). Face centered CCD is considered for experimentation to accommodate different levels of peak current, pulse on time, tool work time and tool lift time. Employing this approach, a single set of levels of input parameters is found which minimized all four process outcomes simultaneously. Validation test of the obtained optimum result was not done.

It is observed that selection of weight factors affects the performance of TOPSIS in multiresponse optimization.

From the above discussion in subsection 2.6.1, it appears that direct data based methods are not efficient to explore the search space except from few preselected points. Input-output relationship over full search space is established through representative model of the process. Therefore, considering the representative model as objective function, optimization methods are employed on this. Optimization of objective function is done by either traditional or evolutionary optimization method.

2.6.2 Optimization based on traditional methods

Apart from direct data based methods, traditional optimization techniques are employed on objective functions. Researchers did optimization of EDM process considering representative model as objective function. Thus, possibility of getting global optimum value other than optimum at some predefined levels of input parameters increases. exists. Feasible direction method and Newton's steepest descent method are two gradient based traditional optimization methods employed for optimization.

Liao et al. [105] conducted experiment on WEDM of SKD11 alloy steel by brass wire using L18 orthogonal array to accommodate different levels of input parameters namely pulse on time, pulse off time, table feed, wire speed, wire tension and flushing pressure. They developed regression models of MRR, gap width, surface roughness. Considering the estimated regression model of MRR as objective function, they maximized MRR subjected to the constraint of gap width (0.42 mm) and surface roughness (3 μm) by feasible direction search method. Saha et al. [169] developed a model of temperature distribution in wire of WEDM by copper wire using finite element analysis. The developed model was considered as objective function and used Newton’s steepest descent method for optimization. They minimized wire temperature. In both the studies [105, 169], validation tests of optimum results were not reported.

Performances of traditional optimization methods are suffered from calculation of derivatives. Feasibility of derivative calculation at all points is very low and computation time is high. As, both of this traditional methods follow uni-directional search technique, so, possibility of trapping inside local optimum is very high. Efficiency of traditional methods reduces in searching of global optimum for complex multimodal objective functions. Evolutionary optimization methods are effective in this regard.

2.6.3 Optimization based on evolutionary methods

In practical field of work, optimization problems are suffered from non-convex design spaces, a mix of continuous-discrete variables. Mathematical non-linear programs are found to be inefficient, computationally expensive and in most of the cases searching operation might be trapped near to starting point or local optimum. In this regard, some physical phenomena based or nature inspired soft computing based heuristic or metaheuristic algorithms are developed. Simultaneous handling of number of objective functions and better exploration to search global optimum, make the probabilistic approaches more popular in industrial engineering problems. For optimization of EDM process, three major soft computing techniques are applied namely single point trajectory based method, population based heuristic and metaheuristic methods. There is confusion regarding clear distinction between heuristic and metaheuristic methods. Mukherjee and Roy [170] give a brief idea about the techniques. Among the several alternative solutions, a simple means of identifying the most preferable one with a set of rules is the basic concept of heuristic approach. Compared to heuristic methods, metaheuristic methods are computationally cheaper, chance of finding global optimum is higher and not problem dependent.

2.6.3.1 Single point trajectory based simulated annealing (SA)

Single point trajectory based simulated annealing mimics the cooling phenomena of molten material. As temperature reduces, chance of free movement of atoms gets restricted. Faster cooling may lead to the end state as polycrystalline, whereas, very slow process takes longer time. Therefore, rate of temperature reduction needs to be efficiently controlled to reach global minimum [171, 172]. In each state, a new generated point is accepted with Boltzmann probability distribution. Starting from an initial state, simulated algorithm gradually moves towards global optimum through some intermediate states.

Yang et al. [173] considered weighted combination of the negative of ANN trained model of MRR and the ANN trained model of surface roughness as objective function. Discharge current, pulse on time and pulse off time were chosen as input parameters. Internal parameters of SA were set as initial temperature = 400^{o}C, Boltzmann constant = 10, cooling rate = 0.9 and number of cycles per temperature = 100 and termination criterion = 10^{-5} ^{o}C. Initial starting point was not given. Though, they considered weighted combination of ANN based models, but values of weight factors were not mentioned. They performed 10 trials starting from same initial point factors but it was not mentioned that how the different results were found. As, simulated annealing was generally used for minimization purposes, so, negative of the MRR value was considered along with positive surface roughness value. To avoid this confusion, Aich et al. [174] took the reciprocal of MRR. Without combining to a weighted sum, they simultaneously optimized RSM based models of MRR and surface roughness considering current, pulse on time and pulse of time as input parameters. Starting from 1210 different initial points, they reached 1210 optimum settings and Pareto optima were identified. Though they set the initial temperature as 250^{o}C, number of iteration at a particular temperature as 100, temperature reduction parameter as 0.975, but their termination criterion was not set by predefined iteration number. Accuracy level was set by changes in the values of objective functions of both the outputs simultaneously. Optimum results of MRR and surface roughness were validated with 11.47% and 4.73% average absolute error respectively.

As, simulated annealing is a single point trajectory based optimization, so. in case of multiobjective optimization, choice of initial point may change the final result. No general guidelines are found in literature regarding the choice of different parameters namely Boltzmann constant, temperature reduction parameter, number of iteration at particular temperature and termination criteria.

2.6.3.2 Evolutionary heuristic method - genetic algorithm (GA)

From the idea of Darwin's theory of survival of the fittest, natural genetics inspired biological evolution based genetic algorithm is developed [171, 172]. Population based genetic searching has three basic elements namely reproduction, crossover and mutation. Reproduction operator selects good strings for mating pool and crossover combines the substrings to evolute new population for next generation. Mutation operator is used to alter the strings locally. Probabilistic evolution by the three simple operators gradually pushes the population towards global optimum. Therefore, population size, crossover and mutation probabilities, termination criteria are needed to be chosen properly for better implementation.

Rajesh and Anand [101] did multiobjective optimization of MRR and surface roughness in EDM using GA and found optimum combination of working voltage, working current, oil pressure, pulse on time, pulse off time and spark gap. Though they performed multiobjective optimization by GA, yet, no clear elaboration of the adopted technique for handling multiple objective functions was reported. Selection of internal parameters and results of validation test were not mentioned. Su et al. [175] employed GA for training of ANN based model of MRR, tool wear and surface roughness in EDM. They introduced a fitness function as the weighted combination of absolute error between desired and predicted values of the three outcomes and considered pulse on time, pulse off time, low voltage discharge current, high voltage discharge current, gap size, servo feed, jumping time and working time for rough, middle and finish cut with different machined area as input parameters. Internal parameters of GA were set as length of string = 64, population size = 77, mutation probability = 0.0077 and crossover probability = 0.7. Optimum results obtained after single objective optimization of proposed objective function were validated with insignificant errors.

For adopting multiple objective functions in genetic algorithm, min-max, weighted sum and crowding distance based dominated ranking were used by different researchers. Crowded-comparison operator based selection operation was improvised in non-dominated searching genetic algorithm (NSGA). With further modifications of NSGA, NSGA-II was developed [133]. Mandal et al. [133] did multiobjective optimization of ANN trained models of MRR and absolute tool wear rate in EDM by NSGA-II with population size 100, two point crossover probability 0.9 and bitwise mutation probability 0.04. At the end of 250 generations, they reached a Pareto optimum set of 100 combinations of discharge current, pulse on time and pulse off time. A typical Pareto optimum set was validated with 1.27 % error for MRR and 0.54% error for absolute tool wear rate. Along with MRR and tool wear, crater depth was also considered by Joshi and Pande [134]. They used FEM based EDM data generator and the generated data are trained through neural network architecture. For roughing operation, maximum of MRR and minimum of tool wear were searched by NSGA-II with selection tournament of size 4, simulated binary crossover probability 0.5 and mutation operator with polynomial of the order of 20 with probability 0.1. In case of finishing operation, crater depth was also minimized with MRR and tool wear. Optimum combinations of duty cycle, discharge current, discharge duration and break down voltage for both the roughing and finishing operation were found. Validation of their optimum results appeared as not appropriate.

Presence of different probabilistic calculations reduces the efficiency of GA in multimodal problems. Termination criteria, as set by all the researchers are maximum number of iterations, might not ensure proper convergence to global optimum. Selection of initial population affects the optimum results in multiobjective optimization by GA.

2.6.3.3 Evolutionary metaheuristic algorithm - ant colony optimization (ACO)

Being influenced by the cooperative behavior in real ant colonies, that is collective effort to find the shortest path between their home to food source [171], ant colony optimization (ACO) is developed. Ant lefts a chemical trail named pheromone in their path and amount of pheromone influences the path of other ants. Pheromone amount is updated by the following ants and trail evaporation. Parallel movements of ants in several random ways are represented by multilayered graph connected through discrete data points and the ants always find the minimum possible path length.

Mukherjee et al. [176] employed ACO for both single and multiobjective optimization of non-linear regression and RSM based models of MRR, wear ratio, kerf width, surface roughness in WEDM. For multiobjective optimization, weighted combination of normalized responses namely wear ratio, surface roughness, kerf width and negative value of MRR was considered as objective function. Optimum set of input parameters namely peak current, duty factor, wire tension, water pressure, discharge current, pulse duration, pulse frequency, wire speed and dielectric flow rate were reported for two different set of models. Values of internal parameters of ACO and validation test of optimum result were not reported. Teimouri and Baseri [142] modified standard ACO to easily handle continuous optimization problem that was, maximization of MRR constrained to surface roughness value. They developed ANFIS model of MRR in magnetic field assisted EDM process. As, continuous ACO (CACO) was used for minimization, so, negative value of MRR was considered. Internal parameters of CACO were set as like number of ants 200, pheromone weighting 1.0, evaporating rate of pheromone 0.8, control parameter of pheromone updating 0.9 and changing rate 0.8. Simulation was stopped by maximum number of iteration as 100. Implementing this CACO for maximization of MRR with seven different constraints of maximum surface roughness, optimum sets of magnetic field, rotational speed and product of average current with pulse on time were obtained. Validation test of optimum results were not reported.

Though maximization of MRR constrained to specific surface roughness value is performed, still, physical significance of negative MRR is confusing. Simulation should not be stopped by maximum number of iterations as this might not ensure proper convergence. It is observed that selection of internal parameters affect the performance of ACO.

2.6.3.4 Evolutionary metaheuristic algorithm - particle swarm optimization (PSO)

Flock of birds, swarm of bees, school of fish search their food based on their own intelligence and the information is shared among other members of the group. Particle swarm optimization mimics this behavior. The whole group always maintains an average direction and position of the group [177, 178]. Initially, a set of widely spread particles start their searching and gradually all of them try to converge towards global optimum. Number of particles in swarm, initial population, termination criteria and different internal parameters namely inertia factor, constriction factor, social and cognitive acceleration coefficients should be set properly.

Mohanty et al. [117] developed RSM based models for MRR and surface roughness in EDM process with open circuit voltage, current, pulse on time, duty factor and flushing pressure as input parameters. They performed multiobjective optimization of MRR and surface roughness by PSO. They considered initial size of population as 100 and fixed internal parameters like inertia factor as 0.4, both cognitive and social parameters as 2. They found Pareto optimal solution but no guidelines were given regarding handling of multiple objective functions. Optimum results were not validated. Shayan et al. [179] developed BPNN models of cutting velocity, surface roughness and oversize in WEDM process. They did both single-objective and multiobjective optimization of the three process outcomes by PSO with number of particles in swarm as 200 and both social and cognitive acceleration coefficients as 2.05. They converted multiobjective optimization problem to single-objective problem by combining each of the normalized responses by weight factors. As, PSO is used for minimization purpose, so, negative of cutting velocity is taken along with other responses. They reported optimum set of pulse on time, pulse off time, gap voltage, discharge current and wire tension for both the single-objective and multiobjective optimization. Validation test of their result showed that for both single objective optimization and multiobjective optimization, BPNN-PSO approach performed better than RSM-desirability approach. Mukherjee et al. [176] employed PSO for both single and multiobjective optimization of non-linear regression and RSM based models of MRR, wear rate, kerf width, surface roughness and surface finish in WEDM. For multiobjective optimization, normalized wear ratio, surface roughness and kerf width were combined with negative value of MRR using weight factors and considered as objective function. Optimum set of peak current, duty factor, wire tension, water pressure, discharge current, pulse duration, pulse frequency, wire speed and dielectric flow rate were reported for each of the two different sets of models. Setting of internal parameters of PSO and validation test of optimum result were not reported.

It appears that improper selection of internal parameters affects the performance of PSO. Large number of particles like 200 delays the convergence schedule. It is difficult to set termination criteria like the percentage error in change of the value of objective function in earlier for unknown problem.

2.6.3.5 Evolutionary metaheuristic algorithm - sheep flock optimization (SFO)

Sheep flock optimization (SFO) technique simulates the heredity of sheep flocks in a prairie [180, 181]. Within their own flock, genetic inheritance is maintained through breeding by high fitness sheep. If different flocks are occasionally mixed and then separated by their shepherds, several sheep of one flock are inevitably mixed with sheep of another flock. As, sheep with better fitness characteristics breeds most within flock, so, characteristics of the sheep in neighbor flock could be inherited to the sheep of another flock. Compared to GA, inheritance within one flock and mixing-separation of flocks are similar to sub-chromosome and chromosome level genetic operation respectively.

Mukherjee et al. [176] employed SFO algorithm for both single and multiobjective optimization of non-linear regression and RSM based models of MRR, wear rate, kerf width, surface roughness and finish in WEDM with peak current, duty factor, wire tension, water pressure, discharge current, pulse duration, pulse frequency, wire speed and dielectric flow rate as input parameters. In case of multiobjective optimization, weighted combination of the normalized responses, wear ratio, surface roughness, kerf width and negative value of MRR, was considered as objective function. Selection of internal parameters of SFO algorithm namely chromosome and sub-chromosome level crossover probabilities and validation test of optimum result were not reported.

It is observed that performance of SFO algorithm depends on selection of chromosome and sub-chromosome level crossover probabilities. In case of multiobjective optimization, generation of initial population and choice of termination criteria affect the optimum result.

2.6.3.6 Evolutionary metaheuristic algorithm - artificial bee colony optimization (ABCO)

Artificial bee colony optimization (ABCO) is developed by Karaboga [182] inspired by intelligent foraging behavior of honey bees. In the hive, employed bees are associated with specific food sources, onlooker bees are watching dance of employed bees within the hive to choose a food source and scout bees are searching for foods randomly. In ABCO, position of food sources is treated as possible solution in the search space and the nectar amount of food source represents the objective function of the problem.

RSM based models of MRR and surface roughness in EDM process were developed by Das et al. [111]. Using the developed models, they performed both single objective and multiobjective optimization by ABCO algorithm. In case of multiobjective optimization, they combined the normalized surface roughness with negative of the normalized MRR by equal weight factors (each of 0.5). They set swarm size as 10, number of employed bees as 5, onlooker bees a 5, scout bee as 1 and maximum number of cycles as 1000. They reported optimum set of pulse on time, pulse off time, current and voltage for both the single and multiobjective optimization. In case of single objective optimization, optimum MRR and surface roughness were tested with 0.88% and 0.75% error respectively. For multiobjective optimization, validation test showed 0.97% and 0.91% error corresponding to optimum MRR and surface roughness. Mukherjee et al. [176] employed ABCO for both single and multiobjective optimization of non-linear regression and RSM based models of MRR, wear ratio, kerf width, surface roughness in WEDM with peak current, duty factor, wire tension, water pressure, discharge current, pulse duration, pulse frequency, wire speed and dielectric flow rate as input parameters. Weighted combination of normalized responses was considered as objective function for multiobjective optimization. Values of internal parameters of ABCO and validation test of optimum results were not found.

It appears that selection of internal parameters is very important for reaching global optimum. Choice of termination criteria affects the performance of ABCO.

2.6.3.7 Evolutionary metaheuristic algorithm - biography based optimization (BBO)

From the concept of biological distribution of species, that is migration of species from one island to another, arising of new species and extinction of existing species, biography based optimization (BBO) is developed [183]. Immigration and emigration rate of habitats probabilistically decide the migration of suitability index variable (SIV). A good solution is chosen based on the habitat suitability index (HSI) value that is similar to the objective function value. The two migration rates are the monotonically increasing and decreasing function of HSI respectively.

Mukherjee et al. [176] employed BBO algorithm for both single and multiobjective optimization of non-linear regression and RSM based models of MRR, wear rate, kerf width, surface roughness and finish in WEDM. To convert into a single objective optimization problem, multiple responses namely wear ratio, surface roughness, kerf width and negative of MRR are combined by weight factors. For both the single and multiobjective optimization, optimum sets of peak current, duty factor, wire tension, water pressure, discharge current, pulse duration, pulse frequency, wire speed and dielectric flow rate were reported for two different sets of developed models. No information on the selection of internal parameters, namely habitat modification probability, mutation probability, maximum species count, maximum rates of immigration and emigration, maximum mutation rate, elitism parameter and number of habitats were mentioned. Validation of optimum result was not found.

A number of internal parameters of BBO are to set prior to optimization. For selection of the internal parameters, brief knowledge of search space is necessary. Choice of termination criteria plays crucial role in search of optimum result of multiobjective optimization.

The above discussed optimization techniques are widely used for global optimization problems with optimum settings of their own internal parameters. As the technology advances, number of objective functions, number of constraints, type of constraints increase. If the optimization methods are itself suffering from choice of internal parameters, then, it would become more difficult to implement the techniques in real world applications. Therefore, need of expertise is obvious for each of the problem. In 2011, Rao et al. [184] proposed an algorithm-specific parameter-less evolutionary metaheuristic global optimization technique called as teaching learning based optimization (TLBO).

2.6.4 Teaching learning based optimization (TLBO)

Based on the ideology of teaching-learning process, an algorithm-specific parameter-less optimization technique, teaching learning based optimization (TLBO) was proposed in [184]. Though, no such internal parameters are required to fix in TLBO before simulation starts, yet, two crucial conflicting aspects of a metaheuristic algorithm, namely intensification and diversification, are successfully achieved in it. Exploration of the search space is done in learner phase whereas teaching phase does the exploitation. Knowledge gain of a learner depends on both the teaching ability of the teacher as well as the receiving capacity of the learner. Teacher always tries to pull forward the batch of learners aiming to his/her own level. Sharing of knowledge among learners also helps in improvement of their individual knowledge levels. In this way, in every iteration, values of objective function that is scores of the learners in each subject gradually move toward optimum zone. Since the development of TLBO in 2011, number of researchers modified and used TLBO for different applications. A wide range of applications were listed by Rao [185]. Still, applications in the field of machining technology are very limited.

Rao and Kalyankar [186] maximized cutting velocity in WEDM process with constraint surface roughness below a permissible value. Second-order polynomial model of cutting velocity was taken as objective function for optimization and an optimum set of pulse on time, pulse off time, peak current and servo feed was reported. Number of learners was chosen as 10 and termination criterion was set by maximum number of iteration as 20. Validation of optimum result was not reported.

Pawar and Rao [187] employed TLBO for single objective optimization of abrasive water jet machining, grinding and milling process. In abrasive water jet machining, they maximized MRR with power constraint. In grinding, production cost was minimized and production rate was maximized simultaneously by combining weight factors. In milling, production time was minimized by TLBO. In all three machining processes, optimization by TLBO converged within 20 to 30 iterations. Their results showed that performance of TLBO was much better than other evolutionary metaheuristic techniques like SA, GA, PSO, ACO.

Rao and Kalyankar [188] did both multiobjective optimization and single objective optimization with multiple constraints using TLBO for multi-pass turning operation. In multiobjective optimization, production time and tool life were considered as objective functions. They took cutting force, cutting power and surface roughness as constraints. They compared their results with results obtained by GA. It was observed that with 50 learners, TLBO outperforms GA at the end of 50 iterations. In their single objective optimization, unit production cost was minimized with 20 constraints in rough cutting and finishing zones. For single objective optimization, TLBO also showed better performance than GA in terms of convergence rate and accuracy of the solution.

In case of turning CFRP composite material, Abhishek at al. [189] developed non-linear regression models of MRR, cutting force and surface roughness separately. They did single objective optimization of each of three response parameters and of a weighted combination of all the three models. During optimization, values of objective functions saturated almost at the end of 20 iterations with initial population size 10 and fixed teaching factor 2. They compared their result with genetic algorithm and concluded that TLBO was computationally more efficient.

Teaching-learning based optimization is found to be more promising than other optimization techniques as no such internal parameters are required to fix earlier and convergence rate is much higher (number of iteration is low). Still, maximum number of iterations considered as termination criteria is confusing as it may not ensure global optima. Thus, with modifications, TLBO might be a promising optimization technique for tuning of the internal structural parameters of SVM regression.

2.7 Assessment of surface topography

Characterization of machining process primarily involves measurement of rate of material removal and assessment of surface topography. Levels of machining control parameters directly influence the material removal phenomena. This material removal operation could be assessed both by rate of material removal and by geometry of the marks left by machining process. Rate of material removal includes a quantitative measurement of the amount of material removed. Whereas, investigation of the surface topography leads to study the inherent features of the mechanism of material removal. In EDM process, complex thermo-electrical phenomena, material inhomogeneity, transient behavior of dielectric fluid and material ejection during sparking result critical surface integrity of the machined part.

In general, a surface topography is characterized by different arithmetic parameters of roughness profile, grouped in mostly three categories namely amplitude parameters, spacing parameters and hybrid parameters. Amplitude parameters include center line average, maximum peak to valley, average peak to valley, root mean square etc. Mean spacing of the asperities at the level of the central line, average wavelength, peak count, number of intersections of the profile at the mean line etc. belong to category of spacing parameters. Different hybrid parameters are average slope of profile, root mean square slope of profile, average radius of asperities, developed length of profile etc. [190]. In general, the above parameters are some algebraic combinations of absolute measurements of surface profile variations.

Apart from 2D measurements of surface, Ramasawmy and Blunt [191] measured some 3D surface roughness parameters, namely root mean square height, density of summits, core material volume, core void volume, valley void volume and core roughness depth, on EDM generated surface obtained at different combinations of levels of pulse current, pulse on time and electrode surface area. They observed that root mean square height had linear relation with current but parabolic or quadratic relationship with pulse duration and pulse energy. Similarly, core material volume and core void volume exhibited strong influence of pulse current whereas valley void volume was sensitive to change of pulse duration. Still, no correlation was found between surface texture and surface generation process.

Use of statistical functional parameters is another way of extracting features of surface topography. Generally, height distribution function and autocorrelation function (ACF) are implemented to study the possible features of surface. Mostly, first to fourth order central moments, bearing ratio curve or

Abbott-Firestone curves are different forms of height distribution function of surface profile. Gaussian distribution function with reasonable approximation almost matches with the height distribution function of real engineering surfaces [190]. Zhu et al. [192] studied the surface topography to evaluate cavitation erosion resistance of AlSi10Mg using third (skewness) and fourth (kurtosis) order central moments. They observed that time required for removing original surface finish marks which was closely related to cavitation erosion rate, could be predicted by tracking the changes of the two height distribution functions.

Another statistical approach, autocorrelation function (ACF) of roughness profile, exhibits possible random and periodic features buried on generated surface. Roy et al. [193] analyzed the surface roughness data to find out the relative contribution of the electrolytic dissolution and the pure mechanical grinding in electrochemical grinding.

Murti and Philip [194] characterized the EDM generated surfaces through SEM photographs. The machined surface is a cumulative effect of many independent events. Final surface is consisted of resolidified layers of molten material, overlapping craters of different sizes, networks of micro-cracks and pinholes. The resolidified layer on the machined surface, called as white layer is irregular and non-uniform in thickness. Hardness of this layer is extremely high due to rapid quenching of molten material [195]. Micro-cracks are of two types namely network of fine cracks, which are perpendicular to surface but limited to resolidified layer only and radially distributed cracks. Network of fine cracks are generated by thermal stress and stress due to phase transformation [195]. Jeswani and Basu [195] also identified three types of craters namely normal craters with raised rim of resolidified layer, crater with spilled pool of material caused by ineffective expulsion of molten material and neat crater formed by abrasive effects of flying debris particles. Their model of surface generation claimed that proposed surface was expected to be periodic with wavelength equal to half of crater size. Still, the model was far away from actual results. Stochasticity of the EDM generated surface is due to random variation in energy and location of successive sparks producing a wide variety of crater size, splashing of molten material, ineffective ejection from crater and incomplete solidification of residual material before the onset of next spark [194]. Murti and Phlip [194] finally concluded that machined surface was stochastic in nature and Gaussian with open texture with high repeatability.

Pandit and Rajurkar [196] developed a data dependent system from measured surface profile which "trully" reflected the mechanism of material erosion. They developed a stochastic differential equation and estimated the temperature distribution through construction of isothermals that was correlated to crater shapes. Williams and Rajurkar [197] proposed ARMA (4,3) model to assess wire electric discharge machined surface profile. Their study indicated that higher order model was required for wire electric discharge machined surface compared to die sinking electric discharge machined surface. Non-directional features of surface profile were also observed after wavelength decomposition of machine surface profile. Due to the involvement of complex electrodynamics, electromagnetics, thermodynamics and hydrodynamics, Yeo et al. [198] also considered EDM as stochastic in nature and proposed a model for crater geometry formed on both the tool electrode and the workpiece. Though, their model predicted crater geometry within 7% error, still, they followed deterministic procedure in model development.

In die-sinking EDM, discharge takes place at the spot of least resistance between tool electrode and workpiece. The favorable position of least resistance is governed by material inhomogeneity and gap state. Present gap status is determined from previous spark history. Thus, investigation of location and type of earlier sparks is necessary to understand the present gap status. At the end of each discharge, debris particles are formed. Cracking and chemical decomposition of dielectric also affect debris formation. Due to electrophoresis, debris particles flow in between tool electrode and workpiece in the perpendicular direction to electrode surfaces [199, 200]. It was observed that the debris particles were likely to form chain like bridges parallel to electric field in between tool electrode and workpiece. Hence, various concentrations of contaminants like suspended debris particles and products from dielectric decomposition, that remain even after flushing, result different types of discharge initiation. Statistical investigation of different ignition delays explains the discharge initiation due to the bridge formation by debris particles in between tool electrode and workpiece [201]. The above mentioned observations suggest probabilistic occurrence of discharges. Kunieda and Nakashima [202] reported that probability of occurrence of discharges is a product of probability of discharge per unit area and surface area but they identified the discharge locations in deterministic way.

Cooke and Crookall [203] studied the effect of time interval between successive discharges on distance between them for different parametric settings (capacitance and resistances) on relaxation type pulse generator. As time interval increased, dispersion of debris particles increased, deionization became more effective, as a result of that, mean and variance of the distances between successive discharges increased. Their study recommended the predominant influence of discharge history on next discharges. Kunieda et al. [7] did an extensive literature review on gap phenomena. They reported that discharge locations during stable operation were not random rather chaotic. Each discharge was determined by previous condition but final outcome was almost unpredictable even same control parameters were set. This conclusion was further explained by Gatto et al. [204]. They examined the gap phenomena by characterizing ignition delay. It was summarized that mechanism of material removal in EDM was dependent on initial condition. Formation of gas bubbles and arrangement of debris particles at the end of each discharge influenced consecutive discharges. It was observed that higher concentration of debris and possibility of low voltage discharge or short circuit pulse were interrelated. Higher concentration of debris may result formation of either chain or cluster. Cluster of debris particles causes discharge of higher voltage compared to bridge formation by chain structure. However, current state is related deterministically to earlier one but overall outcome is unpredictable. This spark erosion is recursive and regulated by earlier history. From the comprehensive view of discharge phenomena through examination of ignition delay, Gatto et al. [204] claimed that location and type of discharges were both chaotic in nature. As, concentration of debris increased, then, spark erosion process evolved towards chaotic behavior. Apart from presence of chaos in discharges, chaotic behavior of plasma generated from electrical discharges in gas [205] was also reported in literature.

Lorenz [206] became famous for his pioneer work on searching chaotic dynamics in convection process. After that, in the fields of engineering, physics, biology, earth science, economics, cosmology etc., science behind the underlying process was described based on non-linear time series analysis of their purposefully selected outputs. Tang et al. [207] did a review of already proposed methodologies for the complexity analysis of time series data. Mono and multi-fractality analysis, estimation of attractor invariants and diagram description, structural and dynamical entropy evaluation were some mathematical concepts for building quantitative measurements of the dynamic characteristics of underlying process. Kędra [208] reported a detailed discussion on deterministic chaotic dynamics of river flow data. This discussion provided a comprehensive study of the different approaches taken for analysis of hydrological data. Hu et al. [209] conducted a study on runoff time series data of an inland river. Their cross-scale characterization of chaotic behavior suggested that selection of temporal scale of observed variable played a crucial role behind the confirmation of chaotic pattern. It was observed that along with temporal scale, aggregation of sample data, duration of observation, accuracy of data collection, presence of noise level, flow of information from unobserved to observed variables controlled the effectiveness of the analysis [208]. The non-linear techniques assisted to research on the presence of chaos behind the apparently erratic–looking behavior of physical process.

Though number of researchers analyze the generated machined surface and comment on the machining process, still, no generalized way out is found to declare about stochasticity or chaotic nature of surface generation from machined surface.

The following lacunae in the existing works on modeling of process outcomes, optimization of process performances and assessment of surface topography, are identified by summarizing the foregoing discussions on the literature. The objective and scope for the present thesis are also given with reference to the lacunae.

(i) Modeling:

Modeling methods employed on EDM process available to date are based on either of the three approaches namely analytical, empirical and intelligent. Applicability of analytical models are restricted to limited cases due to their user specific assumptions and closeness to practical situation is reasonably low. Instead of considering some assumptions regarding physical phenomena, empirical models are developed directly from experimental observations. Still, data size affects the performance of modeling by multivariable regression and dimensional analysis. Efficiency of historical data based approaches like grey system theory, time varied predictive modeling depends on sampling rate of data collection and the predefined sequence of data set. Selection of internal functions like basis and criterion functions in GMDH, intrinsic mode function in empirical mode decomposition controls the final structure effectively. Pre-assumed discriminating criteria in instrumental variable approach and time varied predictive modeling reduce the repeatability of the proposed models. Dimensional analysis is not capable of accounting the nature of constants in correlation. Additive or subtractive nature of input-output relationship is not reflected in modeling by dimensional analysis. Even, dimensional analysis could not correlate functions like trigonometric, exponential, logarithmic etc. It is clear that nature of input-output relationship must be preselected before modeling through empirical approaches and developed model is highly sensitive to each of the data set. To some extent, intelligent procedures overcome this problem. Still, allowing same importance to all factors is a common problem in ANN and fuzzy logic. Training of internal parameters in ANN consumes large time and need prior knowledge. Models based on ANN are suffered from efficiency in training, efficiency of testing and over-fitting. Methods of fuzzifcation and defuzzification, setting of combination rules for conjunctive and disjunctive clauses decrease the repeatability and increase uncertainty in final output. In EDM, complex interactive patterns among machining control parameters and process outputs are obvious but global nature is not known at all. Involvement of transient complex thermo-electric phenomena results irregular variations of process outcomes but none of the available methods is capable of absorbing the fluctuations in robust way.

In this context, a supervised batch learning methodology, support vector machine (SVM) regression, is proposed to develop a virtual data generator of EDM process which can predict the process outcomes in a robust way.

(ii) Optimization:

It is observed that performance measurements of EDM process like MRR and surface finish are conflicting in nature. As MRR increases, surface finish decreases. Therefore, a tradeoff should exist. A guideline is necessary to get the optimum MRR without sacrificing surface finish and to select the levels of machining control parameters in EDM machine to meet need-based MRR-surface roughness combination. Researchers employed different direct data based, traditional and evolutionary optimization methods for this purpose. Optimum results obtained by direct data based methods are limited within the preselected levels of available data set. Traditional methods involve calculation of derivatives which results long computation time, poor convergence rate and need large memory. Unidirectional search algorithms might be trapped inside local optimum. Performance of evolutionary method to reach global optimum is higher than traditional methods. Marching procedure of single point evolutionary method like simulated annealing is affected by the choice of initial point specially in case of multiobjective optimization. Along with simulated annealing, all the population based evolutionary optimization methods employed on EDM process available to date are suffering from their own internal parameter tuning. Profound knowledge regarding the influence of internal parameters on simulation steps of optimization algorithm is prerequisite. Further, termination criteria were set either by maximum number of iteration or by a predefined level for the change in objective function value. It is very difficult to know the values earlier for real world multimodal problems.

In this regard, algorithm-specific parameter-less teaching learning based optimization (TLBO) is considered for optimization purpose with some proposed modifications. Pseudo Pareto optimization of MRR and surface roughness is also suggested with the aid of modified TLBO. Further, a inverse solution method is proposed to make a generalized layout for selection of the values of machining control parameters to meet near-optimum achievable specific need based combination of conflicting type process outcomes like MRR and surface roughness. Modified TLBO is also considered for tuning of internal structural parameters of SVM regression. Furthermore, a new way of handling multiple objective functions without affecting their individual impacts is attempted.

(iii) Surface topography consideration:

Due to presence of such phenomena like formation, growth and collapse of plasma channel, transient nature of dielectric medium, mechanism of material removal is complex in nature. As, surface generated in EDM is superposition of craters formed by high frequency, high power density, spatial and sporadic sparks, so, study of surface topography could help to comment on underlying surface generation process. No systematic study has so far been reported correlating the nature of surface generation from surface topography. Random nature of surface topography was reported by different researchers but it is qualitative and no one tried to correlate the process parameters with extent of randomness. Though, some researchers did some remarks on nature of surface generation like stochastic and chaotic, still, no analysis is suggested in its favor.

In the present thesis, therefore, a generalized structure is expounded to unfold the underlying unseen features of surface generation process by analyzing machined surface topography. The objective is to evaluate randomness, periodicity and their relative contributive effects and thereby to analyze the surface topography for chaos in EDM so as to comment on the surface generation process.

2.8 Aims and objectives of the thesis

Aims and objectives of the present work are thus summarized as follows.

- To develop a robust virtual data generator of EDM process with the aid of SVM regression with internal structural parameters tuned by PSO and TLBO.
- To perform pseudo Pareto optimization of MRR and surface roughness using TLBO and to propose an inverse solution procedure for selection of near-optimum achievable machining control parameters to meet specific need based combination of MRR and surface roughness.
- To analyze the machined surface for quantitative assessment of relative contribution of randomness and periodicity in surface topography, for study the presence of chaos in surface topography and thereby to comment on surface generation process.

2.9 Organization of the thesis

Organization of the thesis thus becomes as follows.

- In chapter 2, relevant literatures on modeling, optimization and assessment of surface topography in EDM process are discussed. Lacunae in existing methodologies are identified and thus, aims and objectives of the present work are set.
- Chapter 3 deals with the scheme of experimentation to collect necessary data to meet the aims and objectives of the present work.
- Steps of model development of EDM process outcomes, namely MRR and ASR, with the aid of SVM regression with internal structural parameters tuned by PSO and TLBO are discussed in detail in chapter 4.
- In chapter 5, pseudo Pareto optimization of MRR and ASR, predicted through estimated models, are performed and an inverse solution procedure is proposed to select near-optimum setting of machining control parameters to meet specific need based combination of MRR and ASR.
- In chapter 6, quantitative assessment of surface topography is done using autocorrelation function and logical layout is structured to evaluate the relative contributive effects of randomness and periodicity buried in fluctuations on machined surface. Further, test of chaos present in surface topography is performed. Extent of randomness, periodicity and chaos present in generated surface are studied with the variations of machining control parameters.
- Conclusions are drawn from the present work, recommendations and future scope are reported in chapter 7.

CHAPTER 3

EXPERIMENTS

3.1 Introduction

Robust virtual working system of EDM process is necessary to reduce production time and cost through precise control over the process. Thus, representative models of process outcomes are to be built first and selections of optimum levels of machining control parameters are to be done using developed models. From the review of literature, it is found that predictions of process outcomes are difficult due to complex physical phenomena involved in EDM process and due to lack of robustness of model building methodologies. Advanced supervised batch learning based system would be effective in this regard. During training of supervised batch learning system, feeding of relevant data set is prerequisite. Therefore, sets of different levels of machining control parameters and corresponding process outcomes are to be generated. Larger training set would be good for validation of developed learning system over wide range of working conditions. In keeping with this idea, experiments are carried out in EDM machine and results are stored. Details of experimental set up, measurements of process outcomes and results are given below.

3.2 Experimental set-up

Experiments are carried out on Tool Craft A25 EDM machine (model no. G30/SD, serial no. 294-89) (figure 3.1) equipped with rectangular pulse generator operating with commercially available kerosene oil as dielectric medium and an open circuit voltage of 66 V. Specifications of EDM machine used for the experiment purpose are given table 3.1.

Fig. 3.1 Tool Craft A25 EDM machine

Table 3.1 Specifications of EDM machine and accessories

EDM machine	
Type of construction	'C' type
Size of worktable	300 mm X 200 mm
Size of fixed working chamber	465 mm X 270 mm X 200 mm
Table longitudinal movement	175 mm
Table cross movement	100 mm
Maximum dielectric level over table	140 mm
Maximum workpiece height	90 mm
Maximum workpiece weight	45 kg
Servo head	
Servo system	Stepper drive
Quill travel	150 mm
Electrode platen size	100 mm square
Electrode weight carrying capacity	10 kg
Accuracy of quill movement	0.01 mm over 200 mm
Pulse generator	
Model	A25
Shape of pulse	Square
Peak current	Maximum 25 A through toggle switches
Pulse on time	2 µs to 2 ms
Pulse off time	2 µs to 2 ms
Power source connection	440 V, 50 Hz, 3 phase
Dielectric system	
Dielectric	Commercially available kerosene oil
Viscosity of dielectric	5-6 cSt at 20^{o}C
Tank capacity	160 litre
Filtration	Better than 10 µm
Flushing type	Side
Flushing capacity	Maximum 1.23 litre/min
Flash point	37-67^{o}C

In the EDM machine, electric energy is supplied to the spark gap either in the form of voltage time standard pulse or current time "nal" pulse. Voltage time standard pulse is generally used for testing and finishing purposes. Actual power consumed in each discharge is almost constant and productivity is comparatively high for "nal" pulse. Thus, series of discrete rectangular pulses are generated by current time "nal" pulse for stable and precise machining operation. Servo sense potentiometer and servo feed potentiometer are set at particular positions throughout the experiment to have a stable machining condition with "anti-arc" switch on.

Electrolytic copper rod (density 8904 kg/m^{3}) with cross-sectional diameter of 12 mm is used as tool electrode. Standard high speed steel cutting tool, equivalent to M2 grade, is chosen as the workpiece material and connected to the negative terminal. Measured density of workpiece material is 8006 kg/m^{3}. Detailed specifications of workpiece and tool are given in tables 3.2 and 3.3 respectively.

Table 3.2 Specifications of workpiece

Size	15.875 mm X 15.875 mm X 10 mm
Material	High speed steel, M2 grade (ZEDD)
Composition	C - 0.95%, W - 6%, Mo - 5%, Cr - 4%, V - 2%, Fe - rest
Density	8006 kg/m^{3}
Hardness	62-65 HRC
Elastic modulus	190-210 GPa
Coefficient of thermal expansion	10-12.5 µm/m^{o}C
Thermal conductivity	41.5 W/mK
Melting point	4680 ^{o}C

Table 3.3 Specifications of tool

Size	:	Φ12 mm X 15 mm
Material	:	Electrolytic copper
Composition		99.99% Cu
Density	:	8904 kg/m^3
Elastic modulus	:	110-128 GPa
Coefficient of thermal expansion	:	16.5 µm/mK
Thermal conductivity	:	401 W/m/K
Electrical resistivity	:	1.673 µΩ-cm at 20 ^{o}C
Melting point		1085 ^{o}C

Based on the availability of machine settings, four levels for each of the three most significant machining control parameters (refer table 3.4), namely current (cur), pulse on time (t_{on}) and pulse off time (t_{off}), are selected to operate the machining process in semi-finishing and roughing zones.

Table 3.4 Levels of machining control parameters

	Level 1	Level 2	Level 3	Level 4
Current (A)	6	9	12	15
Pulse on time (µs)	50	100	150	200
Pulse off time (µs)	50	100	150	200

Experiments are performed based on the procedure of full factorial design. Total 64 mutually exclusive treatments of different levels of three machining control parameters are set randomly to the EDM machine.

3.3 Results and discussion

Electric discharge machining process could be well characterized by two major responses – material removal rate (MRR) and average surface roughness (ASR). Representative models of MRR and ASR would meet both the quantitative and qualitative assessment of performance in EDM process.

For the purpose of determining the material removal rate (MRR), weight of workpiece is taken at standard measuring balance (AFCOSET – ER182A) of least count 0.01 mg before (w_{bf}) and after (w_{af}) machining operation. Weight loss is then divided by the measured density of workpiece material (ρ) in order to convert it into volumetric term and is further divided by the actual cutting time (ct) to obtain the MRR in terms of mm^3/min (equation 3.1).

$$\text{MRR (mm}^3\text{/min)} = \frac{w_{bf} - w_{af}}{\text{ct X } \rho} \tag{3.1}$$

Rate of tool lifting and releasing are set at particular positions in control panel of the pulse generator throughout the experiment. During each experimental run, tool idle time and working time are measured for depth of cut around 1 mm to 1.2 mm. It is found that on an average 71.8% of machining time is actually used for cutting operation. The typical machining time with lowest material removal rate is kept as 45 minute for a depth of 1.1 mm. It is observed that material removal rate varies from 1.367 mm^3/min at the combination of cur = 6 A, t_{on} = 50 µs and t_{off} = 200 µs to 28.099 mm^3/min at the combination of cur = 15 A, t_{on} = 200 µs and t_{off} = 50 µs.

Using Taylor Hobson Precision Surtronic 3+ Roughness Checker with stylus tip radius 5 µm, surface profiles of 4 mm length along three mutually 120^o apart directions are measured on each of the 64 generated surfaces. For measurement of surface profiles, cutoff length is 0.8 mm with Gaussian filter, horizontal magnification is 200X and vertical magnification is 2000X. The three surface profiles measured along three 120^o apart directions on each of the 64 machined surfaces are considered as replications of that treatment. For 64 treatments, total 192 surface profiles (3 replications for each of the 64 treatments) are obtained. From each of the 192 surface profiles, roughness profile of evaluation length of 3.2 mm is separated and stored in image format.

For each of the roughness profiles, center line average surface roughness (Ra) value is noted. Mean of three such center line average surface roughness (Ra) values obtained from each of the machined surfaces is calculated and considered as the representative average surface roughness (ASR) of that machined surface.

Variations of ASR with MRR are shown in figure 3.2. It is observed that ASR increases with the increase of MRR. Thus, to maintain the quality of machined surface productivity would be compromised.

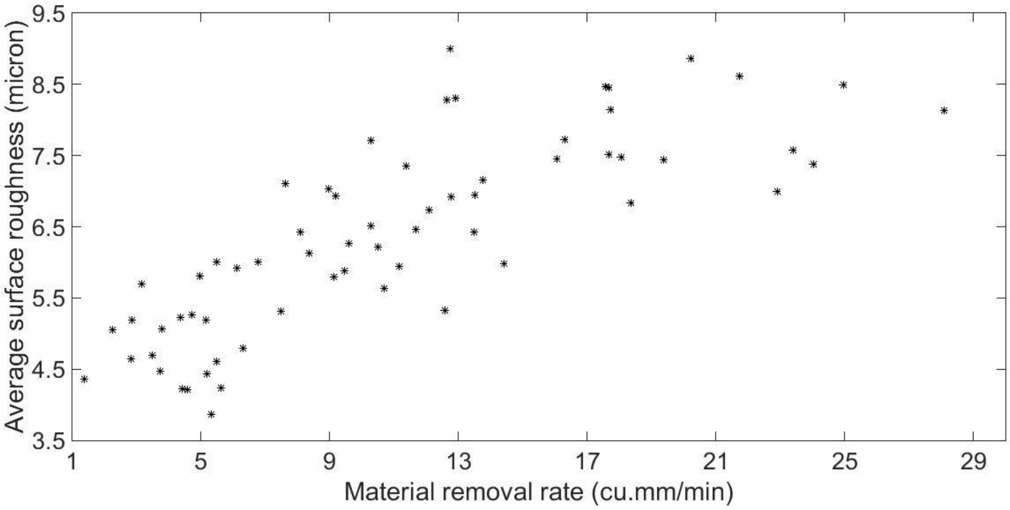

Fig. 3.2 Variations of ASR with MRR

The values of average surface roughness (ASR) vary from 3.87 μm at the combination of cur = 6 A, t_{on} = 200 μs and t_{off} = 50 μs to 9.00 μm at the combination of cur = 15 A, t_{on} = 200 μs and t_{off} = 200 μs. The relative influences of machining control parameters and their interactions on MRR and ASR are estimated through analysis of variance of each of the MRR and the ASR. Percentage contributions of cur, t_{on}, t_{off} and their interactions are given in table 3.5. It is observed that effects of current on the variations of both MRR and ASR are sufficiently higher than the effects of pulse on time, pulse off time and their interactions.

Table 3.5 Percentage contributions of cur, t_{on}, t_{off} and their interactions on MRR and ASR

Machining control parameters and their interactions	Process outcomes	
	MRR	ASR
cur	56.3599	70.9923
t_{on}	12.6495	11.3290
t_{off}	19.7931	0.1466
cur X t_{on}	3.8533	8.2945
cur X t_{off}	6.6506	1.3949
t_{on} X t_{off}	0.2797	4.5744
Between treatments	98.5861	96.7317
Within treatment	1.4139	3.2683

Typical roughness profiles are shown in figure 3.3. In figures 3.3 (a) and (b), values of Ra are very close as 3.61 μm and 3.69 μm. Similarly, values of Ra in figures 3.3 (c) and (d) are very close as 9.76 μm and 9.96 μm. Still, roughness profiles show different patterns and erratic fluctuations exist. Hence, it is understood that value of Ra is not sufficient to properly describe the features of machined surface.

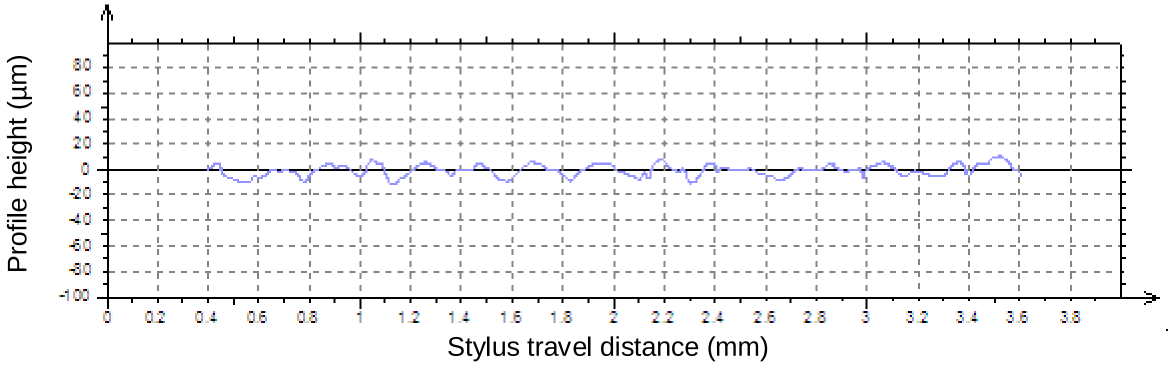

(a) cur = 6 A, t_{on} = 200 µs & t_{off} = 150 µs (Ra = 3.61 µm)

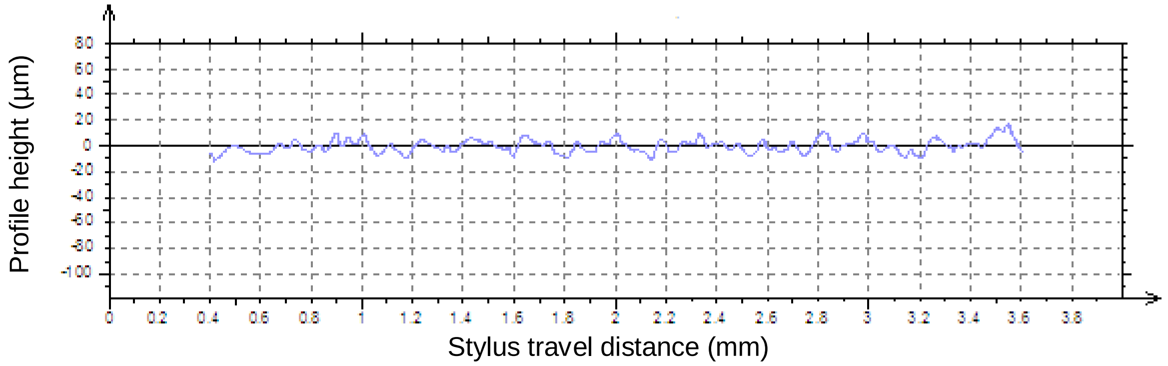

(b) cur = 6 A, t_{on} = 50 µs & t_{off} = 50 µs (Ra = 3.69 µm)

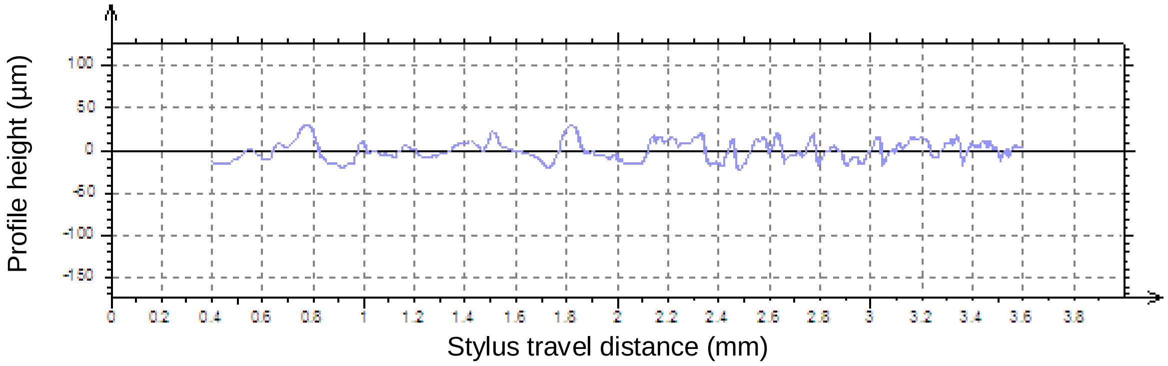

(c) cur = 15 A, t_{on} = 150 µs & t_{off} = 100 µs (Ra = 9.76 µm)

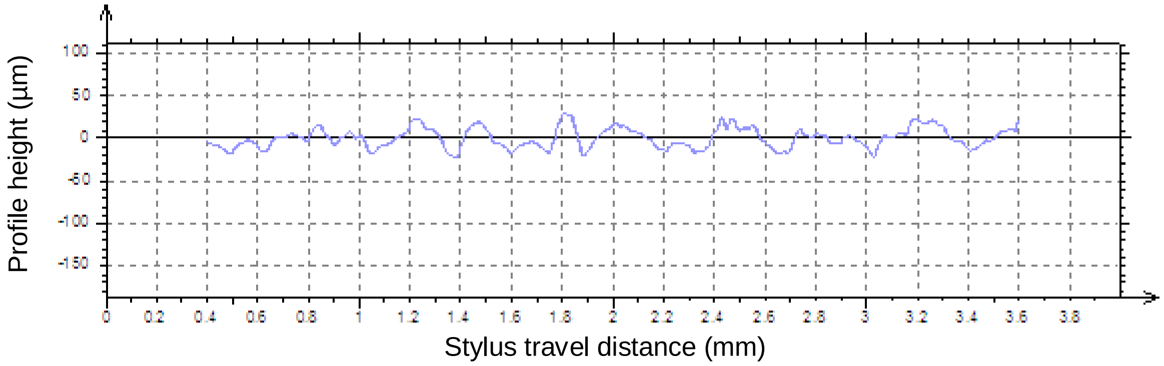

(d) cur = 12 A, t_{on} = 150 µs & t_{off} = 50 µs (Ra = 9.96 µm)

Fig. 3.3 Typical roughness profiles measured on machined surfaces

Therefore, along with center line average surface roughness (Ra), few other measurements of surface roughness namely maximum peak to valley height over evaluation length (Rt), skewness of the distribution of profile heights (Rsk), kurtosis of the distribution of profile heights (Rku), root mean square of profile heights (Rrms), root mean square of slopes of profile (RΔq) and developed length of profile (RLo) are also taken. Variations of the six roughness parameters with corresponding values of Ra are shown in figure 3.4.

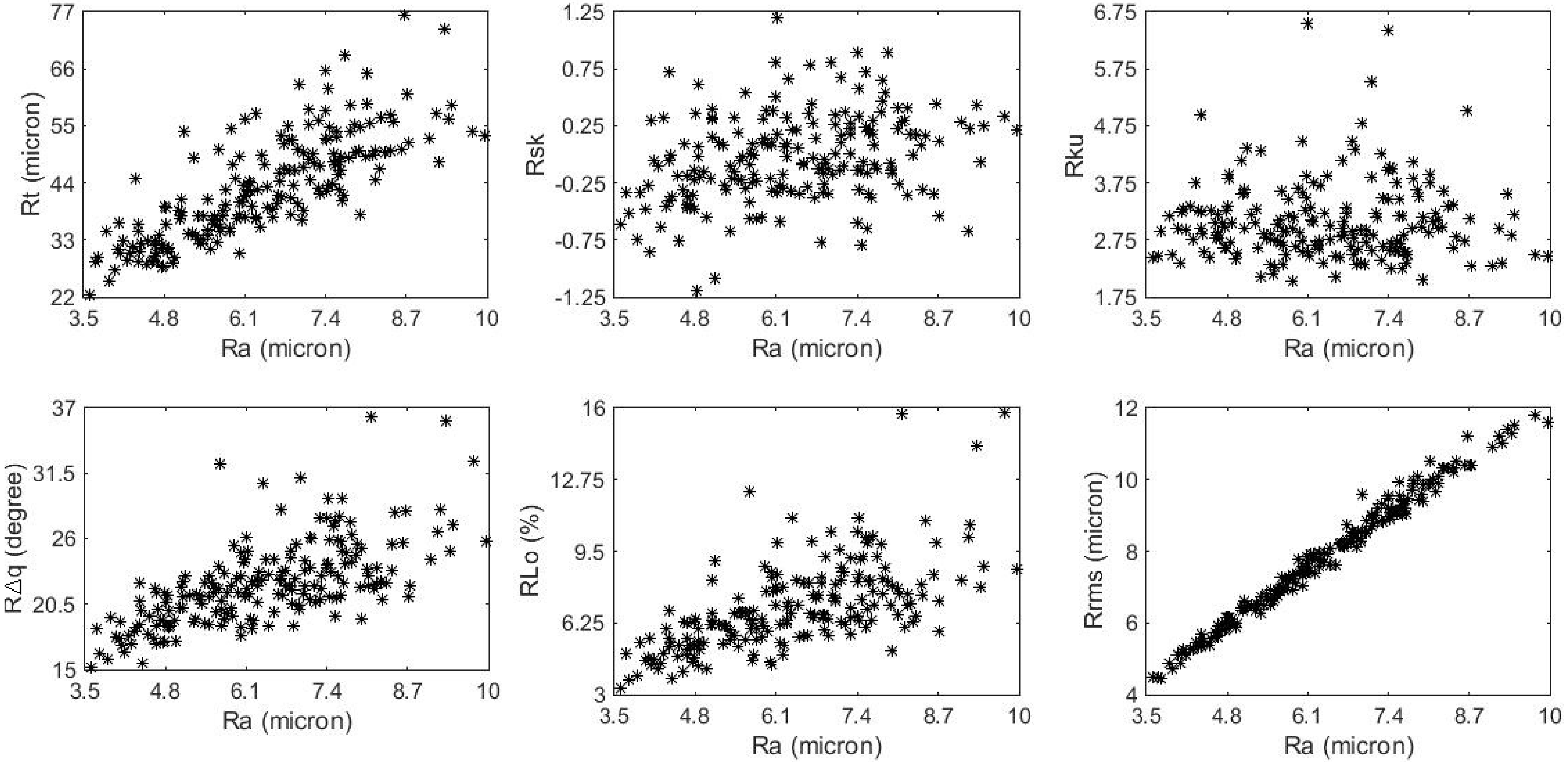

Fig. 3.4 Variations of Rt, Rsk, Rku, RΔq, RLo and Rrms with Ra

In figure 3.4, it is observed that with almost same Ra value, values of Rt, Rsk, Rku, RΔq, RLo for different surfaces show large variations. Values of Rt lie within a large range of 22.3 µm and 76.3 µm. Most of the values of Rsk are close to zero (varies from -1.19 to 1.19) which indicates near symmetrical distribution of profile heights [190] and value of Rsk increases with the increase of Ra. Further, fourth order central moment of profile heights, that is Rku, varies from 2.03 to 6.54. Most of the Rku lie above 3 which indicates the presence of high randomness in profile heights [190]. Increasing patterns of both RΔq and RLo with the increment of Ra are observed. Surface having higher slope of profile (RΔq) attributes better retaining of lubricants [190] and large developed length of profile (RLo) suggests openness of machined surface [190].

To obtain the percentage contributions of machining control parameters and their interactions on the roughness parameters (table 3.6), analysis of variance is performed on each of Rt, Rsk, Rku, RΔq, RLo and Rrms. From table 3.6, it is found that current has the most contributive effects on the variations of Rt, RΔq, RLo and Rrms. In case of Rsk and Rku, variations within treatment are much higher than variations between treatments. Therefore, presence of uncontrollable erratic fluctuations in profile heights is expected [210]. As, all the measurements of surface roughness are some algebraic treatment of profile heights measured at some specific locations, so, to understand the actual features of machined surface, scanning electron micrographs of machined surfaces are taken.

Table 3.6 Percentage contributions of cur, t_{on}, t_{off} and their interactions on Rt, Rsk, Rku, RΔq, RLo and Rrms

Machining control parameters and their interactions	Process outcomes					
	Rt	Rsk	Rku	RΔq	RLo	Rrms
cur	52.2921	22.0873	4.5336	43.0532	42.1082	65.2541
t_{on}	4.9448	9.9932	1.4083	2.0705	2.0660	9.8947
t_{off}	0.4673	1.5779	0.3414	0.1201	0.1850	0.1194
cur X t_{on}	3.4000	2.8350	6.7595	5.7138	3.5748	6.3114
cur X t_{off}	1.1185	3.9495	2.8919	3.5439	2.9544	1.3062
t_{on} X t_{off}	2.7544	4.5445	3.0844	3.8414	5.1136	4.2758
cur X t_{on} X t_{off}	7.1434	12.6187	14.9195	13.0179	11.5482	3.3473
Between treatments	72.1205	57.6061	33.9386	71.3608	67.5502	90.5089
Within treatment	27.8795	42.3939	66.0614	28.6392	32.4498	9.4911

3.3.1 Study of surface topography by SEM

Scanning electron micrographs of typical machined surfaces are taken by JEOL JSM-6360 scanning electron microscope. Typical images of SEM are shown in figures 3.5 through 3.16.

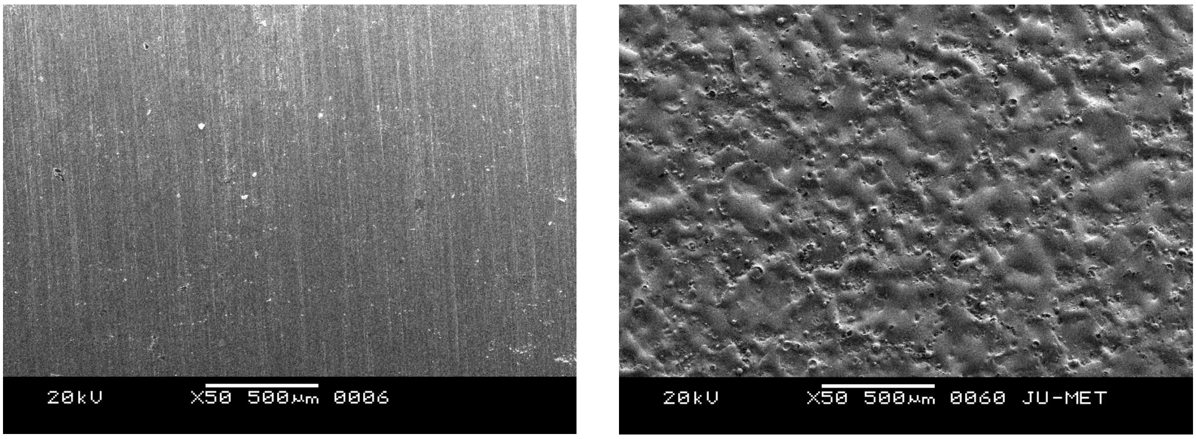

(a) Ground surface before EDM (b) cur = 6 A, t_{on} = 200 μs and t_{off} = 200 μs

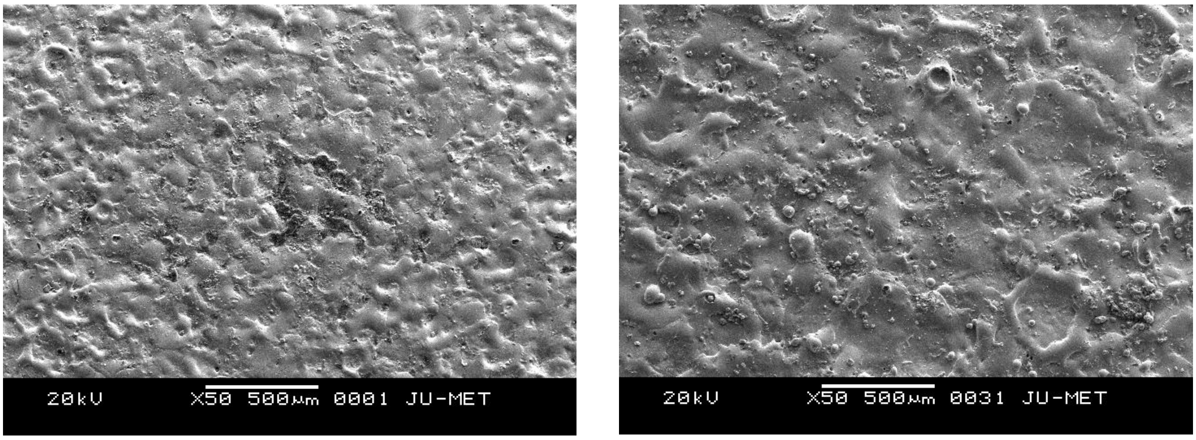

(c) cur = 6 A, t_{on} = 50 μs and t_{off} = 200 μs (d) cur = 15 A, t_{on} = 200 μs and t_{off} = 200 μs

Fig. 3.5 Obliteration of parent surface towards "random" texture patterns

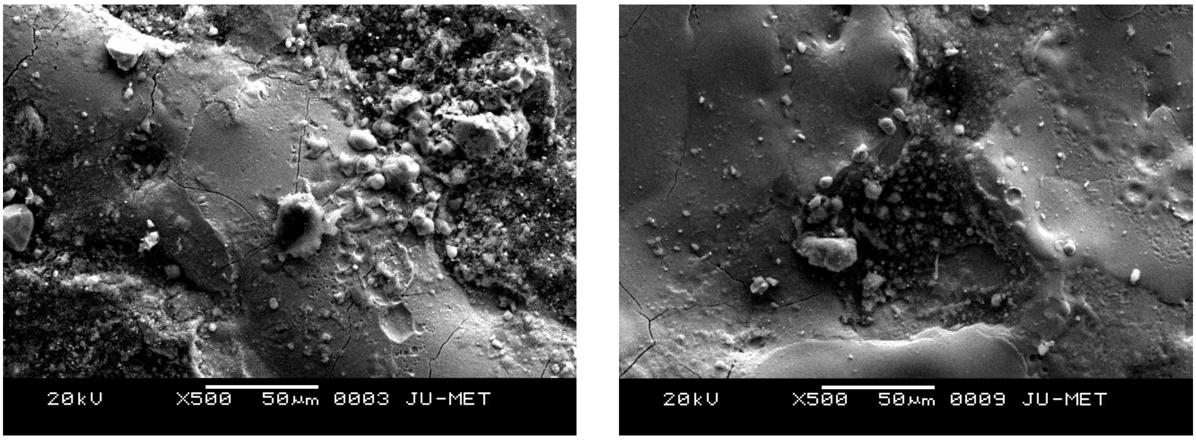

(a) cur = 6 A, t_{on} = 50 μs and t_{off} = 200μs (b) cur = 6 A, t_{on} = 50 μs and t_{off} = 200μs

Fig. 3.6 Distribution of debris particles on machined surface

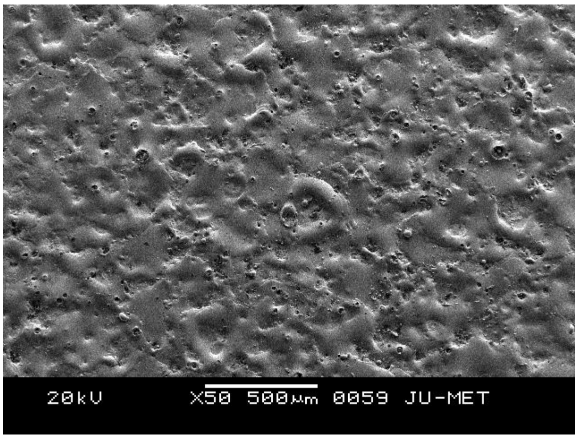

Fig. 3.7 Pinholes on machined surface
(cur = 6 A, t_{on} = 200 μs and t_{off} = 200 μs)

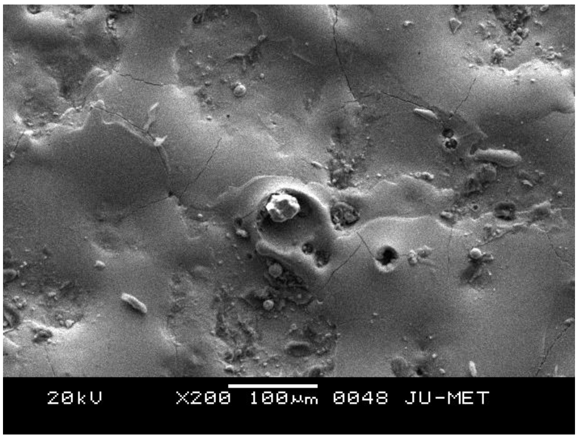

Fig. 3.8 Residual material at the rim of crater
(cur = 6 A, t_{on} = 200 μs and t_{off} = 200 μs)

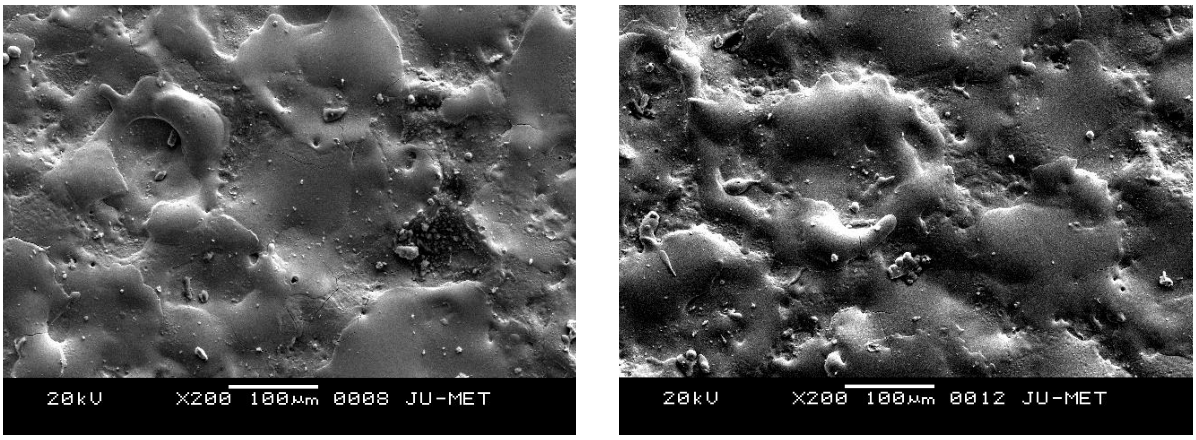

(a) cur = 6 A, t_{on} = 50 μs and t_{off} = 200μs (b) cur = 6 A, t_{on} = 50 μs and t_{off} = 200μs

Fig. 3.9 Violent explosion of molten material assisted with severe turbulence

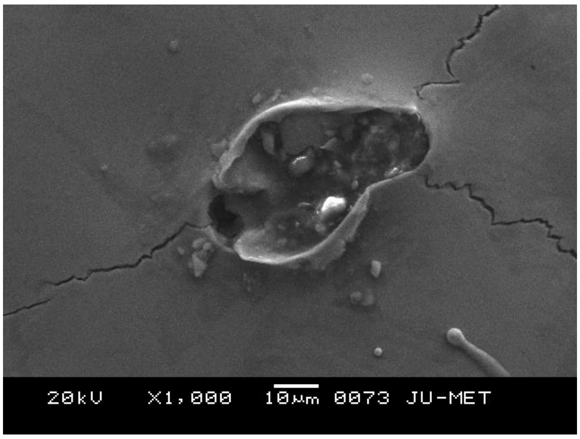

Fig. 3.10 Material exploded forming outward bend
(cur = 6 A, t_{on} = 200 μs and t_{off} = 50 μs)

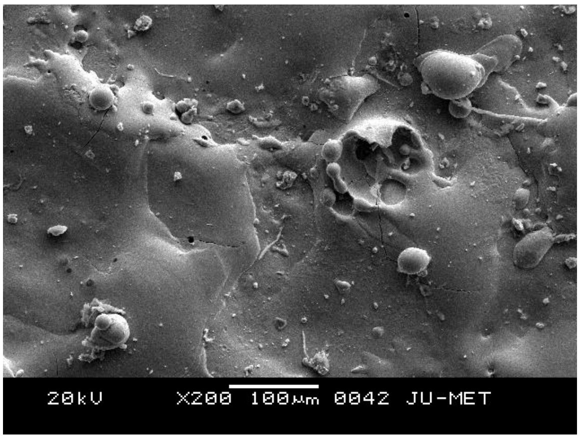

Fig. 3.11 Material exploded forming inward bend
(cur = 15 A, t_{on} = 200 μs and t_{off} = 200 μs)

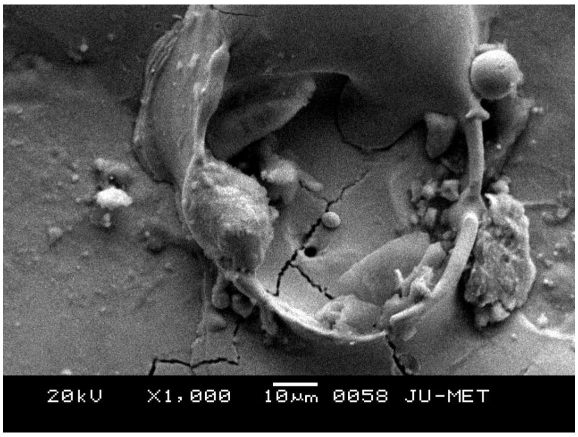

Fig. 3.12 Normal crater with raised rim
(cur = 6 A, t_{on} = 200 μs and t_{off} = 200 μs)

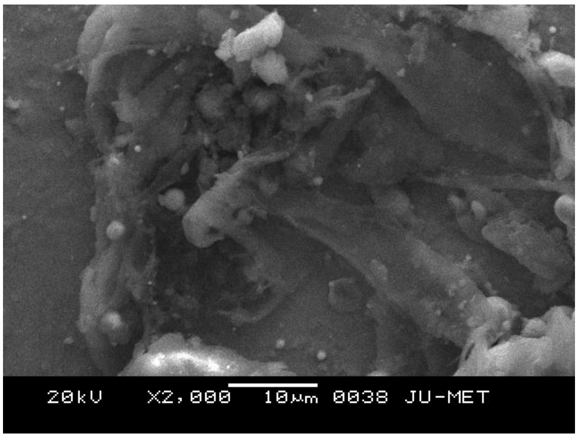

Fig. 3.13 Crater with spilled pool of molten material
(cur = 15 A, t_{on} = 200 μs and t_{off} = 200 μs)

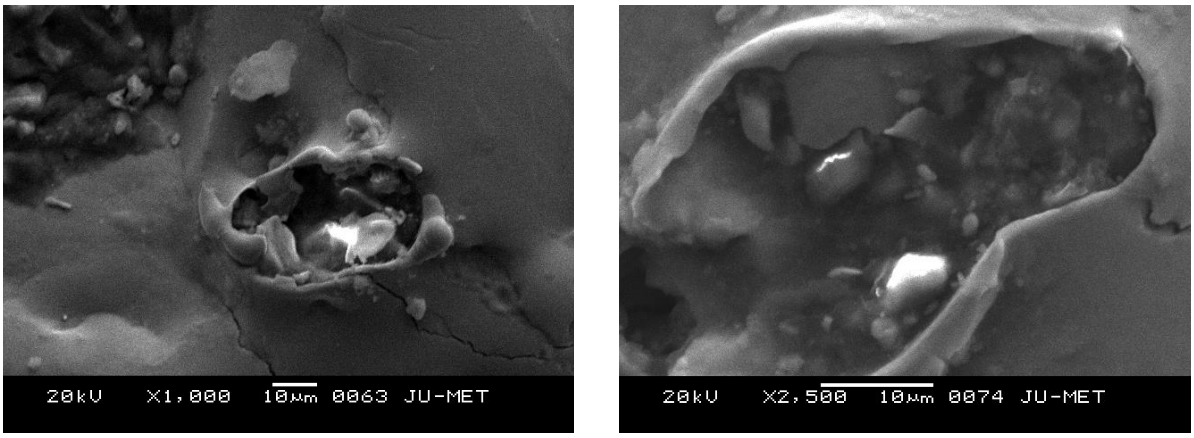

(a) cur = 6 A, t_{on} = 200 μs and t_{off} = 50 μs
(b) cur = 6 A, t_{on} = 200 μs and t_{off} = 50 μs

Fig. 3.14 Crater with frozen droplets inside

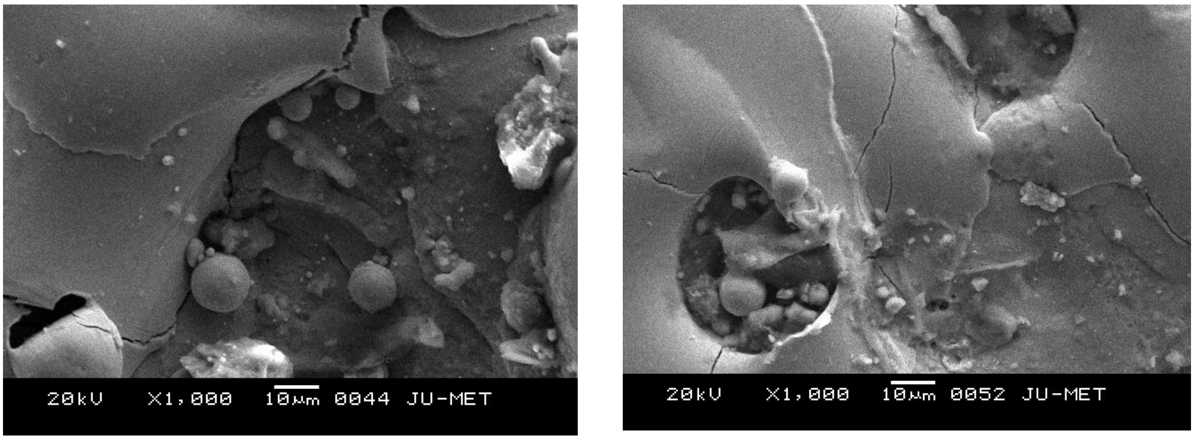

(a) cur = 15 A, t_{on} = 200 μs and t_{off} = 200 μs
(b) cur = 6 A, t_{on} = 200 μs and t_{off} = 200 μs

Fig. 3.15 Micro-cracks

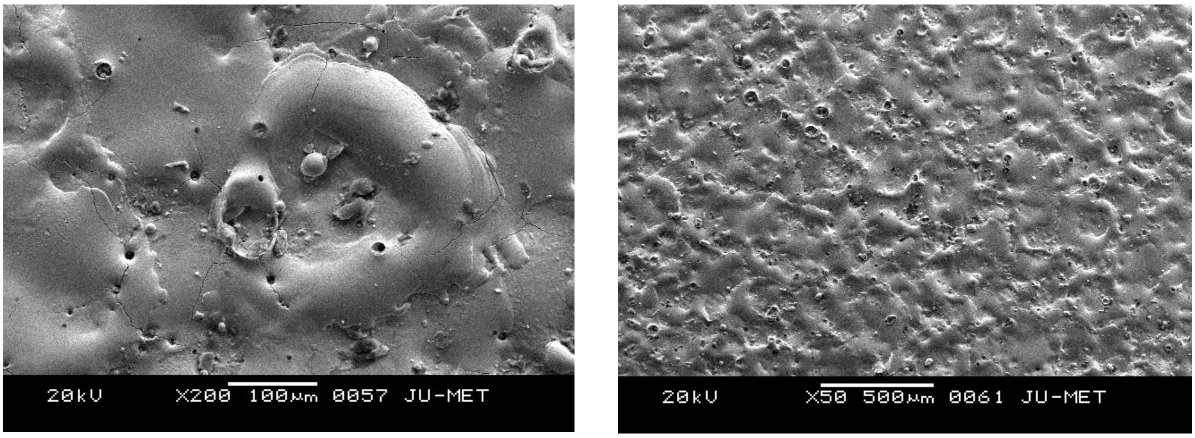

(a) cur = 6 A, t_{on} = 200 μs and t_{off} = 200 μs (b) cur = 6 A, t_{on} = 200 μs and t_{off} = 50 μs

Fig. 3.16 Pock marks formed after bursting of blisters

Scanning electron micrographs of EDM generated surface carries some typical features of machining process itself. In general, gradual obliteration of parent surface towards irregular pattern in surface texture is observed (figure 3.5). The "random" features of machined surface are due to superposition of debris particles (figure 3.6), pinholes (figure 3.7), different modes of molten material expulsion (figures 3.8 through 3.13), frozen droplets of molten material (figure 3.14), overlapping of craters, cracks (figures 3.6(a), 3.8, 3.10, 3.12, 3.14, 3.15, 3.16(a)). Presence of residual material at the rim of crater (figure 3.8) indicates ineffective violent expulsion associated with severe turbulence (figure 3.9).

Detailed study of scanning electron micrographs suggests different possible modes and critical features of material removal. During each discharge, as dielectric starts to vaporize, plasma channel expands. This expansion of discharge channel generates huge pressure and expels the molten metal in the form of fin. Effectiveness of this expulsion depends on the available time before pressure starts falling due to heat dissipation to surroundings. If pressure starts decreasing before complete expulsion, crater with raised rim having outward bend is formed (figure 3.10). If discharge channel collapses and cavitation starts before complete expulsion, outgoing material is forced to move inside forming an inward bend (figure 3.11). Inward moving molten material is freezed and forms almost spherical droplets. The droplets either retain their attachment with parent surface encompassing the entire generated crater or are moved away by dielectric in the form of debris. Sub-surface boiling and bursting of blisters [30, 41, 211] also attribute to the formation of different types of fin at the rim of crater and formation of spherical droplets.

However, it is obvious that formation of neat crater is a rare event. Craters surrounded by raised rim either with outward bend or with inward bend, craters with spilled pool and frozen droplets inside are frequently observed.

Crack formation on EDM generated surface exhibits some typical features. Due to high temperature gradients, cycle of severe thermal stress is generated and network of fine micro-cracks is formed. Appearance of the micro-cracks looks like a draught affected land (figures 3.6(a) and 3.8). The micro-cracks in many situations propagate perpendicular to surface but restricted to the thickness of resolidified layer (figure 3.15 (a)). Phase transformation of material adds transformational stress to existing one and makes the situation more adverse. Apart from this type of micro-cracks, radial cracks (figure 3.10 and 3.15 (b)) are also generated from pock marks formed by bursting of blisters. As a product of pyrolysis, hydrogen gas is generated. Solubility of hydrogen decreases with temperature and resolidified layer is super saturated even at ambient temperature with very high equilibrium pressure. When this equilibrium pressure crosses the failure stress, bursting of blisters happens, pock marks are formed (figure 3.16) and crack propagates radially. Almost all the above features are matched with the propositions made by Murti and Philip [194], Jeswani and Basu [195]. Study of scanning electron micrographs, therefore, indicates the presence of different irregular features of surface generation in EDM process.

3.4 Summary

From experimental results following conclusions are drawn.

- Current exhibits strong influences on the variations of MRR, ASR, Rt, RΔq, RLo and Rrms.

- Effects of the variations within treatments on Rsk and Rku are comparatively larger than the effects of variations between treatments indicating the presence of uncontrollable erratic fluctuations in profile heights.

- Fluctuations in MRR and ASR demand such modeling techniques that can absorb the irregular fluctuations in robust way.

- As, MRR increases, surface finish decreases, so a tradeoff, that is Pareto optimal, should exist.

- Values of Rku indicate the presence of high randomness in the distribution of profile heights of machined surface.

- Scanning electron micrographs exhibit complex patterns, irregular variations and overall random features of machined surface.

Thus, for near-accurate prediction, models of process outcomes like MRR and ASR are to be developed by such method that is capable of capturing uncontrollable fluctuations in robust way. The representative models would be used to search Pareto optimum combinations of MRR and ASR. Further, assessment of surface topography by some advanced techniques is necessary to comment on surface generation process in logical way.

CHAPTER 4

MODELING OF EDM PROCESS BY SVM REGRESSION

4.1 Introduction

At the end of chapter 2, two measurable process outcomes, MRR and ASR, are considered for development of representative models of EDM process. Sequence diagram for modeling of EDM process is shown on figure 4.1 in next page. After experimentation, uncontrollable fluctuations in MRR and ASR at different combinations of levels of control parameters are observed. As a consequence, predictability of each of the performances becomes very low. Though, number of approaches are taken by the researchers, still, searching of robust modeling method is persuaded by process engineers. Advanced structural risk minimization [144] learning based system, support vector machine (SVM) regression, would be effective in such situation. A meaningful physical significance of the insensitive zone of learned system provides a space to allow the tolerances on uncontrollable variations in EDM process. Besides, the insensitive zone of SVM regression absorbs the small scale irregular fluctuations appeared in responses. It is beneficial for other researchers to apply the models on different products obtained in different batches.

Suppose, with a key assumption of disjoint, independent and identical distributed data set $\{(x_1, y_1), (x_2, y_2), \ldots\ldots (x_N, y_N)\}$, model is to be developed in d dimensional input space (i.e. $\boldsymbol{x} \in \boldsymbol{R}^d$). Nonlinearity in the relation between input and output pattern is handled through mapping the high dimensional input space to a feature space $\Phi(\boldsymbol{x})$ via kernel functions. Here, an insensitive zone wrapped around the estimated function is improvised. This zone captures the fluctuations within permissible tolerances specified with process outcome. Thereby, radius of this hyper tube directly controls the allowable complexity of the learning system. Detailed discussion on SVM regression [144-150] is given in appendix A.1. However, the final model with optimum choice of internal structural parameters namely, C, ε and σ, may be presented as [146]

$$f(\boldsymbol{x}) = \sum_{i=1}^{N} (\alpha_i - \alpha_i^*) \, K(x_i, \boldsymbol{x}) + b \, \Bigg|_{\substack{C_{\text{optimum}} \\ \varepsilon_{\text{optimum}} \\ \sigma_{\text{optimum}}}} \tag{4.1}$$

$$\text{with } K(x_i, \boldsymbol{x}) = e^{-\frac{\|x_i - \boldsymbol{x}\|^2}{2\sigma^2}} \, \Bigg|_{\sigma_{\text{optimum}}}$$

In the present chapter, independent explicit SVM regression based learning system for each of the MRR and the ASR is developed. For robust modeling, controlling of internal structural parameters is necessary. Therefore, to develop optimal learning system, internal structural parameters namely regularization parameter (C), radius of loss insensitive hyper-tube (ε) and standard deviation of Gaussian radial basis function (σ) chosen as kernel function ($K(x_i, \boldsymbol{x})$) for SVM regression are to be properly tuned. One of the nature inspired advanced evolutionary metaheuristic optimization algorithm, particle swarm optimization (PSO), is employed for tuning of the three internal structural parameters. Teaching learning based optimization (TLBO) procedure is next applied for tuning of the three internal structural parameters of SVM regression in quest of reduction of the computational time. A comparison is then made between two procedures. A unified learning system is then developed using modified TLBO for concurrent predictions of MRR and ASR.

4.2 Modeling by modified PSO assisted SVM regression

For the development of robust virtual data generator, above mentioned three internal structural parameters, C, ε and σ, are to be optimally tuned. With the different sets of C, ε and σ, different learning systems are developed. Using PSO, such combination of C, ε and σ is searched which would give minimum training error. For the purpose of model building through SVM regression learning system, 54 data sets are taken randomly for training. Fitted models are tested through rest 10 sets of data.

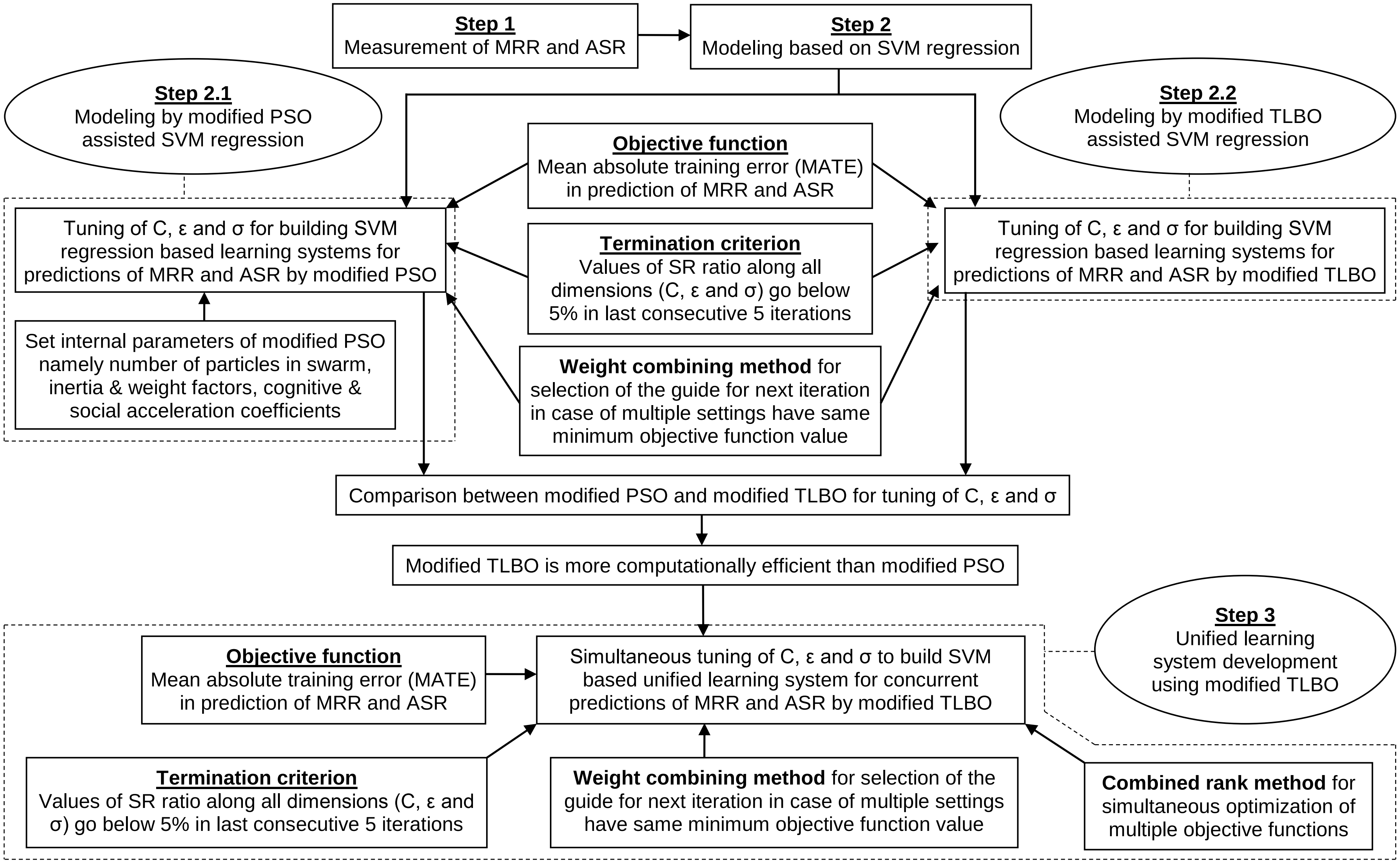

Fig. 4.1 Sequence diagram for proposed modeling of EDM process

4.2.1 Marching procedure and results

Training of experimental results with proper internal structural parameters of SVM regression (C, ε and σ) is necessary to get a near-exact representation of the process. So, the three internal structural parameters should be optimally tuned. Here, PSO with certain modifications is employed for this tuning operation.

Particle swarm optimization is an advanced evolutionary computational intelligence based stochastic optimization method for optimizing real world multimodal problems. Kennedy and Eberhart [178] proposed PSO, mimicking the natural behaviors found especially in flock of birds or school of fish for seeking their best food sources. In PSO algorithm, set of initial position and velocity vectors are to be randomly generated, inertia factor, constriction factor, social and cognitive acceleration coefficients need to be logically updated for better local exploitation and global exploration in searching operation. Detailed discussion on PSO [178, 212 - 217] is given in appendix A.2. For improvement of the performance of PSO, number of modifications in estimating the internal parameters is done by theoretical analysis, mathematical inference and empirical research. Different sets of C, ε and σ, reshape the learning system and modified PSO is employed to search optimum internal structural parameter setting that would train the experimental results with minimum training error. With optimum set of C, ε and σ, a set of Lagrange multipliers is calculated and thus model of each of the responses, MRR and ASR, is estimated using equation (4.1).

Searching techniques should be robust to get a general result. Wide range of search space may be a good choice but irrelevant movement would take lot of time to converge. So, searching ranges of C, ε and σ should be logically chosen. Actually, the regularization parameter C should lie within the response values. Thus, range of experimental values of the corresponding response parameter might be a robust reasonable choice for searching range of C.

$$(MRR_{exp})_{min} \leq C_{MRR} \leq (MRR_{exp})_{max}$$
$$(ASR_{exp})_{min} \leq C_{ASR} \leq (ASR_{exp})_{max} \qquad (4.2)$$

Besides, searching ranges of ε and σ are chosen as [150, 218]

$$\varepsilon = [\frac{\bar{y}}{30}, \frac{\bar{y}}{10}] \text{ and } \sigma = [(0.1)^{1/z}, (0.5)^{1/z}] \qquad (4.3)$$

Here, z indicates number of most influencing attributes in the process. In EDM it is 3, namely, current (cur), pulse on time (t_{on}) and pulse off time (t_{off}). Using equations (4.2) & (4.3), searching ranges of C, ε and σ are calculated (table 4.1).

Table 4.1 Searching ranges of internal structural parameters (C, ε and σ) of SVM regression

Internal structural parameters of SVM regression	Material removal rate	Average surface roughness
C	(1.3666, 28.0986)	(3.87, 9.00)
E	(0.3682, 1.1045)	(0.2127, 0.6380)
Σ	(0.4642, 0.7937)	

For better implementation of this estimated search range it was suggested [150, 218] to normalize the training inputs within the range [0, 1]. So, the chosen machining control parameters of EDM process, current, pulse on time and pulse off time, are normalized using the following formulae.

$$x_{1,norm} = \frac{cur - 6}{15 - 6} \text{ ; } x_{2,norm} = \frac{t_{on} - 50}{200 - 50} \text{ ; } x_{3,norm} = \frac{t_{off} - 50}{200 - 50} \qquad (4.4)$$

Choice of internal structural parameters, C, ε and σ, changes the values of Lagrange multipliers and thus shape of the prediction model changes. Best model should be selected for near-accurate estimation of responses. Chance of generalization error is reduced in SVM regression learning and internal parameters must be tuned in such a fashion as to reduce the training error in learning process. Thereby, in this study, mean absolute training error (MATE) in prediction of each of the process responses, MRR and ASR, is chosen as objective function.

$$\text{MATE (\%)} = \frac{100}{\mathrm{N}} \sum_{\mathrm{i}=1}^{\mathrm{N}} \left| \frac{y_{\mathrm{i,experimental}} - y_{\mathrm{i,estimated}}}{y_{\mathrm{i,experimental}}} \right| \tag{4.5}$$

Minimization of MATE is carried out for selection of three internal structural parameters of SVM regression. In the marching steps for optimization of MATE, different combinations of C, ε and σ change the values of Lagrange multipliers. Subsequently, learning system is getting reshaped, responses are predicted and MATE is evaluated using equation (4.5). Here, this optimization is performed by particle swarm optimization.

Though, PSO is a evolutionary population based metaheuristic optimization technique, still, to get this benefit in optimizing any non-linear high-dimensional objective function, termination criteria should be logically defined. In most of the optimization techniques, a termination criterion is defined by the maximum number of iterations or change in objective function value below a predefined margin. When, optimizing a new objective function, it is very difficult to know earlier the required number of iterations to meet a certain target. Even to attain certain accuracy, change in objective function values may vary due to their different scale range. In some cases, attainable optimum objective function value is difficult to predict earlier. As such, a general termination criterion is required to propose for population based searching techniques. In the present work, a general meaningful criterion is suggested based on spread of population relative to searching ranges in different dimensions that is spread-range (SR) ratio defined as a ratio of standard deviation of population (std) to span of searching range (Rng) (expressed in %).

$$\text{SR ratio (\%)} = 100 \text{ X } \frac{\mathrm{std}}{\mathrm{Rng}} \tag{4.6}$$

Thereby, simulation will be stopped when this SR ratio along each of the dimensions of input parameters simultaneously goes down below a predefined limit. Here, this limit is chosen as 5% that is termination of searching operation would be flagged on when SR ratio along C, ε and σ dimensions simultaneously drop below 5%.

Metaheuristic techniques are marched to the global optimum with some randomly generated probabilistic logical movement. Whatever might be the termination criterion that is considered, if simulation is stopped by watching that the specific user defined measurement just reaches below a certain value in any iteration, then, it may be erroneous. Simulation should be allowed for a few more iterations to finally freeze down below that specified limit. In the present work, termination criteria is defined by SR ratio of latest population along each of the three dimensions, C, ε and σ and simulation is terminated when values of SR ratio along all three dimensions (C, ε and σ) satisfy the termination criteria that is go below 5% in last consecutive 5 iterations.

In case of population based optimization technique, a widely spread initial population must be assured for better exploration in the whole searching range. As discussed earlier, a proposal has been raised to consider latest population based termination criteria that is SR ratio of the latest population along each dimension, so, initial SR ratio of the population must have high value along all of the three dimensions to ensure proper exploration of the search space.

In the present study, number of particles in swarm (n) is chosen as 20. In PSO, a widely dispersed set of particles is good for better exploitation and exploration of searching algorithm. Thus, initial position vectors of 20 particles along three dimensions, C, ε and σ, are randomly generated within specified search space (table 4.1) with more than 40% SR ratio (refer table D.3). Velocity vectors are also randomly generated (refer table D.4) with absolute value lies within their respective range of searching space. Inertia factor (ω) influences the degree of maintaining original velocity and constriction factor (ψ) affects the convergence of PSO. Here, linear variation of inertia factor and constriction factor are considered in the range [0.9, 0.4] [216]. Cognitive (cog) and social (soc) acceleration coefficients both vary linearly within same range [2.5, 0.5] but in opposite order [217].

In most of the published studies of different population based optimization algorithms [171], it is reported that the best one of the latest population works as the guide for next iteration e.g. p_{best} and g_{best} in PSO. The best one is chosen with either minimum or maximum objective function value. However, if more than one best setting in the population with same minimum or maximum objective function value are found, then, confusion will come to choose only one among all those best settings.

Improper choice of the best may guide the following iterations in wrong way and finally might be trapped inside any local optimum. In the present work, a simple methodology, namely weight combining method, is proposed to avoid this condition. A weighted combination of all the best settings should be evaluated which either having lower objective function than the second best (for first iteration) or lower (higher for maximization) than the objective function value of the best setting in immediate last iteration. Say, in case of minimization of a two-variable objective function within search space ([0, 20], [0, 20]), at any iteration two particles (13.4, 2.3) and (6.6, 17.7) score same minimum value 70.85. Minimum score at last iteration was 73.45. Now, it is required to choose the guide among the two particles for next iteration. No such clear guidance is reported till now to choose the right one among the two. Here, a weighted combination of the two particles along their corresponding dimensions is calculated. Randomly two weights (rw_1, rw_2) are generated between (0, 1) such that $rw_1 + rw_2 = 1$. A new particle is evoluted as (rw_1 X 13.4 + rw_2 X 6.6, rw_1 X 2.3 + rw_2 X 17.7). For $rw_1 = 0.3$ and $rw_2 = 0.7$, new particle would be (8.64, 13.08) which scores 11.34. New evoluted particle scores less than the minimum score at last iteration (73.45) (in case of first iteration, comparison would be done with second minimum). This particle (8.64, 13.08) would be the guide for next iteration otherwise the steps are repeated with another random set of weights (rw_1, rw_2) till the condition is fulfilled. However, there is no need to update current population with this evaluated guide. This proposition is expected to be effective to avoid ambiguity to choose the right optimum at any iteration. For selecting p_{best} and g_{best} in case of multiple particles have same minimum objective function value, above proposed methodology is incorporated in the present modified PSO algorithm.

Adapting all the above mentioned modifications over standard PSO algorithm, simulation steps for searching optimum sets of C, ε and σ by minimization of MATEs in estimation of MRR and ASR separately are discussed as follows.

Step 1 : Set n = 20, $\omega_{initial} = 0.9$, $\omega_{final} = 0.4$, $cog_{initial} = 2.5$, $cog_{final} = 0.5$, $soc_{initial} = 0.5$, $soc_{final} = 2.5$, $\psi_{initial} = 0.9$, $\psi_{final} = 0.4$ and termination criteria as SR ratio along each dimension ≤ 5% for consecutive 5 iterations.

Step 2 : Set $iter_{max} = 250$. Randomly initialize the position of 20 particles that is 20 sets of initial combination of C, ε and σ with SR ratio along each of the three dimensions > 40% within search space (table 4.1). Initialize velocity vectors corresponding to each of the 20 particles. Absolute value of each of the velocity vectors should lie within the range of respective search space.

Step 3 : Set iter = 1. Current position of i^{th} particle is set to the p^i_{best}. Go to step 5.

Step 4 : Calculate MATE for each of the 20 particles. If the current position of i^{th} particle has lower objective function value (MATE) than the already selected p^i_{best}, then, replace the p^i_{best} with new position of i^{th} particle, otherwise, p^i_{best} is kept unaltered.

Step 5 : Identify the particle having minimum MATE and set the corresponding particle as g_{best}. If number of particles having same minimum MATE, then, go to step 6, otherwise, go to step 7.

Step 6 : Particles having same minimum objective function value, are identified and make a weighted combination of those such that the new evaluated particle must score lower than either the second minimum objective function value at current set of particles (applicable only for first iteration) or the minimum objective function value gained at last iteration. The new evaluated particle is selected as g_{best}.

Step 7 : Calculate SR ratio along all three dimensions C, ε and σ. Store the maximum among the three SR ratio values in a separate matrix called "DECISION". If iter < 5, go to step 10, otherwise, go to step 8.

Step 8 : If the maximum of last five consecutive entries in matrix "DECISION" contains SR ratio values is lower than 5%, then, current g_{best} would be declared as the optimum setting of C, ε and σ, stop the simulation and minimum achievable MATE in estimation of response is calculated with the obtained optimum set of C, ε and σ, otherwise, go to step 9.

Step 9 : If iter = $iter_{max}$, then, go to step 2, restart the simulation with higher $iter_{max}$, otherwise, go to step 10.

Step 10 : Evaluate the dynamic internal parameters as

$$\omega_{iter} = \omega_{\text{initial}} + \frac{(\omega_{\text{final}} - \omega_{\text{initial}})}{(\text{iter}_{\text{max}} - 1)} (\text{iter} - 1) \tag{4.7}$$

$$cog_{iter} = cog_{\text{initial}} + \frac{(cog_{\text{final}} - cog_{\text{initial}})}{(\text{iter}_{\text{max}} - 1)} (\text{iter} - 1) \tag{4.8}$$

$$soc_{iter} = soc_{\text{initial}} + \frac{(soc_{\text{final}} - soc_{\text{initial}})}{(\text{iter}_{\text{max}} - 1)} (\text{iter} - 1) \tag{4.9}$$

$$\psi_{iter} = \psi_{\text{initial}} + \frac{(\psi_{\text{final}} - \psi_{\text{initial}})}{(\text{iter}_{\text{max}} - 1)} (\text{iter} - 1) \tag{4.10}$$

Step 11 : Calculate velocity vector as

$$v^{k}_{iter+1,\,d} = \omega^{k}_{iter}\, v^{k}_{iter} + cog_{iter}\,(\text{rand})\,(p^{k}_{best,d} - x^{k}_{d}) + soc_{iter}\,(\text{rand})\,(g_{best,\,d} - x^{k}_{iter,\,d}), \quad \boldsymbol{k} = 1(1)n \text{ and } \boldsymbol{d} = 1(1)3 \tag{4.11}$$

Step 12 : Update velocity corrected position vector as

$$x^{k}_{iter+1,\,d} = x^{k}_{iter,\,d} + cf_{iter}\, v^{k}_{iter+1,\,d}, \quad \boldsymbol{k} = 1(1)n \text{ and } \boldsymbol{d} = 1(1)3 \tag{4.12}$$

Set iter = iter + 1 and go to step 4.

Therefore, latest g_{best} is selected as optimum settings of C, ε and σ. With the optimum settings of C, ε and σ, set of Lagrange multipliers is calculated and thus the model of the corresponding response could be represented by equation (4.1). Using this equation, estimated response parameter value is calculated and finally achieved training error (MATE) is determined. The above mentioned steps for tuning of internal structural parameters of SVM regression, C, ε and σ, by modified PSO and thereby for prediction of MRR and ASR separately are coded in the platform of MATLAB.

Now, using the above said PSO algorithm adapted with all discussed modifications, training errors in prediction of MRR and ASR (refer equation (4.5)) are minimized separately for different settings of C, ε and σ. As the simulation marches, with different values of C, ε and σ, shape of estimated model of each response is getting modified and training error is changed. Finally, the optimum settings of C, ε and σ within the specified searching range (refer table 4.1) with minimum mean absolute training error (MATE) in estimation of MRR and ASR separately are found and reported in table 4.2.

Table 4.2 Results of tuning internal structural parameters of SVM regression by modified PSO

Response	Optimum internal structural parameters of SVM regression			Simulation time (s)	No. of support vectors	bias	Performance	
	C	ε	σ				MATE (%)	r^2
MRR	28.0969	0.3699	0.4642	10338.9618	41	0	5.55	0.9869
ASR	9.00	0.2127	0.4642	15160.9776	41	0	3.76	0.9622

Optimum values of C for both of the MRR and ASR are shifted towards the upper end of search space. This indicates the complexity of the model which is in favor of the stochastic behavior of EDM process. The random fluctuations could be controlled by proper choice of ε. Here, lower values of ε for both of MRR and ASR indicate that the complex models could be able to absorb the random variations adequately. Besides, small σ values for both MRR and ASR indicate that oscillatory patterns in outputs outside the insensitive zones are properly entrapped.

With the simulated results of C, ε and σ listed in table 4.2, set of Lagrange multipliers (α_i, α_i^*) are calculated (refer table D.5) and estimated models of MRR and ASR are as follows.

MRR:

$$f(\boldsymbol{x}) = \sum_{i=1}^{N}(\alpha_i - \alpha_i^*)\, K(x_i, \boldsymbol{x}) + b \quad \left| \begin{array}{l} C = 28.0969 \\ \varepsilon = 0.3699 \\ \sigma = 0.4642 \end{array} \right. \tag{4.13}$$

$$\text{with } K(x_i, \boldsymbol{x}) = e^{-\frac{\|x_i - \boldsymbol{x}\|^2}{2\sigma^2}} \quad \left| \; \sigma = 0.4642 \right.$$

ASR:

$$f(\boldsymbol{x}) = \sum_{i=1}^{N}(\alpha_i - \alpha_i^*)\, K(x_i, \boldsymbol{x}) + b \quad \left| \begin{array}{l} C = 9.0000 \\ \varepsilon = 0.2127 \\ \sigma = 0.4642 \end{array} \right. \tag{4.14}$$

$$\text{with } K(x_i, \boldsymbol{x}) = e^{-\frac{\|x_i - \boldsymbol{x}\|^2}{2\sigma^2}} \quad \left| \; \sigma = 0.4642 \right.$$

Marching steps for optimum selection of C, ε and σ in estimation of MRR and ASR separately are given in the following flow chart (figure 4.2). Gradual decaying pattern of MATE in estimation of MRR and ASR are represented in figures 4.3 through 4.6.

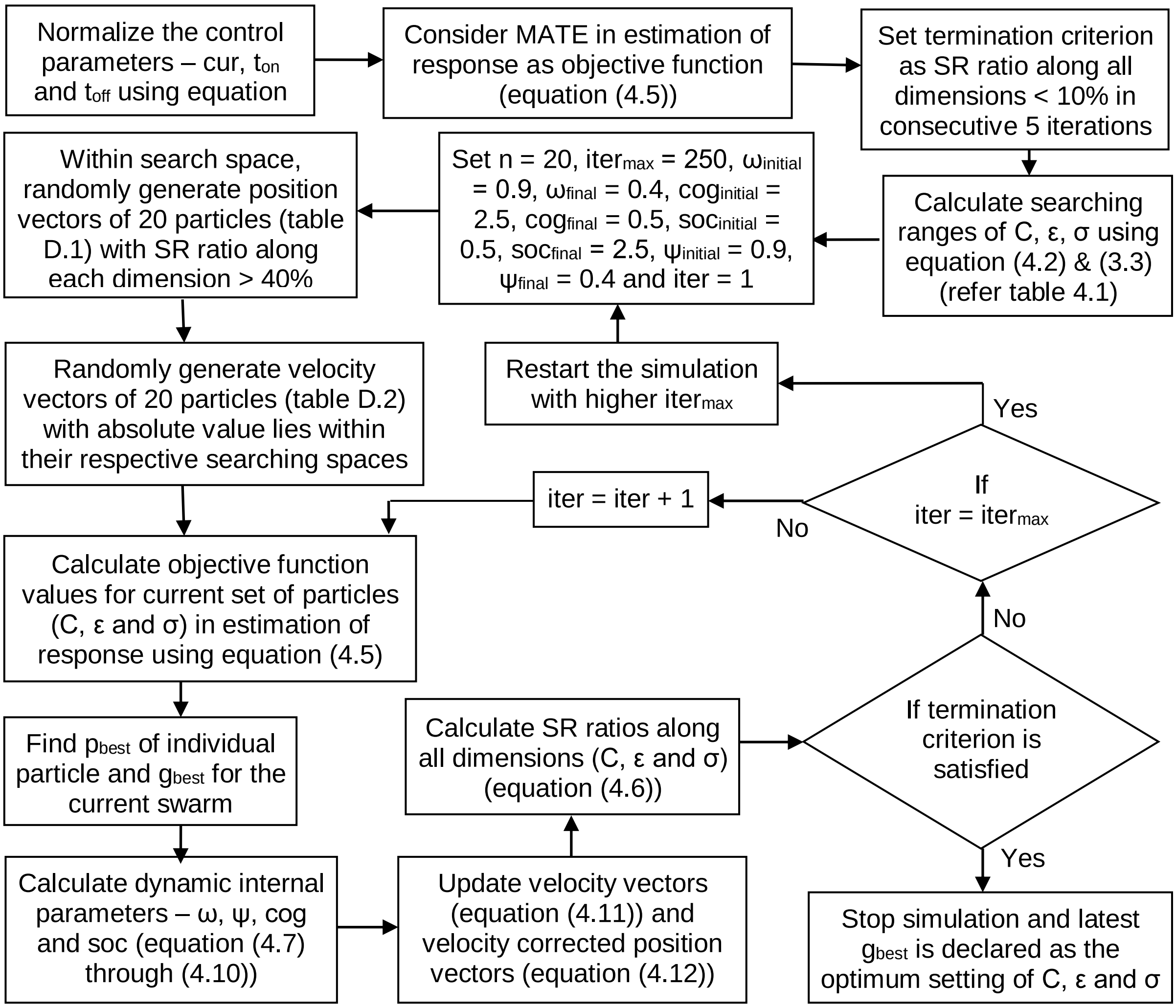

Fig. 4.2 Detailed steps in modeling by modified PSO assisted SVM regression

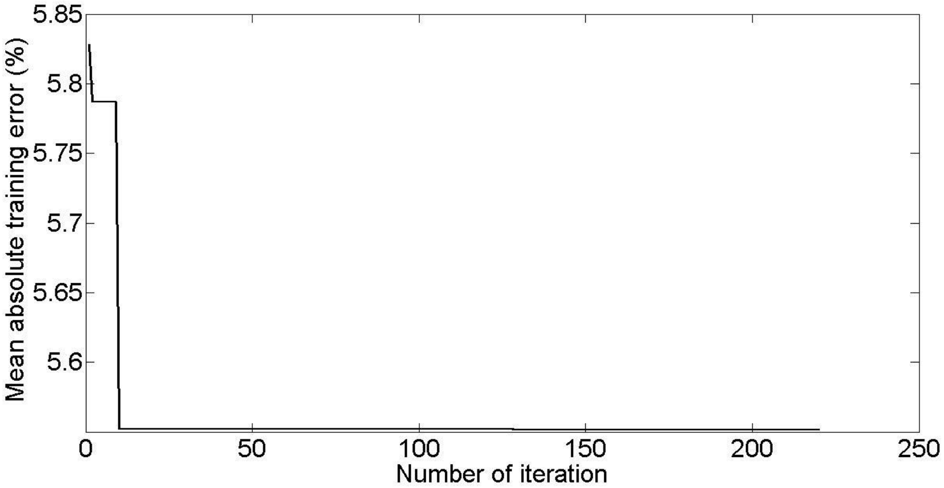

Fig. 4.3 Marching steps to minimize MATE in estimation of MRR with C, ε and σ tuned by modified PSO

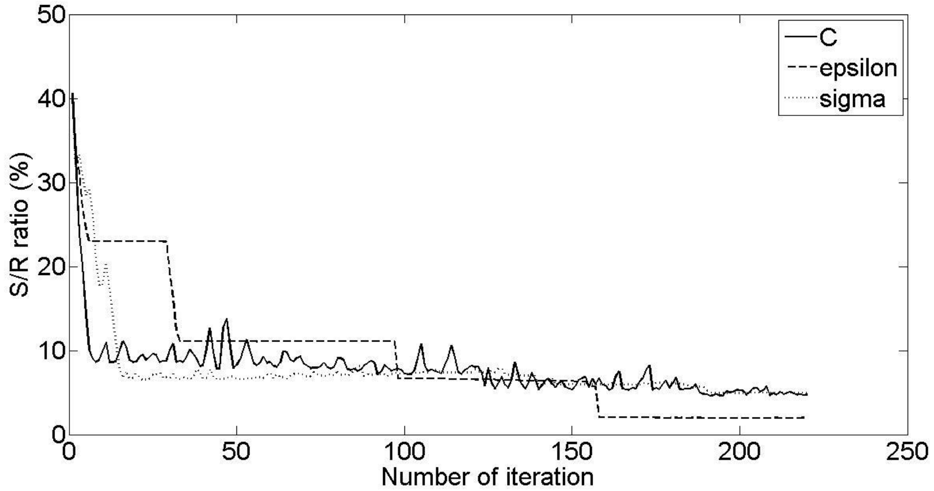

Fig. 4.4 Changes of SR ratios along C, ε and σ tuned by modified PSO to minimize MATE in estimation of MRR

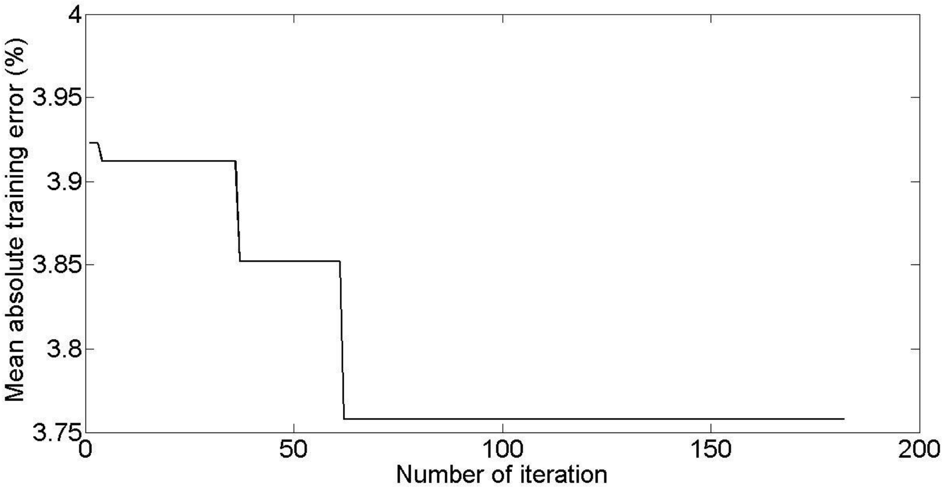

Fig. 4.5 Marching steps to minimize MATE in estimation of ASR with C, ε and σ tuned by modified PSO

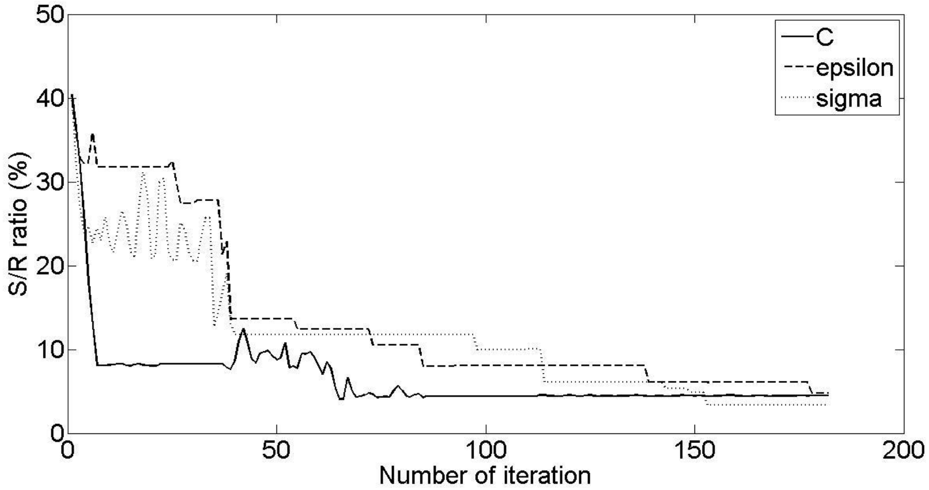

Fig. 4.6 Changes of SR ratios along C, ε and σ tuned by modified PSO to minimize MATE in estimation of ASR

In case of minimizing MATE in estimation of MRR, relative to C and σ, the effect of ε is lower, as SR ratio for ε decreases at a faster rate than that of C and σ (figure 4.4). Whereas, all three parameters, C, ε and σ, influence the model of ASR to almost same pattern (figure 4.6).

Though, the higher values of coefficient of determinations, r^2 (refer table 4.2), indicate the high correlation between experimental and estimated response values from the trained models (equations (4.13) & (4.14)), still, testing of the models with separate data sets from training sets is necessary for using the models as representatives of the EDM process outcomes.

4.2.2 Testing of estimated models

Trained models of MRR and ASR, equations (4.13) & (4.14), are tested with 10 disjoint data sets obtained from separate follow up experimental runs.

Table 4.3 Testing of estimated MRR model with C, ε and σ tuned by modified PSO

Sl. no.	Machining condition			Material removal rate		
	cur (A)	t_{on} (μs)	t_{off} (μs)	Experimental (mm^3/min)	Estimated (mm^3/min)	Absolute error (%)
1	6	100	50	5.48126	5.20270	5.08
2	6	100	200	2.25924	2.43427	7.75
3	6	200	150	4.56557	4.76071	4.27
4	9	100	100	9.13364	8.60190	5.82
5	9	150	50	13.50951	12.67906	6.15
6	9	200	100	10.48887	10.32156	1.60
7	12	50	50	14.41525	15.38597	6.73
8	12	150	200	11.36906	11.38677	0.16
9	15	100	100	18.06487	16.61805	8.01
10	15	150	50	24.95816	25.57226	2.46
Mean absolute testing error (%)						4.80

Table 4.4 Testing of estimated ASR model with C, ε and σ tuned by modified PSO

Sl. no.	Machining condition			Average surface roughness		
	cur (A)	t_{on} (μs)	t_{off} (μs)	Experimental (μm)	Estimated (μm)	Absolute error (%)
1	6	100	50	4.61	4.44	3.69
2	6	100	200	5.05	4.95	1.98
3	6	200	150	4.21	4.27	1.43
4	9	100	100	5.79	6.03	4.15
5	9	150	50	6.95	6.66	4.17
6	9	200	100	6.22	6.47	4.02
7	12	50	50	5.98	6.23	4.18
8	12	150	200	7.35	7.62	3.67
9	15	100	100	7.48	7.23	3.34
10	15	150	50	8.49	8.31	2.12
Mean absolute testing error (%)						3.27

Mean absolute testing errors (table 4.3 and 4.4) for both MRR (4.80%) and ASR (3.27%) indicate the practical adequacy of the models in their experimental ranges.

With the aid of modified PSO, internal structural parameters of SVM regression based learning system are tuned in optimal way and prediction of MRR and ASR from developed learning systems are fair. Still, few drawbacks exist for practical use of developed learning system.

It is observed that, internal parameters of PSO namely inertia factor, weight factor, cognitive and social acceleration coefficients are decided before starting of optimization process. Selection of such internal parameters is crucial for final result. Even, improper selection not only consumes more simulation time, but global optimum could not be reached. Simulation time for developing each independent model is in the order of 10^4 second which is very high for developing a system with new set of experimental results. Therefore, need of fast and global algorithm-specific parameter-less optimization algorithm is evident. Teaching learning based optimization algorithm (TLBO) [184] may be effective in this regard.

4.3 Modeling by modified TLBO assisted SVM regression

From the ideology of teaching-learning process, a evolutionary metaheuristic algorithm-specific parameter-less optimization algorithm, teaching learning based optimization (TLBO), is developed [184]. Though, no such internal parameters are required to fix in TLBO before simulation starts, yet, two crucial conflicting aspects of a metaheuristic algorithm, namely intensification and diversification are successfully achieved in it. Exploration of the search space is done in learner phase whereas, teaching phase does the exploitation. Detailed discussion on TLBO [184, 219, 220] is given in appendix A.3. In searching of optimum sets of internal structural parameters of SVM regression, C, ε and σ, MATEs in estimation of process outcomes, MRR and ASR, are minimized separately by modified TLBO. Some modifications as discussed in subsection 4.2.1, namely population based termination criterion, initialize population with high dispersion and way of choosing guide in case of multiple best particles performing same score, are further adapted for more smoothing convergence.

4.3.1 Marching procedure and results

Searching ranges of C, ε and σ are kept same as in subsection 4.2.1 (refer table 4.1). Training input vectors that is machining control parameters of EDM (cur, t_{on} and t_{off}) are normalized using equation (4.4). Mean absolute training errors (MATE, refer equation (4.5)) in estimation of MRR and ASR are separately considered as objective functions for searching optimum sets of C, ε and σ. With the corresponding training vectors and optimum set of C, ε and σ, set of Lagrange multipliers could be evaluated for each of MRR and ASR. Estimated models of MRR and ASR would be constructed separately using the sets of Lagrange multipliers.

Termination criterion for stopping the searching operation is defined by suggested SR ratio (refer equation (4.6)). Simulation will be terminated when all of the SR ratio values along three dimensions, C, ε and σ, simultaneously go below 5%. After crossing this limit (SR ratio along each dimension < 5%), searching of global optimum is further continued for 5 more iterations for better assurance in freezing of simulation process.

In TLBO, a widely dispersed set of particles is good for better exploitation and exploration of searching algorithm. In the present work, considering initial SR ratio as at least 40% along each direction, a set of 20 learners are randomly generated within specified search space (refer table 4.1). For maintaining the repeatability of the simulation steps, initial learners are given in table D.6.

In every step of iteration, with different sets of learners that is sets of C, ε and σ, shapes of trained model change. Teacher for any iteration is selected as that set of C, ε and σ having lowest training error (MATE) value. Delivering capability of teacher is controlled by adapting a teaching factor evaluated from the latest condition of the students in the population. Here, teaching factor is modified as a ratio of mean of the values of learners to the value of teacher of latest population [220], instead of any randomly chosen integer either 1 or 2 [219]. This adaptive teaching factor aids in converging the simulation with lesser time.

A easy way of selecting teacher for next iteration in case of multiple learners have same minimum score, weight combining method, as proposed in subsection 4.2.1, is also incorporated in the present modified TLBO algorithm.

Adapting all the above mentioned modifications, simulation steps of modified TLBO for searching optimum sets of C, ε and σ by minimization of MATEs in estimation of MRR and ASR separately are discussed as follows.

Step 1 : Set number of learners (n) = 20 and termination criteria as SR ratio along each dimension ≤ 5% for consecutive 5 iterations. Randomly initialize the position of 20 learners that is 20 sets of initial combination of C, ε and σ with SR ratio along each of the three dimensions > 40% within search space (refer table 4.1).

Step 2 : Set $iter_{max} = 250$ and iter = 1.

Step 3 : Calculate mean of all the learners and evaluate score of the individual learner that is objective function value (refer equation (4.5)) for each of the 20 sets of C, ε and σ. Identify the minimum objective function value and set the corresponding learner as current teacher. If multiple learners have same minimum score, then, go to step 4 otherwise go to step 5.

Step 4 : Learners having same minimum score, are identified and make a weighted combination of those such that the new evaluated learner must score lower than either the second minimum score at current set of learners (applicable only for first iteration) or the minimum score gained at last iteration. The new evaluated learner is selected as teacher.

Step 5 : Calculate adapted teaching factor (TF) as

$$TF_{iter,\,d} = \frac{CM_{iter,d}}{CT_{iter,d}}, \quad \boldsymbol{d} = 1(1)3 \tag{4.15}$$

With calculated adaptive teaching factor, evaluate new values of learners according to the following relation.

$$x^k_{new,\,d} = x^k_{iter,\,d} + rand \text{ X } (CT_{iter,\,d} - TF_{iter,\,d} \text{ X } CM_{iter,\,d}), \quad \boldsymbol{k} = 1(1)n \text{ and } \boldsymbol{d} = 1(1)3 \tag{4.16}$$

If score of each of the new evaluated learners is lower than its corresponding earlier score before this modification, then, replace the old value with new one otherwise old learner is kept unaltered.

Step 6 : For each of the learners (x_{new}), choose another learner randomly (x^r_{new}). If score of this randomly chosen learner is lower or higher than that of current learner, then, update the current learner as follows otherwise it is kept unaltered.

Lower : $x^k_{iter+1,\,d} = x^k_{new,\,d} + \text{rand X } (x^k_{new,\,d} - x^r_{new,\,d})$

Higher : $x^k_{iter+1,\,d} = x^k_{new,\,d} + \text{rand X } (x^r_{new,\,d} - x^k_{new,\,d}),\quad \boldsymbol{k} = 1(1)n,\ \boldsymbol{d} = 1(1)3 \qquad (4.17)$

Step 7 : Calculate SR ratio along all three dimensions C, ε and σ. Store the maximum among the three values of SR ratio in a separate matrix called “DECISION”. If iter < 5, set iter = iter + 1 and go to step 3, otherwise, go to step 8.

Step 8 : If the maximum of last five consecutive entries in matrix “DECISION” contains SR ratio values is lower than 5%, then, current teacher of the learners would be declared as the optimum setting of C, ε and σ, stop the simulation and minimum achievable MATE in estimation of response is calculated with obtained optimum set of C, ε and σ, otherwise, go to step 9.

Step 9 : If iter = $iter_{max}$, then, go to step 2, restart the simulation with higher $iter_{max}$, otherwise, iter = iter + 1, go to step 3.

Therefore, latest teacher is selected as optimum settings of C, ε and σ. With the optimum settings of C, ε and σ, set of Lagrange multipliers is calculated and thus the model of the corresponding response could be represented by equation (4.1). Using this equation, value of response parameter is estimated and finally achieved training error (MATE) is determined. The above mentioned steps for tuning of internal structural parameters of SVM regression, C, ε and σ, by modified TLBO and thereby for prediction of MRR and ASR separately are coded in the platform of MATLAB. Simulated results and some performance measurements are given in table 4.5.

Table 4.5 Results of tuning internal structural parameters of SVM regression by modified TLBO

Response	Optimum internal structural parameters of SVM regression			Simulation time (s)	No. of support vectors	bias	Performance	
	C	ε	σ				MATE (%)	r^2
MRR	28.0986	0.3968	0.4642	323.5959	41	0	5.55	0.9867
ASR	9.00	0.2127	0.4642	303.9827	41	0	3.76	0.9622

Optimum values of C for both of the MRR and ASR are shifted towards the upper end of search space. This indicates the complexity of the model which is in favor of the stochastic behavior of EDM process. The random fluctuations could be controlled by proper choice of ε. Here, lower values of ε for both of MRR and ASR indicate that the complex models could be able to absorb the random variations adequately. Besides, small σ values for both MRR and ASR indicate that oscillatory patterns in outputs outside the insensitive zones are properly entrapped.

With the optimum set of C, ε and σ, corresponding set Lagrange multipliers for each of the responses, MRR and ASR, is calculated (refer table D.7). Models of MRR and ASR could be represented using equation (4.1). Finally achieved MATEs are determined using the representative models (equations (4.18) and (4.19)) fed by their corresponding sets of Lagrange multipliers.

MRR:

$$f(\boldsymbol{x}) = \sum_{i=1}^{N} (\alpha_i - \alpha_i^*)\, K(x_i, \boldsymbol{x}) + b \quad \left|\ \begin{array}{l} C = 28.0986 \\ \varepsilon = 0.3968 \\ \sigma = 0.4642 \end{array}\right. \qquad (4.18)$$

$$\text{with } K(x_i, \boldsymbol{x}) = e^{-\frac{\|x_i - \boldsymbol{x}\|^2}{2\sigma^2}} \quad \left|\ \sigma = 0.4642\right.$$

$$\text{ASR:} \quad f(\boldsymbol{x}) = \sum_{i=1}^{N}(\alpha_i - \alpha_i^*)\, K(x_i, \boldsymbol{x}) + b \quad \left| \begin{array}{l} C = 9.0000 \\ \varepsilon = 0.2127 \\ \sigma = 0.4642 \end{array} \right. \qquad (4.19)$$

$$\text{with } K(x_i, \boldsymbol{x}) = e^{-\frac{\|x_i - \boldsymbol{x}\|^2}{2\sigma^2}} \quad \left| \; \sigma = 0.4642 \right.$$

Marching steps for optimum selection of C, ε and σ in estimation of MRR and ASR separately are given in the following flow chart (figure 4.7). Gradual decaying patterns of MATE in estimation of MRR and ASR are represented in figures 4.8 through 4.11.

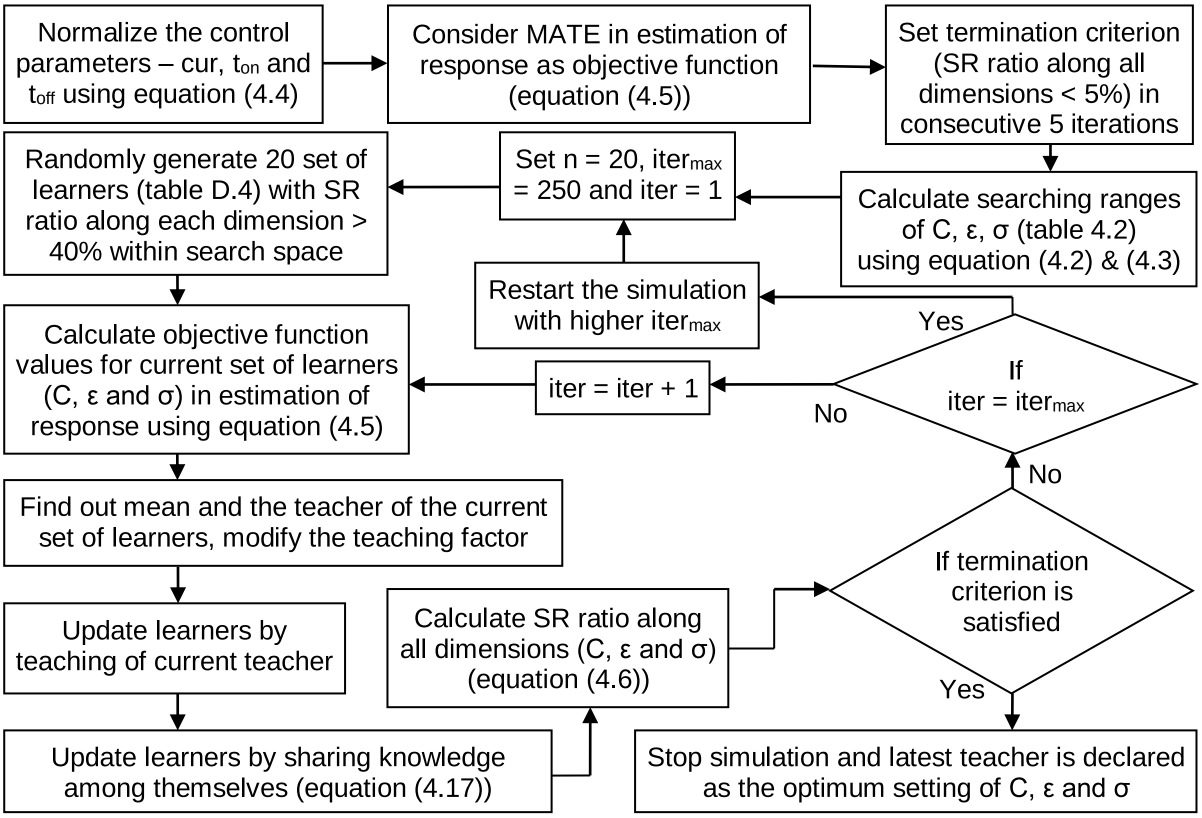

Fig. 4.7 Detailed steps in modeling by modified TLBO assisted SVM regression

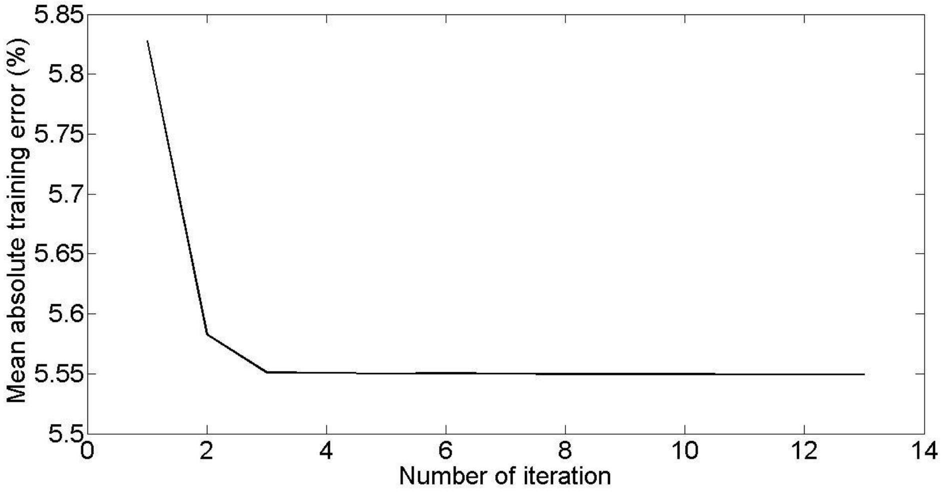

Fig. 4.8 Marching steps to minimize MATE in estimation of MRR with C, ε and σ tuned by modified TLBO

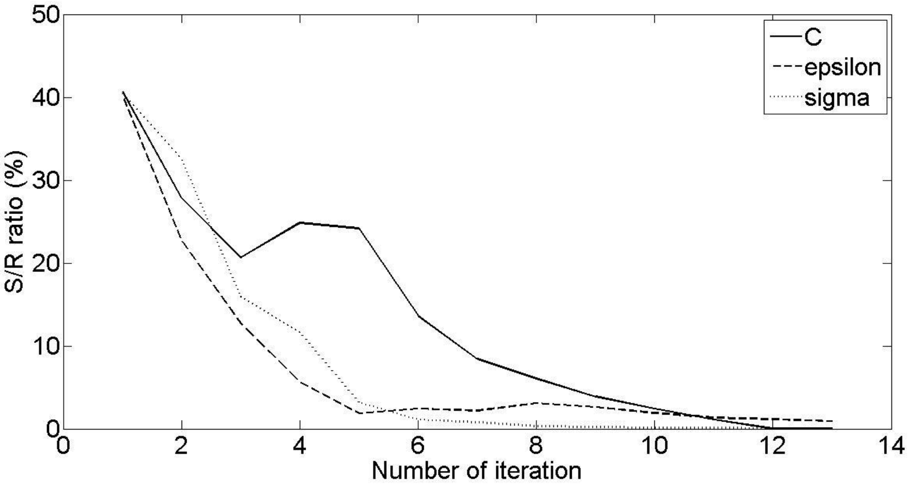

Fig. 4.9 Changes of SR ratios along C, ε and σ tuned by modified TLBO to minimize MATE in estimation of MRR

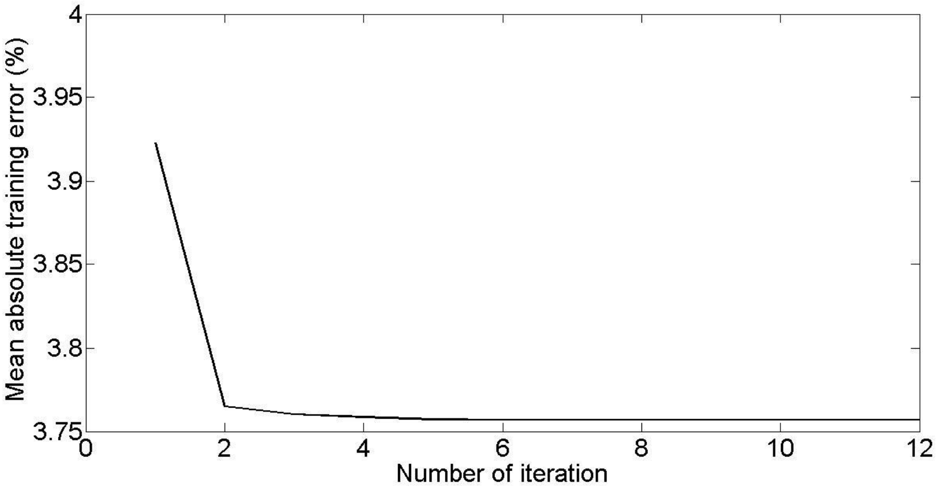

Fig. 4.10 Marching steps to minimize MATE in estimation of ASR with C, ε and σ tuned by modified TLBO

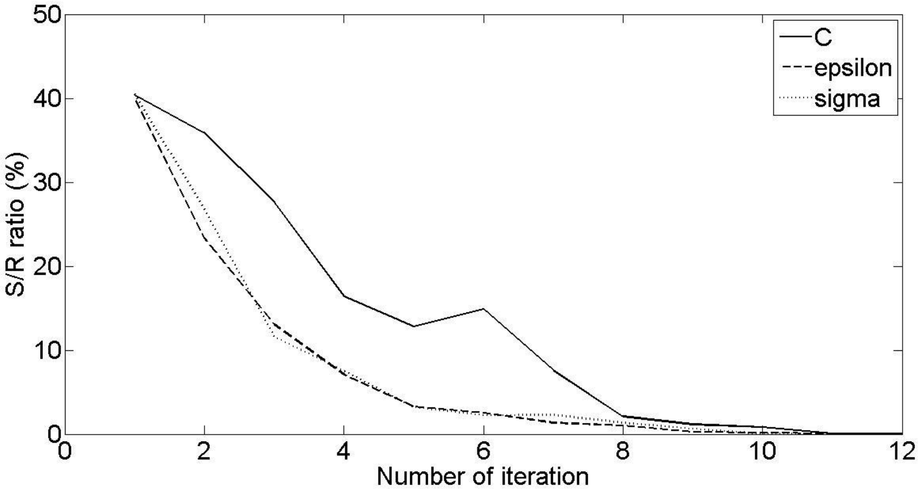

Fig. 4.11 Changes of SR ratios along C, ε and σ tuned by modified TLBO to minimize MATE in estimation of ASR

In case of minimizing MATE in estimation of MRR, relative to C and σ, the effect of ε is lower, as SR ratio for ε decreases at a faster rate than that of C and σ (figure 4.9). Whereas, all three parameters C, ε and σ influence the model of ASR to almost same pattern (figure 4.11).

Though, the higher values of coefficient of determinations, r^2 (table 4.5), indicate the high correlation between experimental and estimated values of response parameter from the trained models (equations (4.18) and (4.19)), still, testing of the models with separate data sets from training sets is necessary for using the models as representatives of the EDM process outcomes.

4.3.2 Testing of estimated models

Trained models of MRR and ASR, equations (4.18) & (4.19), are tested with 10 disjoint data sets obtained from separate follow up experimental runs.

Table 4.6 Testing of estimated MRR model with C, ε and σ tuned by modified TLBO

Sl. no.	Machining condition			Material removal rate		
	cur (A)	t_{on} (μs)	t_{off} (μs)	Experimental (mm^3/min)	Estimated (mm^3/min)	Absolute error (%)
1	6	100	50	5.48126	5.20824	4.98
2	6	100	200	2.25924	2.40183	6.31
3	6	200	150	4.56557	4.74119	3.85
4	9	100	100	9.13364	8.62213	5.60
5	9	150	50	13.50951	12.70765	5.94
6	9	200	100	10.48887	10.34725	1.35
7	12	50	50	14.41525	15.39080	6.77
8	12	150	200	11.36906	11.40655	0.33
9	15	100	100	18.06487	16.59244	8.15
10	15	150	50	24.95816	25.56967	2.45
Mean absolute testing error (%)						4.57

Table 4.7 Testing of estimated ASR model with C, ε and σ tuned by modified TLBO

Sl. no.	Machining condition			Average surface roughness		
	cur (A)	t_{on} (μs)	t_{off} (μs)	Experimental (μm)	Estimated (μm)	Absolute error (%)
1	6	100	50	4.61	4.44	3.69
2	6	100	200	5.05	4.95	1.98
3	6	200	150	4.21	4.27	1.43
4	9	100	100	5.79	6.03	4.15
5	9	150	50	6.95	6.66	4.17
6	9	200	100	6.22	6.47	4.02
7	12	50	50	5.98	6.23	4.18
8	12	150	200	7.35	7.62	3.67
9	15	100	100	7.48	7.23	3.34
10	15	150	50	8.49	8.31	2.12
Mean absolute testing error (%)						3.27

Mean absolute testing errors (table 4.6 and 4.7) for both MRR (4.57%) and ASR (3.27%) indicate the practical adequacy of the models in their experimental ranges.

However, independent models of MRR and ASR in EDM process with internal structural parameters, C, ε and σ, tuned by modified PSO and modified TLBO are separately developed with SVM regression based learning systems. In next section, comparison between performances two evolutionary algorithms, modified PSO and modified TLBO for independent learning system development is discussed.

4.4 Comparison between SVM regression based independent model building assisted by modified PSO and modified TLBO

Simulated results and performances of modified PSO and modified TLBO in searching of optimum sets of C, ε and σ separately for MRR and ASR are listed in table 4.8.

Table 4.8 Comparison between modified PSO and modified TLBO in tuning of C, ε and σ

		Optimization technique	Optimum value	
			MRR	ASR
Internal structural parameters of SVM regression	C	modified PSO	28.0969	9.00
		modified TLBO	28.0986	9.00
	ε	modified PSO	0.3999	0.2127
		modified TLBO	0.3668	0.2127
	σ	modified PSO	0.4642	0.4642
		modified TLBO	0.4642	0.4642
Performance measurements	MATE (%)	modified PSO	5.55	3.76
		modified TLBO	5.55	3.76
	r^2	modified PSO	0.9869	0.9622
		modified TLBO	0.9867	0.9622
	Mean absolute testing error (%)	modified PSO	4.80	3.27
		modified TLBO	4.57	3.27
	Simulation time (s)	modified PSO	10338.9618	15160.9776
		modified TLBO	323.5959	303.9827

Though, the simulated optimum sets of C, ε and σ, training errors, r^2 values and mean absolute testing errors for MRR and ASR are almost same, still, simulation time in modified PSO is much higher (about 30 times for MRR and 50 times for ASR) than simulation time in modified TLBO. More simulation time causes higher computational cost. Therefore, it can be concluded that modified TLBO procedure is much more efficient in respect of computational time than the modified PSO. Hence, independent learning systems developed with the aid of modified TLBO (equations (4.18) & (4.19)) are used as representative models of EDM process in the experimental domain of present work.

4.5 Effects of machining control parameters on MRR and ASR

To depict the effects of different machining control parameters (current, pulse on time and pulse off time) on responses, surface plots for MRR and ASR are generated using the estimated models with parameters tuned by modified TLBO (equations (4.18) & (4.19)) being trained by their corresponding training data sets and shown in figure 4.12 through 4.17.

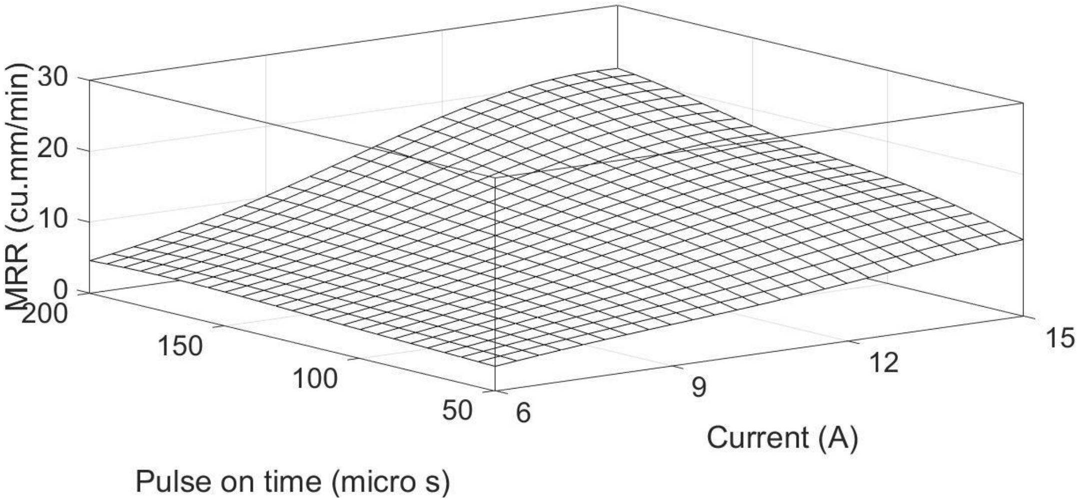

Fig. 4.12 Effects of current & pulse on time on MRR at pulse off time = 125 µs

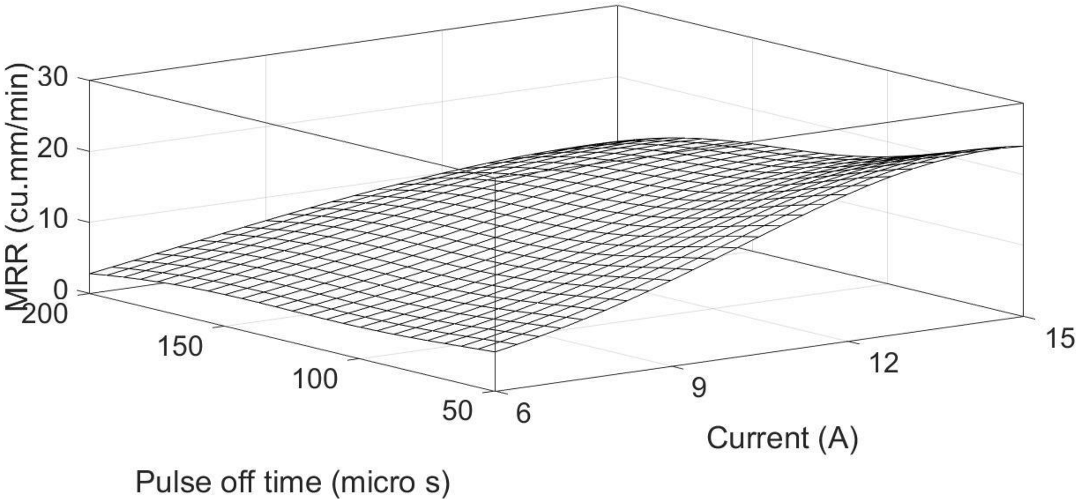

Fig. 4.13 Effects of current & pulse off time on MRR at pulse on time = 125 µs

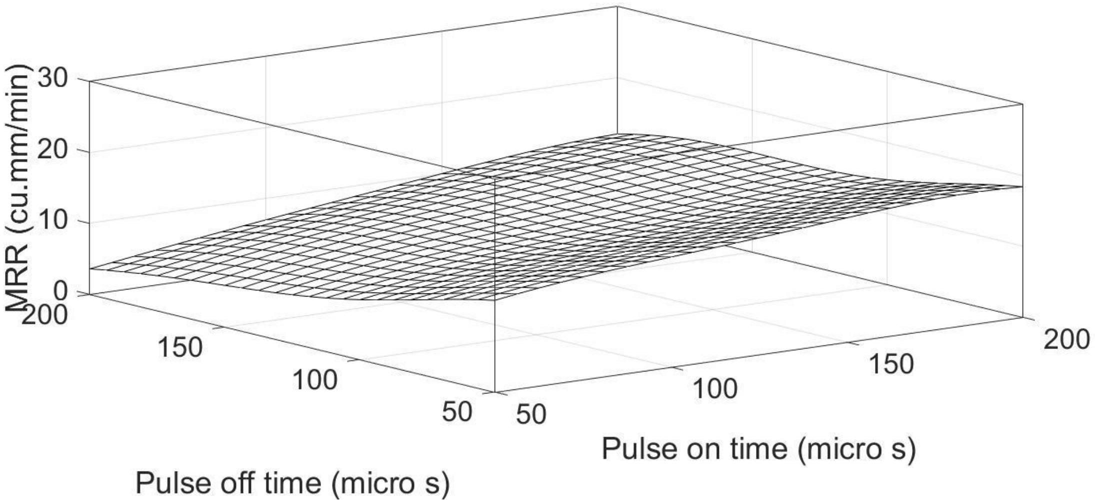

Fig. 4.14 Effects of pulse on time & pulse off time on MRR at current = 10.5 A

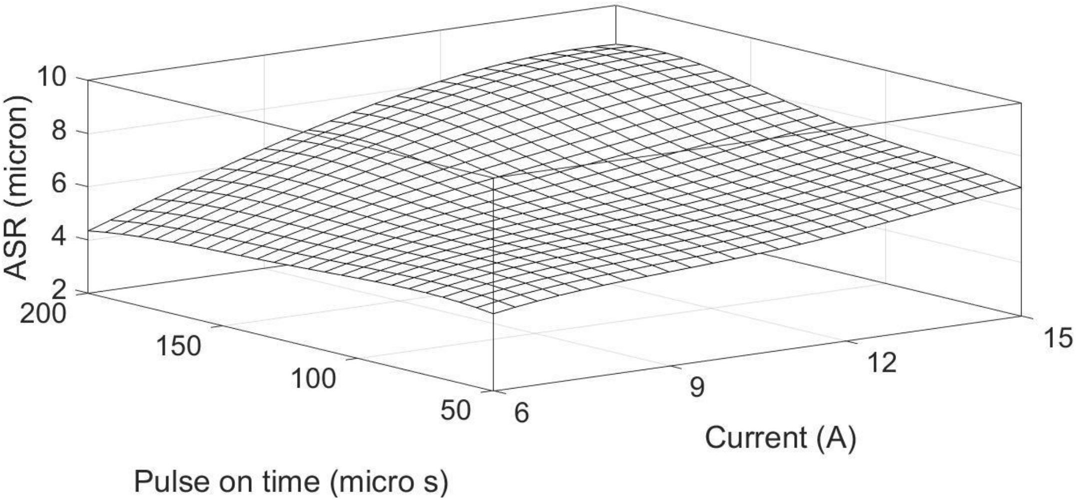

Fig. 4.15 Effects of current & pulse on time on ASR at pulse off time = 125 µs

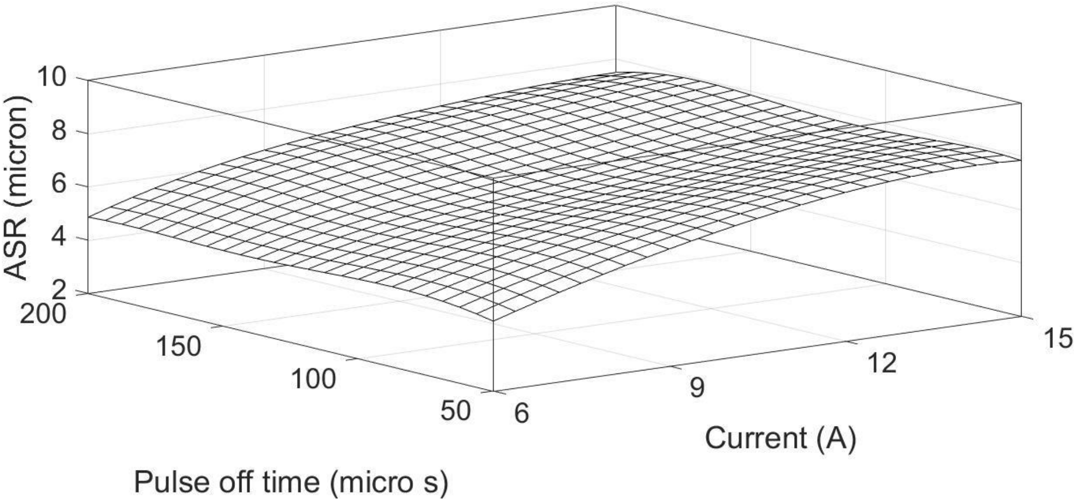

Fig. 4.16 Effects of current & pulse off time on ASR at pulse on time = 125 µs

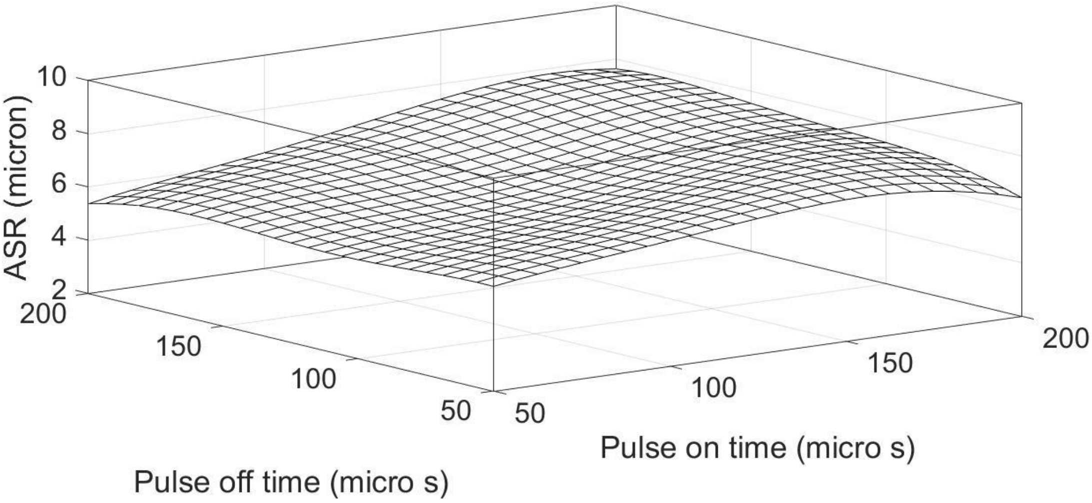

Fig. 4.17 Effects of pulse on time & pulse off time on ASR at current = 10.5 A

For both MRR and ASR, current shows a strong positive influence, whereas, other two control parameters, pulse on time and pulse off time, are found to be not so effective with their changes. At lower values of current, effects of both pulse on time and pulse off time on MRR and ASR are almost insignificant. In the higher zone of current values, higher MRR could be obtained by increasing pulse on time or lowering pulse off time. Though, variation of pulse off time does not show significant change in ASR even at higher values of current, but with increase of pulse on time, ASR is found to be increased at upper zone of current space.

With the aid of modified TLBO, internal structural parameters of SVM regression are tuned for developing two independent learning systems, one for each of the two individual process outcomes, MRR and ASR, in EDM process. Compared to modified PSO, selection of internal parameters of optimization technique itself is no longer required in modified TLBO. Thus, methodology of independent learning systems becomes user-friendly, yet, multiple sets of optimum internal structural parameters of learning system do not permit use of the methodology for concurrent predictions of multiple responses, MRR and ASR, for the same set of input parameters. Therefore, a unified learning system is developed that could estimate multiple responses from a single set of internal structural parameters.

4.6 Unified learning system development using modified TLBO

In the present section, development of a unified structure of SVM regression for predicting multiple responses is attempted. Unified learning is performed by simultaneous minimization of errors in estimation of MRR and ASR by modified TLBO. This development is an advancement of mathematical modeling towards the compact virtual data generator. In the proposed modified TLBO, combined rank method, an improvement in multi-objective optimization by TLBO, is suggested for simultaneous optimization of multiple objective functions and an optimum unique set of C, ε and σ is obtained. With the optimum unique set of SVM internal structural parameters, C, ε and σ, two separate sets of Lagrange multipliers one for each of the MRR and ASR are calculated on feeding respective training vectors. Subsequently, MRR and ASR are estimated from the calculated corresponding sets of Lagrange multipliers. It is to be noted that in subsection 4.3.1, two sets of Lagrange multipliers (each for MRR and ASR) from two independent sets of C, ε and σ are generated. The novelty of the present section lies in the development of such unification of SVM regression structures for concurrent predictions of conflicting type multiple responses with the aid of modified TLBO. This modification could be generalized for solving any such multiple objective functions in efficient way. The proposed procedure may become a building block for expert system.

For the purpose of building a unified structure of SVM regression learning system that provides concurrent predictions of multiple responses, randomly 54 data sets are taken for training. Different sets of randomly chosen 54 data are taken and same results are obtained. Here, results of learning system development with a typical set of randomly chosen 54 data are reported. Fitted learning systems are tested through rest 10 sets of data.

Structure of SVM regression learning system should vary for each of the different input-output combinations. In case of multiple process outcomes of a manufacturing process with same settings in machine control parameters, there should be separate sets of optimum C, ε and σ for each of the process outcomes. In the present section, a methodology is proposed to develop a unified structure of SVM regression learning system for concurrent predictions of multiple process outcomes of a manufacturing process. That is, an optimum unique set of internal structural parameters, C, ε and σ, is searched to exist instead of multiple sets of optimum C, ε and σ corresponding to multiple responses. Robust optimization techniques could be employed to tune the internal structural parameters, C, ε and σ. In this regard, algorithm-specific parameter-less teaching learning based optimization (TLBO) would be a justified choice.

In the present section, TLBO is modified by introducing a combined ranking method with weight infected rank selection (wherever necessary) for simultaneous optimization of multiple objective functions and thus employed for tuning the internal structural parameters of SVM regression. Different modifications as discussed in subsection 4.3.1, namely population based termination criterion, initialize population with high dispersion and way of choosing guide in case of multiple best learners performing same score, are also adapted.

4.6.1 Marching procedure and results

Proper choice of searching ranges is prerequisite for faster convergence of modified TLBO. In addition, objective function should be justifiably selected according to the proposed goal.

Searching ranges of C, ε and σ are decided based on the experimental values of respective response parameter. In the present subsection, as an optimum unique set of C, ε and σ for both of MRR and ASR is to be looked, searching ranges of C, ε and σ for MRR and ASR should be the same. Experimental values of MRR and ASR lie in different ranges. Therefore, they are normalized using equation (4.20).

$$\text{MRR}_{\text{norm}} = \frac{\text{MRR}-1.00}{28.25-1.00}\ ;\ \text{ASR}_{\text{norm}} = \frac{\text{ASR}-3.50}{9.25-3.50} \qquad (4.20)$$

Limits of searching ranges are revised based on the normalized response values. Combined searching range is obtained by union operation between the two individual searching ranges of C, ε and σ. For example, based on normalized MRR and ASR, searching ranges of ε are calculated first using equation (4.2) and (4.3). For MRR it is (0.0123, 0.0369) and for ASR (0.0167, 0.0501). Performing union operation between the two ranges, combined search range is identified. Lower limit of combined searching range of ε is estimated as max (0.0123, 0.0167) and upper limit as min (0.0369, 0.0501). Finally, combined search range of ε is decided as (0.0167, 0.0369). Similarly, searching ranges of C and σ are also identified. Optimum unique values of C, ε and σ are to be searched within their corresponding combined searching ranges (table 4.9).

Table 4.9 Searching ranges of internal structural parameters of SVM regression for unified learning

SVM internal structural parameters	Material removal rate	Average surface roughness	Combined
C	(0.0000, 1.0000)	(0.0000, 1.0000)	(0.0000, 1.0000)
ε	(0.0123, 0.0369)	(0.0167, 0.0501)	(0.0167, 0.0369)
σ	(0.4642, 0.7937)	(0.4642, 0.7937)	(0.4642, 0.7937)

Choice of different sets of internal structural parameters, C, ε and σ, changes the values of Lagrange multipliers for each of MRR and ASR.

To build the best structure of the learning system for near-accurate predictions of responses, chance of generalization errors should be reduced in learning process. Hence, internal structural parameters (C, ε and σ) must be tuned in such a fashion as to reduce the training errors in learning process. Thereby, in this subsection also, mean absolute training errors (MATE) in prediction of process responses, MRR (MATE_1) and ASR (MATE_2), are chosen as two objective functions (refer equation (4.5)).

Training by experimental results with proper internal structural parameters of SVM regression (C, ε and σ) is necessary to get near-exact representation of the process. The three internal structural parameters should be optimally tuned for each individual output-input combination. Thus, for multiple responses of a process with same input control parameters, separate sets of optimum C, ε and σ for different responses are expected. In this subsection, a methodology is proposed to build a unique structure of SVM regression for predicting multiple responses, that is, to search an optimum unique set of C, ε and σ instead of separate sets of C, ε and σ for the responses. In the proposed steps, simultaneous minimization of MATE_1 and MATE_2 is carried out for selection of optimum unique set of internal structural parameters of SVM regression. Teaching learning based optimization with certain modifications is employed for this tuning operation. During simulation process, different sets of C, ε and σ reshape the learning system. With same training input vectors and a particular set of C, ε and σ, two different sets of Lagrange multipliers for two responses are calculated using corresponding individual training output vectors. Subsequently, with the two sets of Lagrange multipliers, normalized MRR and normalized ASR are predicted. The predicted values are denormalized with the help of equation (4.20) and corresponding MATEs are evaluated using equation (4.5) based on denormalized MRR and ASR. Finally, two different sets of Lagrange multipliers are calculated from the simulated optimum unique set of C, ε and σ. When training errors become stable at their achievable minimum value, with corresponding set of Lagrange multipliers, MRR and ASR are estimated separately using equation (4.1). Here, this multiobjective optimization is performed by algorithm-specific parameter-less modified TLBO.

Within the estimated searching ranges (table 4.9), modified TLBO is applied for simultaneous minimization of $MATE_1$ and $MATE_2$. Though, TLBO is a parameter less optimization technique, still, to get this benefit in optimizing any non-linear high-dimensional objective function, termination criteria should be logically defined. As discussed in the subsection 4.3.1, SR ratio of the latest population that is learners in each direction, C, ε and σ, is used as termination criterion and simulation is terminated when SR ratio values along all dimensions (C, ε and σ) satisfy the termination criterion that is go below 1% in last consecutive 5 iterations. To ensure better exploration in whole searching range, considering initial SR ratio as at least 40% along each of the three directions, a set of 20 learners are randomly generated within specified search space (table 4.9). For maintaining the repeatability of the simulation steps, initial learners are given in table D.8.

In each step of iteration, with different set of learners that is set of C, ε and σ, shape of learning system changes. Teacher of any iteration should be selected as that set of C, ε and σ having lowest training error (MATE) value. When optimizing multiple objective functions, the same set of C, ε and σ might not give minimum value for both the objective functions. To overcome this difficulty, here, combined ranking method is proposed. In a typical iteration, at first, rank the learners separately according to the values of objective functions. Thus, the current set of learners gets two sets of ranks, $rank_1$ based on $MATE_1$ and $rank_2$ based on $MATE_2$. The two rank matrices are element-wise multiplied to get a combined rank for all of the current set learners. Say, a learner that is a set of C, ε and σ, gets two ranks namely 4 and 17. The two rank values are multiplied that is 17 X 4 = 68. Similarly, combined ranks of other learners are calculated. The combined rank values always lie between 1 and (number of learners)^2. According to this combined rank matrix, best learner is marked and set as teacher for subsequent teaching purpose. Here, values of objective functions are not multiplied at all, combined rank values are obtained only by element-wise multiplication of $rank_1$ and $rank_2$ matrices.

Though, combined rank values are proposed to select the current teacher, still, difficulty is present to select the current teacher if multiple learners give same combined rank value. Improper choice may guide the following iterations in wrong way and finally might be trapped inside any local optimum. A weight combining method is already proposed in subsection 4.3.1. Though, the proposed method is applied on learners having same objective function value, here, similar approach is taken on learners give same combined rank value. In the present subsection, a weighted combination of all those learners is to be evoluted such that new evoluted learner must give both $MATE_1$ & $MATE_2$ lower (higher for maximization) than either of the $MATE_1$ & $MATE_2$ corresponding to the learner having second best combined rank at current population applicable only for first iteration or the minimum $MATE_1$ & $MATE_2$ gained at immediate last iteration. For example, in case of simultaneous minimization of bi-variable two objective functions within search space ([0, 20], [0, 20]), at any iteration, one learner (9.7, 13.5) gets two ranks as 12 and 3 and another learner (18.2, 7.3) gets two ranks as 4 and 9. Therefore, two learners have same combined rank 12 X 3 = 4 X 9 = 36. At last iteration, minimum $MATE_1$ and minimum $MATE_2$ were 53.92 and 24.73 respectively. Now, it is required to choose the teacher among the two learners for next iteration. No such clear guidance is reported till now to choose the right one among the two. Here, a weighted combination of the two learners along their respective dimensions is calculated. Randomly two weights (rw_1, rw_2) are generated between (0, 1) such that $rw_1 + rw_2 = 1$. A new learner is evoluted as (rw_1 X 9.7 + rw_2 X 18.2, rw_1 X 13.5 + rw_2 X 7.3). For $rw_1 = 0.4$ and $rw_2 = 0.6$, new learner would be (14.80, 9.78) which gives $MATE_1$ as 19.66 and $MATE_2$ as 10.29. New evoluted learner gives both $MATE_1$ and $MATE_2$ less than the minimum $MATE_1$ (53.92) and $MATE_2$ (24.73) gained at last iteration. In case of first iteration, comparison would be done with $MATE_1$ and $MATE_2$ corresponding to the learner having second best combined rank at current population. Thus, learner (14.80, 9.78) would be the teacher for next iteration otherwise the steps are repeated with another random set of weights (rw_1, rw_2) till the above said condition is fulfilled. However, there is no need to update current population with this evoluted teacher. This proposition is expected to be effective to avoid ambiguity to choose the right teacher at any iteration.

Adapting all the above said modifications, steps of modified TLBO algorithm used for searching optimum unique set of C, ε and σ by simultaneously minimizing MATEs (refer equation (4.5)) in estimation of both the responses MRR ($MATE_1$) and ASR ($MATE_2$) are discussed below.

Step 1 : Normalize the control parameters, cur, t_{on}, t_{off}, and process responses, MRR and ASR, using equations (4.4) and (4.20) respectively. Mean absolute training errors (refer equation (4.5)) in estimation of MRR ($MATE_1$) and that of ASR ($MATE_2$) are separately considered as two objective functions. Set n = 20 and $iter_{max}$ = 250.

Step 2 : Calculate two searching ranges of C, ε and σ based on normalized MRR and ASR separately. Do the union operation between the two searching ranges and get the combined searching ranges of C, ε and σ (table 4.9).

Step 3 : Set iter = 1 and termination criterion as SR ratio along all three dimensions < 1% in consecutive 5 iterations. Randomly (following uniform distribution) generate 20 set of learners (refer table D.8) with SR ratio along each dimension > 40% within corresponding search space.

Step 4 : With normalized training input and output vectors, for each of the current set of 20 learners, two different sets of Lagrange multipliers for normalized MRR and normalized ASR are calculated separately. With the Lagrange multipliers, normalized MRR and normalized ASR are estimated corresponding to current set of learners. The estimated normalized MRR and normalized ASR are denormalized with the help of equation (4.20), corresponding $MATE_1$ and $MATE_2$ are calculated.

Step 5 : Rank all 20 learners with respect to their corresponding $MATE_1$ and $MATE_2$, store the two sets of ranks in $rank_1$ and $rank_2$ matrices respectively. Get combined rank by element-wise multiplication of $rank_1$ and $rank_2$ matrices. If multiple learners have same best combined rank, go to step 6, otherwise, learner having best combined rank is selected as CT_{iter} and go to step 7.

Step 6 : Learners having same best combined rank are identified. Make a weighted combination of those identified learners such that the new evoluted learner must give both $MATE_1$ & $MATE_2$ lower than either the $MATE_1$ & $MATE_2$ corresponding to the learner having second best combined rank at current population (applicable only for first iteration) or the minimum $MATE_1$ & $MATE_2$ gained at immediate last iteration. The new evoluted learner is selected as CT_{iter}.

Step 7 : Find out mean of current all 20 learners and estimate adapted teaching factor (TF) using equation (4.15).

Step 8 : Calculate SR ratio along all three dimensions namely C, ε and σ. If termination criterion is satisfied, stop simulation and latest teacher is declared as the optimum unique set of C, ε and σ, otherwise, go to step 9.

Step 9 : If iter = $iter_{max}$, then, go to step 3 and restart the simulation with higher $iter_{max}$, otherwise, set t = 1 and go to step 10.

Step 10 : Calculate new t^{th} learner taught by CT_{iter} following the equation (4.16).

Step 11 : If $MATE_{1,\, new\, t} < MATE_{1,\, t}$ and $MATE_{2,\, new\, t} < MATE_{2,\, t}$, then, replace t^{th} learner of current population by new t^{th} learner and go to step 12, otherwise, t^{th} learner of current population is kept unaltered and go to step 12.

Step 12 : If t = n, then, set k = 1 and go to step 13, otherwise, set t = t + 1 and go to step 10.

Step 13 : Select random integer r between 1 and n except k.

Step 14 : If $MATE_{1,\, k} < MATE_{1,\, r}$ and $MATE_{2,\, k} < MATE_{2,\, r}$, then, calculate new k^{th} learner sharing knowledge with current r^{th} learner using equation (4.21) and go to step 16, otherwise, go to step 15.

$$x^{k}_{iter+1,\, d} = x^{k}_{iter,\, d} + rand \text{ X } (x^{k}_{iter,\, d} - x^{r}_{iter,\, d}), \quad \boldsymbol{d} = 1(1)3 \tag{4.21}$$

Step 15 : If $MATE_{1,\ k} > MATE_{1,\ r}$ and $MATE_{2,\ k} > MATE_{2,\ r}$, then, calculate new kth learner sharing knowledge with current rth learner using equation (4.22) and go to step 16, otherwise, kth learner of current population is kept unaltered and go to step 16.

$$x^{k}_{iter+1,\ d} = x^{k}_{iter,\ d} + \text{rand} \times (x^{r}_{iter,\ d} - x^{k}_{iter,\ d}), \quad \boldsymbol{d} = 1(1)3 \tag{4.22}$$

Step 16 : If k = n, replace the learners of current population by corresponding new learners, set iter = iter + 1 and go to step 4, otherwise, set k = k + 1 and go to step 13.

Therefore, latest teacher is selected as optimum unique set of C, ε and σ. With the optimum unique set of C, ε and σ, two separate sets of Lagrange multipliers are calculated using the corresponding normalized training output vectors of MRR and ASR. The unified structure of SVM regression learning system of EDM process could be represented by equation (4.1). Predictions of normalized MRR and normalized ASR could be done separately by pouring their respective set Lagrange multipliers into this equation (4.1). Predicted normalized MRR and ASR are denormalized and subsequently finally achieved training errors, $MATE_1$ and $MATE_2$, are estimated. The above mentioned steps for searching of optimum unique set of internal structural parameters of SVM regression, C, ε and σ, by modified TLBO and thereby for prediction of MRR and ASR simultaneously are coded in the platform of MATLAB.

Now, using the above said modified teaching learning based optimization algorithm adapted with all discussed modifications, training errors in prediction of MRR ($MATE_1$) and that of ASR ($MATE_2$) are minimized simultaneously for different settings of C, ε and σ within combined searching ranges (table 4.9). As the simulation marches, with different sets of values of C, ε and σ, shapes of learning system are getting modified and consequently training errors are changed. Finally, the optimum unique set of C, ε and σ within the specified searching ranges (refer table 4.9) with achievable minimum mean absolute training errors, $MATE_1$ and $MATE_2$, is found and reported in table 4.10.

Table 4.10 Results of tuning internal structural parameters of SVM regression for unified learning

Response	Optimum unique internal structural parameters of SVM regression for normalized responses			Simulation time (s)	No. of support vectors	bias	Performance	
	C	ε	σ				MATE (%)	r^2
MRR	1.0000	0.0167	0.4642	871.0905	37	0	6.50	0.9855
ASR					49	0	3.31	0.9527

Optimum unique value of C is shifted towards the upper end of search space. This indicates the complexity of the model which is in favor of the chaotic behavior of EDM process. The irregular fluctuations could be controlled by proper choice of ε. Here, lower value of ε indicates that the learning system could be able to absorb the random variations adequately. Besides, small σ value claims that the unified learning system is stable and generalized by entrapping the oscillatory patterns in outputs outside the insensitive zones. The higher values of coefficient of determinations, r^2 (table 4.10), indicate the strong correlations between experimental and estimated responses (denormalized).

With the optimum unique set of C, ε and σ (table 4.10), two sets of Lagrange multipliers (α_i, α_i^*) for normalized MRR and that for ASR are calculated separately (refer table D.9). Representative models of the developed unified structure of SVM regression learning system are given by equation (4.23).

$$f(\boldsymbol{x}) = \sum_{i=1}^{N} (\alpha_i - \alpha_i^*)_j \, K(x_i, \boldsymbol{x}) + b \quad \left| \begin{array}{l} C = 1.0000 \\ \varepsilon = 0.0167 \\ \sigma = 0.4642 \end{array} \right. \tag{4.23}$$

with j = 1 for normalized MRR, 2 for normalized ASR and

$$\text{with } K(x_i, \boldsymbol{x}) = e^{-\frac{\|x_i - \boldsymbol{x}\|^2}{2\sigma^2}} \quad \left| \; \sigma = 0.4642 \right.$$

Marching steps for searching optimum unique set of C, ε and σ in simultaneous estimation of MRR and ASR are given in figure B.1 in appendix B. Corresponding to current teacher$_{iter}$ of each iteration, MATE$_1$ and MATE$_2$ are calculated and their gradual decaying patterns are represented in figures 4.18 and 4.19. Observing the components of SR ratio of current population at the end of each iteration, influence of three internal structural parameters, C, ε and σ, on simultaneous minimization could be understood (figure 4.20).

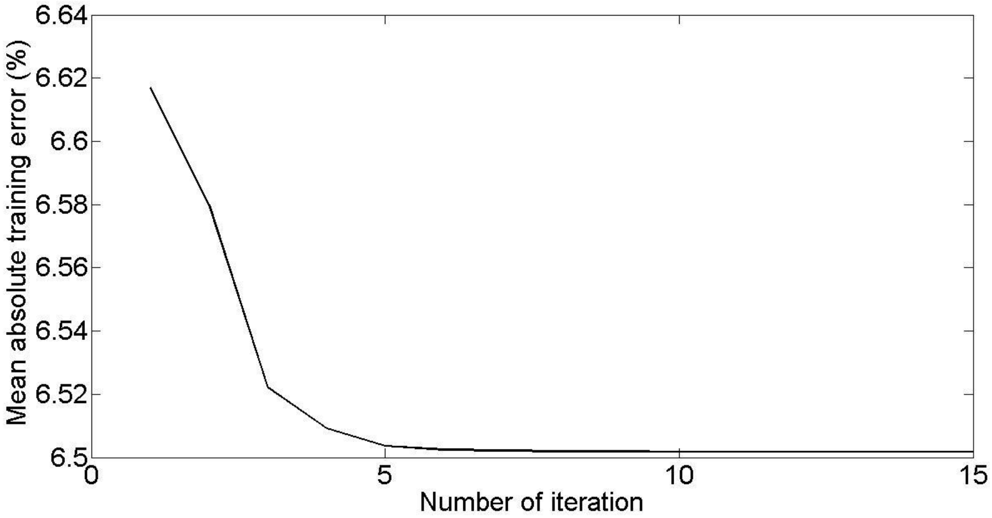

Fig. 4.18 Changes of MATE in estimation of MRR (MATE$_1$)

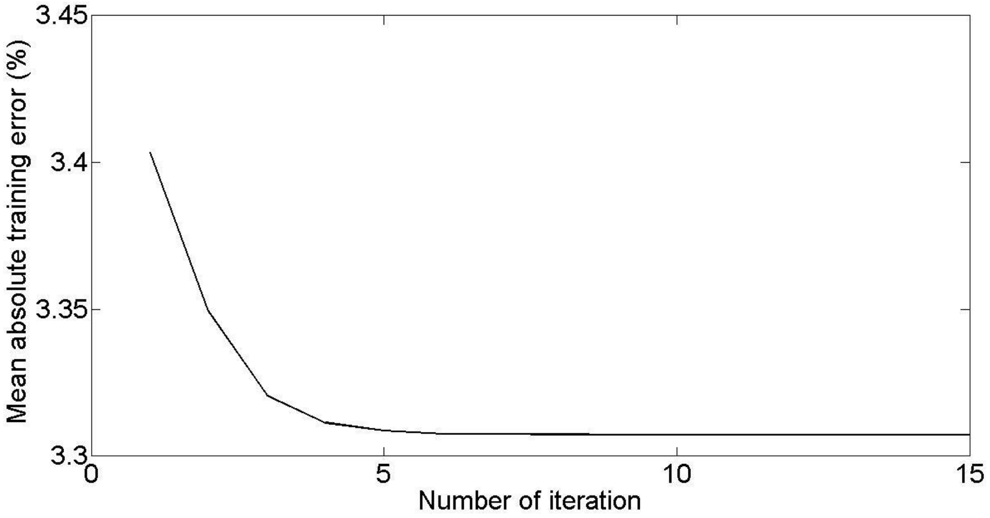

Fig. 4.19 Changes of MATE in estimation of ASR (MATE$_2$)

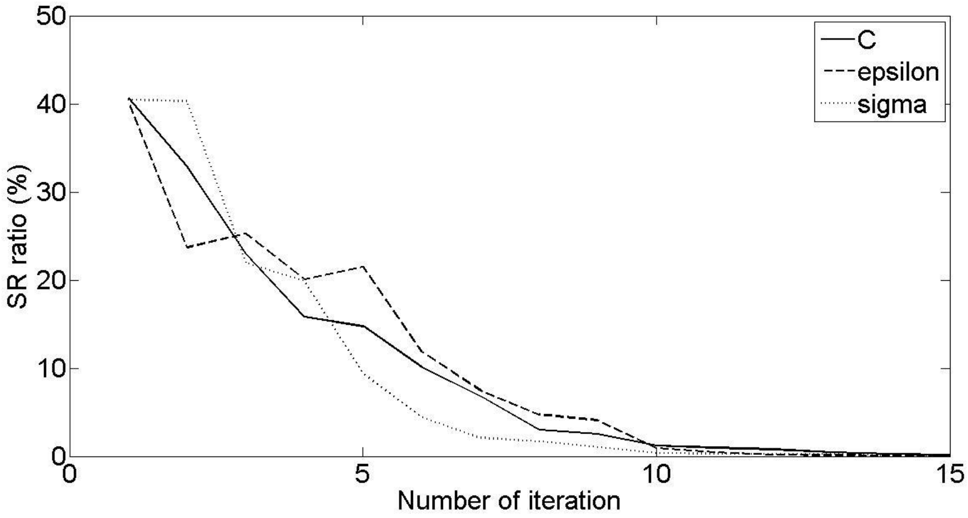

Fig. 4.20 Changes of SR ratios along C, ε and σ during simultaneous minimization of $MATE_1$ and $MATE_2$

In case of minimizing MATEs, $MATE_1$ and $MATE_2$, relative to C and ε, the effect of σ is marginally lower, as SR ratio for σ decreases at a faster rate relative to C and ε (figure 4.20). After few iterations, absence of irregular fluctuations of SR ratios along all three dimensions indicates the convergence of simulation procedure towards global optimum in smooth way. Steps for concurrent estimations of MRR and ASR in testing are shown in figure 4.21.

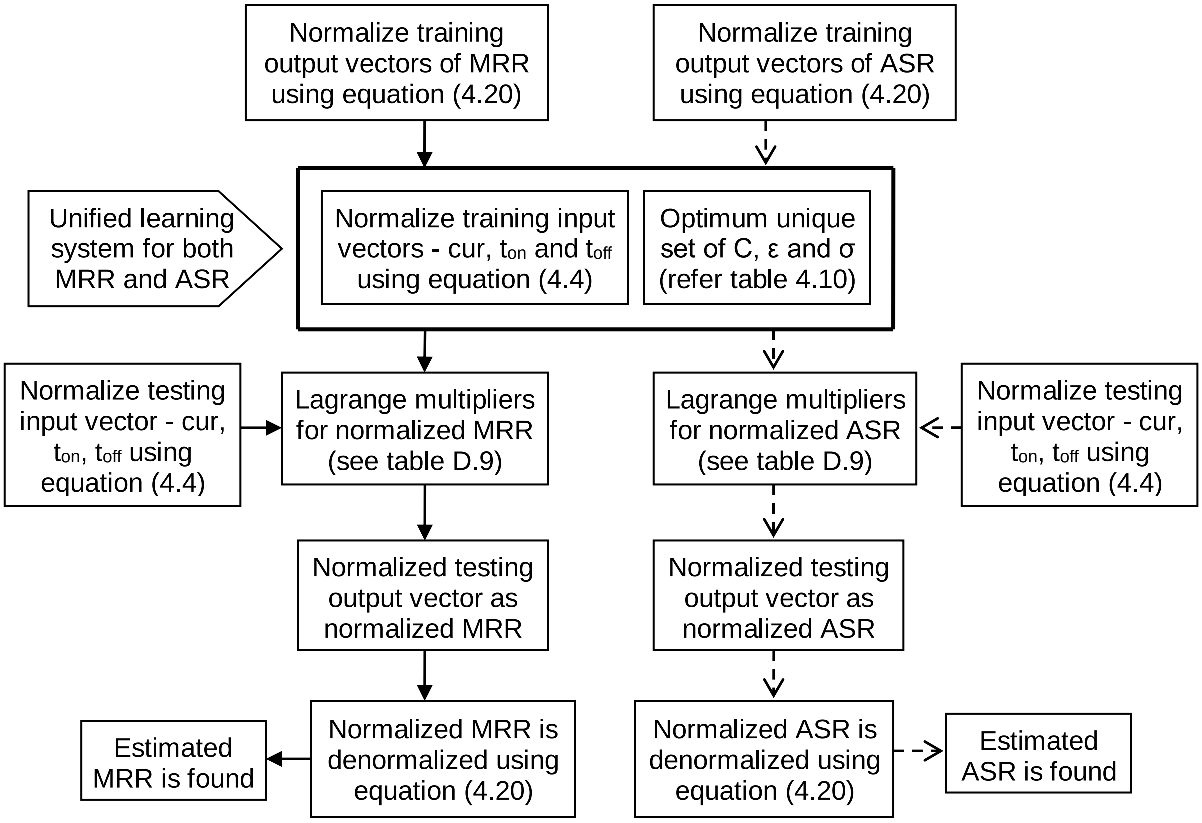

Fig. 4.21 Detailed steps for concurrent estimations of MRR and ASR from unified learning system

4.6.2 Testing of unified learning system

Unified learning system of MRR and ASR, equation (4.23), is tested with 10 disjoint data sets obtained from separate follow up experimental runs. For testing purpose, testing input vectors are normalized using equation (4.4). Sets of Lagrange multipliers of normalized MRR and normalized ASR (refer table D.9) are separately fed to the learning system, equation (4.23), and testing output vectors, normalized MRR and normalized ASR, are estimated separately. The estimated normalized outputs are denormalized with the help of equation (4.20). The absolute errors in prediction with corresponding experimental values are calculated and presented in table 4.11 and 4.12.

Table 4.11 Testing of estimated MRR from unified learning system

Sl. no.	Machining condition			Material removal rate		
	cur (A)	t_{on} (μs)	t_{off} (μs)	Experimental (mm^3/min)	Estimated (mm^3/min)	Absolute error (%)
1	6	100	50	5.48126	5.51254	0.57
2	6	200	150	4.56557	4.79086	4.93
3	9	100	100	9.13364	8.60628	5.77
4	9	150	50	13.50951	12.70528	5.95
5	9	200	100	10.48887	10.45321	0.34
6	12	50	100	9.46479	9.93234	4.94
7	12	100	50	19.36570	18.94783	2.16
8	12	150	200	11.36906	11.43744	0.60
9	15	100	100	18.06487	16.80110	7.00
10	15	150	50	24.95816	25.65435	2.79
Mean absolute testing error (%)						3.51

Table 4.12 Testing of estimated ASR from unified learning system

Sl. no.	Machining condition			Average surface roughness		
	cur (A)	t_{on} (μs)	t_{off} (μs)	Experimental (μm)	Estimated (μm)	Absolute error (%)
1	6	100	50	4.61	4.59	0.43
2	6	200	150	4.21	4.31	2.38
3	9	100	100	5.79	6.00	3.63
4	9	150	50	6.95	6.40	7.91
5	9	200	100	6.22	6.20	0.32
6	12	50	100	5.88	5.78	1.70
7	12	100	50	7.44	6.90	7.26
8	12	150	200	7.35	7.55	2.72
9	15	100	100	7.48	7.26	2.94
10	15	150	50	8.49	8.12	4.36
Mean absolute testing error (%)						3.37

Mean absolute testing errors (table 4.11 and 4.12) for both MRR (3.51%) and ASR (3.37%) indicate the practical adequacy of the developed unified structure of SVM regression learning system for prediction of MRR and ASR in EDM process within their experimental ranges.

4.7 Summary

In the present chapter, independent models of MRR and ASR are first trained through SVM regression based learning system with internal parameters tuned by modified PSO as well as modified TLBO. Conclusions drawn are listed below.

- As regularization parameter (C) of SVM regression makes a tradeoff between flatness and complexity of trained learning system, therefore, higher value of C for each of the MRR and the ASR indicates complex relation among machining control parameters and process outcomes.
- ε-insensitive hyper-tube of support vector machine is capable to effectively capture the uncontrollable fluctuations in responses of EDM which is beneficial for other researchers to apply the models on different products obtained in different batches.
- High-dimensional effects of machining control parameters on MRR and ASR can be handled through kernel function namely Gaussian radial basis function.
- Current population based stopping criterion, as proposed in the present chapter, could be a prominent global guideline for termination of population based evolutionary optimization techniques.
- Initial population with stopping criterion based high relative dispersion could ensure better exploration of search space.
- Proposition of weight combining method for selection of guide (p_{best}, g_{best} for PSO, teacher for TLBO) for next iteration in case of multiple particles or learners having same optimum score could be implemented for other population based evolutionary optimization methods.
- With the proposed modifications, modified TLBO gives more smoothing convergence compared to modified PSO.
- Modified TLBO is found as computationally more efficient than modified PSO.

Next, a simple methodology is devised to develop a unified structure of SVM regression based learning system of material removal rate (MRR) and average surface roughness (ASR) in EDM process with internal structural parameters tuned by modified TLBO. The conclusions drawn are

- Modification over standard TLBO, combined rank method, as introduced for simultaneous minimization of MATEs in estimation of MRR and ASR, could be employed for handling multiple objective functions in multiobjective optimization.
- In combined rank method, learners of current population are to be combined with weight vectors instead of objective functions ($MATE_1$ and $MATE_2$) to reserve the independent impacts of objective functions.
- An optimum single set of SVM regression internal structural parameters, C, ε and σ, for both the MRR and the ASR could be obtained instead of two separate sets of C, ε and σ for two individual responses.

Though, independent learning system is almost capable to capture irregular fluctuations in process outcomes of EDM process, still, use of the data generator is not readily amenable for shop-floor use. Therefore, to meet the specific need-based customer demand, optimum selection of control parameters in EDM process is necessary. Considering developed independent learning systems as representative models of EDM process, an easy way out for selection of optimum levels of control parameters is proposed in the next chapter. It is to be noted here that while MRR is increased in EDM, surface finish reduces and thus, a trade-off is necessary between them.

CHAPTER 5

OPTIMIZATION OF EDM PROCESS

5.1 Introduction

In the previous chapter, representative model for each of MRR and ASR in EDM process is developed through SVM regression based learning system. Though, capability of SVM regression based learning system is found as efficient in handling of uncontrollable fluctuations in process outcomes, yet, due to lack of tractable representation of the system, it would become difficult for workshop use by engineers. On the other hand, to freeze the design at product development stage, selection of near-optimum setting of control parameters in EDM machine to obtain the specific need based MRR-ASR combination is necessary. A procedure is proposed in this chapter to that effect.

In the present chapter, power law models of MRR and ASR are developed first using proposed independent learning systems as virtual data generators. Then, varying the weight factors, different weighted combinations of the inverse of MRR and the ASR are minimized by modified TLBO. Pseudo Pareto front passing through the optimum results, thus obtained, gives a guideline for selection of optimum achievable value of ASR for a specific demand of MRR. Further, inverse solution procedure is elaborated to find the near-optimum setting of machining control parameters in EDM machine to obtain the specific need based MRR-ASR combination. Sequence diagram for proposed optimization of EDM process is shown in figure 5.1.

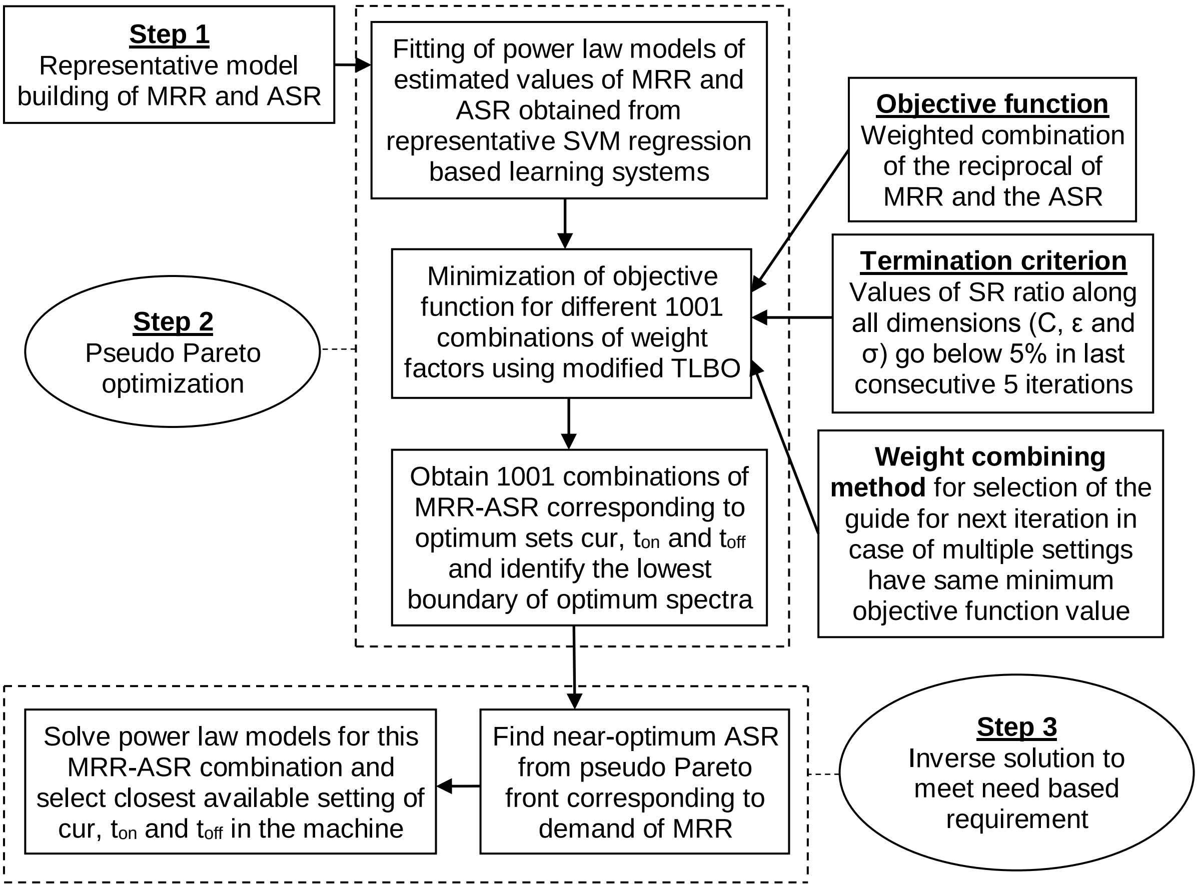

Fig. 5.1 Sequence diagram for proposed optimization of EDM process

5.2 Pseudo Pareto optimization

Using the SVM regression based independent learning systems (refer equations (4.18) & (4.19)) as the virtual data generators, data sets of the two responses, MRR and ASR, are generated with 64 different combinations of the levels of machining control parameters. The generated data sets are further used for developing power law models of MRR and ASR. Generated data are fitted through power law model due to its ready amenability and easy back tracking to process parameters from need based requirements of process outputs.

Here, power law models (PLM) of MRR and ASR are considered as

$$MRR = e^{a0}\, cur^{a1}\, t_{on}^{a2}\, t_{off}^{a3} \quad (5.1)$$
$$ASR = e^{b0}\, cur^{b1}\, t_{on}^{b2}\, t_{off}^{b3} \quad (5.2)$$

To estimate the unknown coefficients, natural logarithm is taken at both sides.

$$\ln (MRR) = a_0 + a_1 \ln (cur) + a_2 \ln (t_{on}) + a_3 \ln (t_{off}) \quad (5.3)$$
$$\ln (ASR) = b_0 + b_1 \ln (cur) + b_2 \ln (t_{on}) + b_3 \ln (t_{off}) \quad (5.4)$$

The coefficients are estimated by linear regression with 64 non-repeated data sets generated from SVM regression based learning systems (refer equations (4.18) & (4.19)). Using linear multivariable regression analysis, coefficients of equations (5.3) and (5.4) are estimated as follows.

$$\ln (MRR) = - 0.9421 + 1.5264 \ln (cur) + 0.4418 \ln (t_{on}) – 0.5176 \ln (t_{off}) \quad (5.5)$$
$$\ln (ASR) = - 0.1080 + 0.5484 \ln (cur) + 0.1203 \ln (t_{on}) + 0.0238 \ln (t_{off}) \quad (5.6)$$

Finally, the fitted power law models (PLM) are represented as

$$MRR = e^{-0.9421}\, cur^{1.5264}\, t_{on}^{0.4418}\, t_{off}^{-0.5176} \quad (5.7)$$
$$ASR = e^{-0.1080}\, cur^{0.5484}\, t_{on}^{0.1203}\, t_{off}^{0.0238} \quad (5.8)$$

The above developed fitted models are used as representatives of MRR and ASR for pseudo Pareto optimization. In case of machining, rate of material removal determines the productivity of the process that is higher MRR results higher productivity. Besides, to meet the specific functional aspects of product, quality must be maintained. One of the major surface quality measurements is the average surface roughness. As they are conflicting in nature, therefore, a tradeoff between MRR and ASR is expected to exist. Hence, the process should be controlled to meet both of the features in an optimal way. Conflicting type performance measures of any manufacturing process still involve a difficulty to get simultaneous optimum outcomes. Concept of Pareto optimality of multiple outcomes is expected to be useful in this regard.

In contrast to single objective optimization, a solution to a multiobjective problem is more of a concept than a definition. In case of single objective problem, the global optimum is unique. For multiobjective cases, in many of the situations, there exists a number of solution set of parameters, all of which equally satisfy the optimality criterion.

For any given multiobjective optimization problem, there may be an infinite number of pseudo Pareto optimal points constituting the pseudo Pareto optimal set. But the engineers are very much concerned on the extreme limit of the solution spectrum, called pseudo Pareto front. Practically, pseudo Pareto front suggests a guideline to engineers not to go beyond this limit.

By definition, pseudo Pareto solution set is the non-dominated solutions among the all optimum points. The predominant concept in defining an optimal point is that of pseudo Pareto optimality [221] which is defined as follows.

Definition 1: Pseudo Pareto Optimal: A point, $x^* \in \boldsymbol{x}$, is pseudo Pareto optimal if there does not exist another point, $x^\# \in \boldsymbol{x}$, such that $F(x^\#) \leq F(x^*)$, and $F_i(x^\#) < F_i(x^*)$ for at least one function.

All pseudo Pareto optimal points lie on the boundary of the optimum criterion space [222]. Often, algorithms provide solutions that may not be pseudo Pareto optimal but may satisfy other criteria, making them significant for practical applications. For instance, weakly pseudo Pareto optimal is defined as follows.

Definition 2: Weakly pseudo Pareto Optimal: A point, $x^* \in \boldsymbol{x}$, is weakly pseudo Pareto optimal if there does not exist another point, $x^\# \in \boldsymbol{x}$, such that $F(x^\#) < F(x^*)$.

A point is weakly pseudo Pareto optimal if there is no other point that improves all of the objective functions simultaneously. In contrast, a point is pseudo Pareto optimal if there is no other point that improves at least one objective function without detriment to another function. All pseudo Pareto optimal points are weakly pseudo Pareto optimal, but all weakly pseudo Pareto optimal points are not pseudo Pareto optimal.

A pseudo Pareto set is developed using the concept of an archive where the non-dominated solutions seen so far are stored and is constantly updated. In the present chapter, the developed power law models (equations (5.7) and (5.8)) are used for pseudo Pareto optimization within their experimental range of inputs and outputs. To maintain both the productivity and quality of products, higher MRR and lower ASR are always preferred. So, functions of MRR and ASR (equations (5.7) and (5.8)) are to be maximized and minimized respectively. In general, TLBO is used for minimization purpose. Reciprocal of MRR is therefore, taken to convert it into a minimization problem (equation (5.9)).

$$f_1\,(\mathrm{cur}, t_{on}, t_{off}) = \frac{1}{\mathrm{MRR}} \tag{5.9}$$

$$f_2\,(\mathrm{cur}, t_{on}, t_{off}) = \mathrm{ASR} \tag{5.10}$$

For pseudo Pareto optimization, a weighted combination of the functions (equations (5.9) and (5.10)) are considered. With different combination of weight factors (w_1, w_2), objective function is modified. Further, each of the responses is to be normalized to avoid the effects of their different scale ranges.

$$\text{Objective function} = w_1 \frac{f_1 - (\frac{1}{\mathrm{MRR_{exp}}})_{\min}}{(\frac{1}{\mathrm{MRR_{exp}}})_{\max} - (\frac{1}{\mathrm{MRR_{exp}}})_{\min}} + w_2 \frac{f_2 - (\mathrm{ASR_{exp}})_{\min}}{(\mathrm{ASR_{exp}})_{\max} - (\mathrm{ASR_{exp}})_{\min}} \tag{5.11}$$

Here, 1001 different combinations of weight factors (w_1, w_2) between (0, 1) are chosen subject to the condition of $w_1 + w_2 = 1$. As a result, almost all possible practical combinations are considered and near exhaustive search is done. Two extreme combinations are nothing but the normalized f_1 (for $w_1 = 1$ & $w_2 = 0$) and f_2 (for $w_1 = 0$ & $w_2 = 1$) respectively. So, starting from one normalized response, as the weight factors change, the objective function gradually shifts to the other normalized response. For minimization of the objective function (equation (5.11)), modified TLBO as proposed in section 4.3 is again employed.

In every iteration during optimization, evaluations of MRR and ASR from equations (5.7) and (5.8) are restricted to 10% of the lower end and the upper end of experimental observations (equations (5.12) and (5.13)), so as to get a Pareto front very close to the exact experimental boundaries.

$$0.9(\mathrm{MRR_{exp}})_{\min} \le \mathrm{MRR} \le 1.1(\mathrm{MRR_{exp}})_{\max} \tag{5.12}$$

$$0.9(\mathrm{ASR_{exp}})_{\min} \le \mathrm{ASR} \le 1.1(\mathrm{ASR_{exp}})_{\max} \tag{5.13}$$

The constraints are tagged with previously discussed modified TLBO in section 4.3. Number of learners is also kept at 20. Searching range of each of the three machining control parameters is thus obtained (table 5.1).

Table 5.1 Searching ranges of machining control parameters for pseudo Pareto optimization

Machining control parameter	Searching range
Current (A)	(6, 15)
Pulse on time (μs)	(50, 200)
Pulse off time (μs)	(50, 200)

To maintain the repeatability of the simulation process initial setting of learners in modified TLBO is to be memorized. A wide spread (SR ratio above 40%) initial settings are generated within searching range subject to the constrained criteria (equations (5.12) and (5.13)). The initial settings are listed in appendix D (refer table D.10). Objective functions (equation (5.11)) with 1001 different weighted combinations are then minimized by modified TLBO. Each of the weight factor combinations gives a set of optimum MRR and ASR. Thus, 1001 sets of optimum MRR and ASR are found (figure 5.2). A typical variation in marching steps to minimize objective function (equation (5.11)) with $w_1 = 0.88$ and $w_2 = 0.12$ under constraint equations (5.12) and (5.13) is shown in figure 5.3. Corresponding changes of SR ratios along cur, t_{on} and t_{off} are plotted in figure 5.4. Obtained optimum control parameters are $\mathrm{cur}_{opt} = 11.92$, $t_{on,opt} = 200.00$ and $t_{off,opt} = 50.00$ and corresponding minimum objective function value is 0.0849.

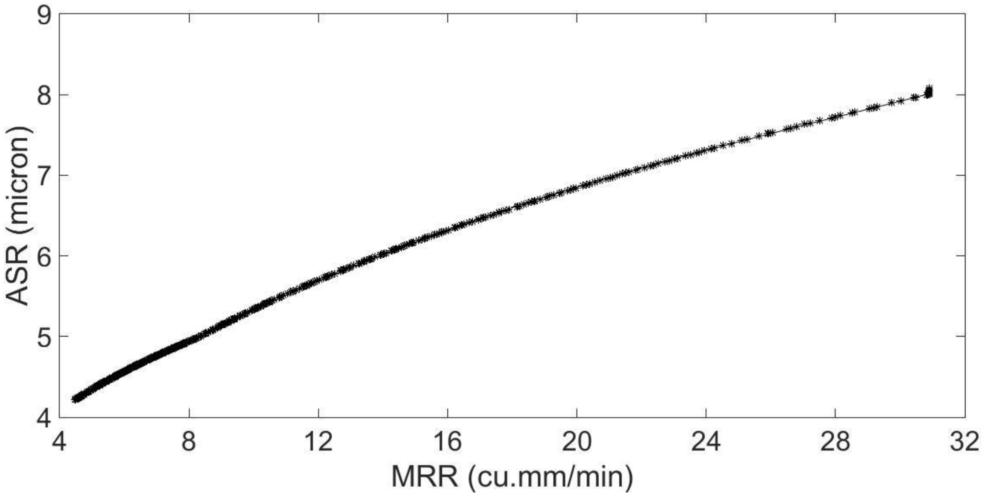

Fig. 5.2 Pseudo Pareto front

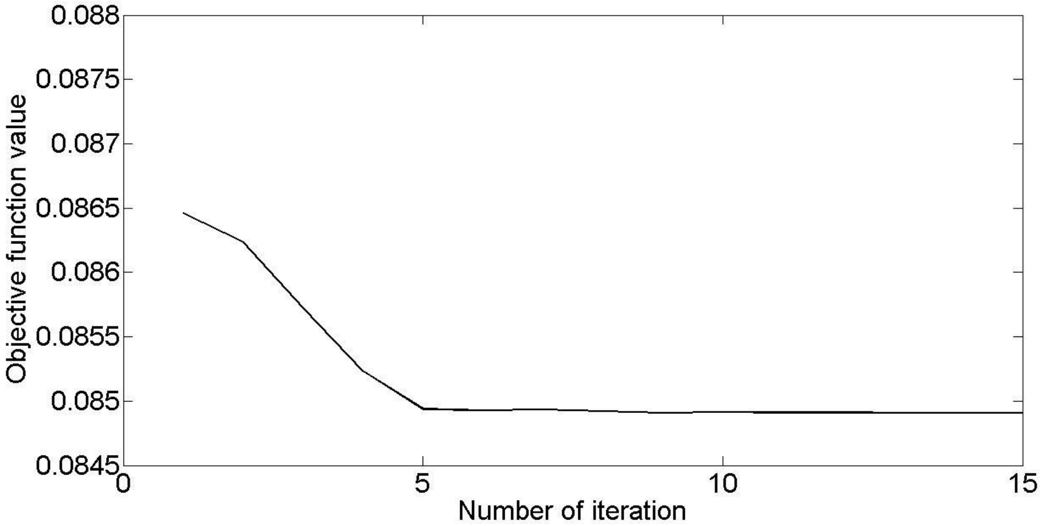

Fig. 5.3 Marching steps to minimize a typical objective function (equation (5.11)) with $w_1 = 0.88$ and $w_2 = 0.12$ by modified TLBO

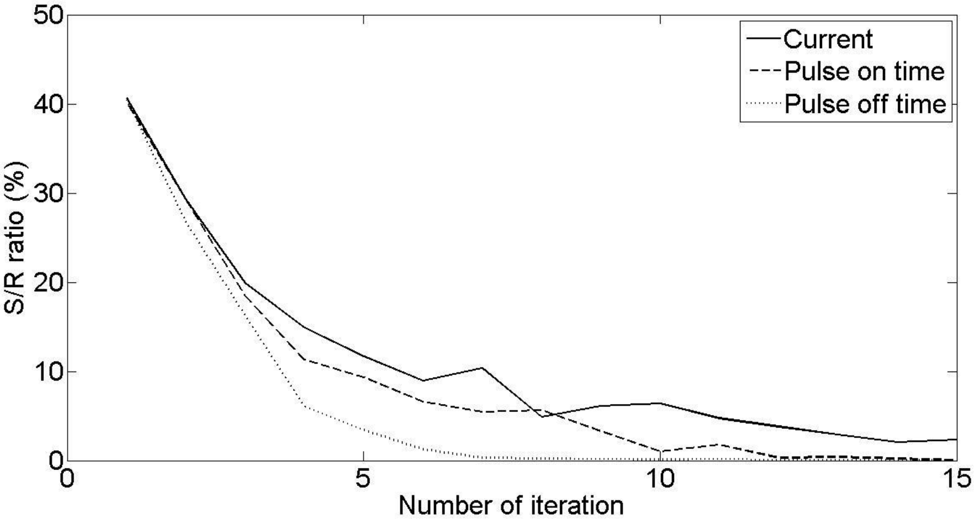

Fig. 5.4 Changes of SR ratios along cur, t_{on} and t_{off} in minimization of a typical objective function (equation (5.11)) with $w_1 = 0.88$ and $w_2 = 0.12$ by modified TLBO

As, almost all the points lie on a non-linear curve, a 4th order polynomial is fitted through the optimum MRR and ASR combinations and represented as

$$ASR = 3.1883986596 + 0.2404369670\,(MRR) - 0.0019712434\,(MRR)^2 - 0.0000808326\,(MRR)^3 + 0.0000018202\,(MRR)^4 \quad (5.14)$$

This representation of ASR, as a function of MRR, indicates the pseudo Pareto front (figure 5.2) and suggests the limiting situation. Significance of this pseudo Pareto front is that, no other optimum setting of both the responses, MRR and ASR, could be achieved simultaneously below this boundary. For a particular MRR, different values of ASR are achievable, but lowest possible value lies on that pseudo Pareto front. Pseudo Pareto front is validated (table 5.2) through follow up experimental observations. Optimum ASR, that is estimated from equation (5.14), lies within 10% from corresponding experimental values (table 5.2).

Table 5.2 Pseudo Pareto front validation

Sl. no.	Material removal rate (mm^3/min)	Average surface roughness		
		Experimental (µm)	Estimated (µm)	Absolute error (%)
1	4.40340	4.22	4.20	0.41
2	4.56557	4.21	4.24	0.67
3	24.03488	7.38	7.31	0.90
4	5.17459	4.43	4.37	1.36
5	14.41525	5.98	6.08	1.69
6	18.36007	6.83	6.64	2.71
7	22.91674	6.99	7.19	2.90
8	10.69728	5.64	5.46	3.20
9	6.30850	4.79	4.61	3.77
10	5.48126	4.61	4.44	3.79
11	23.41897	7.58	7.25	4.39
12	28.09859	8.13	7.73	4.93
13	5.61611	4.23	4.46	5.53
14	11.16288	5.94	5.54	6.69
15	13.49733	6.42	5.94	7.54
16	12.58347	5.33	5.79	8.56
17	7.48679	5.31	4.85	8.67
18	19.36570	7.44	6.77	8.95
19	3.72697	4.47	4.05	9.32

5.3 Inverse solution to meet specific need based requirement

Pseudo Pareto front suggests a boundary for setting simultaneous optimum MRR and ASR. This near exhaustive search meets almost all of the practical possible requirements of customer within the experimental domain. For each combination of optimum MRR and ASR, corresponding to each point of figure 5.2, a set of optimum machining control parameters (cur, t_{on}, and t_{off}) exists, though, it is difficult to set the exact value in real world EDM machine. So, near-optimum settings should be found out to get a particular MRR and ASR combination. Here, the inverse solution of this problem is outlined.

Maintaining a specific productivity, products with different quality are possible, that is to meet a particular MRR value, different ASR could be achieved. Lower ASR is always preferred. The pseudo Pareto front guides to select possible minimum ASR for a particular MRR value. Using equation (5.14), optimum ASR is found for a specific MRR requirement. Yet, setting of the machining control parameters (cur, t_{on}, and t_{off}) is to be determined to get the optimum combination of MRR and ASR. Thus, a back tracking is required. Power law model is therefore, chosen for the inverse solution.

Once, the desired value of MRR and corresponding estimated optimum value of ASR value are put in equations (5.5) and (5.6), it just becomes a set of two linear equations with three unknowns (cur, t_{on}, and t_{off}), and has infinite number of solutions. As, pulse off time (t_{off}) has lowest influence on the responses compared to current (cur) and pulse on time (t_{on}), some specific values might be set for this purpose. For the sake of simplicity, four available setting of t_{off} are chosen (50 μs, 100 μs, 150 μs and 200 μs). Putting each of the four values of t_{off}, the equations become a set of two equations with two unknowns and has one exact solution set. With four different values of t_{off}, four different sets of (cur and t_{on}) are found. Each of them yields the same specific MRR-ASR combination. However, out of range settings are just omitted for the lack of availability in machine settings.

As for example, to obtain MRR as 13.50951 mm^3/min, different ASR values are possible. Using pseudo Pareto front equation (5.14), lowest possible ASR value is found as 5.94 μm. The two values are then put in equations (5.5) and (5.6) to yield the equations (5.15) and (5.16).

$$\ln(13.50951) = -0.9421 + 1.5264 \ln(cur) + 0.4418 \ln(t_{on}) - 0.5176 \ln(t_{off}) \quad (5.15)$$
$$\ln(5.94) = -0.1080 + 0.5484 \ln(cur) + 0.1203 \ln(t_{on}) + 0.0238 \ln(t_{off}) \quad (5.16)$$

The equations have infinite number of solutions and so, we put either of 50 μs, 100 μs, 150 μs or 200 μs for t_{off}. In case of 50 μs, equations (5.15) and (5.16) become

$$\ln(13.50951) = -0.9421 + 1.5264 \ln(cur) + 0.4418 \ln(t_{on}) - 0.5176 \ln(50) \quad (5.17)$$
$$\ln(5.94) = -0.1080 + 0.5484 \ln(cur) + 0.1203 \ln(t_{on}) + 0.0238 \ln(50) \quad (5.18)$$

Equations (5.17) and (5.18) have an exact set of solution that is cur = 8.21 A and t_{on} = 207.43 μs. Other solutions obtained from putting pulse off time as 100 μs, 150 μs and 200 μs, the estimated combinations of cur and t_{on} are far away from available experimental settings of machining control parameters.

All 64 experimental values of MRR are set on pseudo Pareto front equation and corresponding optimum ASR are estimated. Following the above procedure, with four values of t_{off}, combinations of optimum cur and t_{on} are calculated. Some of the results within the experimental zone are listed in table 5.3. Nearest available machining control parameter settings and corresponding outcomes are compared with the solution from above mentioned back tracking steps.

Table 5.3 Validation of optimum machining control parameter settings

Sl. no.		cur (A)	t_{on} (μs)	t_{off} (μs)	MRR (mm^3/min)	ASR (μm)
1	Optimum	5.79	94.99	50.00	5.61611	4.46
	Experimental	6.00	100.00	50.00	5.48126	4.61
	Absolute error (%)	3.50	5.01	-	2.46	3.47
	SVM generated	6.00	100.00	50.00	5.08446	4.45
	Absolute error (%)	3.50	5.01	-	10.46	0.22
2	Optimum	5.80	89.48	50.00	5.48126	4.44
	Experimental	6.00	100.00	50.00	5.48126	4.61
	Absolute error (%)	3.33	10.52	-	-	4.55
	SVM generated	6.00	100.00	50.00	5.08446	4.45
	Absolute error (%)	3.33	10.52	-	7.80	0.22
3	Optimum	8.21	207.43	50.00	13.50951	5.94
	Experimental	9.00	200.00	50.00	12.58347	5.33
	Absolute error (%)	8.78	2.71	-	7.36	11.44
	SVM generated	9.00	200.00	50.00	12.98027	5.54
	Absolute error (%)	8.78	2.71	-	4.08	7.22

Sl. no.		cur (A)	t_{on} (μs)	t_{off} (μs)	MRR (mm^3/min)	ASR (μm)
4	Optimum	7.81	209.49	50.00	12.58347	5.79
	Experimental	9.00	200.00	50.00	12.58347	5.33
	Absolute error (%)	13.22	4.74	-	-	8.63
	SVM generated	9.00	200.00	50.00	12.98027	5.54
	Absolute error (%)	13.22	4.74	-	3.06	4.51
5	Optimum	8.60	204.80	50.00	14.41525	6.08
	Experimental	9.00	200.00	50.00	12.58347	5.33
	Absolute error (%)	4.44	2.40	-	14.56	14.07
	SVM generated	9.00	200.00	50.00	12.98027	5.54
	Absolute error (%)	4.44	2.40	-	11.05	9.75
6	Optimum	8.20	207.47	50.00	13.49733	5.94
	Experimental	9.00	200.00	50.00	12.58347	5.33
	Absolute error (%)	8.89	3.73	-	7.26	11.44
	SVM generated	9.00	200.00	50.00	12.98027	5.54
	Absolute error (%)	8.89	3.73	-	3.98	7.22
7	Optimum	12.10	200.22	50.00	24.03488	7.31
	Experimental	12.00	200.00	50.00	24.03488	7.38
	Absolute error (%)	0.83	0.11	-	-	0.95
	SVM generated	12.00	200.00	50.00	23.63808	7.59
	Absolute error (%)	0.83	0.11	-	1.68	3.69
8	Optimum	11.76	198.18	50.00	22.91674	7.19
	Experimental	12.00	200.00	50.00	24.03488	7.38
	Absolute error (%)	2.00	0.91	-	4.65	2.57
	SVM generated	12.00	200.00	50.00	23.63808	7.59
	Absolute error (%)	2.00	0.91	-	3.05	5.27
9	Optimum	12.37	201.93	50.00	24.95816	7.41
	Experimental	12.00	200.00	50.00	24.03488	7.38
	Absolute error (%)	3.08	0.96	-	3.84	0.41
	SVM generated	12.00	200.00	50.00	23.63808	7.59
	Absolute error (%)	3.08	0.96	-	5.58	2.37
10	Optimum	13.32	204.63	50.00	28.09859	7.73
	Experimental	15.00	200.00	50.00	28.09859	8.13
	Absolute error (%)	11.2	2.31	-	-	4.92
	SVM generated	15.00	200.00	50.00	27.70179	7.92
	Absolute error (%)	11.2	2.31	-	1.43	2.40
11	Optimum	11.91	199.07	50.00	23.41897	7.25
	Experimental	12.00	200.00	50.00	24.03488	7.38
	Absolute error (%)	0.75	0.46	-	2.56	1.76
	SVM generated	12.00	200.00	50.00	23.63808	7.59
	Absolute error (%)	0.75	0.46	-	0.93	4.48

Optimum machining control parameters lay within 15% of corresponding experimental setting and claim in favor of the practical applicability of this study.

Above proposed steps for power law model development, pseudo Pareto front generation and inverse solution for selection of nearest available machining control parameter settings to meet specific need-based MRR-ASR combination are given in figure 5.5.

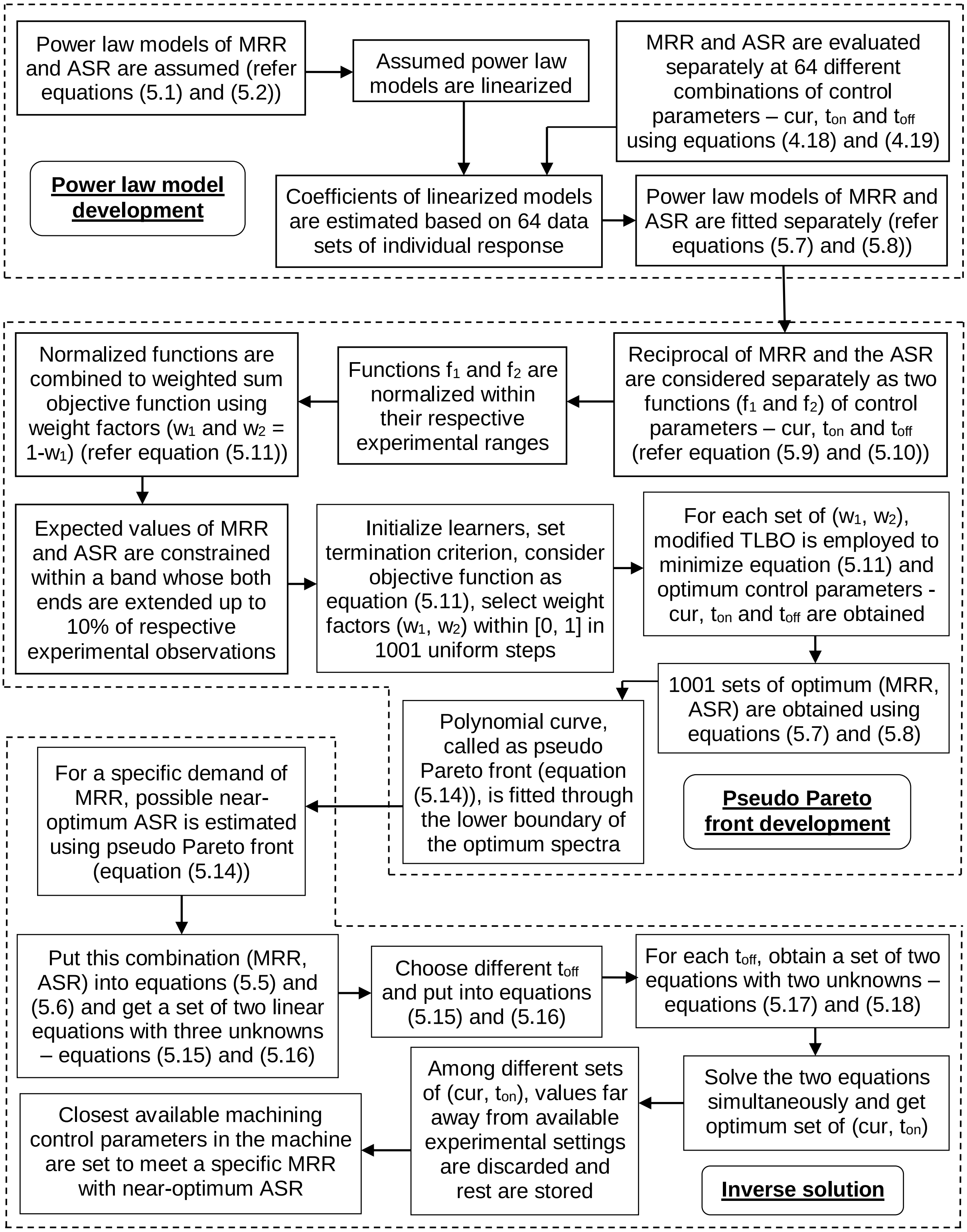

Fig. 5.5 Detailed steps in pseudo Pareto optimization and inverse solution for optimum available machining control parameter settings to meet specific MRR with near-optimum ASR

5.4 Summary

Conclusions drawn from the work presented in this chapter are listed as follows.

- Complex representation of SVM regression based learning system is taken as virtual data generator and simplified power law models (PLM) of process outcomes are developed for ready accessibility in shop-floor use.

- Pseudo Pareto front of two conflicting type EDM responses, MRR and ASR, would guide to achieve highest possible quality of surface without sacrificing the production rate.

- The inverse solution procedure helps for reverse mapping of process response to machining control parameters.

The proposed inverse solution procedure, a novel advancement in searching of near-optimum levels of machining control parameters to meet specific MRR-ASR combination in EDM process, would be applicable for pseudo Pareto optimization of conflicting process outcomes in any such process.

In last two chapters 4 and 5, irregular fluctuations are taken into account in building near-accurate representation of process outcomes and thereby setting of machining control parameters to meet specific need based optimum process outcomes is confirmed. Further investigation for the complex surface generation process is necessary (refer chapter 3). In the next chapter, a generalized structure is framed to reveal the underlying features of surface generation process in EDM through methodical assessment of machined surface topography.

CHAPTER 6

ASSESSMENT OF SURFACE TOPOGRAPHY

6.1 Introduction

In chapter 4, it is observed that insensitive zones wrapped around the estimated representative models of EDM process effectively capture the uncontrollable fluctuations in process outcomes. As, the process outcomes are results of some complex phenomena involved in mechanism of material removal, so, further investigation of surface generation process would be helpful for near-accurate representation of EDM process. Requirement of kernel function in intelligent modeling indicates the possibility of the presence of underlying features in high-dimensional space. Surface generated in EDM is a superposition of craters formed by series of discrete high frequency, high power density, spatial and sporadic electric discharges (sparks). Thus, mechanism of material removal is preserved in surface topography. Engraved features of erosion mechanism of parent machining operation could be postulated by analyzing the surface profiles.

In the present chapter, therefore, an organized approach is expounded to analyze the surface characteristics of electric discharge machined surface. Sequence diagram for assessment of surface topography is shown in figure 6.1. To start with, representative time series corresponding to each of the roughness profiles is generated by image analysis. The generated time series are used for characterization of machined surface topography. Contributive effects of randomness and periodicity in roughness profiles are assessed using autocorrelation function. Investigation for the presence of chaos in generated surface topography is performed next.

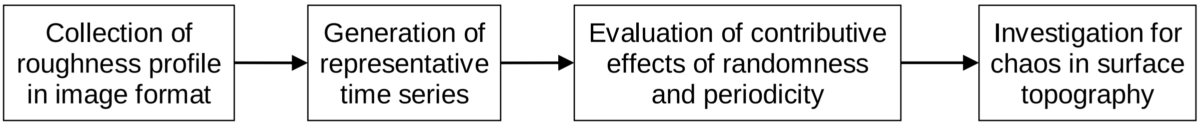

Fig. 6.1 Sequence diagram for assessment of surface topography in EDM process

6.2 Generation of representative time series of roughness profile

Roughness profiles of evaluation length 3.2 mm along three directions at 120^{o} apart, measured on each of the 64 machined surfaces, are collected in image format. For each of the combinations of different levels of cur, t_{on} and t_{off}, three images containing apparently erratic fluctuations of profile heights are stored. Sequence of peaks and valleys for each of the profiles is extracted by image analysis.

In the image of roughness profile, pixels along the roughness profile have distinct color. Hence, based on the color of pixel, identification of either peak or valley is done. A typical roughness profile measured along a specific direction on machined surface is presented in figure 6.2 in next page.

From figure 6.2, it is observed that grids along horizontal and vertical axes have different color than the fluctuating roughness profile. In the following image analysis, colors of all the pixels are stored in a matrix. Position of the horizontal zero line is identified. From this horizontal zero line, positions of other pixels are calculated. Ordinates of the pixels on roughness profile from this zero line give the corresponding profile heights. Scale is required to convert the pixel height from number of pixels to micron. Profile heights in micron are shown along vertical axis. Scale is evaluated from suitable choices of pixel heights on vertical axis. In figure 6.2, heights of the pixels corresponding to +50 µm and -50 µm from zero line are counted. From the two values, average value of each pixel in micron along vertical direction is estimated. This value is considered as scale factor in this image analysis.

Variations of profile heights at different locations along horizontal zero line are measured. Selection of the measurement locations is a critical issue in image analysis. Measurement locations at long gap may not capture the true fluctuating behavior of roughness profile. On the other hand, very close locations may gather redundant information. Hu et al. [209] studied the cross-scale behavior of runoff time series in an inland river of Central Asia. They concluded that time series having finer resolution would be able to reveal more complex underlying features of time series than coarser scales. In the present study, possible finest resolution is 8 µm. Hence, measurement of profile heights is done at locations of 8 µm apart. At a uniform gap of 8 µm along horizontal zero-reference line, measuring locations are decided. From the length of 3.2 µm long roughness profile, 401 measuring locations are set. At each location, colors of the pixels along vertical direction are checked. As pixels lying on roughness profile have a distinct color value, thus, corresponding pixel along vertical direction at each of the measuring locations is identified. Ordinate of the profile at the measuring location is calculated by multiplying the scale factor with the measured pixel height from zero line. This calculated value gives profile height in µm at this specific location. Similarly, profile heights at all 401 measuring locations are evaluated. Mean of all absolute values of 401 profile heights is calculated as 6.36 µm which deviates 0.93% from the value of average surface roughness shown in Talysurf (6.42 µm).

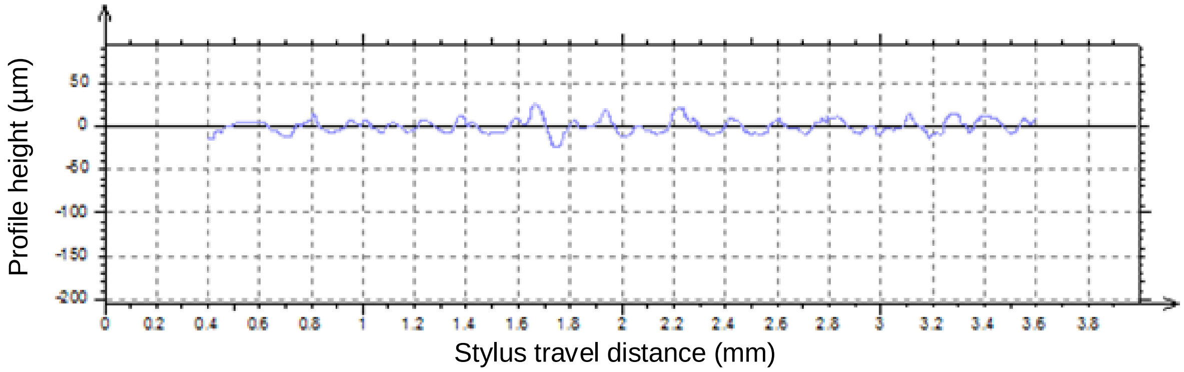

(a) Roughness profile (measured Ra = 6.42 µm)

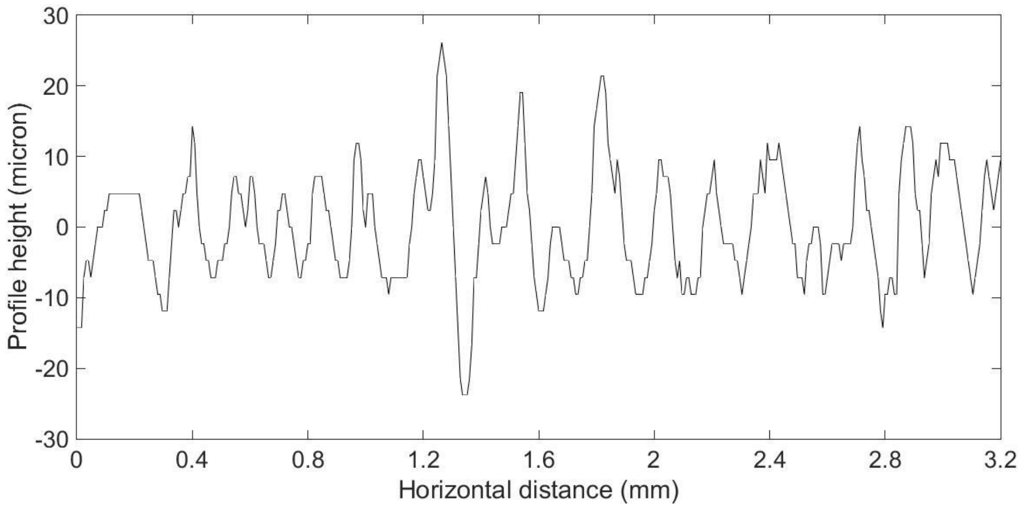

(b) Generated time series (estimated Ra = 6.36 µm)

Fig. 6.2 Roughness profile and corresponding generated representative time series (Treatment - cur = 12 A, t_{on} = 50 µs and t_{off} = 150 µs)

Thus, from the image of a roughness profile measured along a specific direction, a sequel of 401 ordinates is found. Average of the 401 absolute values gives the arithmetic average surface roughness of that machined surface in measured direction. It is found that for all 192 roughness profiles, calculated surface roughness value varies with 3% average error from the measured arithmetic average surface roughness (Ra) obtained from Talysurf.

Each sequence of ordinates is a collection of finite numerical data measured at uniform interval with one observation at a specific location on the machined surface. Therefore, the set of 401 ordinate values in successive order is considered as a finite time series presenting the corresponding roughness profile (figure 6.2). Steps for generation of time series from corresponding roughness profile are given in figure 6.3.

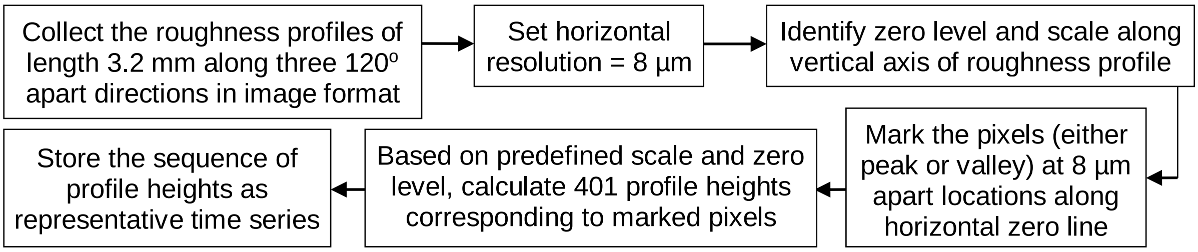

Fig. 6.3 Steps for generation of representative time series of roughness profile

The generated 192 representative time series are first used for the assessment of contributive effects of randomness and periodicity and then for evaluations for chaotic nature of surface topography.

6.3 Evaluation of contributive effects of randomness and periodicity

Autocorrelation function (ACF) is taken as an effective tool for comparative study of random and periodic behavior of the surface. Each of the ACF curves is assumed as a sum of multiple freely induced decays (FIDs) which are exponentially damped sinusoidal in nature. Parameters namely amplitude, decay rate, frequency and phase of FIDs are estimated by backward linear prediction method. With the estimated decay rate and frequency, characteristic correlation lengths and periods buried in the surface are calculated. Based on a non-dimensional index, periodicity to randomness ratio (PR ratio) is estimated. It is then, employed for comparing the relative effects of randomness and periodicity under different machining conditions. Variations of PR ratios and characteristic correlation lengths within and between treatments are studied through a non-parametric statistical test. The estimated PR ratios of EDM generated surfaces are further correlated with machining process parameters. The organized procedure for assessment of contributive effects of randomness and periodicity is shown in figure 6.4.

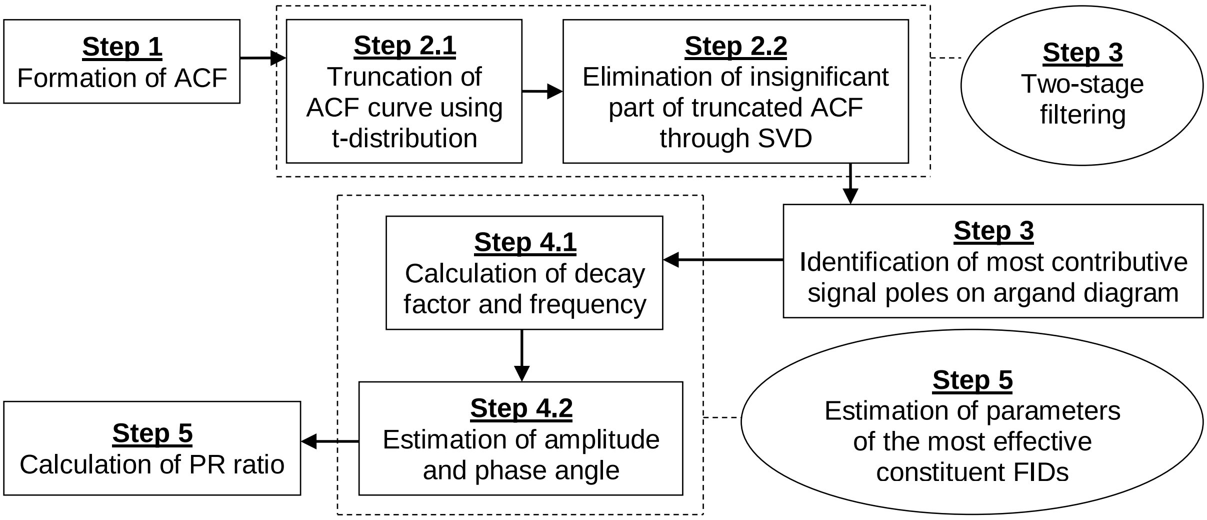

Fig. 6.4 Sequence diagram to calculate PR ratio for assessment of contributive effects of randomness and periodicity

6.3.1 Formation of ACF from time series

In the present study, ACF is chosen as representative of generated machined surface features. In this connection, autocorrelation function (ACF) for different lags (τ) are calculated from the discrete time series containing roughness profile information using the following formula [223].

$$\mathrm{ACF}(\tau)=\frac{\frac{1}{n}\sum_{i=1}^{n-\tau}(y_i-\bar{y})(y_i-\bar{y})}{\sigma^2}, \quad \tau=0(1)N-1 \tag{6.1}$$

where, n = number of profile heights collected, y_i = i^{th} profile height, $\bar{y}$ = mean of n profile heights and σ^2 = variance of n profile heights. This ACF could give an indication of expected relative relation between different zones of the time series. Typical ACF curves are shown in figure 6.5. i^{th} lag in mm is obtained by multiplying horizontal resolution, that is, 0.008 mm with corresponding lag τ_i.

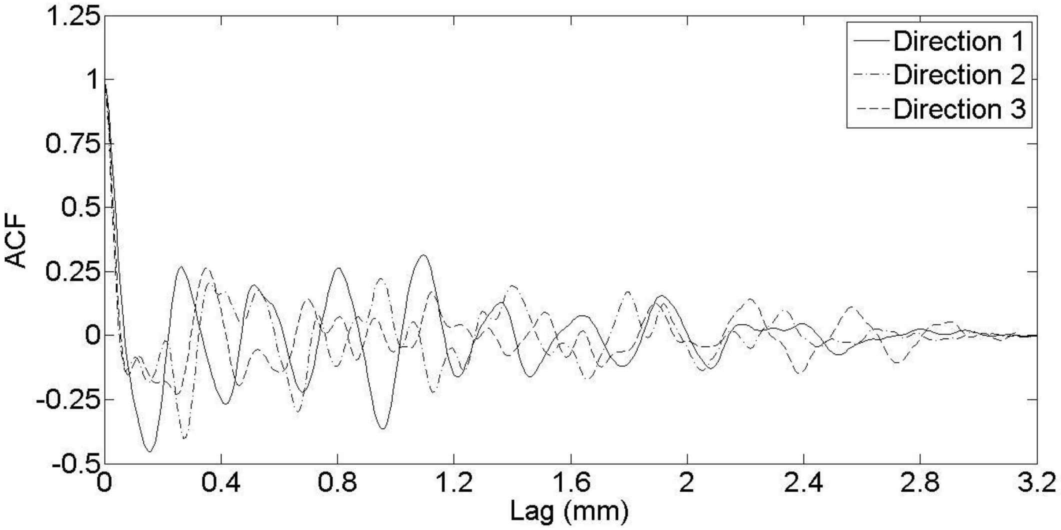

Fig. 6.5 Correlograms of roughness profiles measured along three directions (120° apart) on machined surface generated in the treatment - cur = 12 A, t_{on} = 150 μs and t_{off} = 150 μs

Autocorrelation function value indicates the extent of correlation present between two time series of same length collected from same parent time series separated by a definite lag value e.g. from a time series having length of 400 observations, two time series of length 300 are generated like one from observation 1 to 300 and another from observation 7 to 306. They are correlated with lag 6. Higher ACF value that is close to 1, implies that there might be high correlation between the two time series, whereas, close to mean value implies no such significant correlation existed between the time series. Therefore, significant correlation may not found beyond that lag where ACF values are damped close to their corresponding mean value. Hence, significant portion of each of the ACF curves is to be identified before further analysis.

6.3.2 Truncation of ACF curve

Values of autocorrelation function at different lags are calculated from the discrete time series. The generated discrete time series is a sample of total population consisting of profile peaks or valleys at some specific locations (8 μm apart) of the whole machined surface which is generated at a particular combination of levels of machining parameters. In practice, population mean and population variance are unknown. Yet, it could be estimated from sample statistics. Thus, sample mean ($\bar{x}$) and sample standard deviation (s) which are considered as mean and standard deviation of autocorrelation function are calculated. Following t-distribution, 99% confidence interval is identified about the mean value of ACF. Boundary values of the 99% confidence interval (CI) around mean value are marked using the following formula [210]

$$\mathrm{CI} = \bar{x} \pm t^{*}_{\alpha,v}\,\frac{s}{\sqrt{n}} \tag{6.2}$$

where, n = sample size (here n = 401), $t^*_{\alpha,v}$ is estimated from the probability density function of $t(\bar{x}, \frac{s}{\sqrt{n}})$ with degrees of freedom v = n - 1 and α is 0.005 for both sides. From available standard table, it is found that for v larger than 120, $t^*_{0.005,\infty} = 2.576$.

For each of the ACF curves, the lag value is marked beyond which fluctuation of ACF curve is completely damped within its corresponding confidence interval (CI) around mean value obtained from equation (6.2). Significance of this confidence interval is that with 99% confidence, it could be said that significant autocorrelation could be found up to this marked lag value. Hence, each of the ACF curves is trimmed off at their corresponding marked lag value. The remaining ACF values corresponding to lag zero to the marked one are stored. Only the truncated ACF curves are used for further analysis. Truncation of a typical ACF curve in direction 1 of figure 6.5 (refer table D.11) is presented in figure 6.6.

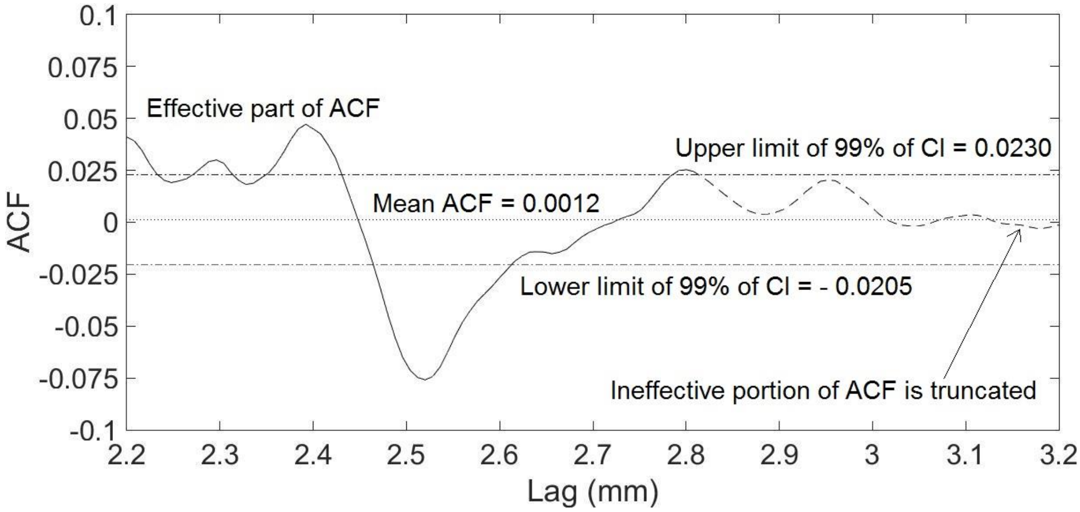

Fig. 6.6 Truncation of a typical ACF curve

6.3.3 Formulation of truncated ACF curve with constituent FIDs

Sharp falling of ACF curves to zero within 0.05 to 0.10 mm lag and then damped fluctuations around mean line (not necessarily zero) are observed as common features of correlograms (refer figure 6.5). Still, no such exact decay rate or period is observed. For pure random observations of a time series, ACF at lag zero is 1, after that a sharp fall towards mean value is observed. Whereas, for time series values with exact periodic nature, ACF exhibits damped periodic pattern with fixed period. Typical patterns of ACF curves, observed in the present study (refer figure 6.5), indicate the presence of both the features, random and periodic, at multiple levels in each ACF curve. Thus, a number of independent damped sinusoids might be buried.

Therefore, the truncated ACF is represented as a sum of multiple exponentially damped sinusoids with different decay rates and periods (equation (6.3)).

$$\mathrm{ACF}(\boldsymbol{\tau}) = \sum_{i=1}^{K} A_i e^{-\alpha_i \boldsymbol{\tau}} \cos(\omega_i \boldsymbol{\tau} + \varphi_i), \quad \boldsymbol{\tau} = 0(1)N-1 \tag{6.3}$$

where, $\boldsymbol{A}$, $\boldsymbol{\alpha}$, $\boldsymbol{\omega}$ and $\boldsymbol{\varphi}$ are amplitude, decay rate, angular frequency and phase angle (in radian) respectively. Decomposition of ACF curve to K free-induced-decay (FID) may provide a measurement of random and periodic behavior existed in the roughness profile. Decay rate of exponential term and frequency of trigonometric term of each FID would exhibit possible random and periodic features.

Hence, estimation of $\boldsymbol{A}$, $\boldsymbol{\alpha}$, $\boldsymbol{\omega}$ and $\boldsymbol{\varphi}$ from each of the truncated ACF curves are to be done to identify the expected random and periodic feature buried in it. Complex variable analysis is an efficient tool to solve this problem. Cosine term of equation (6.3) can be expressed as

$$\cos(\omega_i \boldsymbol{\tau} + \varphi_i) = \text{Real } e^{j(\omega_i \boldsymbol{\tau} + \varphi_i)}, \quad j = \sqrt{-1} \tag{6.4}$$

As, all ACF values are real and no imaginary values are present, equation (6.3) is rewritten as [224]

$$\mathrm{ACF}(\boldsymbol{\tau}) = \sum_{i=1}^{K} A_i e^{-\alpha_i \boldsymbol{\tau}} \; e^{j(\omega_i \boldsymbol{\tau} + \varphi_i)} \tag{6.5}$$

Further, variable and constant parts with respect to $\boldsymbol{\tau}$ of equation (6.5) are separated.

ACF($\boldsymbol{\tau}$) = $\sum_{i=1}^{K} \mathrm{CA_i}\, \mathrm{SP_i}$ (6.6)

where, $\mathrm{CA_i} = \mathrm{A_i} e^{j\varphi_i}$ and $\mathrm{SP_i} = e^{(-\alpha_i + j\omega_i)\boldsymbol{\tau}}$

Autocorrelation function (ACF) is thus represented as sum of K FIDs and each FID is expressed as a product of constant "complex amplitude" (***CA***) and variable "signal pole" (***SP***) terms [225]. The unknown coefficients of ***CA*** and ***SP*** are to be estimated from the truncated ACF curves.

Complexity of the nonlinear behavior of equation (6.6) causes the estimation of unknown coefficients troublesome. This problem is circumvented by employing linear prediction with singular value decomposition (LPSVD) technique. There are two types of linear prediction techniques namely forward and backward. For stable response, in backward prediction method, only significant signal poles lie outside the unit circle and insignificant ones lie inside. Whereas, in forward prediction, no such clear boundary between signal poles could be drawn [226]. As, significant FIDs are need to be picked out, thus, backward prediction should be more feasible one in the present work.

6.3.4 Extraction of significant FIDs

In the backward linear prediction with predictor order L, ACF($\boldsymbol{\tau}$) is expressed as a linear combination of its L succeeding values. N-L equations are generated. Then, prediction coefficients d_is are to be estimated.

ACF($\boldsymbol{\tau}$) = $\sum_{i=1}^{L} \mathrm{d_i} \mathrm{ACF}(\boldsymbol{\tau} + \mathrm{i})$, $\boldsymbol{\tau}$=1(1)N-L (6.7)

Left-side of equation (6.7), ACF($\boldsymbol{\tau}$), will form a Hankel matrix ***H*** of order N-L x L. Choice of predictor order (L) plays a crucial role in prediction accuracy. Near the lower values of L where L< K cannot be able to dig the most effective signals out. Whereas, at the higher side of L values where L > N/2 may include more insignificant signals to significant zone [225]. Hence, a judicious selection is L ≤ rank of Hankel matrix (***H***). For L > 0.5N, this condition will not be satisfied. Therefore, L is selected as the largest integer ≤ 0.5N. It is expected that number of most effective FIDs are far below L.

Different algebraic techniques are available to calculate d_is. Techniques using inverse operation would not be a robust choice because value of N/2 may differ from L and for large data set, computation time will be too high. In this regard, singular value decomposition (SVD), a signal-subspace technique could be implemented to avoid the cumbersome inverse operation. Besides, rank-revealing feature of SVD [224] may help to identify the most significant FIDs.

Singular value decomposition of ***H*** (equation (6.8)) gives a set of singular values arranged in descending order along principal diagonal of $\boldsymbol{S^H}$.

$\boldsymbol{H}_{(\text{n-L x L})} = \boldsymbol{U^H}_{(\text{n-L x n-L})} \boldsymbol{S^H}_{(\text{n-L x L})} (\boldsymbol{V^H}_{(\text{L x L})})^{T}$ (6.8)

Number of singular values not exceedingly close to zero is one guideline for determining the rank of H. Here, a gradual monotonically decreasing pattern of singular values is observed. Singular values below 10% of S^H_{max} are considered (refer table D.12) as it may not provide any such significant information regarding the features of machined surface. Corresponding to those singular values, respective parts of $\boldsymbol{U^H}$ and $\boldsymbol{V^H}$ are separated. Insignificant part of ***H***, that is, $\boldsymbol{H}_{insign}$ is enumerated as

$\boldsymbol{H}_{\text{insign (N-L x L)}} = \boldsymbol{U^H}_{\text{insign (N-L x N-L)}} \boldsymbol{S^H}_{\text{insign (N-L x L)}} (\boldsymbol{V^H}_{\text{insign (L x L)}})^{T}$ (6.9)

$\boldsymbol{H}_{\text{insign (N-L x L)}}$ is Hankelized by averaging the anti-diagonal elements and ACF($\boldsymbol{\tau}$)$_{insign}$ is constructed.

ACF($\boldsymbol{\tau}$)$_{sign}$ = ACF($\boldsymbol{\tau}$) - ACF($\boldsymbol{\tau}$)$_{insign}$ (6.10)

Hence, truncated ACF($\boldsymbol{\tau}$) is modified by subtracting ACF($\boldsymbol{\tau}$)$_{insign}$ (refer table D.11). Separation of corresponding ACF($\boldsymbol{\tau}$)$_{sign}$ and ACF($\boldsymbol{\tau}$)$_{insign}$ of a typical truncated ACF curve (refer figure 6.6) is shown in figure 6.7.

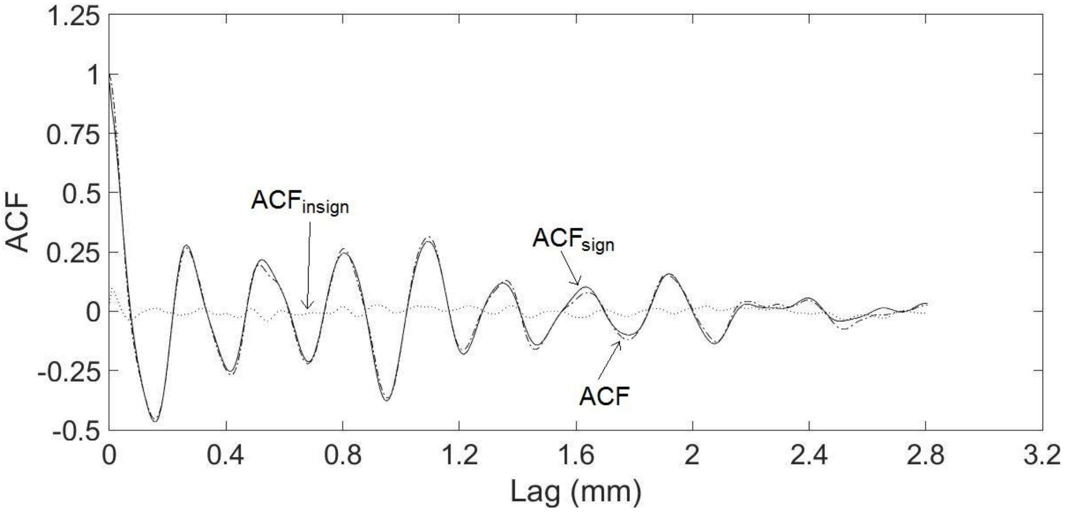

Fig. 6.7 Separation of $ACF(\boldsymbol{\tau})_{sign}$ and $ACF(\boldsymbol{\tau})_{insign}$ of a typical truncated ACF curve

The $ACF(\boldsymbol{\tau})_{sign}$ is decomposed with the help of corresponding significant parts of $\boldsymbol{U^H}$ or $\boldsymbol{U^H}_{sign}$, of $\boldsymbol{S^H}$ or $\boldsymbol{S^H}_{sign}$ and of $\boldsymbol{V^H}$ or $\boldsymbol{V^H}_{sign}$. Then, parameters, $\boldsymbol{A}$, $\boldsymbol{\alpha}$, $\boldsymbol{\omega}$ and $\boldsymbol{\varphi}$, of constituent significant FIDs of $ACF(\boldsymbol{\tau})_{sign}$, are estimated. First, parameters of signal poles, α_is and ω_is, are determined and other two parameters related to complex amplitude, A_is and φ_is, are found by substituting the values of estimated "signal pole" SP_is in equation (6.6).

6.3.4.1 Estimation of *α* and *ω*

Backward linear prediction coefficients d_is are estimated using the following formula.

$$\boldsymbol{d}_{(L \times 1)} = \boldsymbol{V^H}_{sign\ (N-L \times N-L)} \left(\boldsymbol{S^H}_{sign\ (N-L \times L)} \left(\left(\boldsymbol{U^H}_{sign\ (L \times N-L)}\right)^T ACF(\boldsymbol{\tau})_{sign\ (N-L \times 1)}\right)\right) \quad (6.11)$$

Decay rate ($\boldsymbol{\alpha}$) and angular frequency ($\boldsymbol{\omega}$) of FIDs encoded in prediction coefficients (d_is) are extracted from the following polynomial [227].

$$\boldsymbol{R}^L - \sum_{i=1}^{L} d_i \boldsymbol{R}^{L-i} = 0 \quad (6.12)$$

Roots of the equation (6.12) will give the signal poles of truncated significant ACF. Roots of the equation (6.12) are calculated and plotted on argand diagram. For a typical set of d_is (corresponding to figure 6.7), obtained roots R^is are shown in figure 6.8 (refer table D.13).

In figure 6.8, it is observed that most of the L roots (R^is) lie inside the unit circle drawn in the complex plane. Backward linear prediction technique is employed for estimation of signal poles due to its exclusive capability to classify the estimated poles. The most contributive signal poles, which lie outside the unit circle (distance from origin greater than one unit), are to be selected. As signal poles, lie outside the unit circle contain complex conjugates, signal poles found in 1st quadrant and outside the unit circle are marked (figure 6.8). The marked signal poles are considered for identifying the most effective FIDs.

Natural logarithms of the marked poles (refer table D.13) are taken.

$$R_i' = \ln(R^i_{outside}) \quad (6.13)$$

Real and imaginary part of R_i's give decay rate (α_i) and angular frequency (ω_i) respectively.

$$\alpha_i = \mathrm{Real}(R_i'),\ \omega_i = \mathrm{Imag}(R_i') \quad (6.14)$$

From estimated angular frequencies (ω_is), length of the periods in mm are calculated as follows (horizontal resolution 8 µm).

$$\lambda_i = 0.008\,\frac{2\pi}{\omega_i} \qquad (6.15)$$

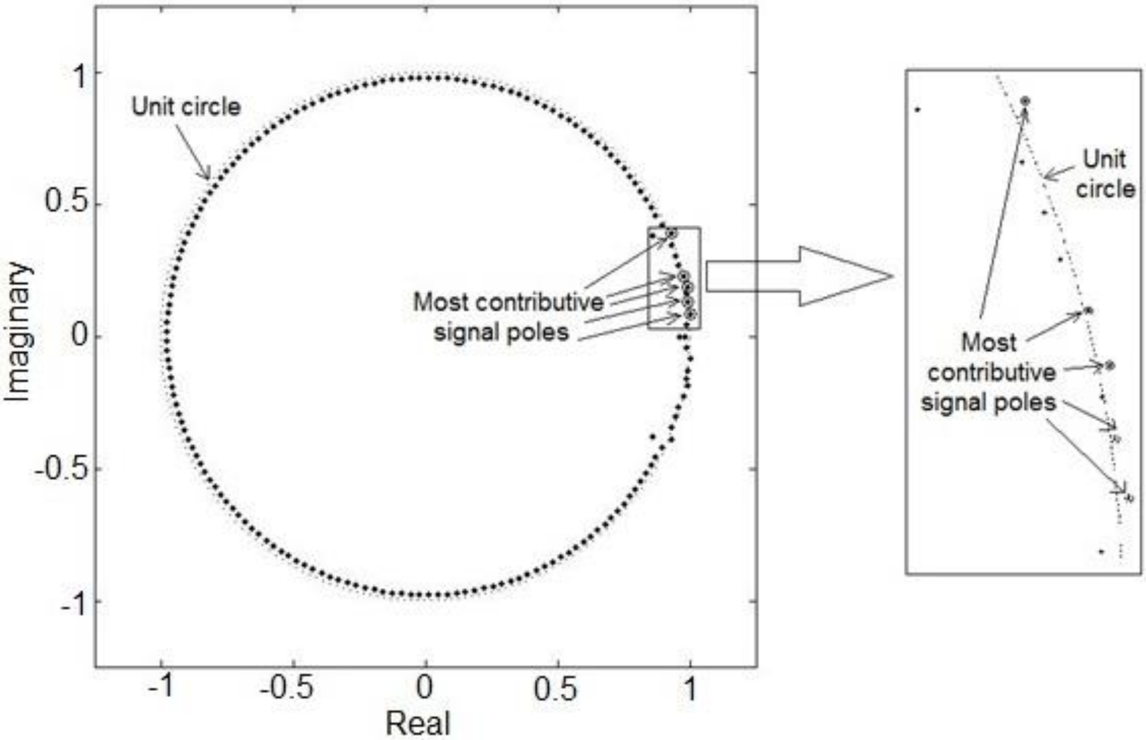

Fig. 6.8 Argand diagram of roots (***R***) of equation (6.12) consisting of d_is obtained from a typical ACF_{sign} curve

Values of ***λ*** greater than 1 mm are discarded. Finally, the FIDs having λ_i < 1 mm are considered as most effective and corresponding α_is are picked out. For each of the 3 replications of 64 treatments comprising of different levels of machining control parameters, namely current, pulse on time and pulse off time, the most contributive FIDs are identified. Number of FIDs buried in a particular roughness profile varies from 2 to 15. To represent the behavior of each FID, along with the estimated α_is and ω_is, other two coefficients A_is and φ_is of equation (6.3) are to be determined.

6.3.4.2 Estimation of *A* and *φ*

Most effective signal poles SP_is are thus found. With the known values of SP_is, equation (6.6) becomes a system of simultaneous linear equations with unknown coefficients CA_is. To avoid the unacceptable rounding errors in inverse operation, the unknown coefficients (CA_is) are estimated through a stable linear least square technique [224, 225].

Using linear least square technique, values complex amplitude CA_is are estimated. From the estimated values of CA_is, amplitude and phase angles are extracted. Using the polar form in complex variable, A_is and φ_is are calculated using the following formulae.

$$A_i = 2 \text{ x modulus } (CA_i) \qquad (6.16a)$$
$$\varphi_i = \text{angle } (CA_i) \qquad (6.16b)$$

Hence, with all the estimated A_i, α_i, ω_i and φ_is for each of the ACF curves, respective FIDs could be reconstructed. Set of FIDs of a typical ACF_{sign} curve (refer figure 6.7) is shown in figure 6.9 and estimated parameters of those FIDs, A_i, α_i, ω_i and φ_i, are given in table 6.1.

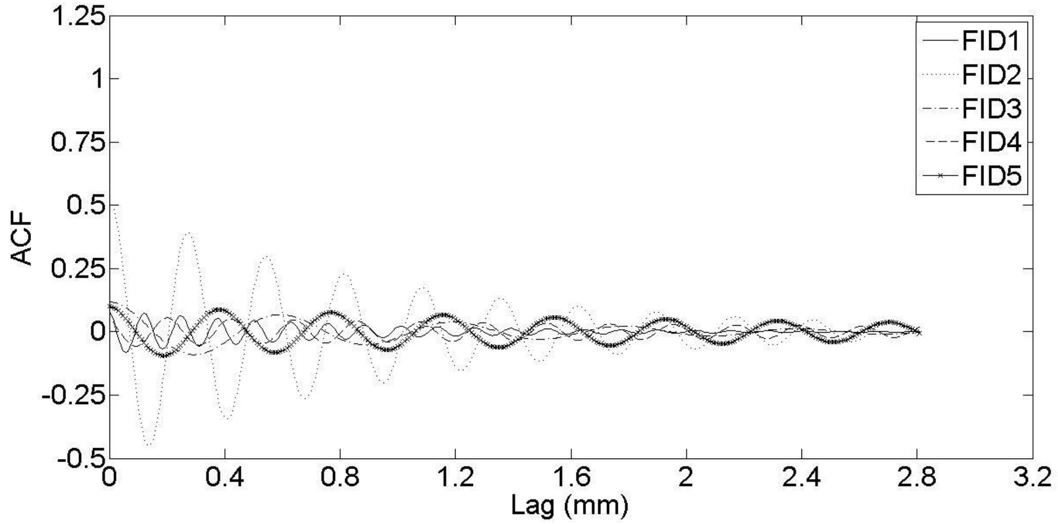

Fig. 6.9 The most effective constituent FIDs of a typical ACF_{sign} curve

Table 6.1 Estimated parameters of the most effective constituent FIDs of a typical ACF_{sign} curve

FIDs	Parameters of the most effective constituent FIDs			
	A	***α***	***ω***	***φ***
FID1	0.1139	0.0146	0.3966	0.2269
FID2	0.1264	0.0079	0.0846	-0.1022
FID3	0.5252	0.0079	0.1852	-0.0272
FID4	0.1202	0.0038	0.1302	0.0350
FID5	0.0579	0.0028	0.2290	0.6100

All the above steps are summarized in the flow chart in figure 6.10 in next page.

6.3.5 Results

Parameters of buried FIDs are estimated and respective FIDs of that roughness profile are constructed. From the estimated parameters, α_is and ω_is, extent of randomness and periodicity present in the underlying FIDs could be understood. In the next subsection, relative contributions of randomness and periodicity on surface characteristics are evaluated using a non-dimensional index, PR ratio, and variations of PR ratios with different levels of machining control parameters are discussed. Further, representative model for average PR ratio is developed.

6.3.5.1 Calculation of PR ratio

Each of the FIDs for a particular roughness profile has its own set of (***A***, ***α***, ***ω*** and ***φ***). Therefore, different decay rates and angular frequencies are buried on the surface. Exponential part of equation (6.3) provides information regarding randomness. Here, a measurement of randomness called as correlation length (***β***) is considered. Correlation length is the minimum lag after which profile heights are not correlated further as the random events die out. Correlation length is calculated (in mm) as the length along ***τ*** axis, at which exponential part falls down to 10% of its maximum initial amplitude (equation (6.17), horizontal resolution 8 µm) [190]. Higher value of β_i claims in favor of random characteristics of surface.

$$A_i e^{-0.008\alpha_i\beta_i} = \frac{A_i}{10} \tag{6.17}$$

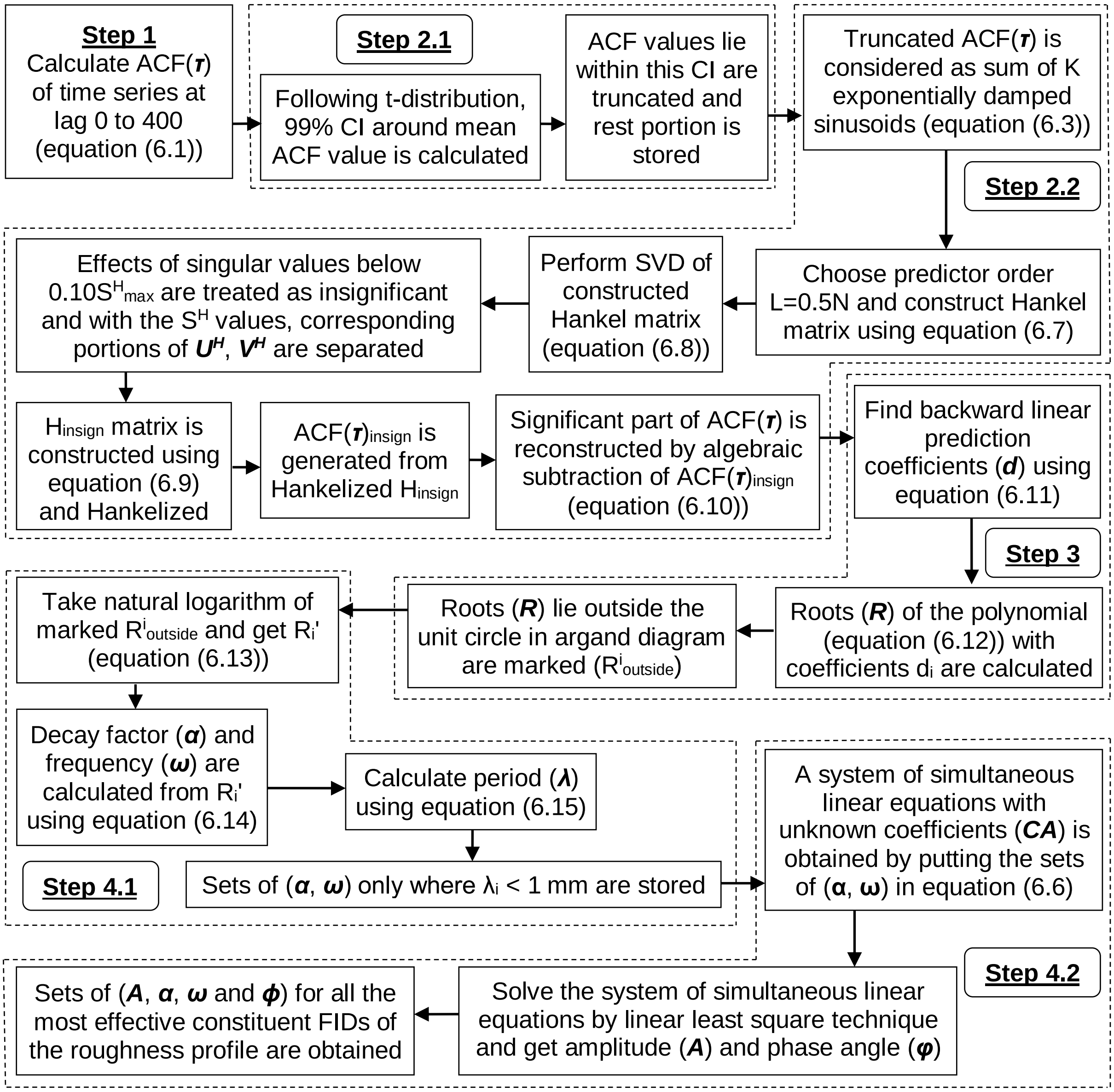

Fig. 6.10 Detailed steps for estimation of parameters of the most effective constituent FIDs of representative time series

As, each of the roughness profiles is found as summation of multiple FIDs, so, multiple sets of (***β***, ***λ***) exist in each of the roughness profile (refer table D.14). To compare the relative contributions of randomness and periodicity, a non-dimensional index, periodicity to randomness ratio (PR ratio), is considered [193].

$$\text{PR ratio of } i^{th} \text{ FID} = \frac{\lambda_i}{\beta_i} \tag{6.18}$$

Lower PR ratios of FIDs of a particular surface mean large correlation length and small period. It indicates the presence of wide band of random fluctuation and small repetition distance in the surface.

6.3.5.2 Variations of PR ratios with different treatments

To depict the variations of PR ratios, PR ratio vs $\boldsymbol{\lambda}$ plots are drawn for roughness profiles. For each of the treatments, comprising of different combinations of different levels of current, pulse on time and pulse off time, three surface profiles are collected. Following the above steps, for each setting of (cur, t_{on} and t_{off}), three sets of (PR ratio, $\boldsymbol{\lambda}$) are obtained corresponding to three directions. All the three sets are taken together and shown in a single PR ratio vs $\boldsymbol{\lambda}$ plot (figure 6.11).

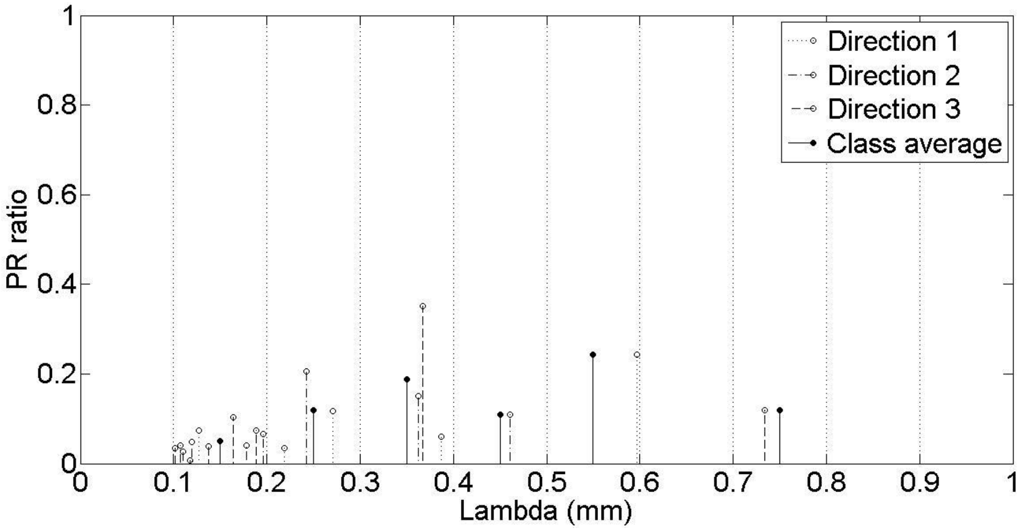

Fig. 6.11 Obtained PR ratios in all three directions and class averages
(Treatment - cur = 12 A, t_{on} = 150 µs and t_{off} = 150 µs)

Along the $\boldsymbol{\lambda}$ axis, 10 equi-length classes are marked. Mean value of all PR ratios corresponding to the λ_is fall in each class are calculated (refer table D.14). Mean PR ratio is considered as a representative index of that $\boldsymbol{\lambda}$-zone and is drawn at mid-value of that class (figure 6.11). With this scheme of representation, variations of mean PR ratios of different classes with change in levels of current, pulse on time and pulse off time are plotted (refer figure C.1 through C.4 in appendix C).

In overall, a very low PR ratio is observed in figures C.1 through C.4. Near zero PR ratio claims large correlation length ($\boldsymbol{\beta}$) that means random characteristics of machined surface continues over a long distance. Thus, randomness predominates on the surface topography and thereby in surface development process.

6.3.5.3 Contributive effects of machining control parameters on randomness

In the present study, main objective is to explore the irregular features of the surface caused by the complex erosion mechanism of the concerned machining operation EDM. Thus, a further study is done to estimate the contributive effects of different machining control parameters, current, pulse on time and pulse off time, on random characteristics of machined surface. Characteristic correlation length ($\boldsymbol{\beta}$) of surface is chosen as a measure of randomness present on the surface. For each of the surface profiles, multiple β_is are found. To perform the analysis of variance, a representative measure for each of the replications should be identified and all of which together are expected to follow normal distribution. Different measures like maximum, mean of all β_is found in each profile, etc. are checked but normality condition is not satisfied at all. Therefore, non-parametric statistical test [228] is considered.

In non-parametric statistical test, to bypass the necessity of normality condition, a rank is assigned to each of the β_is instead of using their original values. For ranking purpose, at first, β_is corresponding to all 192 profiles are listed together. Total 1399 β_is are found. All the listed β_is are sorted and ranked in ascending order. Larger β_i gets higher rank. Ascending order is selected because large β_i indicates high randomness. Hence, each profile gets a set of rank values (not necessarily consecutive ranks) in place of β_is. For each of the profile, mean of the assigned ranks is calculated and stored as an index of that profile (refer table D.14). With this mean rank values calculated for each replication of each of the treatments, analysis of variance is performed in the same way as for parametric test. Results are shown in table 6.2.

Table 6.2 Analysis of variance for mean rank

	Sum of squares	% effect	DOF	Mean squares	Test statistic	$F^*_{0.05}$ value
cur	7286.1776	0.23	3	2428.7259	0.1469	2.65
t_{on}	28460.8970	0.89	3	9486.9657	0.5737	2.65
t_{off}	10840.1254	0.34	3	3613.3751	0.2185	2.65
cur X t_{on}	247052.2375	7.70	9	27450.2486	1.6600	1.93
cur X t_{off}	100519.8543	3.13	9	11168.8727	0.6754	1.93
t_{on} X t_{off}	210096.2128	6.55	9	23344.0236	1.4117	1.93
cur X t_{on} X t_{off}	486877.8411	15.18	27	18032.5126	1.0905	1.52
Between treatments	1091133.3457	34.02	63	17319.5769	1.0474	
Within treatment	2116577.2381	65.98	128	16535.7597		
Total	3207710.5838		191			

It is observed from table 6.2 that contributive effects of each of the machining control parameters (cur, t_{on} and t_{off}), two factor interactions and three factor interaction are not significant at 95% confidence level. Total contribution of between treatments compared to variation within treatment is significantly lower. Contributive effect of variation within treatment on total variations is found as 66% which implies randomly dispersed observations among replications within a specific treatment [210]. Relatively large variation within treatment concludes that spatial distribution of the features of machined surface are highly random in nature.

All the above steps for calculation of PR ratio, to study the variations of PR ratios with different treatments and to analyze the contributive effects of machining control parameters on randomness are summarized in figure 6.12.

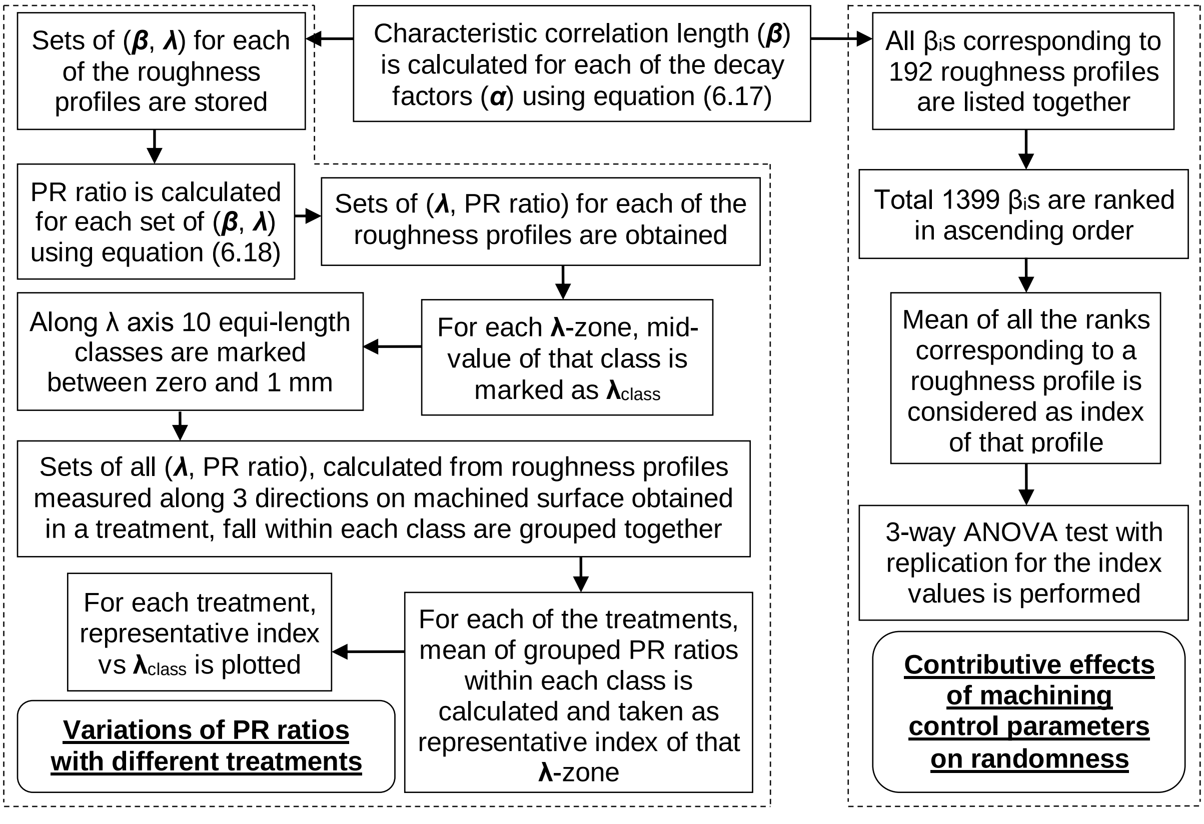

Fig. 6.12 Detailed steps for calculations of variations of PR ratios with different treatments and contributive effects of machining control parameters on randomness

6.3.5.4 Development of correlation between PR ratio$_{avg}$ and machining control parameters

Dominance of randomness over periodicity in surface topography of EDM generated surface for different combinations of levels of machining control parameters, cur, t_{on} and t_{off}, is revealed (refer subsection 6.3.5.2). Even, no significant contributive effects of machining control parameters on randomness are noticed in subsection 6.3.5.3. Therefore, a relationship between machining control parameters and PR ratio is built up for verification of the influence of machining control parameters on the change in values of PR ratio.

Here, a mathematical approach is taken to build a representative model of PR ratio with current (cur), pulse on time (t_{on}) and pulse off time (t_{off}) as input parameters. Due to axis independence, affine invariance and tractable computation, Bezier hyper-surface with Bernstein function as blending function [229] is found as compatible in this regard.

For each of the 64 mutually exclusive combinations of levels of machining control parameters, cur, t_{on} and t_{off}, all PR ratios along three directions are listed. From the listed values of PR ratios, average PR ratio (PR ratio$_{avg}$) is estimated for each of the combinations of different levels of machining control parameters (refer table D.15). As for example, at cur = 12 A, t_{on} = 150 µs and t_{off} = 150 µs, all PR ratios along three directions are listed (refer table D.14). From the list of PR ratios, PR ratio$_{avg}$ is calculated as 0.0972 (refer table D.15).

Vector valued parametric equation of Bezier hyper-surface (BHS) is given as follows [229].

$$\mathrm{BHS}(\boldsymbol{u},\boldsymbol{v},\boldsymbol{w}) = \sum_{i=1}^{m}\sum_{j=1}^{n}\sum_{k=1}^{p} \mathrm{B}_{i-1,m-1}(\boldsymbol{u})\mathrm{B}_{j-1,n-1}(\boldsymbol{v})\mathrm{B}_{k-1,p-1}(\boldsymbol{w})\, \mathrm{x}_{i,j,k} \tag{6.19}$$

where, $\mathrm{BHS}(\boldsymbol{u},\boldsymbol{v},\boldsymbol{w}) = [\mathrm{cur}(\boldsymbol{u},\boldsymbol{v},\boldsymbol{w})\quad t_{on}(\boldsymbol{u},\boldsymbol{v},\boldsymbol{w})\quad t_{off}(\boldsymbol{u},\boldsymbol{v},\boldsymbol{w})\quad \mathrm{PR\ ratio}_{avg}(\boldsymbol{u},\boldsymbol{v},\boldsymbol{w})]$,

$\boldsymbol{u}$, $\boldsymbol{v}$, $\boldsymbol{w}$ are parameters along three dimensions of corresponding machining control parameters namely cur, t_{on} and t_{off}

$\boldsymbol{u}, \boldsymbol{v}, \boldsymbol{w} \in [0,1]$,

m, n, p are number of control points along three dimensions $\boldsymbol{u}$, $\boldsymbol{v}$, $\boldsymbol{w}$ (here, m=n=p=4),

$B_{i-1,m-1}(\boldsymbol{u})$, $B_{j-1,n-1}(\boldsymbol{v})$, $B_{k-1,p-1}(\boldsymbol{w})$ are Bernstein basis functions with relations

$B_{i-1,m-1}(\boldsymbol{u}) = {}^{m-1}C_{i-1}\, \boldsymbol{u}^{i-1}(1-\boldsymbol{u})^{m-i}$,

$B_{j-1,n-1}(\boldsymbol{v}) = {}^{n-1}C_{j-1}\, \boldsymbol{v}^{j-1}(1-\boldsymbol{v})^{n-j}$,

$B_{k-1,p-1}(\boldsymbol{w}) = {}^{p-1}C_{k-1}\, \boldsymbol{w}^{k-1}(1-\boldsymbol{w})^{p-k}$

and $x_{i,j,k}$ is the control point on hyper-surface.

Now, putting the values of PR ratio$_{avg}$ in equation (6.19), vector valued parametric form of PR ratio$_{avg}$ is obtained as

$$\mathrm{PR\ ratio}_{avg}(\boldsymbol{u},\boldsymbol{v},\boldsymbol{w}) = \sum_{i=0}^{3}\sum_{j=0}^{3}\sum_{k=0}^{3} a_{i,j,k}\, \boldsymbol{u}^{i}\boldsymbol{v}^{j}\boldsymbol{w}^{k} \tag{6.20}$$

where, $a_{i,j,k}$ is coefficient of parametric equation of PR ratio$_{avg}$ (refer table D.16) and $\boldsymbol{u}, \boldsymbol{v}, \boldsymbol{w}$ are computed as follows.

$$u_i = \frac{\mathrm{cur}-6}{15-6},\ v_j = \frac{t_{on}-50}{200-50} \text{ and } w_k = \frac{t_{off}-50}{200-50} \tag{6.21}$$

To depict the effects of change in values of machining control parameters on PR ratio$_{avg}$, the bi-cubic Bezier surfaces are generated and presented in figure 6.13 through 6.15.

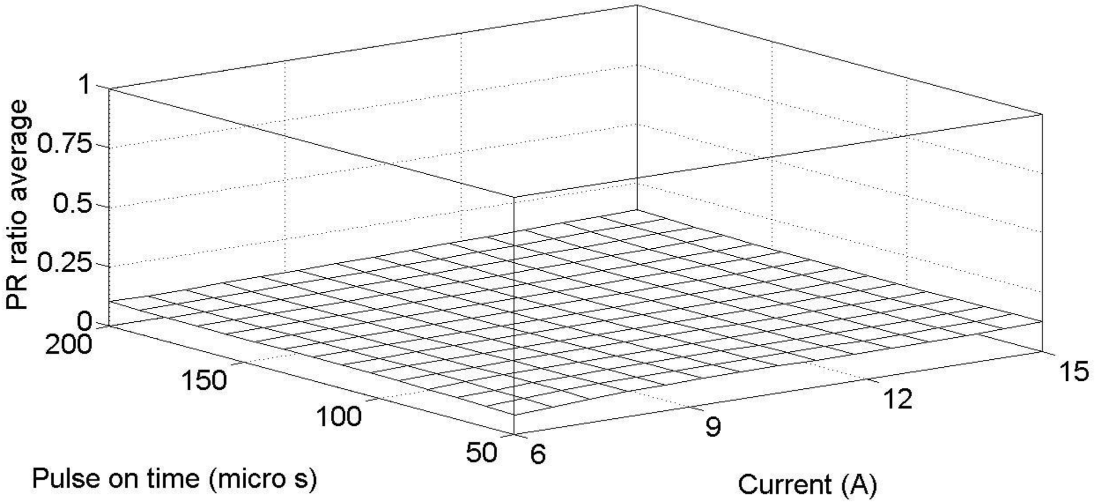

Fig. 6.13 Bi-cubic Bezier surface for PR ratio$_{avg}$ at t_{off} = 125 µs

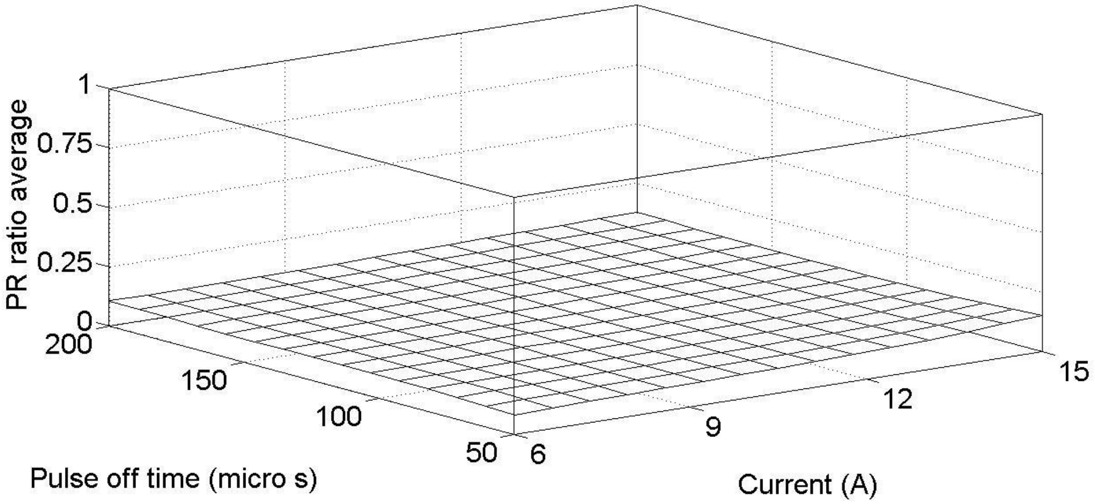

Fig. 6.14 Bi-cubic Bezier surface for PR ratio$_{avg}$ at t_{on} = 125 µs

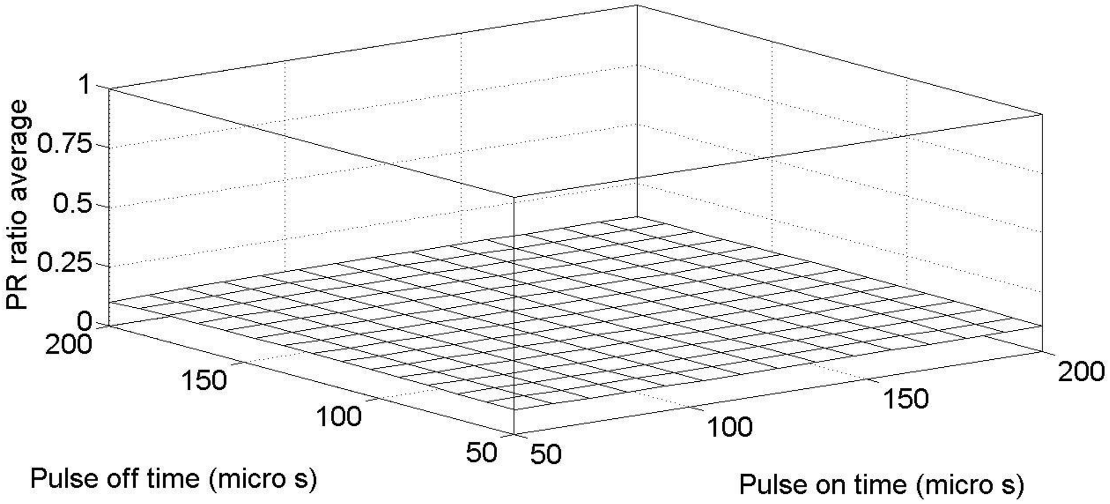

Fig. 6.15 Bi-cubic Bezier surface for PR ratio$_{avg}$ at cur = 10.5 A

Variations of PR ratio$_{avg}$ are found within the range between 0.0534 and 0.1797 which is almost 12.63% of the possible total range [0,1] of PR ratio. From figure 6.13 through 6.15, it is observed that there is as such no remarkable influence of different levels of any of the three machining control parameters, current, pulse on time and pulse off time, or their interactions on the values of PR ratio$_{avg}$. The insignificant impacts of machining control parameters on PR ratio$_{avg}$ indicate that EDM generated surface topography is predominantly random in nature. As randomness in surface topography predominates, surface topography might be chaotic in nature. In the next section, a logical investigation for the presence of chaos in surface topography is conducted.

6.4 Investigation for chaos in surface topography

In the last section, predominance of randomness in EDM generated surface topography is confirmed. The word "random" is commonly used for the system having seemingly irregular fluctuations in output variable. In the branch of science that deals with nonlinear dynamics of system, behavior of system during evolution and final outcome are the two most important aspects. Based on final outcome, a system would be either predictable or unpredictable. On the other hand, evolution of dynamic system either follows a governing law or not. If the evolution of a dynamic system follows a governing law, then, it is obvious that evolutionary pattern exhibits sensitive dependence on initial condition. A small perturbation in initial state will cause almost impossible rendering of long-term prediction [206, 230] leading to chaos. If it does not follow a governing law, the evolution is chaotic by itself [206, 230].

Compared to the definition of chaos, it is easier to describe the properties of a system as chaotic [231, 232]. A dynamic system having almost predictable outcome, that is, a regular system has a clear distinction from chaotic system. Chaotic system is always unpredictable. Since the pioneer work of Lorenz [206] on chaotic dynamics, different mathematical and statistical approaches are devised by researchers to comment on the underlying dynamics of various practical problems. In section 6.3, predominance of randomness in surface topography is observed. Therefore, to gain further insight into the surface topography, test for chaos is required.

In the present section, an organized procedure is structured to investigate the possibility of presence of chaos in EDM generated surface topography using representative time series and two different approaches (figure 6.16).

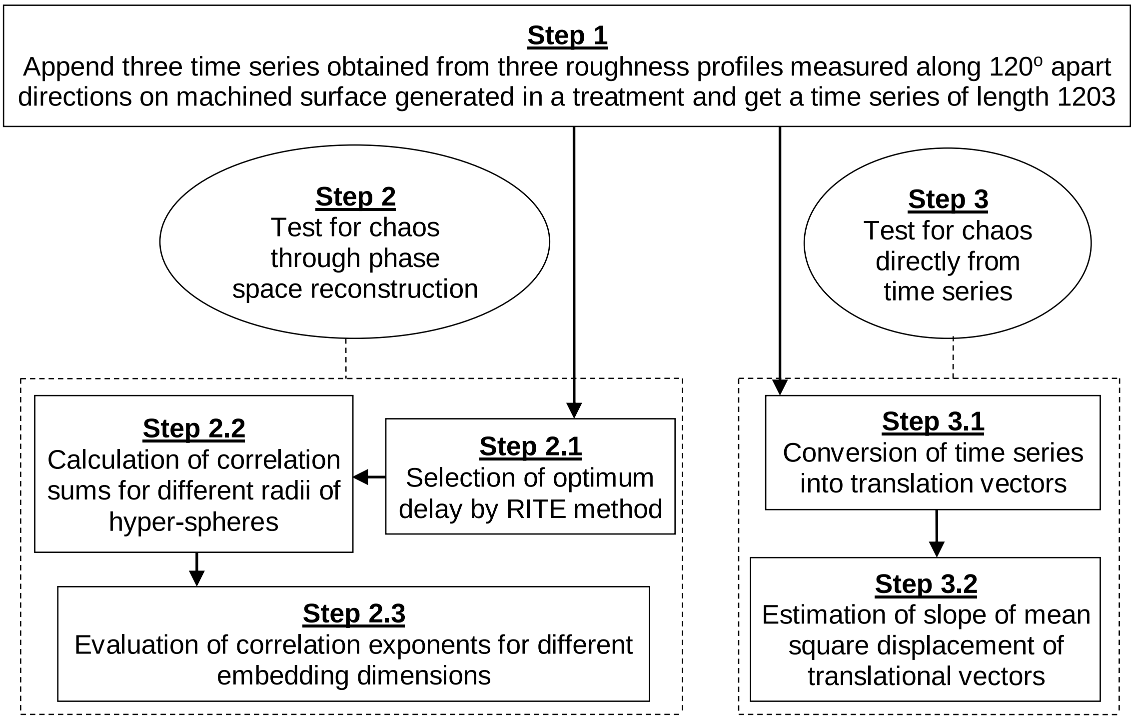

Fig. 6.16 Sequence diagram of investigation for chaos in surface topography

For each of the 64 machined surfaces, three roughness profiles are measured along three 120° apart directions. Using the above discussed steps in figure 6.3, three sequences of profile heights are obtained from corresponding roughness profiles. For the purpose of better characterization of roughness profiles, it is suggested [233] that time series of length n > 1000 gives almost reliable interpretation for system having 1 to 7 degrees of freedom. In the present study, three most significant machining control parameters of EDM, current, pulse on time and pulse off time, are considered. Therefore, time series containing at least 1000 observations is necessary for analysis of surface topography generated by EDM. Hence, three sequences of profile heights measured on same machined surface are appended together. As a result, for each of the 64 combinations of different levels of cur, t_{on} and t_{off}, a time series of length 1203 is obtained. With the 64 representative time series corresponding to different values of cur, t_{on} and t_{off}, presence of chaos in EDM generated surface topography is investigated. This investigation is carried out from two different directions. In the first approach, phase space is reconstructed from representative time series and test is performed on the reconstructed phase space. In the second approach, test is done directly from representative time series.

6.4.1 Test for chaos through phase space reconstruction

Behavior of dynamic system could be better understood in reconstructed phase space than representative one dimensional time series. The dispersive patterns and relative locations of phase vectors in phase space give a good indication of the nature of the dynamic system. To characterize the distributional properties of phase vectors typical measurements are used namely correlation dimension [234, 235], maximum Lyapunov exponent [236] etc.

Presence of self-similarity [236] in one dimensional time series is investigated by estimating fractal dimension. A second-order fractal dimension, called as correlation dimension (CD), represents the space-filling property of underlying dynamic evolution. To quantify the extent of proximity during dynamic evolution, correlation dimension is estimated through relative measurement of inter-point distances in phase space [237]. Hyper-spheres of different radii are placed at each of the points on the trajectory in phase space and number of points lie inside the hyper-spheres are counted. Number of counted points is related with the scale parameter that is radii of hyper-sphere by power-law relationship. The exponent of scale parameter gives the estimation of a invariant measure called as correlation dimension [234]. Through the steps of the evaluation of correlation dimension, presence of chaos in surface topography will be tested.

6.4.1.1 Evaluation of correlation dimension

At first, one dimensional time series is mapped to a phase space with chosen set of embedding dimension (m) and embedding delay (τ_{opt}). Next, all the inter-point Euclidian distances are calculated. If there are M points in phase space, then, total M*(M-1) non-zero distances are obtained. Now a hyper-sphere with a particular radius is selected and placed at all the points in phase space one by one. At each point, number of neighbors lie inside the hyper-sphere are counted. Counted neighbors are those whose Euclidean distances from the center point of hyper-sphere are lesser than radius of the hyper-sphere. With the change of radius of hyper-sphere, number of neighbors inside the hyper-sphere may vary. Therefore, for different radii, a list is obtained containing the number of neighboring points having Euclidean distance less than corresponding radius. Total number of neighbors lie within the hyper-sphere of specific radius (r) is divided by the total number of possible inter-point distances in phase space (equation (6.22)) and called as correlation sum (***CS***) [236].

$$\mathrm{CS}(\boldsymbol{r}) = \frac{2}{\mathrm{M(M-1)}} \sum_{\mathrm{i=1}}^{\mathrm{M-1}} \sum_{\mathrm{j=i+1}}^{\mathrm{M}} \mathrm{H}\left(\boldsymbol{r} - \left|\boldsymbol{Y_i} - \boldsymbol{Y_j}\right|\right) \qquad (6.22)$$

where, H is Heaviside step function with H(x) = 0 for x ≤ 0 and H(x) = 1 for x > 1, $\boldsymbol{Y_i}$ = phase vector on the trajectory of dynamical system at i^{th} evolution with embedding dimension (m) and embedding delay (τ) and M is the number of phase vectors. Hence, choices of different radii give sets of ***CS*** values (equal values of ***CS*** are also possible). If variation of the values of ***CS*** with different radii is plotted in log-log scale, then, a linear zone is expected to exist. In this linear zone, slope of the graph is calculated. This slope is called as correlation exponent (CE) of the time series at that given embedding dimension. Therefore, selection of the scaling region that is linear part in log-log graph is important for proper estimation of correlation exponent [238] and thereby correlation dimension from one dimensional representative time series of surface topography.

As discussed above, appropriate phase space reconstruction is prerequisite to evaluate correlation exponents, thus, before going into detail calculations of correlation exponents, a brief discussion on phase space reconstruction is given.

6.4.1.2 Phase space reconstruction

To investigate the chaotic behavior of surface generation process from one dimensional time series $y_1, y_2, \ldots, y_n$, phase space of the dynamical system is to be reconstructed. According to Takens' embedding theorem [239], m-dimensional phase space portraying the underlying dynamical system of surface generation process could be presented as

$$\boldsymbol{Y_i} = [y_i \; y_{i+\tau} \; y_{i+2\tau} \ldots\ldots\ldots \; y_{i+(m-1)\tau}], \quad \boldsymbol{i}=1(1)M \tag{6.23}$$

where, $\boldsymbol{Y_i}$ = phase vector on the trajectory of dynamical system at i_{th} evolution, y_i = value of one dimensional time series at i_{th} position, m = embedding dimension, τ = embedding delay and M = number of phase vector = n-(m-1)τ. The trajectory of phase vectors, called as attractor, is followed during the dynamic evolution of underlying system. As time evolves, states of the dynamical system would be uniquely defined by the points on the attractor. From equation (6.23), it is observed that phase space reconstruction from one dimensional time series depends on embedding dimension (m) and embedding delay (τ).

Embedding dimension (m) should be adequately selected to uniquely define any state of the system in constructed phase space. Appropriate value of m should be greater than active degrees of freedom of the underlying system [236]. Value of embedding delay (τ) controls time coverage by each of the points in phase space. Lower value of τ may not capture adequate new information which may lead to underestimation of the dimension, whereas, for large τ, dimension might be overestimated as relevant information regarding the divergence of neighboring trajectories may not be gathered. Hence, for characterization of underlying system through phase space reconstruction, optimum values of two prerequisite parameters, m and τ, should be justifiably selected.

In the methods, based on autocorrelation function, average mutual information is generally used for selection of optimum delay. Still, selections of m and τ using the techniques are not independent to each other. Luo and Small [234] proposed a methodology based on second order autocorrelation (SOAC) to select a suitable delay without any information regarding the embedding dimension.

According to information theory, small τ leads to gather redundant information between y_i and $y_{i+\tau}$, whereas, $y_{i+\tau}$ contains irrelevant information with respect to y_i when τ is large. As τ increases, redundancy decreases but irrelevance increases. Therefore, a tradeoff between the redundancy and irrelevance should exist. Luo and Small [234] suggested a statistic to measure the tradeoff between redundancy and irrelevance which is defined as follows.

$$\mathrm{RITE}(\boldsymbol{\tau}) = \frac{\overline{y^2}\,\mathrm{SOAC}(\boldsymbol{\tau}) + \bar{y}^2\left(1-\mathrm{SOAC}(\boldsymbol{\tau})\right)}{\overline{y^2}+\bar{y}^2} \tag{6.24}$$

where, RITE = redundance and irrelevance tradeoff exponent, $\mathrm{SOAC}(\boldsymbol{\tau}) = \frac{\langle (y_i-\bar{y})(y_{i+\tau}-\bar{y})\rangle}{{\sigma_y}^2}$ and <···> denotes the expectation over i. From equation (6.24), it is observed that RITE($\boldsymbol{\tau}$) is calculated as a weighted combination of the two measurements namely redundancy and irrelevance. SOAC($\boldsymbol{\tau}$) controls the measures of redundancy with a weight factor $\frac{\overline{y^2}}{\overline{y^2}+\bar{y}^2}$ and 1-SOAC(τ) controls the measures of irrelevance with weight factor $\frac{\bar{y}^2}{\overline{y^2}+\bar{y}^2}$. As embedding delay increases from zero, value of RITE($\boldsymbol{\tau}$) drops from $\frac{\overline{y^2}}{\overline{y^2}+\bar{y}^2}$. After a certain value of embedding delay, RITE($\boldsymbol{\tau}$) again increases. Hence, embedding delay corresponding to first local minimum of RITE($\boldsymbol{\tau}$) would give optimum embedding delay (τ_{opt}) of the phase space reconstructed from original one dimensional time series. With the obtained optimum embedding delay, phase spaces at different embedding dimensions are constructed and corresponding correlation exponents are estimated. Marching procedure and results for evaluation of correlation exponents are discussed in next subsection.

6.4.1.3 Marching procedure and results

The optimum phase space reconstruction from one dimensional time series is thus prerequisite for estimation of correlation exponents. To construct the optimum phase space, optimum values of τ and m are to be decided first. Detailed steps of phase space construction and selection of optimum embedding delay are discussed in subsection 6.4.1.2.

For better characterization, each of the representative time series (***y***) of length 1203 is normalized using equation (6.25).

$$\boldsymbol{y}_{norm} = \frac{y - y_{\min}}{y_{\max} - y_{\min}} \qquad (6.25)$$

Using equation (6.24), for τ = 0 to integer(n/2) that is 601, values of RITE($\boldsymbol{\tau}$) are calculated for $\boldsymbol{y}_{norm}$. First local minimum of RITE($\boldsymbol{\tau}$) indicates the optimum embedding delay (τ_{opt}) of the corresponding one dimensional time series. Typical variations of RITE is given in figure 6.17.

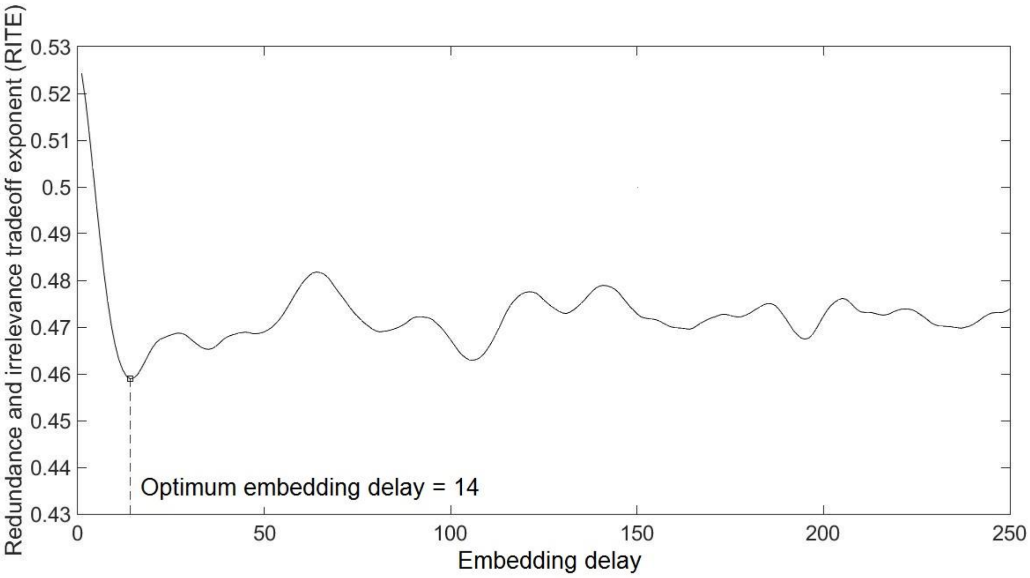

Fig. 6.17 Typical variations of RITE with embedding delays
(Treatment - cur = 9 A, t_{on} = 150 µs and t_{off} = 200 µs)

In the present study, for each of the 64 representative normalized time series ($\boldsymbol{y}_{norm}$) of length 1203, optimum embedding delay (τ_{opt}) is evaluated by employing RITE method. The results are given in table 6.3. The optimum embedding delays (τ_{opt}) are considered for further analysis.

Table 6.3 Values of optimum embedding delay (τ_{opt}) and correlation dimension (CD)

Sl. no.	Machining condition			τ_{opt}	CD	Sl. no.	Machining condition			τ_{opt}	CD
	cur (A)	t_{on} (µs)	t_{off} (µs)				cur (A)	t_{on} (µs)	t_{off} (µs)		
1	6	50	50	13	7.84	33	12	50	50	16	5.73
2	6	50	100	10	8.02	34	12	50	100	14	7.91
3	6	50	150	13	6.04	35	12	50	150	11	8.37
4	6	50	200	9	7.44	36	12	50	200	24	7.06
5	6	100	50	12	7.97	37	12	100	50	15	7.33
6	6	100	100	12	8.06	38	12	100	100	14	7.52
7	6	100	150	11	7.66	39	12	100	150	16	5.05
8	6	100	200	12	6.03	40	12	100	200	15	6.73
9	6	150	50	13	7.11	41	12	150	50	17	8.03
10	6	150	100	12	6.90	42	12	150	100	13	7.52
11	6	150	150	22	6.12	43	12	150	150	20	6.62
12	6	150	200	11	5.92	44	12	150	200	18	8.71
13	6	200	50	11	7.68	45	12	200	50	16	5.02
14	6	200	100	12	10.29	46	12	200	100	18	6.03
15	6	200	150	21	7.21	47	12	200	150	17	5.03
16	6	200	200	12	6.52	48	12	200	200	21	5.75
17	9	50	50	12	7.98	49	15	50	50	20	6.88
18	9	50	100	10	5.00	50	15	50	100	12	6.94
19	9	50	150	11	8.58	51	15	50	150	15	6.39
20	9	50	200	17	7.08	52	15	50	200	10	7.00
21	9	100	50	14	8.43	53	15	100	50	19	6.11
22	9	100	100	15	9.07	54	15	100	100	18	6.11
23	9	100	150	14	7.11	55	15	100	150	11	7.18
24	9	100	200	13	6.79	56	15	100	200	15	8.04
25	9	150	50	15	7.09	57	15	150	50	21	4.84
26	9	150	100	14	7.08	58	15	150	100	19	8.04
27	9	150	150	16	6.45	59	15	150	150	15	7.06
28	9	150	200	14	8.14	60	15	150	200	17	6.32
29	9	200	50	15	6.69	61	15	200	50	26	4.06
30	9	200	100	17	8.07	62	15	200	100	17	5.86
31	9	200	150	14	6.89	63	15	200	150	17	8.97
32	9	200	200	12	7.82	64	15	200	200	20	6.56

Therefore, for each of the 64 treatments, phase vectors could be regenerated at given m-dimensional phase space with calculated τ_{opt} (refer table 6.3). On the reconstructed phase space, correlation exponents are evaluated and thereby corresponding correlation dimension is estimated.

As discussed earlier, to estimate the correlation dimension, hyper-spheres of different radii are to be placed at different points on phase space. In the present study, machined surfaces are generated with different levels of cur, t_{on} and t_{off}. Therefore, with each of the estimated τ_{opt}, phase spaces are reconstructed from the corresponding representative normalized time series ($\boldsymbol{y}_{\boldsymbol{norm}}$) of length 1203 at the embedding dimensions (m) 3 to 35.

For a particular set of τ_{opt} and m, all inter-point Euclidean distances in reconstructed phase space are measured. During measurement of inter-point Euclidean distances, temporally correlated pairs of phase vectors which lie within Theiler window (W) that is which are "accidentally" very close to each other are discarded [240]. By trial and error and space-time separation plot [241], it is found that pairs which are separated by at least W = 5*τ_{opt}, may be ignored.

Radii of hyper-spheres are selected within the range of measured Euclidean distances. In logarithmic scale, 500 equi-length bins [242] are generated between the obtained range of Euclidean distances. Logarithmic scale is chosen to select more radii in lower zone. Upper boundaries of the 500 bins are considered for radii of hyper-spheres. For each of the 500 radii ($\boldsymbol{r}$), total number of points lie inside the hyper-sphere are counted by placing the hyper-sphere at all points in phase space one by one and value of corresponding CS($\boldsymbol{r}$) is evaluated using equation (6.22).

Thus, for particular embedding dimension (m), 500 values of ***CS*** are obtained for 500 different radii. The above steps are repeated for different values of m ranging from 3 to 35. For each of the values of m, obtained values of ***CS*** are plotted against ***r*** in log-log scale. Different curves are obtained for different embedding dimensions. A typical variation of ***CS*** with ***r*** in log-log scale is shown in figure 6.18. Now, slope of the near linear zone of each curve is estimated. Identification of near linear zone is very crucial [243].

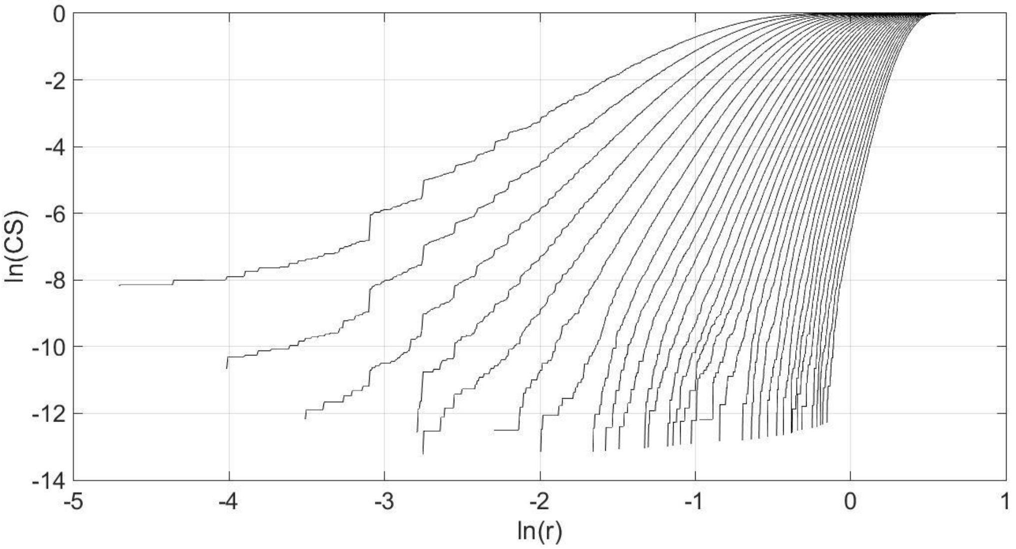

Fig. 6.18 Typical variations of correlation sums with radii in log-log scale
(Treatment - cur = 9 A, t_{on} = 150 µs and t_{off} = 200 µs)

By trial and error, out of 500 points on each curve, points lie above the cumulative position of 225 points are fitted with average error below 3%. For each curve, a scale of 50 points are set. Consecutive near linear zones are marked and slopes are evaluated for each near linear zone. Mean value of all near linear zone on each curve is taken as representative correlation exponent. In this way, for each embedding dimension ranging from 3 to 35, correlation exponents are calculated. Typical variations of correlation exponents are shown in figure 6.19.

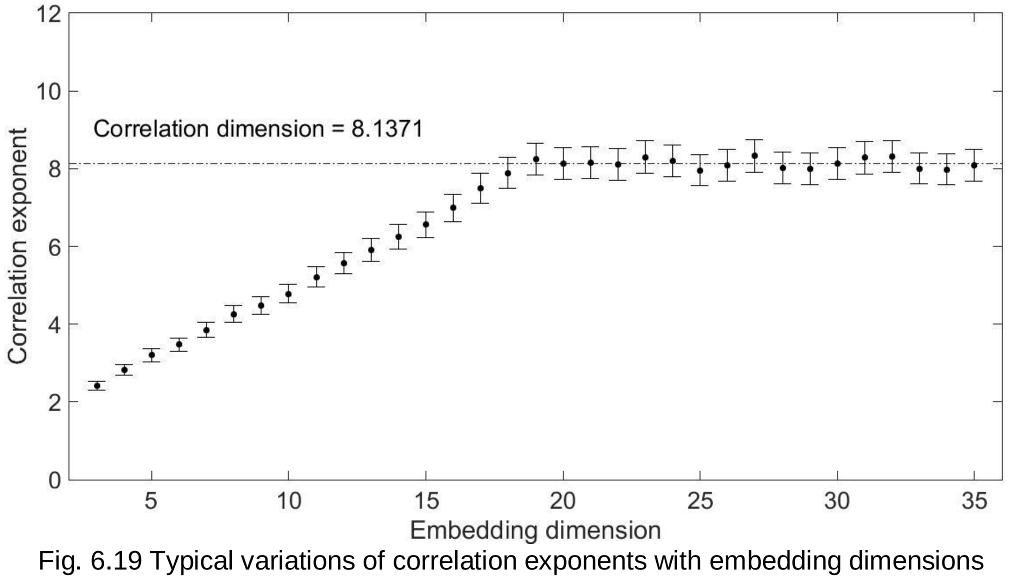

Fig. 6.19 Typical variations of correlation exponents with embedding dimensions
(Treatment - cur = 9 A, t_{on} = 150 µs & t_{off} = 200 µs)

It is observed that, for each of the 64 representative time series, correlation exponents increase with the increase of embedding dimensions but saturate after certain embedding dimension (refer figures C.5 through C.8 in appendix C). This saturation indicates the presence of chaos in surface topography. Saturated value of correlation exponents gives correlation dimension [244] of that particular surface topography. Values of correlation dimension for different treatments are given in table 6.3. All values of correlation dimension are fraction and vary from 4.06 to 10.29. Detailed steps for calculation of correlation dimension is shown in figure 6.20.

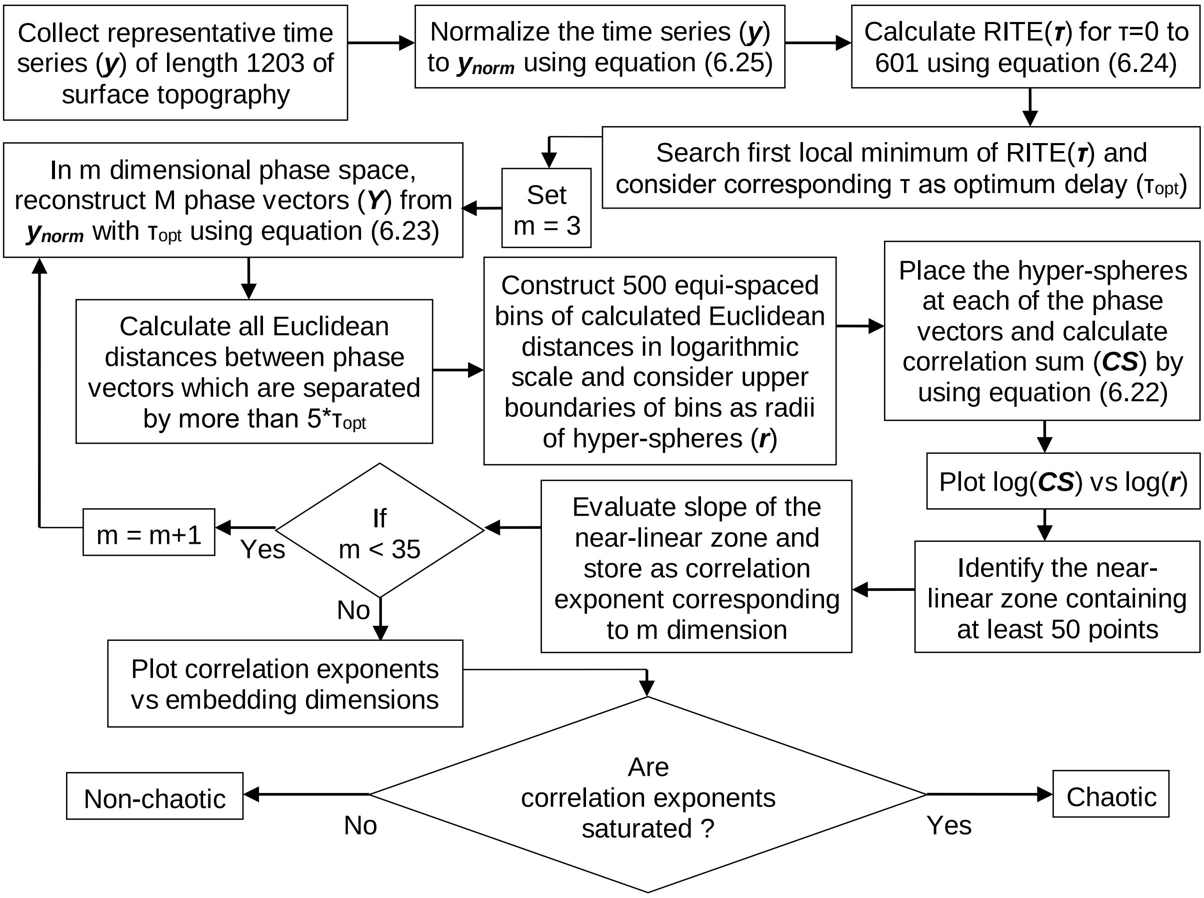

Fig. 6.20 Detailed steps in test for chaos through phase space reconstruction

Hence, chaotic nature of surface generation in EDM is confirmed through fractal dimension based approach. It is observed that, mapping of one dimensional time series to high dimensional phase space is necessary for this approach. Thus, reconstruction of phase space and selection of near-linear zone play crucial role in estimation of correlation dimension. Presence of noise in underlying system and finite length of time series data restrict the robustness of this approach. Therefore, in the next subsection, an exclusive approach is devised directly from one dimensional representative time series to comment on the presence of chaos in surface topography. A value between 0 and 1 is squashed from each of the 64 representative time series through some mathematical transformations.

6.4.2 Test for chaos directly from time series

As mentioned at the end of last subsection, rigorous computation is necessary to calculate the correlation dimension after phase space reconstruction from time series. Without phase space reconstruction, Gottwald and Melbourne [245] proposed a universally acceptable 0-1 test on dynamic system to distinguish between chaotic and non-chaotic behavior. This method for distilling a binary quantity from power spectrum is further modified [246] to handle the time series even contaminated by moderate level of noise.

6.4.2.1 0-1 test

In 0-1 test, a unique value between 0 and 1 is condensed from representative one dimensional time series of length (n) 1203. At first, one dimensional time series y_1, y_2, ….., y_n is converted to two translational vectors $p_c(\boldsymbol{t})$ and $q_c(\boldsymbol{t})$ using the following relations.

$$p_c(\boldsymbol{t}) = \sum_i^t y_i \cos(ic), \quad \boldsymbol{t}=1(1)n \tag{6.26}$$

$$q_c(\boldsymbol{t}) = \sum_i^t y_i \sin(ic), \quad \boldsymbol{t}=1(1)n \tag{6.27}$$

where, c is a randomly chosen value in the range (0, π). In general, different regular patterns are found in $\boldsymbol{p_c}$-$\boldsymbol{q_c}$ plot for regular system but for the case of chaotic system, diffusive behavior might be observed [245, 246].

For a selected value of c, patterns of translational vectors $\boldsymbol{p_c}$ and $\boldsymbol{q_c}$ are quantified by calculating the mean square displacement $M_c(\boldsymbol{t})$. Mean square displacement $M_c(t)$ is enumerated using equation (6.28) [246]

$$M_c(\boldsymbol{t}) = \frac{1}{n-t} \sum_i^{n-t} [\{p_c(i+t) - p_c(i)\}^2 + \{q_c(i+t) - q_c(i)\}^2], \quad \boldsymbol{t}=1(1)n_{cut} \ll n \tag{6.28}$$

For regular system, $M_c(\boldsymbol{t})$ is a bounded function of n but for chaotic system $M_c(\boldsymbol{t})$ almost maintains linear relationship with $\boldsymbol{t}$. Measurement of the asymptotic growth of $M_c(\boldsymbol{t})$ is the foundation of 0-1 test for chaos. For better convergence, $M_c(\boldsymbol{t})$ is further modified to $D_c(\boldsymbol{t})$ using equation (6.29). This modification regularizes the linear behavior of $M_c(\boldsymbol{t})$ by subtracting the oscillatory part [246].

$$D_c(\boldsymbol{t}) = M_c(\boldsymbol{t}) - \bar{y}^2 \frac{1-\cos(tc)}{1-\cos(c)}, \quad \boldsymbol{t}=1(1)n_{cut} \ll n \tag{6.29}$$

Hence, for each of the values of $\boldsymbol{t}$, corresponding value of $D_c(\boldsymbol{t})$ is calculated. Now, asymptotic growth rate of $D_c(\boldsymbol{t})$, denoted by K_c, is calculated by correlation method. For the evaluation of K_c, two new variables ξ and δ are defined as [246]

$$\boldsymbol{\xi} = [1, 2, \ldots\ldots\ldots\ldots, n_{cut}], \quad \boldsymbol{t}=1(1)n_{cut} \ll n \tag{6.30}$$

$$\boldsymbol{\delta} = [D_c(1), D_c(2), \ldots\ldots\ldots\ldots, D_c(n_{cut})], \quad \boldsymbol{t}=1(1)n_{cut} \ll n \tag{6.31}$$

To measure the strength of correlation between $D_c(\boldsymbol{t})$ and linear growth, asymptotic growth rate K_c is calculated as the correlation coefficient (refer equation (6.32)) between $\boldsymbol{\xi}$ and $\boldsymbol{\delta}$.

$$K_c = \frac{\mathrm{covariance}(\xi,\delta)}{\sigma_\xi \sigma_\delta} \tag{6.32}$$

Near 1 value of K_c indicates a strong correlation between mean square displacement and linear growth and thereby the system is chaotic in nature, whereas, close to zero value of K_c suggests non-chaotic behavior of the underlying system [245, 246].

However, for a particular choice of c within the range (0, π), a value of K_c is obtained. As, K_c is dependent on c, thus, multiple values of c are chosen randomly within the specified range. For each of the randomly selected values of c, value of corresponding K_c is estimated. Finally, the median of the values of K_c (K) is evaluated and considered as the distinguishing criterion between chaos and regular [245, 246].

The above discussed method is now implemented on each of the representative 64 time series obtained from the surface generated in different combinations of levels of cur, t_{on} and t_{off}.

6.4.2.2 Results and discussion

To investigate the possibility of presence of chaos in surface topography, 0-1 test is conducted on each of the 64 representative time series. From each of the representative time series ***y***, two translational vectors, $\boldsymbol{p_c}$ and $\boldsymbol{q_c}$, are to be generated using equation (6.26) and (6.27). According to equation (6.26) and (6.27), for the calculation of $\boldsymbol{p_c}$ and $\boldsymbol{q_c}$, proper selections of c and n_{cut} are necessary. Gottwald and Melbourne [246] reported to randomly select 100 to 1000 values of c within the range $(\frac{\pi}{5}, \frac{4\pi}{5})$ to avoid the distortion of results due to resonance in the system. They also suggested to choose $n_{cut} = n/10$ to reduce finite size effects. Therefore, in the present study, 1000 values of c are randomly selected within the range $(\frac{\pi}{5}, \frac{4\pi}{5})$. For each of the selected values of c and $n_{cut} = n/10$, $\boldsymbol{p_c}$ and $\boldsymbol{q_c}$ are calculated using equation (6.26) and (6.27). A typical plot of the two translational vectors $\boldsymbol{p_c}$ and $\boldsymbol{q_c}$ is shown in figure 6.21.

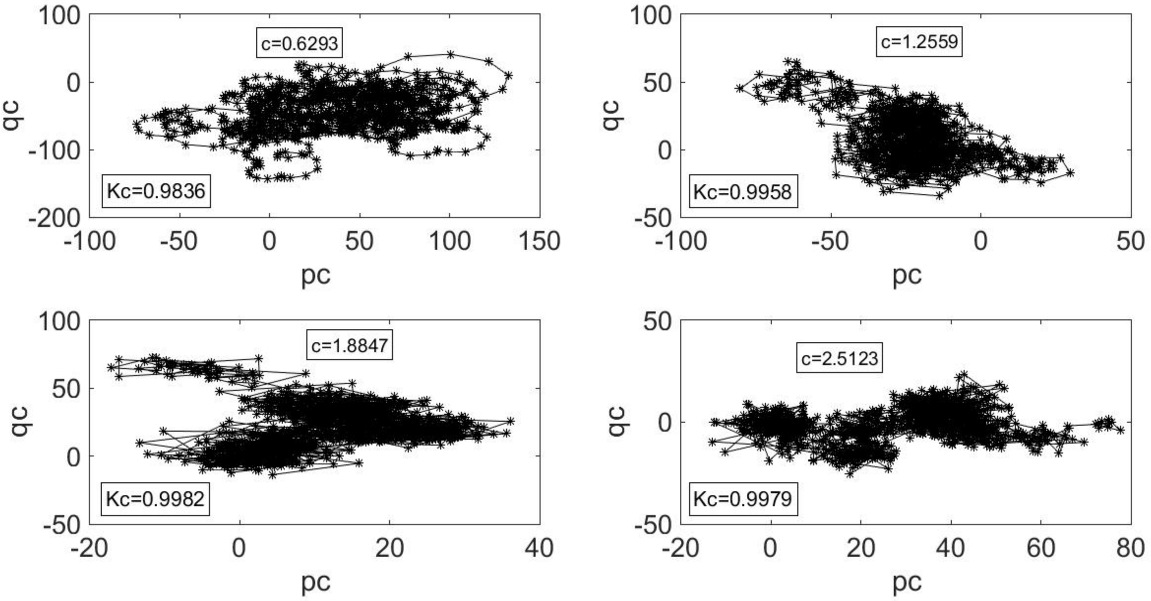

Fig. 6.21 Patterns of translational vectors in 0-1 test for chaos
(Treatment - cur = 12 A, t_{on} = 50 µs and t_{off} = 150 µs)

Diffusive patterns in figure 6.21 give a glimpse of the presence of chaos in surface topography. From the obtained $\boldsymbol{p_c}$ and $\boldsymbol{q_c}$, modified mean square displacements are calculated using equations (6.28) and (6.29) for each of the randomly preselected values of c. Then, for each of the 1000 values of c, asymptotic growth rate K_c is evaluated using equations (6.30) - (6.32). Finally, median of the 1000 values of K_c that is K for representative time series is estimated (table 6.4).

From table 6.4, it is observed that for all the combinations of the different levels of cur, t_{on} and t_{off}, values of K are very close to 1. The lowest K is found as 0.9655. All near to 1 values of K assert the chaotic behavior of surface topography. Detailed steps involved in test for chaos are given in figure 6.22.

Table 6.4 Values of K in 0-1 test for chaos

Sl. no.	Machining condition cur (A)	t_{on} (µs)	t_{off} (µs)	K	Sl. no.	Machining condition cur (A)	t_{on} (µs)	t_{off} (µs)	K
1	6	50	50	0.9952	33	12	50	50	0.9923
2	6	50	100	0.9941	34	12	50	100	0.9914
3	6	50	150	0.9953	35	12	50	150	0.9965
4	6	50	200	0.9968	36	12	50	200	0.9951
5	6	100	50	0.9951	37	12	100	50	0.9946
6	6	100	100	0.9945	38	12	100	100	0.9919
7	6	100	150	0.9956	39	12	100	150	0.9899
8	6	100	200	0.9951	40	12	100	200	0.9862
9	6	150	50	0.9945	41	12	150	50	0.9866
10	6	150	100	0.9942	42	12	150	100	0.9929
11	6	150	150	0.9971	43	12	150	150	0.9882
12	6	150	200	0.9942	44	12	150	200	0.9895
13	6	200	50	0.9961	45	12	200	50	0.9917
14	6	200	100	0.9948	46	12	200	100	0.9928
15	6	200	150	0.9904	47	12	200	150	0.9896
16	6	200	200	0.9951	48	12	200	200	0.9655
17	9	50	50	0.9964	49	15	50	50	0.9929
18	9	50	100	0.9957	50	15	50	100	0.9968
19	9	50	150	0.9959	51	15	50	150	0.9874
20	9	50	200	0.9935	52	15	50	200	0.9963
21	9	100	50	0.9836	53	15	100	50	0.9938
22	9	100	100	0.9933	54	15	100	100	0.9940
23	9	100	150	0.9905	55	15	100	150	0.9953
24	9	100	200	0.9931	56	15	100	200	0.9954
25	9	150	50	0.9839	57	15	150	50	0.9917
26	9	150	100	0.9922	58	15	150	100	0.9868
27	9	150	150	0.9830	59	15	150	150	0.9897
28	9	150	200	0.9929	60	15	150	200	0.9921
29	9	200	50	0.9843	61	15	200	50	0.9822
30	9	200	100	0.9883	62	15	200	100	0.9895
31	9	200	150	0.9933	63	15	200	150	0.9824
32	9	200	200	0.9932	64	15	200	200	0.9850

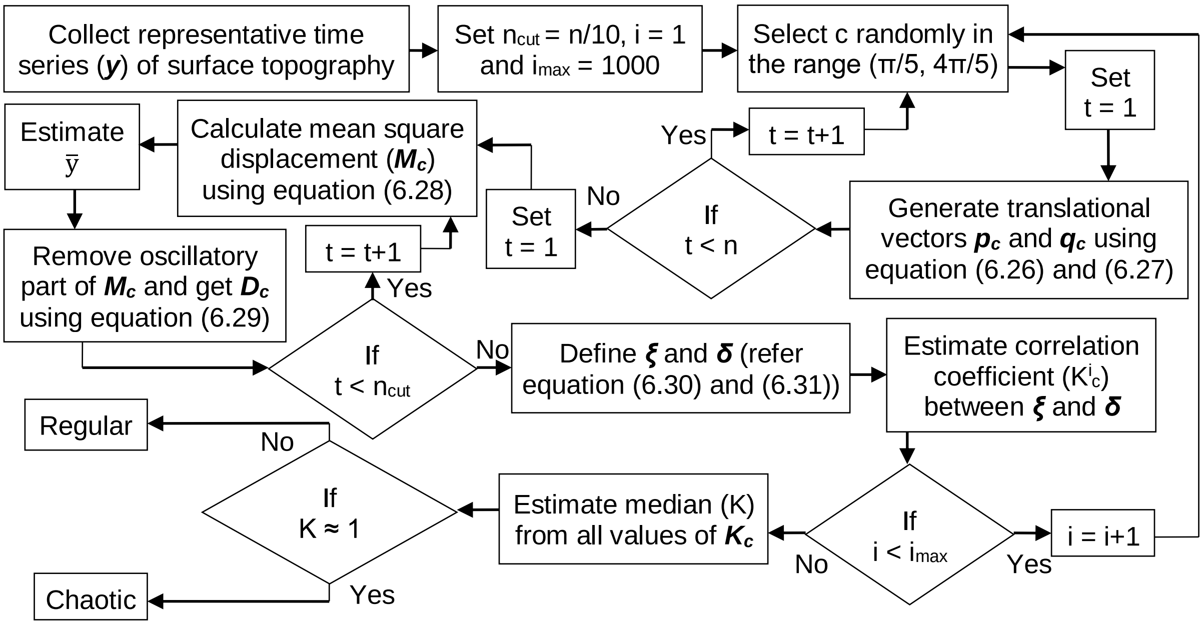

Fig. 6.22 Detailed steps in test for chaos directly from time series

However, evidence in favor of chaotic behavior of surface topography is also found in subsection 6.4.1. As, calculation of correlation dimension is done there through phase space construction, separate approach, which is based on time series directly, is further considered. Thus, presence of chaos in EDM generated surface topography is substantiated explicitly.

In qualitative support of the analysis made so far, typical scanning electron micrographs of EDM generated surfaces are presented in figure 6.23. The EDM generated surface is composed of pock marks resulting as a consequence of bursting of blisters, remelting and redeposition of debris mostly in globular form complete or incomplete and resolidification of unexpelled molten material in and around the crater formed in an uncontrollable fashion by each spark [35]. The features attribute to the formation of chaos in the EDM generated surface topography. Lower is the spark energy, lesser are the above mentioned effects and smoother is the surface.

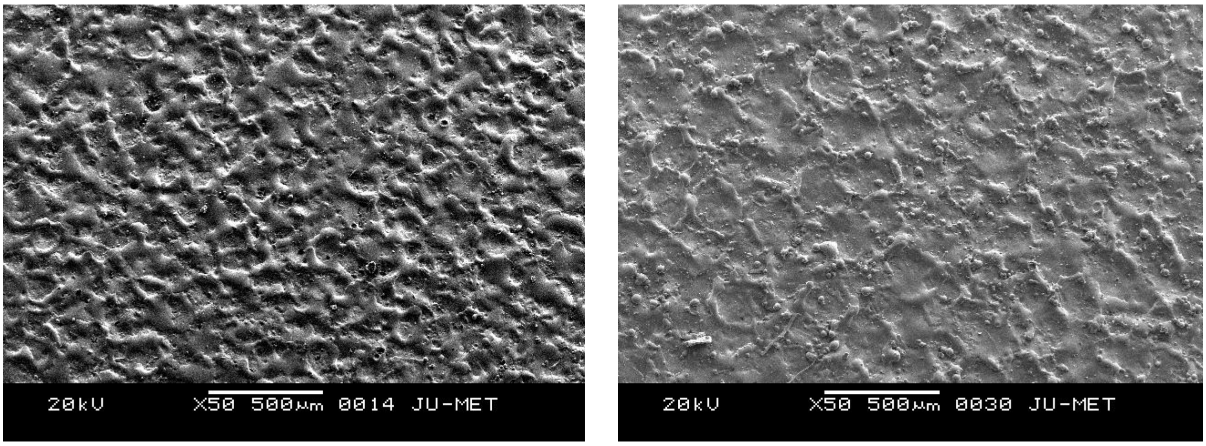

(a) cur = 6 A, t_{on} = 50 µs and t_{off} = 200 µs (b) cur = 15 A, t_{on} = 50 µs and t_{off} = 200 µs

Fig. 6.23 Scanning electron micrographs of EDM generated surfaces

6.5 Summary

Surface generated through any machining process carries the inherent features of that process. Therefore, inspecting the surface characteristics, a frame of unseen behavior of that surface development process could be drawn. Meticulous analysis of a justifiably selected observed variable of a dynamic system is an indirect way to reveal the characteristics of underlying dynamical system. In the present chapter, roughness profiles measured on EDM generated surface are considered as time series. The time series are analyzed through autocorrelation function and following conclusions are drawn.

- Sharp drooping and subsequent damped oscillating behavior of ACF curves suggest the existence of both random and periodic features in the EDM generated surface.

- Two-stage filtering of ACF curves and the exclusive distributional properties of roots in backward linear prediction are proposed to estimate the parameters of the most effective constituent FIDs.

- Variation of characteristic correlation lengths ($\boldsymbol{\beta}$) within treatment is found as the most contributive on overall variations in all treatments with their replications. This claims in favor of the randomness of the surface generated in EDM process.

- A non-dimensional index, PR ratio, for each of the FIDs is calculated to assess the relative contribution of randomness and periodicity in the surface topography. In all cases, near zero values of PR ratio at different machining conditions indicate overall randomness of machined surface irrespective of the settings of machining control parameters.

- The correlation between PR ratio_{avg} of surface topography and machining control parameters (cur, t_{on} and t_{off}) further substantiates the predominant randomness in EDM generated surface topography.

Further, nonlinear time series analysis is performed to investigate the presence of chaos in surface topography and thereby in the surface generation process of EDM. As the outcome, following conclusions are drawn.

- Saturation of correlation exponents for all 64 treatments claims in favor of the presence of chaos in EDM generated surface topography.

- Non-integer values of correlation dimension indicate the fractal nature of surface topography.

- Patterns of translational vectors $\boldsymbol{p_c}$ and $\boldsymbol{q_c}$ suggest the diffusive behavior of the surface generation process.

- Values of K obtained from 0-1 test for all the 64 treatments are close to 1 which substantiate the presence of chaos in generated surfaces and thereby in the occurrence of discharges during surface generation by EDM itself.

The proposed methodology could be applied in general, to any such process to directly unveil the underlying features of surface generation from surface profiles. This layout could be used for extraction of unseen characteristic attributes of surface generation in any such process.

CHAPTER 7

CONCLUSIONS
RECOMMENDATIONS AND FUTURE SCOPE

Based on the work presented in the previous chapters, the following conclusions are drawn. Recommendations and the scope for future work are also presented.

CONCLUSIONS

(i) The latest modeling techniques are suffering from curse of dimensionality of process parameters, efficiency of training, efficiency of testing, over-fitting and algorithm parameter tuning. In EDM, irregular variations in material removal rate (MRR) and average surface roughness (ASR), obtained at different treatments of machining control parameters, suggest that robust modeling method is necessary for near-accurate representation of the process.

(ii) Experimental values of MRR and ASR show that surface finish decreases with increase of production rate. Therefore, a tradeoff is required. Results of modern optimization methods are not yet completely effective as their performances are affected by selection of their own internal parameters, choice of termination criteria etc. Algorithm-specific parameter-less optimization method with some pertinent modifications, like population base termination criterion, appears to be effective in this regard.

(iii) It is observed from experimental study that for skewness and kurtosis of profile height distribution, variation within treatment is more significant than between treatments. Measured values of developed length of roughness profile indicate openness of machined surface. Scanning electron micrographs of EDM generated surfaces exhibit complex pattern, erratic fluctuations and overall random features. Hence, assessment of surface topography is inevitable.

(iv) In support vector machine (SVM) regression based both independent and unified learning systems of MRR and ASR, higher values of optimum regularization parameter (C) indicate complex relation among machining control parameters and process outcomes.

(v) ε-insensitive hyper-tube wrapped around SVM regression based learning system absorbs the irregular fluctuations in efficient way and estimated models allow to do the production within predefined tolerance effectively.

(vi) During model development by SVM regression based methodology, high dimensional input space is mapped to a comparatively low dimensional feature space through kernel function. Use of kernel function helps to circumvent the curse of dimensionality that is adverse effects of complex interactive patterns are bypassed.

(vii) In searching of the optimum set of internal structural parameters of SVM regression based models, particle swarm optimization (PSO) and teaching learning based optimization (TLBO) are implemented with some proposed modifications. Modifications, namely current population based stopping criterion, initial population with stopping criterion based high relative dispersion and weight combining method for selection of guide (p_{best}, g_{best} for PSO, teacher for TLBO) for next iteration in case of multiple particles or learners having same optimum score, are improvised and worked successfully towards the smoother convergence.

(viii) With the proposed modifications, modified TLBO is proved to be computationally more efficient than modified PSO as modified PSO takes 30 and 50 times more simulation time than modified TLBO in searching of optimum set of C, ε and σ for SVM regression based modeling of MRR and ASR respectively.

(ix) Separate learning system for each of the process outcomes demands an independent set of internal structural parameters of SVM regression based model. In the present work, method for developing a SVM regression based unified learning system for both the MRR and the ASR that uses a unique set of C, ε and σ is proposed and expounded. The developed procedure works effectively.

(x) In multiobjective optimization, way of handling of multiple objective functions imposes a huge impact in final results. In the context of simultaneous minimization of training errors during the development of unified learning system of MRR and ASR, combined rank method, a new way of handling multiple objective functions by preserving their individual impacts is devised. It performs adequately.

(xi) Pseudo Pareto optimization of two conflicting type responses, MRR and ASR, is proposed considering different sets of weight factors for the purpose of combining the representative models of MRR and ASR. The generated pseudo Pareto front provides a guideline to achieve highest possible quality of surface without sacrificing the production rate.

(xii) Setting of the optimum available levels of machining control parameters in EDM machine to get optimum combination of MRR and ASR is a tedious job to process engineers. In the present work, a readily accessible idea, inverse solution procedure, is framed to get near-optimum levels of machining control parameters to achieve customer demand based pseudo Pareto optimum combination of MRR and ASR.

(xiii) For assessment of surface topography, ordered sequence of profile heights, measured on EDM generated surface, is considered as representative time series of that machined surface and autocorrelation function is taken as a typical analytical tool for the assessment purpose. Sharp drooping and damped oscillating behavior of ACF curves anticipate the presence of both random and periodic features in surface topography.

(xiv) Each of the ACF curves is assumed as a summation of multiple exponentially damped sinusoidal freely induced decays. Two-stage filtering of ACF curves and the exclusive distributional properties of roots in backward linear prediction are proposed that could estimate the parameters of the most effective constituent freely induced decays buried in machined surface.

(xv) Characteristic correlation length ($\boldsymbol{\beta}$) is considered as a typical yardstick for randomness present in the machined surface and evaluated from the estimated parameters of freely induced decays. Variation of $\boldsymbol{\beta}$ within treatment is found as the most contributive on overall variations in all treatments with their replications. This claims in favor of the predominance of randomness in the surface generated and thereby the random nature of surface development in EDM process.

(xvi) A non-dimensional index, PR ratio, is calculated from the estimated parameters of freely induced decays and taken as a derived measurement of the relative contributive effect of randomness and periodicity. Close to zero value of PR ratio for all the treatments and negligible variation with chosen levels of machining control parameters indicate overall randomness of machined surface and thereby random behavior of surface generation process in EDM.

(xvii) Analysis of surface topography through phase space reconstruction shows the saturation of correlation exponents with the increase of embedding dimension and thereby indicates the chaotic nature of surface topography. Non-integer value of correlation dimension claims in favor of the fractal nature of surface topography.

(xviii) Chaotic nature of the surface topography and thereby the presence of chaos in the occurrence of discharges during surface generation by EDM are further substantiated by 0-1 test which is conducted directly on representative time series without phase space reconstruction. In 0-1 test, patterns of translational vectors also suggest diffusive behavior of surface topography.

(xix) Chaos in topography of EDM generated surface justifies the application of SVM regression method in model building of EDM.

RECOMMENDATIONS AND FUTURE SCOPE

(i) Robust model development by SVM regression methodology could be implemented for representative model building for any such machining process.

(ii) As, ε-insensitive zone around estimated SVM regression based model absorbs the irregular variations in process outcome, so, the proposed model could help other researchers to apply the model on different products obtained in different batches.

(iii) Proposed modifications on PSO and TLBO could be generalized and improvised to other population based evolutionary optimization methods.

(iv) The suggested procedure of pseudo Pareto front generation for conflicting type responses and inverse solution method could be implemented in any such process.

(v) The proposed way of handling multiple objective functions is a novel advancement in multiobjective optimization problem and could be applied to other optimization methods with large number of objective functions.

(vi) Further study on chaos is necessary to identify whether it is deterministic or stochastic in nature.

(vii) Inverse procedure for virtual generation of 3D surface topography in EDM from developed models could be attempted for the purpose of off-line analysis and prediction.

(viii) The proposed methodology for modeling, optimization and assessment of surface topography could be implemented in any such manufacturing process for building an expert system.

(ix) The analysis of randomness, periodicity and estimation of PR ratio on surface topography could be employed for identifying impending vibration in machines tools.

(x) Experimental conformation of the chaotic nature of surface topography might be performed by measurement and analysis of sporadic spark locations on EDM surface.

(xi) Molecular dynamics based approach could be attempted for better understanding of chaotic surface topography in EDM.

REFERENCES

1. Jain V.K., Advanced machining processes, Allied Publishers Private Limited, India, 2002.
2. Benedict G.F., Nontraditional manufacturing processes, Marcel Dekker Inc., New York and Basel, 1987.
3. Mishra P.K., Nonconventional machining, Narosa Publishing House Private Limited, India, 1997.
4. Pandey P.C., Shan H.S., Modern machining processes, Tata McGraw-Hill Publishing Company Limited, India, 1980.
5. Lazarenko B.R., To invert the effect of wear on electric power contacts, Dissertation of The All-Union Institute for Electro Technique in Moscow, 1943.
6. Konig W., Dauw D.F., Levy G., Panten U., EDM future steps towards the machining of ceramics, CIRP Annals, 37(2) (1988) 623-631.
7. Kunieda M., Lauwers B., Rajurkar K.P., Schumacher B.M., Advancing EDM through fundamental insight of the process, CIRP Annals, 54(2) (2005) 599-622.
8. Karafuji H., Development of researches and applications of spark erosion and electrolytic machining in Japan, 14th CIRP General Assembly, 13(3) (1964) 313-324.
9. Niwa Y., Fujimoto R., Lecture manuscript, Japan Society of Electrical Discharge Machining, 1961, No. 23.26.6.
10. Inoue K., Electric power supply apparatus for electric discharge machining, United States Patent Office, 3054931, 1959.
11. Motoki K., Hashiguchi K., Energy distribution at the gap in electric discharge machining, CIRP Annals, 14 (1967) 485-489.
12. Satio N., Kobayashi K., Machining principle and characteristics of electrode discharge machining, Mitsubishi Denki Giho, 41 (10) (1967) 1222-1230.
13. Fujimoto R., Togashima T., Observation of electrode erosion phenomena, Journal of The Japan Society of Electrical Machining Engineers, 6 (11) (1973) 48-63.
14. Williams E.M., Theory of electric spark machining, Transactions of AIEE, 71 (1952) 105-108.
15. Singh A., Ghosh A., A thermo-electric model of material removal during electric discharge machining, International Journal of Machine Tools & Manufacture, 39 (1999) 669-682.
16. Huntress E.M., Electrical discharge machining, American Machinist, August, 1978, 83-98.
17. Singh H., Experimental study of distribution of energy during EDM process for utilization in thermal models, International Journal of Heat and Mass Transfer, 55 (2012) 5053-5064.
18. DiBitonto D.D., Eubank P.T., Patel M.R., Barrufet M.A., Theoretical models of the electrical discharge machining process. I. A simple cathode erosion model, Journal of Applied Physics, 66 (1989) 4095-4103.
19. Patel M.R., Barrufet M.A., Eubank P.T., DiBitonto D.D., Theoretical models of the electrical discharge machining process. II. The anode erosion model, Journal of Applied Physics, 66 (1989) 4104-4111.
20. Shankar P., Jain V.K., Sudararajan T., Analysis of spark profiles during EDM process, Machining Science and Technology: An International Journal, 1(1997) 195-217.
21. Zhang Y., Liu Y., Shen Y., Li Z., Ji R., Wang F., A new method of investigation the characteristic of the heat flux of EDM plasma, Procedia CIRP, 6 (2013) 450-455.
22. Marafona J., Chousal J.A.G., A finite element model of EDM based on the Joule effect, International Journal of Machine Tools & Manufacture, 46 (2006) 595-602.
23. Mirinoff N., Electro-erosive metal working, its physical fundamentals and industrial applications: part I – the nature of metal removal by spark discharges, Microtecnic, 19 (1965) 149-153.
24. Jameson E.C., Electrical discharge machining, Society of Manufacturing engineers, Dearborn, Michigan, 2001.
25. Boothroyd G., Winston A.K., Non-conventional machining processes, in: Fundamentals of machining and machine tools, Marcel Dekker, Inc., New York, 1989, pp 491.
26. McGeough J.A., Electrodischarge machining, in: Advanced methods of machining, Chapman & Hall, London, 1988, pp 30.
27. Richardson P.D., Heat and mass transfer in spark machining, Proceedings 6th International Heat Transfer Conference, Toronto, 4 (1978) 73-78.
28. Livshits A.L., The mechanism of the electrical discharge machining process, Machines and Tooling, 38 (1967) 4-8.
29. Rajurkar K.P., Pandit S.M., Formation and ejection of EDM debris, Transactions of ASME: Journal of Engineering for Industry, 108 (1966) 22-26.
30. VanDijck F., Crookall J.R., Heuvelman C.J., Snoeys R., Some results of physical research in EDM, IV International Symposium for Electromachining, vol.1, pp. 68-85.

31. Erden A., Kaftanoğlu B., Thermo-mathematical modelling and optimization of energy pulse forms in electric discharge machining (EDM), International Journal of Machine Tool Design and Research, 21 (1) (1981) 11-22.
32. Erden A., Effects of materials on the mechanism of electric discharge machining (EDM), Transactions of ASME, Journal of Engineering Materials and Technology, 108 (1983) 247-251.
33. Zingermann A.S., About the development of the discharge channel in electroerosive metal machining, Journal of Technical Physics, 26 (5) (1956) 1015-1020.
34. Zolotykh B.N., The mechanism of electrical erosion of metals in liquid dielectric media, Soviet Physics-Technical Physics, 4(12) (1959) 13701373.
35. Ho K.H., Newman S.T., State of the art electrical discharge machining (EDM), International Journal of Machine Tools and Manufacture, 43 (2003) 1287-1300.
36. Zhang Y., Liu Y., Ji R., Zheng C., Shen Y., Wang X., Transient dynamics simulation of the electrical discharge-generated bubble in sinking EDM, International Journal of Advanced Manufacturing Technology, 68 (2013) 1707-1715
37. Guerrero-Alvarez J.L., Greene J.E., Turkovich B.F.V., Study of the electro-erosion phenomenon of Fe and Zn, Journal of Engineering for Industry, 95(4) (1973) 965-971.
38. Yang X., Han X., Zhou F., Kunieda M., Molecular dynamics simulation of residual stress generated in EDM, Procedia CIRP, 6 (2013) 432-437.
39. Zhang G., Guo J., Ming W., Huang Y., Shao X., Zhang Z., Study of the machining process of nano-electrical discharge machining cased on combined atomistic-continuum modeling method, Applied Surface Science, 290 (2014) 359-367.
40. Kumar P.D., Study of thermal stresses induced surface damage under growing plasma channel in electro-discharge machining, Journal of Materials Processing Technology, 202 (2008) 86-95.
41. VanDijck, F., Physico-mathematical analysis of EDM process, Dissertation of Katholieke Universiteit te Leuven, 1973.
42. VanDijck F., Snoeys R., A theoretical and experimental study of the main parameters governing the electro-discharge machining process, Proceedings of GAMI Conference 1975, pp 9-16.
43. Hass P., Pontelandolfo P., Perez R., Particle hydrodynamics of the electrical discharge machining process, part 2: die sinking process, Procedia CIRP, 6 (2013) 47-52.
44. Petrofes N.F., Gadalla A.M., Electrical discharge machining of advanced ceramics, American Ceramic Bulletin, 67 (1988) 1048-1052.
45. Lee T.C., Lau W.S., Some characteristics of electrical discharge machining of conductive ceramics, Materials and Manufacturing Processes, 6 (1991) 635-648.
46. Lauwers B., Kruth J.P., Liu W., Eeraerts W., Schacht B., Bleys P., Investigation of material removal mechanisms in EDM of composite ceramic materials, Journal of Materials Processing Technology, 149 (2004) 347-352.
47. Ferraris E., Reynaerts D., Lauwers B., Micro-EDM process investigation and comparison performance of Al_3O_2 and ZrO_2 based ceramic composites, CIRP Annals, 60 (2011) 235-238.
48. Malek O., Vleugels J., Vanmeensel K., Electrical discharge machining of $(Nb_xZr_{1-x})B_2$-SiC composites, Procedia CIRP, 6 (2013) 186-191.
49. Izquierdo B., Plaza S., Sanchez J.A., Pombo I., Ortega N., Numerical prediction of heat affected layer in the EDM of aeronautical alloys, Applied Surface Science, 259 (2012) 780-790.
50. Nair M.S., Kuriachen B., Vijayakumar R., Mathew J., Modelling of Micro Electric Discharge Machining Using FEM, Proceeding of 26th AIMTDR conference, IIT Guwahai, Guwahati, India, 2014, pp 333-1-6.
51. Hanaoka D., Fukuzawa Y., Ramirez C., Miranzo P., Osendi M.I., Belmonte M., Electrical discharge machining of ceramic/carbon nanostructure composites, Procedia CIRP, 6 (2013) 95-100.
52. Mamalis A.G., Grabchenko A.I., Magazeev M.G., Krukova N.V., Prohaszka J., Vaxevanidis N.M., Two-stage electr-discharge machining fabricating superhard cutting tools, Journal of Materials processing Technology, 146 (2004) 318-325.
53. Wei C., Zhao L., Hu D., Ni J., Electrical discharge machining of ceramic matrix composites with ceramic fiber reinforcements, International Journal of Advanced Manufacturing Technology, 64 (2013) 187-194.
54. Vishwakarma U.K., Dvivedi A., Kumar P., FEA modeling of material removal rate in electrical discharge machining of Al6063/SiC composites, International Scholarly and Scientific Research & Innovation, 6 (3) (2012) 586-591.
55. Liu K., Reynaerts D., Lauwers B., Influence of the pulse shape on the EDM performance of Si3N4-TiN ceramic composite, CIRP Annals, 58 (2009) 217-220.

56. Ojha K., Garg R.K., Singh K.K., MRR improvement in sinking electrical discharge machining: a review, Journal of Minerals and Materials Characterization & Engineering, 9(8) (2010) 709-739.
57. Choudhary S.K., Jadoun R.S., Current advanced Research development of electric discharge machining (EDM): a review, International Journal of Research in Advent Technology, 2(3) (2014) 273-297.
58. Gnannavel C., Saravanam R., Chandrasekaran M., Pugazhenthi R., Restructured review on electrical discharge machining - a state of the art, IOP conference series: Materials Science and Engineering, 183 (2017) 012015-1-13.
59. Mamalis A.G., Vaxevanidis N.M., Pantelis D.I., On the Electrodischarge machining of ceramic plasma-sprayed steel plates, CIRP Annals, 41(1) (1992) 235-238.
60. Paramashivan S.S., Mathew J., Mahadevan S., Mathematical modeling of aerosol emission from die sinking electrical discharge machining process, 36 (2012) 1493-1503.
61. Pandey P.C., Jilani S.T., Plasma channel growth and the resolidified layer in EDM, Precision Engineering, 8 (1986) 104-110.
62. Eubank P.T., Daryl D., Theoretical models of the electrical discharge machining process III, the variable mass, cylindrical plasma model, Journal of Applied Physics, 73 (1993) 7900-7909.
63. Albinski K., Musiol K., Miernikiewicz A., Labuz S., Malota M., The temperature of a plasma used in electrical discharge machining, Plasma Sources Science Technology, 5 (4) (1996) 736-742.
64. Lou L.M., Study on Computer Simulation of EDM, Ph. D. thesis, Shanghai Jiaotong University, China, 2000.
65. Das S., Klotz M., EDM simulation: finite element based calculation of deformation, microstructure and residual stresses, Journal of Materials Processing Technology, 142 (2003) 434-451.
66. Descoeudres A., Hollenstein C., Demellayer R., Walder G., Optical emission spectroscopy of electrical discharge machining plasma, Journal of Materials Processing Technology, 149 (2004) 184-190.
67. Kunieda M., Kobayashi T., Clarifying mechanism of determining tool electrode wear ratio in EDM using spectroscopic measurement of vapor density, Journal of Materials Processing Technology, 149 (2004) 284-288.
68. Revaz B., Emery J., Witz G., Flukiger R., Perez R., Carron J., Rappaz M., Local temperature response to pulse discharges in electronic discharge machining (EDM) environment, IEEE transactions Plasma Science, 33 (3) (2005) 1066-1071.
69. Kojima A., Natsu W., Kunieda M., Spectroscopic measurement of arc plasma diameter in EDM, CIRP Annals, 57 (2008) 203-207.
70. Izquierdo B., Sanchez J.A., Plaza S., Pombo I., Ortega N., A numerical model of the EDM process considering the effect of multiple discharges, International Journal of Machine Tools & Manufacture, 49 (2009) 220-229.
71. Ahsan A., Role of heat transfer on process characteristic during electrical discharge machining, in: Developments in Heat Transfer, (2009) pp 417-435.
72. Salonitis K., Stournaras A., Stavropoulos P., Chryssolouris G., Thermal modeling of the material removal rate and surface roughness for die-sinking EDM, International Journal of Advanced Manufacturing Technology, 40 (2009) 316-323.
73. Joshi S.N., Pande S.S., Thermo-physical modeling of die-sinking EDM process, Journal of Manufacturing Processes, 12 (2010) 45-56.
74. Guo Y.B., Klink A., Klocke F., Multiscale modeling of sinking-EDM with Gaussian heat flux via user subroutine, Procedia CIRP, 6 (2013) 438-443.
75. Zhang Y., Liu Y., Shen Y., Li Z., Ji R., Cai B., A novel method of determining energy distribution and plasma diameter of EDM, International Journal of Heat and Mass Transfer, 75 (2014) 425-432.
76. Perez R., Rojas H., Walder G., Flukiger R., Theoretical modeling of energy balance in electroerosion, Journal of Materials Processing Technology, 149 (2004) 198-203.
77. Nagahanumaiah, J. Ramkumar, Glumac N., Kapoor S.G., Devor R.E., Characterization of plasma in micro-EDM diascharge using optical spectroscopy, Journal of Manufacturing Process, 11 (2009) 82-87.
78. Jilani S.T., Pandey P.C., An analysis of surface erosion in electrical discharge machining, Wear, 84 (1983) 275-284.
79. Martin E.A., Experimental investigation of a high-energy density, high pressure arc plasma, Journal of Applied Physics, 31(2) (1960) 255-267.
80. Robinson J.W., Measurements of plasma energy density and conductivity from 3 to 120 kbar, Journal of Applied Physics, 38(1) (1967) 210-216.

81. Robinson J.W., Ham M., Balaster A.N., Ultraviolet radiation from electrical discharges in water, Journal of Applied Physics, 44(1) (1973) 72-75.
82. Snoeys R., VanDijck F., Plasma channel diameter growth affects stock removal in EDM, CIRP Annals, 21 (1972) 39-40.
83. Spur G., Schnbeck J., Anode erosion in wire EDM - a theoretical model, CIRP Annals, 42(1) (1993) 253-256.
84. Adineh V.R., Radiative heat loss of electrical discharge machining process through hydrocarbon oil and deionized water dielectric liquids, Plasma Chemistry and Plasma Processing, 32 (2012) 369-392.
85. Adineh V.R., Net emission coefficient of plasma excited in the electrical discharge machining through liquid nitrogen dielectric medium, IEEE Transactions on Plasma Science, 40 (2012) 853-862.
86. Yeo S.H., Kurnia W., Tan P.C., Critical assessment and numerical comparison of electro-thermal models in EDM, Journal of Materials Processing Technology, 203(1-3) (2008) 241-251.
87. Snoeys R., VanDijck F., Investigation of electro discharge machining operations by means of thermo-mathematical model, CIRP Annals, 20 (1971) 35-36.
88. VanDijck F., Dutre W.L., Heat conduction model for the calculation of the volume of molten metal in electric discharges, Journal of Physics D: Applied Physics, 7(6) (1974) 899-910.
89. Beck J.V., Transient temperatures in a semi-infinite cylinder heated by a disk heat source, International Journal of Heat and Mass Transfer, 24 (1981) 1631-1640.
90. Beck J.V., Large time solutions for temperatures in a semi-infinite body with a disk heat source, International Journal of Heat and Mass Transfer, 24 (1981) 155-164.
91. Jilani S.T., Pandey P.C., Analysis and modeling of EDM parameters, Precision Engineering, 4 (1982) 215-221.
92. Guo J., Zhang G., Huang Y., Ming W., Liu M., Huang H., Investigation of the removing process of cathode material in micro-EDM using an atomistic-continuum model, Applied Surface Science, 315 (2014) 323-336.
93. Ming W., Shen D., Zhang Z., Li H., Chen Z., Guo J., Development of an Intelligent Process Model for Micro-EDM Based on TTM-MDS, Journal of Computational Information Systems, 10 (2014) 4855-4866.
94. Yang X., Guo J., Chen X., Kunieda M., Molecular dynamics simulation of the material removal mechanism in micro-EDM, Precision Engineering, 35 (2011) 51-57.
95. Wang T., Zhe J., Zhang Y.Q., Li Y.L., Wen X.R., Thermal and fluid field simulation of single pulse discharge in dry EDM, Procedia CIRP, 6(2013) 427-431.
96. Mahardika M., Tsujimoto T., Mitsui K., A new approach on the determination of ease of machining by EDM process, International Journal of Machine Tools & Manufacture, 48 (2008) 746-760.
97. Hass P., Pontelandolfo P., Perez R., Particle hydrodynamics of the electrical discharge machining process, part 1: physical considerations and wire EDM process improvement, Procedia CIRP, 6 (2013) 41-46.
98. Wang J., Han F., Simulation model of debris and bubble movement in consecutive-pulse discharge of electrical machining, International Journal of Machine Tools & Manufacture, 77 (2014) 56-65.
99. Liu S., Huang Y., Li Y., Plate capacitor model of the EDM process based on the field emission theory, International Journal of Machine Tools & Manufacture, 51 (5011) 653-659.
100. Pandit S.M., Rajurkar K.P., Analysis of electro discharge machining of cemented carbides, CIRP Annals, 30(1) (1981) 111-116.
101. Rajesh R., Anand M.D., The optimization of the electro-discharge machining process using response surface methodology and genetic algorithms, Procedia Engineering, 38 (2012) 3941-3950.
102. Ugrasen G., Ravindra H.V., Prakash G.V.N., Keshavamurthy R., Estimation of machining performances using MRA, GMDH, and artificial neural network in wire EDM of EN-31, Procedia Materials Science, 6 (2014) 1788-1797.
103. Mahapatra S.S., Patnaik A., Optimization of wire electrical discharge machining (WEDM) process parameters using Taguchi method, International Journal of Advanced Manufacturing Technology, 34 (2007) 911-925.
104. Boopathi S., Sivakumar K., Experimental investigation and parameter optimization of near-dry wire-cut electrical discharge machining using multi-objective evolutionary algorithm, international Journal of Advanced Manufacturing Technology, 67 (2013) 2639-2655.

105. Liao Y.S., Huang J.T., Su H.C., A study of the machining-parameters optimization of wire electrical discharge machining, Journal of Materials Processing Technology, 71 (1997) 487-493.
106. Huang J.T., Liao Y.S., Hsue W.J., Determination of finish-cutting operation number and machining-parameters setting in wire electrical discharge machining, Journal of Materials Processing Technology, 87 (1999) 69-81.
107. Al-Ghamdi K.A., Aspinwall E., Modelling an EDM process using multilayer perceptron network, RSM, and high-order polynomial, Advances in Mechanical Engineering, (2014) 791242.
108. Tosun N., Cogun C., An investigation on wire wear in WEDM, Journal of Materials Processing Technology, 134 (2003) 273-278.
109. Petropoulos G., Vaxevanidis N.M., Pandazaras C., Modeling of surface finish in electro-discharge machining based upon statistical multi-parameter analysis, Journal of materials Processing Technology, 155-156 (2004) 1247-1251.
110. Shashikant, Roy A.K., Kumar K., Effect and optimization of various machine process parameters on the surface roughness in EDM for an EN19 material using response surface methodology, Procedia Materials Science, 5 (2014) 1702-1709.
111. Das M.K., Kumar K., Barman T.K., Sahoo P., Application of artificial bee colony algorithm for optimization of MRR and surface roughness in EDM of EN31 tool steel, Procedia Materials Science, 6 (2014) 741-751.
112. Habib S.S., Study of the parameters in electrical discharge machining through response surface methodology approach, Applied Mathematical Modelling, 33 (2009) 4397-4407.
113. Assarzadeh S., Ghoreishi M., Statistical modeling and optimization of process parameters in electro-discharge machining of cobalt-bonded tungsten carbide composite (WC/6%Co), Procedia CIRP, 6 (2013) 463-468.
114. Gopalakannan S., Senthivelan T., Ranganathan S., Modeling and optimization of EDM process parameters on machining of Al 7075-B_4C MMC using RSM, Procedia Engineering, 38 (2012) 685-690.
115. Pal A.K., Banerjee S., Laha D., A comparative study of RSM model and ANN model of electrical discharge machining process, Proceeding of 23th AIMTDR conference, IIT Madras, Chennai, India, 2008.
116. Maji K., Pratihar D.K., Forward and reverse mappings of electrical discharge machining process using adaptive network-based fuzzy inference system, Expert Systems with Applications, 37 (2010) 8566-8574.
117. Mohanty C.P., Mahapatra S.S., Singh M.R., An experimental investigation of machinability of Inconel 718 in electrical discharge machining, Procedia Materials Science, 6 (2014) 605-611.
118. Sahu J., Mohanty C.P., Mahapatra S.S., A DEA approach for optimization of multiple responses in electrical discharge machining of AISI D2 Steel, Procedia Engineering, 51 (2013) 585-591.
119. Yuan J., Wang K., Yu T., Fang M., Reliable multi-objective optimization of high-speed WEDM process based on Gaussian process regression, International Journal of Machine Tools & Manufacture, 48 (2008) 47-60.
120. Yuan J., Liu C.L., Liu X., Wang K., Yu T., Incorporating prior model into Gaussian processes regression for WEDM process modeling, Expert Systems with Applications, 36 (2009) 8084-8092.
121. Ming W., Zhang G., Li H., Guo J., Zhang Z., Huang Y., Chen Z., A hybrid process model for EDM based on finite-element method and Gaussian process regression, International Journal of Advanced Manufacturing Technology, 74 (2014) 1197-1211.
122. Langhaar H.L., Dimensional analysis and theory of models. Wiley, New York, 1957.
123. Wang P.J., Tsai K.M., Semi-empirical model on work removal and tool wear in electrical discharge machining, Journal of Materials Processing Technology, 114 (2001) 1-17.
124. Tsai K.M., Wang P.J., Semi-empirical model on surface finish work removal and tool wear in electrical discharge machining, International Journal of Machine Tools & Manufacture, 41 (2001) 1455-1477.
125. Patil N.G., Brahmankar P.K., Determination of material removal rate in wire electro-discharge machining of metal matrix composites using dimensional analysis, International Journal of Advanced Manufacturing Technology, 51 (2010) 599-610.
126. Deng J.L., Control problems of grey system, System & Control Letters, 1 (1982) 288-294.
127. Liu W., Jia Z., Zou S., Zhang L., A real-time predictive control method of discharge state for micro-EDM based on calamities grey prediction theory, International Journal of Advanced Manufacturing Technology, 72 (2014) 135-144.
128. Chiang K.T., Chang F.P., Applying grey forecasting method for fitting and predicting the performance characteristics of an electro-conductive ceramic (Al_2O_3+30%TiC) during electrical

discharge machining, International Journal of Advanced Manufacturing Technology, 33 (2007) 480-488.

129. Jia Z., Zhang L., Wang F., Liu W., A new method for discharge state prediction of micro-EDM using empirical mode decomposition, Journal of Manufacturing Science and Engineering, 132 (2010) 014501-1-6.
130. Zhou M., Chen Z., Niu J., Building an EDM process model by an instrumental variable approach, Procedia CIRP, 6 (2013) 456-462.
131. Zhou M., Meng X., Qin J., Chen Z., Lian X., Building and EDM process model by an instrumental variable approach based on two interactive Kalman filters, Precision Engineering, 37 (2013) 146-158.
132. Zhou M., Han F., Soichiro I., A time-varied predictive model for EDM process, International Journal of Machine Tools & Manufacture, 48 (2008) 1668-1677.
133. Mandal D., Pal S.K., Saha P., Modeling of electrical discharge machining process using back propagation neural network and multi-objective optimization using non-dominating sorting genetic algorithm-II, Journal of Materials Processing Technology, 186 (2007) 154-162.
134. Joshi S.N., Pande S.S., Intelligent process modeling and optimization of die-sinking electric discharge machining, Applied Soft Computing, 11 (2011) 2743-2755.
135. Rao G.K.M., Rangajanardhaa G., Rao D.H., Rao M.S., Development of hybrid model and optimization of surface roughness in electric discharge machining using artificial neural networks and genetic algorithm, Journal of Materials Processing Technology, 209 (2009) 1512-1520.
136. Wang K., Gelgele H.L., Wang Y., Yuan Q., Fang M., A hybrid intelligent method for modeling the EDM process, International Journal of Machine Tools & Manufacture, 43 (2003) 995-999.
137. Shabgard M.R., Badamchizadeh M.A., Ranjbary G., Amini K., Fuzzy approach to select machining parameters in electrical discharge machining (EDM) and ultrasonic-assisted EDM processes, Journal of Manufacturing Systems, 32 (2013) 32-39.
138. Sengottuvel P., Satishkumar S., Dinakaran D., Optimization of multiple characteristics of EDM parameters based on desirability approach and fuzzy modeling, Procedia Engineering, 64 (2013) 1069-1078.
139. Lin C.L., Lin J.L., Ko T.C., Optimisation of the EDM process based on the orthogonal array with fuzzy logic and grey relational analysis method, International Journal of Advanced Manufacturing Technology, 19 (2002) 271-277.
140. Lin J.L., Lin C.L., The use of grey-fuzzy logic for the optimization of the manufacturing process, Journal of Materials Processing Technology, 160 (2005) 9-14.
141. Tzeng Y.F., Chen F.C., Multi-objective optimization of high-speed electrical discharge machining process using a Taguchi fuzzy-based approach, Materials and Design, 28 (2007) 1159-1168.
142. Teimouri R., Baseri H., Optimization of magnetic field assisted EDM using continuous ACO algorithm, Applied Soft Computing, 14 (2014) 381-389.
143. Salman O., Kayacan M.C., Evolutionary programming method for modeling the EDM parameters for roughness, Journal of Materials Processing Technology, 200 (2008) 347-355.
144. Vapnik V., The Nature of Statistical Learning Theory, Springer, New York, 1995.
145. Cristianini N., Taylor J.S., An Introduction to Support Vector Machines and other kernel-based-learning methods, Cambridge University Press, 2000.
146. Smola A.J., Scholkopf B., A tutorial on support vector regression, Statistics and Computing, 14(3) (2004) 199-222.
147. Sapankevych N.I., Sankar R., Time series prediction using support vector machines: a survey, IEEE Computational Intelligence Magazine, 4(2) (2099) 24-38.
148. Gunn S.R., Support Vector Machines for Classification and Regression, Technical report, University of Southampton, May 10, 1998.
149. Yu P.S., Chen S.T., Chang I.F., Support vector regression for real-time flood stage forecasting, Journal of Hydrology, 328 (2006) 704-716.
150. Levis A.A., Papageorgiou L.G., Customer demand forecasting via support vector regression analysis, Chemical Engineering Research and Design, 83(A8) (2005) 1009–1018.
151. Zhang L., Jia Z., Wang F., Liu W., A hybrid model using supporting vector machine and multi-objective genetic algorithm for processing parameters optimization in micro-EDM, International Journal of Advanced Manufacturing Technology, 51 (2010), 575-586.
152. Çaydaş U., Ekici S., Support vector machines models for surface roughness prediction in CNC turning of AISI 304 austenitic stainless steel, Journal of Intelligent Manufacturing, 23(3) (2012), 639-650.

153. Ramesh R., Kumar K.S.R., Anil G., Automated intelligent manufacturing system for surface finish control in CNC milling using support vector machines, International Journal of Advanced Manufacturing Technology, 42 (2009), 1103-1117.
154. Lela B., Bajić D., Jozić S., Regression analysis, support vector machines, and Bayesian neural network approaches to modeling surface roughness in face milling, International Journal of Advanced Manufacturing Technology, 42 (2009) 1082-1088.
155. Dong H., Wu D., Su H., Use of least square support vector machine in surface roughness prediction model, Proceeding of 3rd International Symposium on Precision Mechanical Measurement, 6280 (2006) 628022.
156. Jiang Z., Intelligent prediction of surface roughness of milling aluminium alloy based on least square support vector machine, IEEE, (2010) 2672-2876.
157. Wang P., Meng Q., Zhao J., Li J., Wang X., Prediction of machine tool condition using support vector machine, Journal of Physics: Conference Series, 305 (2011) 012113.
158. Yusup N., Zain A.M., Hashim S.Z.M., Evolutionary techniques in optimizing machining parameters: review and recent applications (2007-2011), Expert Systems with Applications, 39 (2012) 9909-9927.
159. Rajmohan T., Prabhu R., Subha G.R., Palanikumar K.B., Optimization of machining parameters in electrical discharge machining (EDM) of 304 stainless steel, Procedia Engineering, 38 (2012) 1030-1036.
160. Bergaley A., Sharma N., Optimization of electrical and non electrical factors in EDM for machining die steel using copper electrode by adopting Taguchi technique, International Journal of Innovative Technology and Exploring Engineering, 3 (2013) 44-48.
161. Ramakrishnan R., Karunamoorthy L., Modeling and multi-response optimization of Inconel 718 on machining of CNC WEDM process, Journal of Materials Processing Technology, 207 (2008) 343-349.
162. Gauri S.K., Chakraborty S., A study on the performance of some multi-response optimization methods for WEDM processes, International Journal of Advanced Manufacturing Technology, 49 (2010) 155-166.
163. Scott D., Boyina S., Rajurkar K.P., Analysis and optimization of parameter combinations in wire electrical discharge machining, International Journal of Production Research, 29(11) (1991) 2189-2207.
164. Das M.K., Kumar K., Barman T.K., Sahoo P., Optimization of surface roughness and MRR in EDM using WPCA, Procedia Engineering, 64 (2013) 446-455.
165. Jegan T.M.C., Anand M.M.D., Ravindran D., Determination of electro discharge machining parameters in AISI202 stainless steel using grey relational analysis, Procedia Engineering, 38 (2012) 4005-4012.
166. Vikas, Roy A.K., Kumar K., Effect of optimization of various machine process parameters on the surface roughness in EDM for an EN41 material using Grey-Taguchi, Procedia Materials Science, 6 (2014) 383-390.
167. Goswami A., Kumar J., Optimization in wirecut EDM of Nimonic-80A using Taguchi’s approach and utility concept, Engineering Science and Technology: An International Journal, 17 (2014) 236-246.
168. Dewangan S., Gangopadhyay S., Biswas C.K., Study of surface integrity and dimensional accuracy in EDM using Fuzzy TOSIS and sensitivity analysis, Measurement, 63 (2015) 364-376.
169. Saha. S., Pachon M., Ghoshal A., Schulz M.J., Finite element modeling and optimization to prevent wire breakage in electro-discharge machining, Mechanics Research Communications 31 (2004) 451-463.
170. Mukherjee I., Ray P.K., A review of optimization techniques in metal cutting processes, Computers and Industrial Engineering, 50 (2006) 15-34.
171. Rao S.S., Engineering optimization - Theory and practice, John Wiley & Sons, 2009.
172. Deb K., Optimization for Engineering Design: Algorithms and Example, PHI learning, 2007.
173. Yang S.H., Srinivas J., Mohan S., Lee D.M., Balaji S., Optimization of electric discharge machining using simulated annealing, Journal of Materials Processing Technology, 209 (2009) 4471-4475.
174. Aich U., Pal A.K., Laha D., Banerjee S., Searching for a Pareto optimal solution set of EDM responses applying multi-objective simulated annealing on RSM model, Advanced Materials Research, 622-623 (2013) 51-55.

175. Su J.C., Kao J.Y., Tarng Y.S., Optimisation of the electrical discharge machining process using GA-based neural network, International Journal of Advanced Manufacturing Technology, 24 (2004) 81-90.
176. Mukherjee R., Chakraborty S., Samanta S., Selection of wire electrical discharge machining process parameters using non-traditional optimization algorithms, Applied Soft Computing, 12 (2012) 2506-2516.
177. Goswami A., Kumar J., Investigation of surface integrity, material removal rate and wire wear ratio for WEDM of Nimonic 80A alloy using GRA and Taguchi method, Engineering Science and Technology: an International Journal, 17 (2014) 173-184.
178. Kennedy J., Eberhart R., Particle swarm optimization, Proceeding of IEEE International Conference on Neural Networks, Piscataway, NJ, 4 (1995) 1942-1948.
179. Shayan A.V., Afza R.A., Teimouri A., Parametric study along with selection of optimal solutions in dry wire cut machining of cemented carbide (WC-Co), Journal of Manufacturing Processes, 15 (2013) 644-658.
180. Nara K., Takeyama T., Kim H., A new evolutionary algorithm based on sheep flocks heredity model and its application to scheduling problem, Proceeding of IEEE International Conference on Systems, Man and Cybernetics, (1999) 503-508.
181. Kim H., Ahn B., A new evolutionary algorithm based on sheep flocks heredity model, Proceeding of IEEE Conference on Communications, Computers and Signal Processing, (2001) 514-517.
182. Karaboga D. An artificial bee colony (ABC) algorithm for numeric function optimization, Proceeding of the IEEE swarm intelligence symposium, 2005.
183. Simon D., Biography-based optimization, IEEE Transactions on Evolutionary Computation, 12 (2008) 702-713.
184. Rao R.V., Savsani V.J., Vakharia D.P., Teaching-learning-based optimization: a novel method for constrained mechanical design optimization problems, Computer-Aided Design, 43 (2011) 303-315.
185. Rao R.V., Review of applications of TLBO algorithm and a tutorial for beginners to solve the unconstrained and constrained optimization problems, Decision Science letters, 5 (2016) 1-30.
186. Rao R.V., Kalyankar V.D., Parameter optimization of modern machining process using teaching-learning-based optimization algorithm, Engineering Applications of Artificial Intelligence, 26 (2013) 524-531.
187. Pawar P.J., Rao R.V., Parameter optimization of machining processes using teaching–learning-based optimization algorithm, International Journal of Advanced Manufacturing Technology, 67 (2013) 995-1006.
188. Rao R.V., Kalyankar V.D., Multi-pass turning process parameter optimization using teaching–learning-based optimization algorithm, Scientia Iranica, 20(3) (2013) 967-974.
189. Abhishek K., Kumar V.R., Datta S., Mahapatra S.S., Parametric appraisal and optimization in machining of CFRP composites by using TLBO (teaching–learning based optimization algorithm), Journal of Intelligent Manufacturing, 28 (2017) 1769-1785.
190. Petropoulos G.P., Pandazaras C.N., Davim J.P., Surface texture characterization and evaluation related to machining, in: Davim J.P. (Eds.), Surface integrity in Machining, Springer London, 2010, pp. 37-66.
191. Ramasawmya H., Blunt L., Effect of EDM process parameters on 3D surface topography, Journal of Materials Processing Technology, 148 (2004) 155–164.
192. Zhu Y., Zou J., Zhao W.L., Chen X.B., Yang H.Y., A study on surface topography in cavitation erosion tests of AlSi10Mg, Tribology International, 102 (2016) 419-428.
193. Roy S., Bhattacharyya A., Banerjee S., Analysis of effect of voltage on surface texture in electrochemical grinding by autocorrelation function, Tribology International, 40 (2007) 1387-1393.
194. Murti V.S.R., Philip P.K., Textural characteristics of EDM surfaces, Proceeding of 13th AIMTDR conference, Jadavpur University, Kolkata, India, 1988, F-01-06.
195. Jeswani M.L., Basu S., Electron microprobe study of deposition and diffusion of tool material in EDM, International Journal of Production Research, 17(1) (1979) 1-14.
196. Pandit S.M., Rajurkar K.P., A stochastic approach to thermal modeling applied to electro-discharge machining, Journal of Heat Transfer, 105 (1983) 555-562.
197. Williams R.E., Rajurkar K.P., Study of wire electrical discharge machined surface characteristics, Journal of Materials Processing Technology, 28 (1991) 127-138.
198. Yeo S.H., Kurnia W., Tan PC. Electro-thermal modeling of anode and cathode in micro-EDM, Journal of Physics D: Applied physics, 40 (2007) 2513-2521.

199. Schumacher B.M., About the role of debris in the gap during electro discharge machining. CIRP Annals, 39 (1990) 197-199.
200. Kunieda M., Yanatori K., Study on debris movement in EDM gap, International Journal of Electrical Machining, 2 (1997) 43-49.
201. Bommeli B., Frei C., Ratajski A., On the influence of mechanical perturbation on the breakdown of a liquid dielectric, Journal of Electrostatics, 7 (1979) 123-144.
202. Kunieda M., Nakashima T., Factors determining discharge location in EDM, International Journal of Electrical Machining, 3 (1998) 53-58.
203. Cooke R.F., Crookall J.R., An investigation of some statistical aspects of electro-discharge machining, International Journal of Machine Tool Design and Research, 13 (1973) 271-286.
204. Gatto A., Sofroniou M., Spaletta G., Bassoli E., On the chaotic nature of electro-discharge machining, International Journal of Advanced Manufacturing Technology, 79 (2015) 985-996.
205. Barun T., Lisboa J.A., Francke R.E., Gallas J.A.C., Observation of deterministic chaos in electrical discharges in gas, Physical Review Letters, 59 (1987) 613-616.
206. Lorenz E.N., Deterministic nonperiodic flow, Journal of the Atmospheric Sciences, 20 (1963) 130-141.
207. Tang L., Lv H., Yang F., Yu L., Complexity testing techniques for time series data: a comprehensive literature review, Chaos, Solitons and Fractals, 81 (2015) 117-135.
208. Kędra M., Deterministic chaotic dynamics of Reba river flow (Polish Carpathian mountains), Journal of Hydrology, 509 (2014) 474-503.
209. Hu Z., Zhang C., Luo G., Teng Z., Jia C., Characterizing cross-scale chaotic behaviors of the runoff time series in an inland river of Central Asia, Quaternary International, 311 (2013) 132-139.
210. Goon A.M., Gupta M.K., Dasgupta B., Fundamentals of statistics, vol. I, 5th revised edition, The World Press Private Ltd., Calcutta, India, 1975.
211. Banerjee S., Mahapatro D., Dubey S., Some study on electrical discharge machining of ({WC+TiC+TaC/NbC}-Co) cemented carbide, International Journal of Advanced Manufacturing Technology, 43 (2009) 1177-1188.
212. Hu X., Eberhart R., Multiobjective Optimization using dynamic neighborhood particle swarm optimization, Proceeding of the 2002 Congress on Evolutionary Computation, 2 (2002) 1677-1681.
213. Clerc M., Kennedy J., The particle swarm: explosion stability and convergence in a multi-dimensional complex space, IEEE Transactions on Evolutionary Computation, 6 (2002) 58-73.
214. Tripathi P.K., Bandyopadhyay S., Pal S.K., Multi-objective particle swarm optimization with time variant inertia and acceleration coefficients, Information Science, 177 (2007) 5033-5049.
215. Tang Y., Wang Z., Fang J., Parameters identification of unknown delayed genetic regulatory networks by a switching particle swarm optimization algorithm, Expert Systems with Applications, 28 (2011) 2523-2535.
216. Shi Y., Eberhart R.C., Parameter selection in particle swarm optimization, Proceeding of 7th International Conference on Evolutionary Programming VII, LNCS, New York, Springer-Verlag, 1447 (1998) 591-600.
217. Ratnaweera A., Halgamure S.K., Watson H.C., Self-organizing hierarchical particle swarm optimizer with time-varying acceleration coefficients, IEEE Transactions on Evolutionary Computation, 8 (2004) 240-255.
218. Cherkassky V., Ma Y., Practical selection of SVM parameters and noise estimation for SVM regression, Neural Networks, 17 (2004) 113–126.
219. Rao R.V., Savsani V.J., Vakharia D.P., Teaching-learning-based optimization: an optimization method for continuous non-linear large scale problems, Information Sciences, 183 (2012) 1-15.
220. Rao R.V., Patel V., Multi-objective optimization of two stage thermoelectric cooler using a modified teaching-learning-based optimization algorithm, Engineering Applications of Artificial Intelligence, 26 (2013) 430-445.
221. Marler R.T., Arora J.S., Survey of multi-objective optimization methods for engineering, Structural and Multidisciplinary Optimization, 26(6) (2004) 369–395.
222. Athan T.W., Papalambros P.Y., A note on weighted criteria methods for compromise solutions in multi-objective optimization, Engineering Optimization, 27(2) (1996) 155–176.
223. Box G.E.P., Jenkins G.M., Time series analysis forecasting and control, Revised edition, Holden-Day, Oakland, California, 1976.
224. Koehl P., Linear prediction spectral analysis of NMR data, Progress in Nuclear Magnetic Resonance Spectroscopy, 34 (1999) 257-299.

225. Lin Y.Y., Hodgkinson P., Ernst M., Pines A., A novel detection-estimation scheme for noisy NMR signals: application to delayed acquisition data, Journal of Magnetic Resonance, 128 (1997) 30-41.
226. Porat B., Friedlander B., A modification of the Kumaresan-Tufts method for estimating rational impulse responses, IEEE Transactions on Acoustics, Speech and Signal Processing, 34 (1986) 1336-1338.
227. Zhu G., Bax A.D., Improved linear prediction of damped NMR signals using modified "forward-backward" linear prediction, Journal of Magnetic Resonance, 100 (1992) 202-207.
228. Conover W.J., Iman R.J., Rank transformations as a bridge between parametric and non-parametric statistics, The American Statistician, 35 (1981) 124-129.
229. Pande S.S., Computer Graphics and Product Modeling for CAD/CAM, Narosa Publishing House Pvt. Ltd., New Delhi, India, 2012.
230. Kellert S.H., In the wake of chaos: unpredictable order in dynamical systems, The University of Chicago Press, Chicago and London, 1993.
231. Gleick J., Chaos: Making a new Science. United Kingdom, Viking Books, 1987.
232. Wiggins S., Introduction to Applied Nonlinear Dynamical Systems and Chaos, New York, Springer Verlag, 1990.
233. Isliker H., A scaling test for correlation dimension, Physics Letters A, 169 (1992) 313-322.
234. Luo X., Small M., Geometric measures of redundance and irrelevance tradeoff exponent to choose suitable delay times for continuous systems, arXiv preprint nlin/0312023.
235. Strogatz S.T., Nonlinear Dynamics and Chaos with Applications to Physics, Biology, Chemistry and Engineering, Perseus Book Publishing, L.L.C., 1994.
236. Kantz H., Schreiber T., Nonlinear Time Series Analysis, United Kingdom, Cambridge University Press, 2004.
237. Grassberger P., Procaccia I., Measuring the strangeness of strange attractors, Physica D: Nonlinear Phenomena, 9(1-2) (1983) 189-208.
238. Budáčová H., Štolc S., Measurement, Proceedings of the 9th International Conference on Measurement, Smolenice, Slovakia, 2013.
239. Takens F., Lecture Notes on Mathematics, Springer, Berlin, vol. 898, 1981.
240. Theiler J., Spurious dimension from correlation algorithms applied to limited time-series data, Physical Review A, 34(3) (1986) 2427-2432.
241. Provenzale A., Smith L.A., Vio R., Murante G., Distinguishing between low-dimensional dynamics and randomness in measured time series, Physica D: Nonlinear Phenomena, 58 (1-4) (1992) 31-49.
242. Yu D., Small M., Harrison R.G., Diks C., Efficient implementation of the Gaussian kernel algorithm in estimating invariants and noise level from noisy time series data, Physical Review E, 61 (4) (2000) 3750-3756.
243. Cuicui J., Hua Z., Wei J., Chinese Science Bulletin, 56 (2011) 925-932.
244. Ding C., Zhu H., Sun G., Zhou Y., Zuo X., Chaotic characteristics and attractor evolution of friction noise during friction process, Friction, 6 (1) (2018) 47-61.
245. Gottwald G.A., Melbourne I., A new test for chaos in deterministic systems, Proceedings of The Royal Society of London A, 460 (2004) 603-612.
246. Gottwald G.A., Melbourne I., On the Implementation of the 0-1 Test for Chaos, SIAM Journal of Applied Dynamical Systems, 8 (2009) 129-145.

APPENDICES

APPENDIX A

SUPPORT VECTOR MACHINE REGRESSION
PARTICLE SWARM OPTIMIZATION
AND
TEACHING LEARNING BASED OPTIMIZATION

A.1 Support vector machine (SVM) regression

Suppose, a representative model is developed for a disjoint, independent and identical distributed data set $\{(x_1, y_1), (x_2, y_2), \ldots\ldots (x_N, y_N)\}$ in d dimensional input space (i.e. $\boldsymbol{x} \in \boldsymbol{R}^d$). Target function may be represented in the form [146]

$$f(\boldsymbol{x}) = \langle \boldsymbol{w}, \boldsymbol{x} \rangle + b \tag{A.1}$$

where < , > indicates dot product in vector space. Nonlinearity in the relation between input and output pattern (figure A.1) [145] is handled through mapping the high dimensional input space to a feature space $\Phi(\boldsymbol{x})$ via kernel functions. So, optimal choice of weight factor $\boldsymbol{w}$ and threshold b (bias term) is prerequisite of accurate modeling. Flatness of the model is controlled by minimizing Euclidean norm $||\boldsymbol{w}||$. Besides, empirical risk of training error should also be minimized [147]. So, regularized risk minimization problem for model developing can be written as follows.

$$R_{reg}(f) = \frac{||\boldsymbol{w}||^2}{2} + C \sum_{i=1}^{N} L(y_i, f(x_i)) \tag{A.2}$$

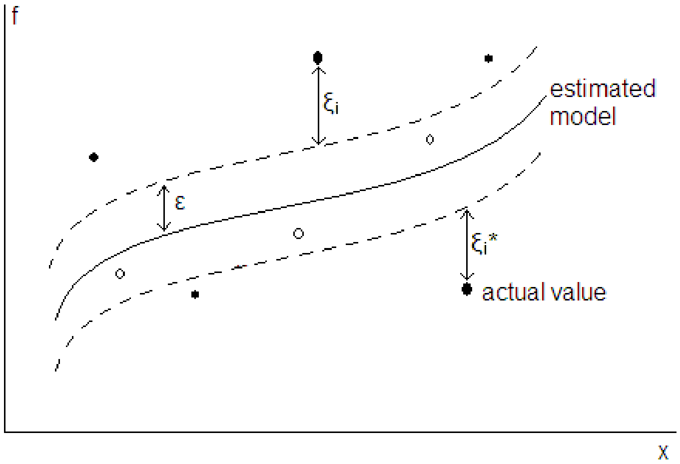

Fig. A.1 Non-linear SVM regression model

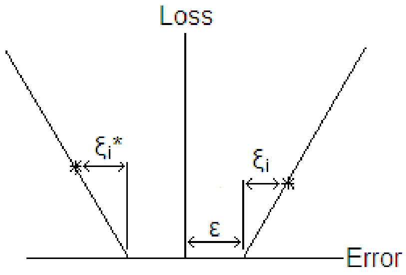

Fig. A.2 ε-insensitive loss function

Weight vector $\boldsymbol{w}$ and the bias term b can be estimated by optimizing this function (equation (A.2)) which minimizes empirical risk along with reduction of generalization error that is over fitting of model simultaneously. Thus, regularization parameter (C) and loss function are introduced to penalize over fitting of model with training vectors.

Different loss functions namely quadratic loss function, Huber loss function, ε-Insensitive loss function etc. are developed for handling different types of problems [148]. In general, the loss functions are some modified measurements of distances between the points and their corresponding estimated values. Squared value of the distance is considered for assigning loss in quadratic loss function. Quadratic loss function corresponds to the conventional least square error criterion. Huber loss function is the combination of linear and quadratic loss functions. This robust loss function exhibits optimal properties when the underlying distribution of the data is unknown. Still, the above said two loss functions, quadratic and Huber, will produce no sparseness in the support vectors. To address the issues, Vapnik [144] proposed ε-insensitive loss function as a trade-off between the robust loss function of Huber and one that enables sparsity within the support vectors. ε-Insensitive loss function (refer figure A.2) may be defined as [145]

$$\begin{aligned} L(y_i, f(x_i)) &= |y_{i,\text{experimental}} - f(x_i)| - \varepsilon, && \text{if } |y_{i,\text{experimental}} - f(x_i)| \geq \varepsilon \\ &= 0, && \text{if } |y_{i,\text{experimental}} - f(x_i)| < \varepsilon \end{aligned} \tag{A.3}$$

In most of the model building techniques, data are fitted through least training error calculation to estimate the unknown coefficients or weight vectors associated with training inputs. All the data are tried to fit as close as possible to the deemed model. In SVM regression, an insensitive zone wrapped around the estimated function is defined. This insensitive zone is expected to capture the fluctuations within predefined permissible tolerance. Thereby, radius of this hyper tube directly controls the allowable complexity of the learning system. In nomenclature, the outliers around this tube are named as support vectors. Here, ε-insensitive loss function (refer equation (A.3)) is considered to penalize over fitting of the system.

As, this radius of insensitive hyper-tube increases, model would become more flat and become unable to reveal the unseen nature of variations in the outcomes, whereas, lower radius might make the model more complex. Thus a trade-off between complexity and flatness of the estimated model is required. Two positive slack variables ξ_i and ξ_i^* are introduced [144, 146] to cope with infeasible constraints of the optimization problem. Hence the constrained problem can be reformulated as

$$\begin{aligned} \text{minimize:} \quad & \frac{\|\boldsymbol{w}\|^2}{2} + \mathrm{C}\sum_{\mathrm{i}=1}^{\mathrm{N}}(\xi_\mathrm{i} + \xi_\mathrm{i}^*) \\ & y_{i,exp} - \langle \boldsymbol{w}, \boldsymbol{x} \rangle_i - b \le \varepsilon + \xi_i \\ \text{subject to:} \quad & \langle \boldsymbol{w}, \boldsymbol{x} \rangle_i + b - y_{i,exp} \le \varepsilon + \xi_i^* \\ & \xi_i, \xi_i^* \ge 0, \quad \boldsymbol{i} = 1(1)N \end{aligned} \tag{A.4}$$

This problem can be efficiently solved by standard dualization principle utilizing Lagrange multipliers. A dual set of variables is introduced for developing Lagrange function. It is found that this function has a saddle point with respect to both primal and dual variables at the solution. Lagrange function can be stated as

$$\begin{aligned} \mathrm{L} = {} & \frac{\|\boldsymbol{w}\|^2}{2} + \mathrm{C}\sum_{\mathrm{i}=1}^{\mathrm{N}}(\xi_\mathrm{i} + \xi_\mathrm{i}^*) - \sum_{\mathrm{i}=1}^{\mathrm{N}}(\eta_\mathrm{i}\xi_\mathrm{i} + \eta_\mathrm{i}^*\xi_\mathrm{i}^*) - \sum_{\mathrm{i}=1}^{\mathrm{N}} \alpha_i(\varepsilon + \xi_\mathrm{i} - \mathrm{y}_\mathrm{i} + \langle \boldsymbol{w}, \boldsymbol{x} \rangle_\mathrm{i} + \mathrm{b}\xi_\mathrm{i}^*) \\ & - \sum_{\mathrm{i}=1}^{\mathrm{N}} \alpha_\mathrm{i}^*(\varepsilon + \xi_\mathrm{i}^* + \mathrm{y}_\mathrm{i} - \langle \boldsymbol{w}, \boldsymbol{x} \rangle_\mathrm{i} - \mathrm{b}) \end{aligned} \tag{A.5}$$

where L is the Lagrangian and η_i, η_i^*, α_i, α_i^* are Lagrange multipliers satisfying $\eta_i, \eta_i^*, \alpha_i, \alpha_i^* \ge 0$. So, partial derivatives of L with respect to w, b, ξ_i, ξ_i^* will give the estimates of $\boldsymbol{w}$ and b.

Support vectors can be easily identified from the values of differences between Lagrange multipliers (α_i, α_i^*). Very small values (close to zero) indicate the points inside the insensitive hyper-tube but non-zero values belong to support vector group [149]. The $\boldsymbol{w}$ can be calculated as follows [146].

$$\boldsymbol{w} = \sum_{\mathrm{i}=1}^{\mathrm{N}}(\alpha_\mathrm{i} - \alpha_\mathrm{i}^*)\, \Phi(\mathrm{x}_\mathrm{i}) \tag{A.6}$$

The idea of kernel function K (x_i, $\boldsymbol{x}$) gives a way of addressing the curse of dimensionality [148]. It helps to enable the operations to be performed in the feature space (Φ ($\boldsymbol{x}$)) rather than potentially high dimensional input space. A number of kernel functions satisfying Mercer's condition are suggested by researchers [149, 150]. Each of the functions has its own specialized applicability. Use of Polynomial kernel function is a popular method for non-linear modeling. The long established multi-layer perceptron with a single hidden layer has a valid kernel representation for certain values of the scale and offset parameters. Fourier series kernel is probably not a good choice because of poor regularization capability, which is evident by consideration of its Fourier transform. Among different splines, specifically B-Spline is also a popular choice for its better flexibility. Exponential radial basis function produces a piecewise linear solution which can be attractive when discontinuities are acceptable. Apart from all the kernel functions, Gaussian radial basis function gets significant attention as this kernel is implicit with each support vector contributing one local Gaussian function centered at that data point.

Here, Gaussian radial basis function with σ standard deviation (equation (A.7)) is used for its better potentiality to handle higher dimensional input space.

$$\mathrm{K}\,(x_i, \boldsymbol{x}) = e^{-\frac{\|\mathrm{x}_\mathrm{i} - x\|^2}{2\sigma^2}} \Bigg|_{\sigma\ \text{optimum}} \tag{A.7}$$

However, representative model of the learning system with optimum choices of the most significant internal structural parameters, namely C, ε and σ, may be presented as [146]

$$f(\boldsymbol{x}) = \sum_{i=1}^{N}(\alpha_i - \alpha_i^*)\, K(x_i, \boldsymbol{x}) + b \,\Bigg|_{\substack{C_{\text{optimum}} \\ \varepsilon_{\text{optimum}} \\ \sigma_{\text{optimum}}}} \tag{A.8}$$

To get the benefit of this exclusive feature of SVM regression over other model development techniques, internal structural parameters of SVM regression, namely the regularization parameter (C) which controls the penalty associated with support vector, radius of insensitive tube (ε) and standard deviation of Gaussian radial basis kernel function (σ), are to be properly tuned. Improper choice of the three parameters may lead to under-fitting or over-fitting of the actual process. Thus, for each set of input-output combination, an optimum set of SVM internal structural parameters, C, ε and σ, is expected.

A.2 Particle swarm optimization (PSO)

Particle swarm optimization (PSO) technique is one of the most advanced evolutionary computational intelligence based optimization methodologies for optimizing real world multimodal problems. Particle swarm optimization mimics natural behavior found in flock of birds or school of fish seeking their best food sources [178]. In this population based swarm intelligence technique, a set of randomly initialized particles is always updated in position and velocity by gathering information from themselves. Effect of each particle and experience of the whole swarm modify the position of population forwarding to optimum zone. Rate of convergence is purposefully controlled by different factors. Convergence is delayed due to improper choice or may lead to entrapping in local optima. For multivariable problem in high dimensional space, time and memory space needed for reaching optimum solution by PSO are very important. Main steps involved in PSO are briefly listed as

Step 1 : p_{best} and g_{best} from current particles are identified.

Step 2 : Inertia factor, weight factor, cognitive and social acceleration coefficients, velocity of each of the particles in swarm are modified with current p_{best} and g_{best}.

Step 3 : Velocity corrected position vector of each of the particles is evaluated.

Step 4 : Check the termination criterion. If satisfied, current g_{best} is declared as optimum setting, otherwise repeat the steps with current upgraded particles till termination criterion is satisfied.

Number of particles (n) in swarm should be within the range (10, 40) [212]. Lower choice may not gather information from whole space but higher value of n will take longer time to converge in optimum zone.

Inertia factor (ω) controls the effect of previous velocity of individual particle on current velocity. To modify the rate of convergence another control on simulation is done by introducing constriction factor (Ψ) [213]. This term bounds the velocity effect of the particles on their positions avoiding clamping of particles to one end of search space [214]. So, higher values of inertia and constriction factor ensure wide searching which are necessary at initial stage but gradual convergence is enhanced at moderately lower values.

Another two important factors are cognitive acceleration coefficient (c_1) and social acceleration coefficient (c_2) which greatly control the influence of the experience of the individual particle and the whole swarm respectively on new velocity of particle. Individual best of each particle that is p^i_{best} of i^{th} particle influences the exploration in the search space but the best position of swarm that is g_{best} always guide to converge near-optimum zone. Therefore, choice of the factors becomes important for converging to global optimum zone quickly avoiding premature entrapping in local optima.

Different values of the control factors are proposed by the researchers for their different types of problems. However, in most of the cases, nearly a same range is suggested irrespective of the nature of problem [215]. Shi and Eberhart [216] suggested linearly decreasing inertia factor from 0.9 to 0.4. Cognitive acceleration coefficient should vary linearly with iterations from 2.5 to 0.5 while the variation of social acceleration coefficient would occur just in reverse order [217]. Since constriction factor directly controls the optimization time, it may be considered as linearly time varying from 0.9 to 0.4.

Further, maximum number of iterations is to be set properly. A large value is necessary for adequate convergence. In other words, simulation will be terminated before reaching this limiting value.

A.3 Teaching learning based optimization (TLBO)

Compared to traditional deterministic approaches for optimization of multimodal, high dimensional non-linear large scale engineering problems, metaheuristic algorithms exhibit more promising performances [219]. Natural phenomena inspired trajectory and population based different algorithms are still suffering from the problem of tuning their own internal parameters [184, 219]. Rao et al. [184] introduced an algorithm-specific parameter-less optimization technique which mimics the ideology of teaching-learning process, called as teaching learning based optimization (TLBO). A class of learners is considered as the population of the optimization algorithm. In TLBO, different subjects offered to the learners and scores of the learners in the offered subjects are analogous to different control variables and values of objective function respectively. Marching steps of TLBO to reach global optimum are broadly divided in two phases namely teacher phase and learner phase.

In teacher phase, teacher always tries to pull forward the batch of learners aiming to his/her own level. Gaining more knowledge from teacher helps the learners to score better marks. Therefore, teacher gradually increases the mean score of the learners according to his/her own capability. Still the knowledge dissemination by the teacher and acquiring of knowledge by the learners are not always same for all teacher-learner combinations. Thus, a teaching factor should play a typical role in this teacher phase. In the present study, adaptive teaching factor [220] depending upon the current performance level of the whole batch is deployed instead of randomly selected integer between 1 and 2 [219]. This adaptive teaching factor (TF), calculated as a ratio of mean of the values of learners to value of teacher of latest population [220], aids in converging the simulation with lesser time.

Gaining of knowledge by the learners is further enhanced through different schemes of interactions among themselves namely group discussions, presentations, formal communications etc. The intra-learner interactions are performed in the second phase that is learner phase. In this learner phase, each of the learners is randomly selected and compared with another randomly selected different learner. If the other learner has more knowledge than him/her, then, the former learner gains some knowledge from the other one. By this way, scores of the learners are increased. Main steps involved in TLBO are briefly listed as

Step 1 : The learner having best score is identified and considered as teacher.

Step 2 : Adaptive TF is calculated and all learners are modified towards the teacher.

Step 3 : All modified learners (two at a time) are randomly selected and upgraded themselves.

Step 4 : Check the termination criterion. If satisfied, current teacher is declared as optimum setting, otherwise repeat the steps with current upgraded learners till termination criterion is satisfied.

However, exploitation of the search space is done in teacher phase, whereas, learner phase does the exploration. In every iteration, values of the objective function that is scores of the current learners in each subject gradually move towards optimum zone.

APPENDIX B

FLOW CHART

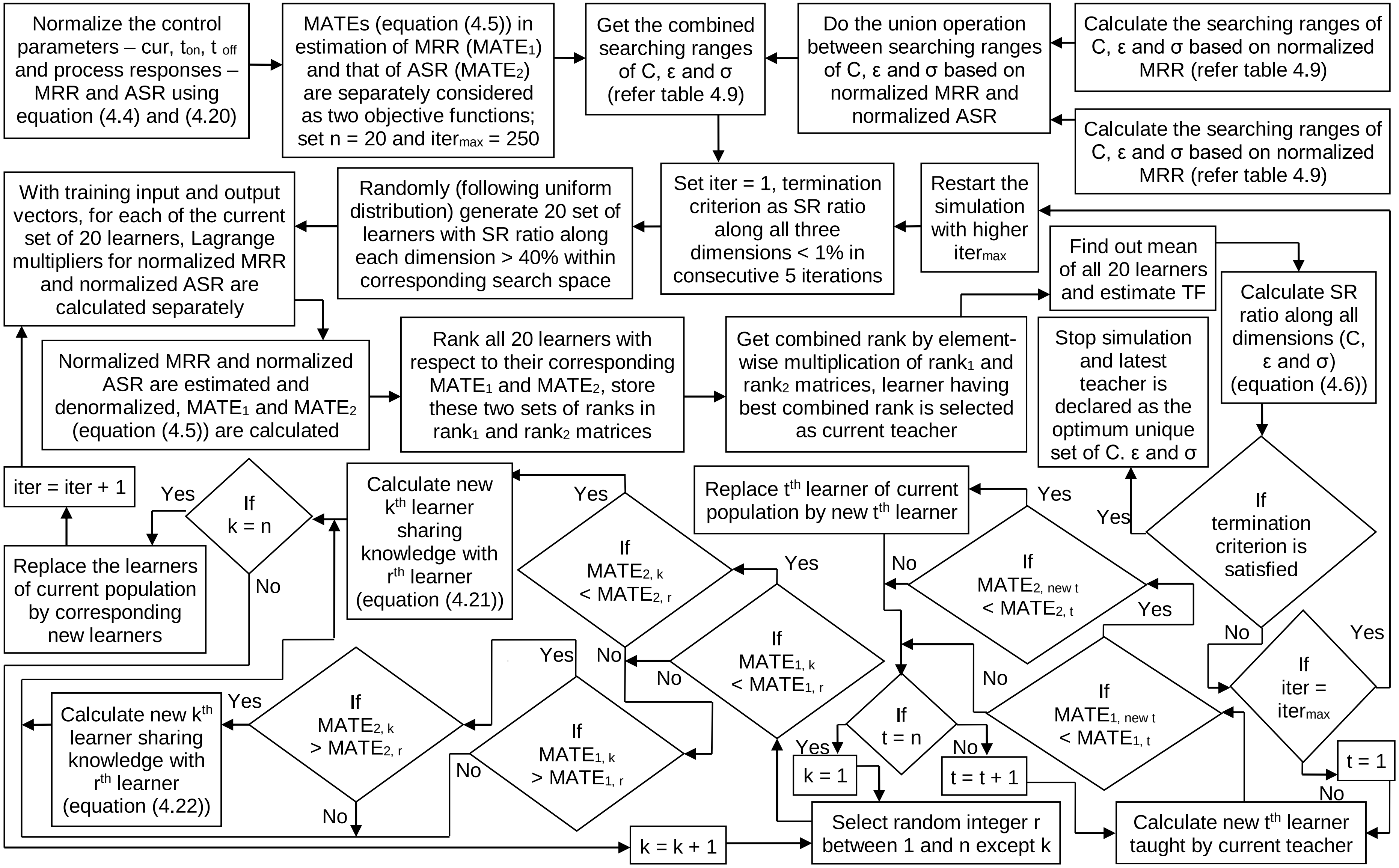

Fig. B.1 Sequence diagram of proposed modified TLBO to search optimum unique set of C, ε and σ by simultaneous minimization of $MATE_1$ and $MATE_2$

APPENDIX C

FIGURES

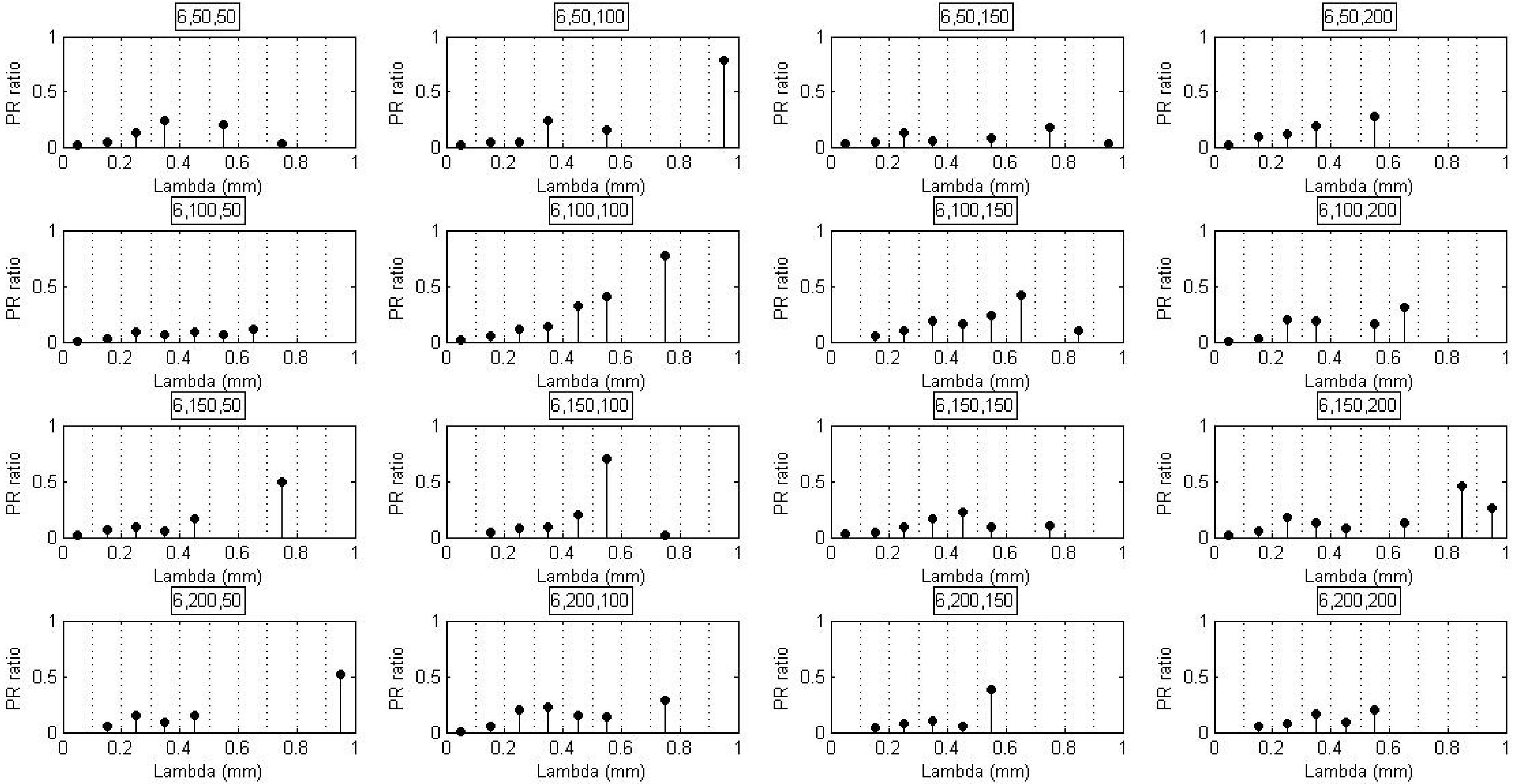

Fig. C.1. Variations of PR ratios at different combinations of levels of t_{on} and t_{off} at cur = 6 A

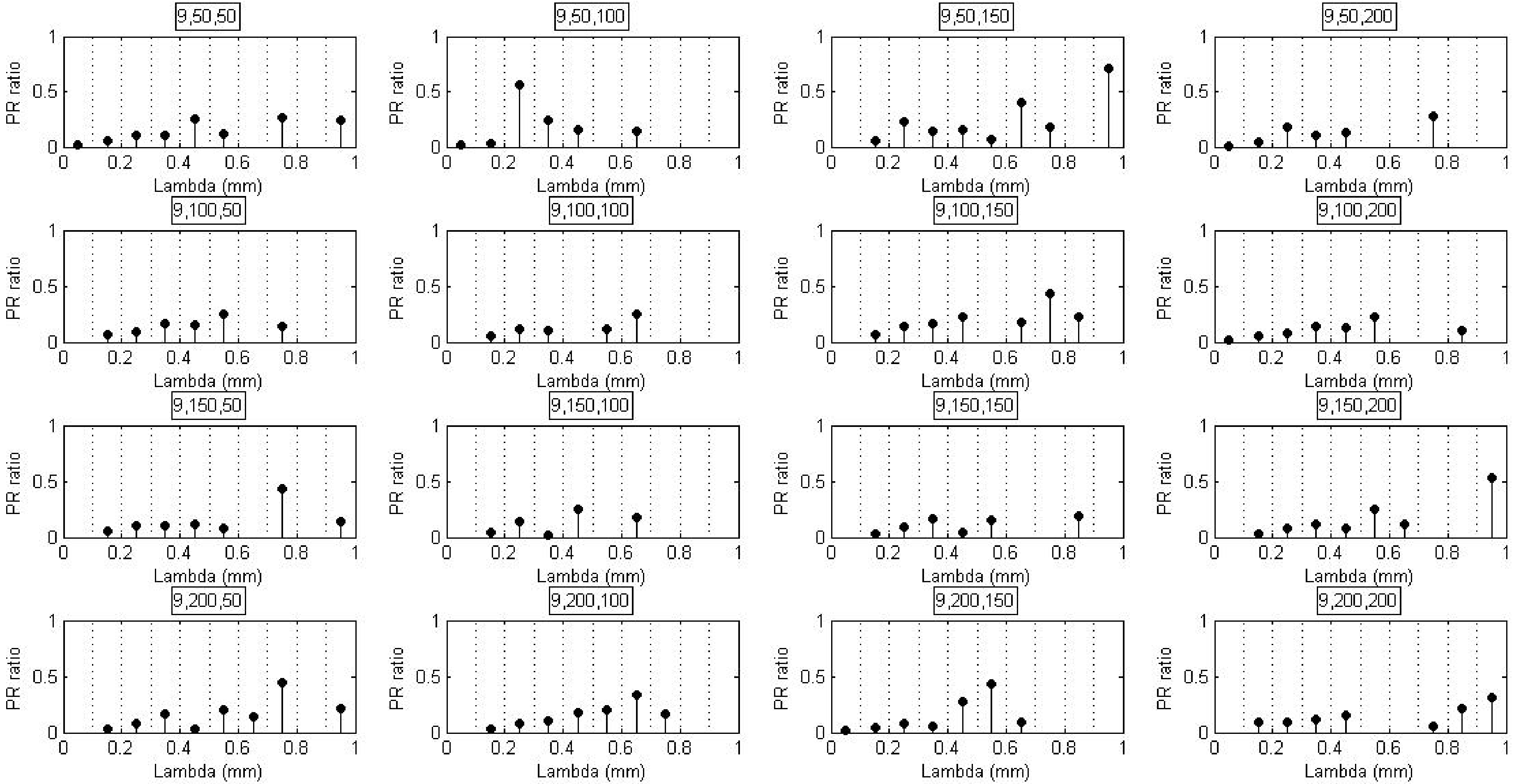

Fig. C.2. Variations of PR ratios at different combinations of levels of t_{on} and t_{off} at cur = 9 A

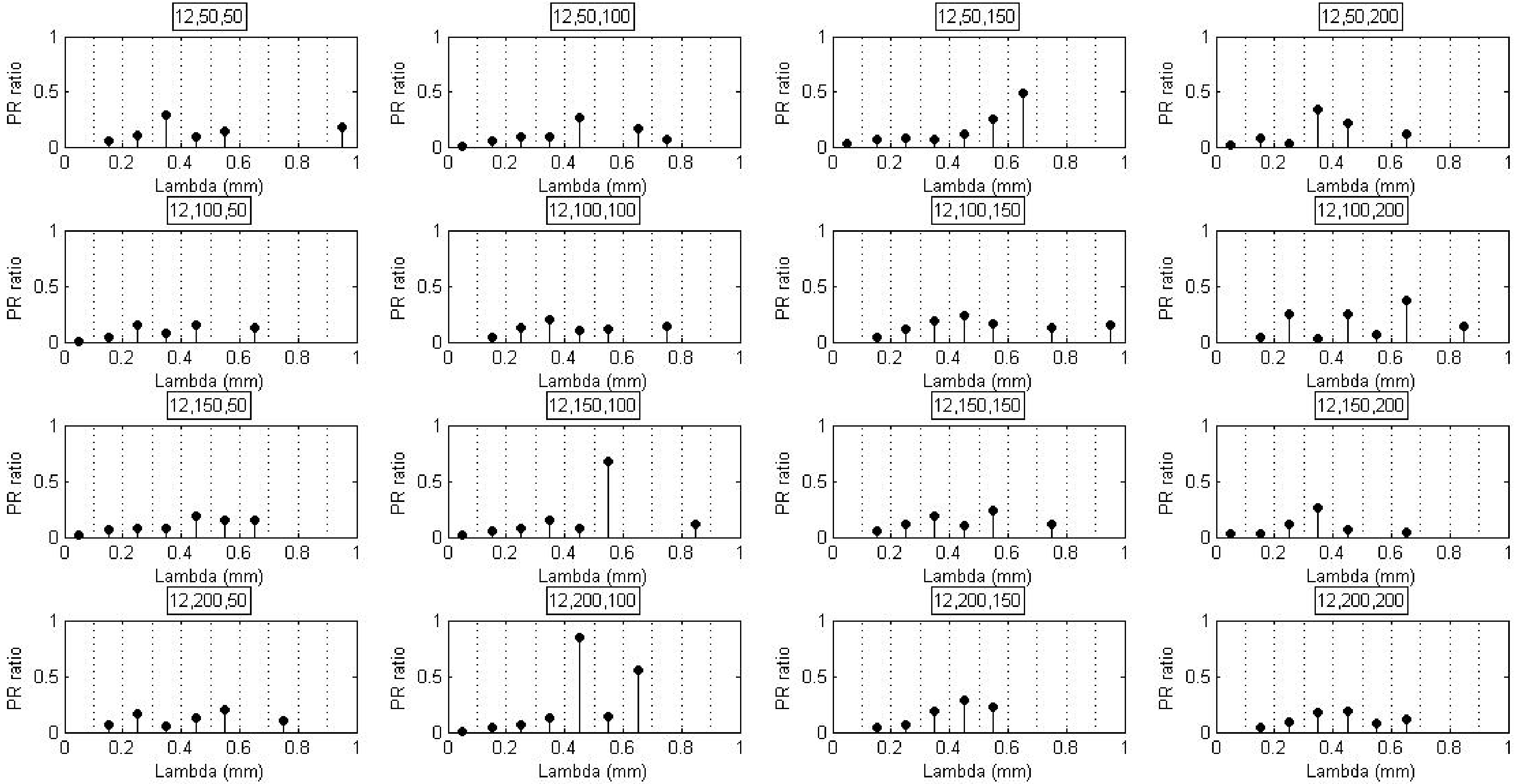

Fig. C.3. Variations of PR ratios at different combinations of levels of t_{on} and t_{off} at cur = 12 A

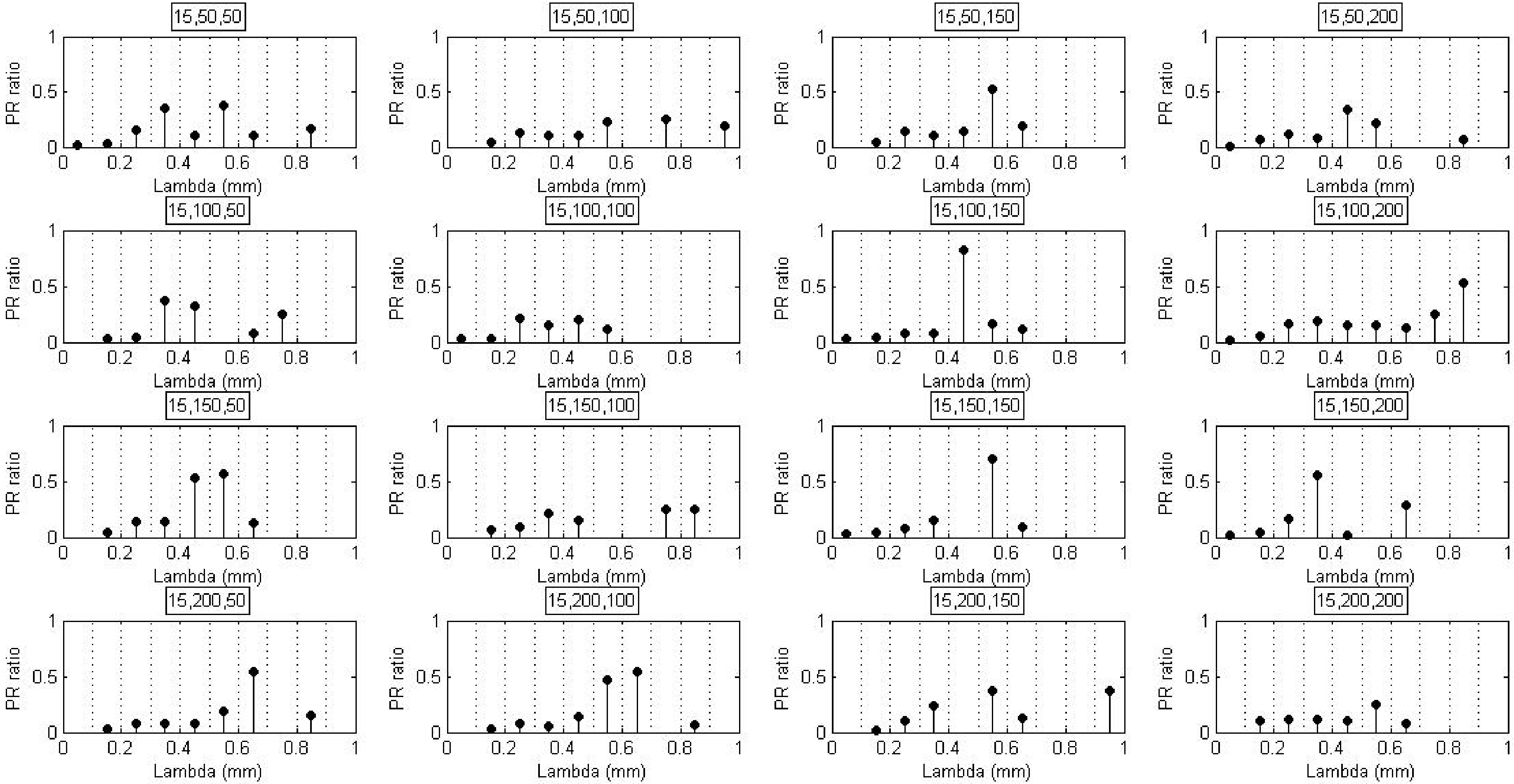

Fig. C.4. Variations of PR ratios at different combinations of levels of t_{on} and t_{off} at cur = 15 A

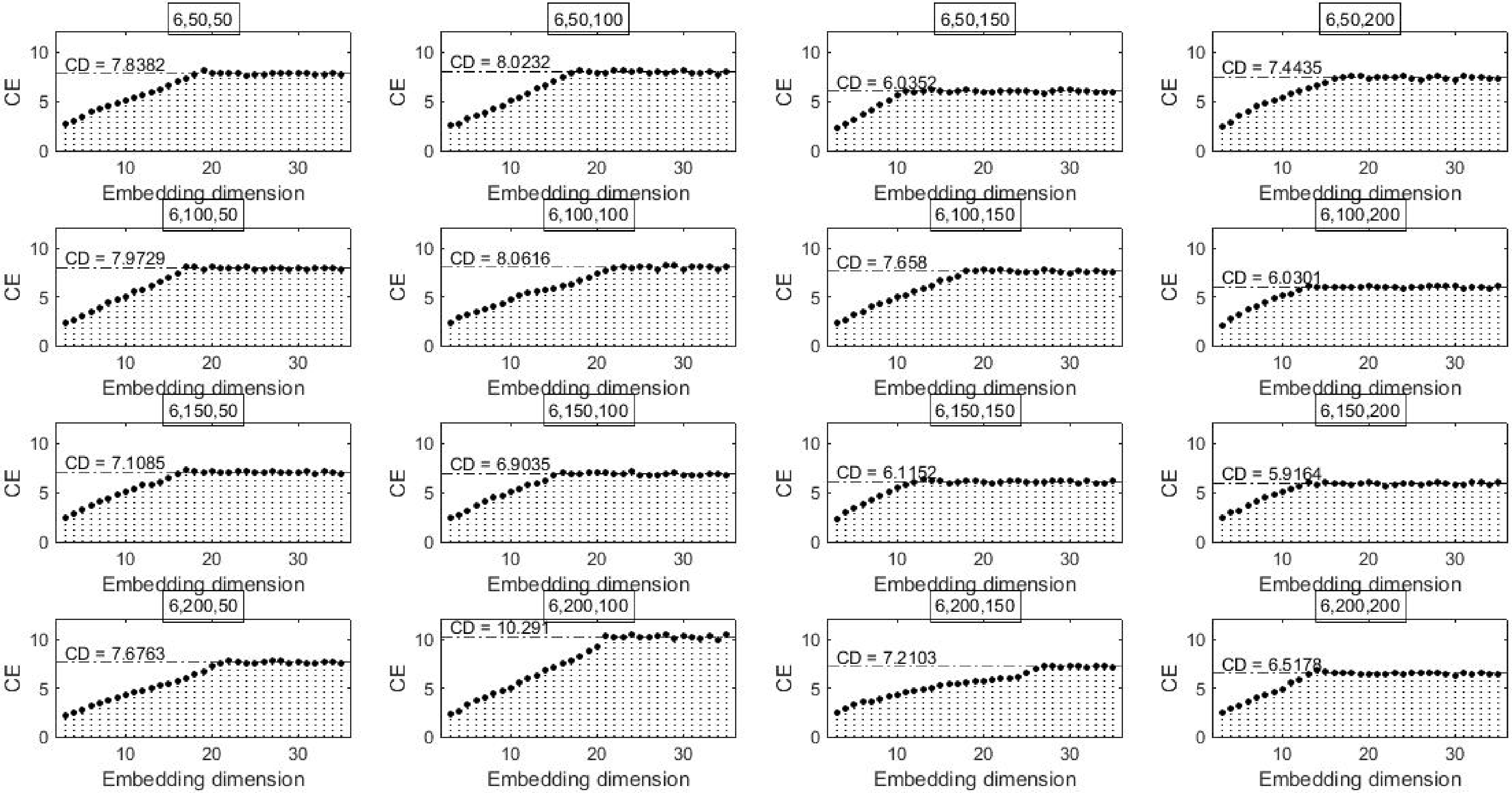

Fig. C.5 Variations of correlation exponents at different combinations of levels of t_{on} and t_{off} at current = 6 A

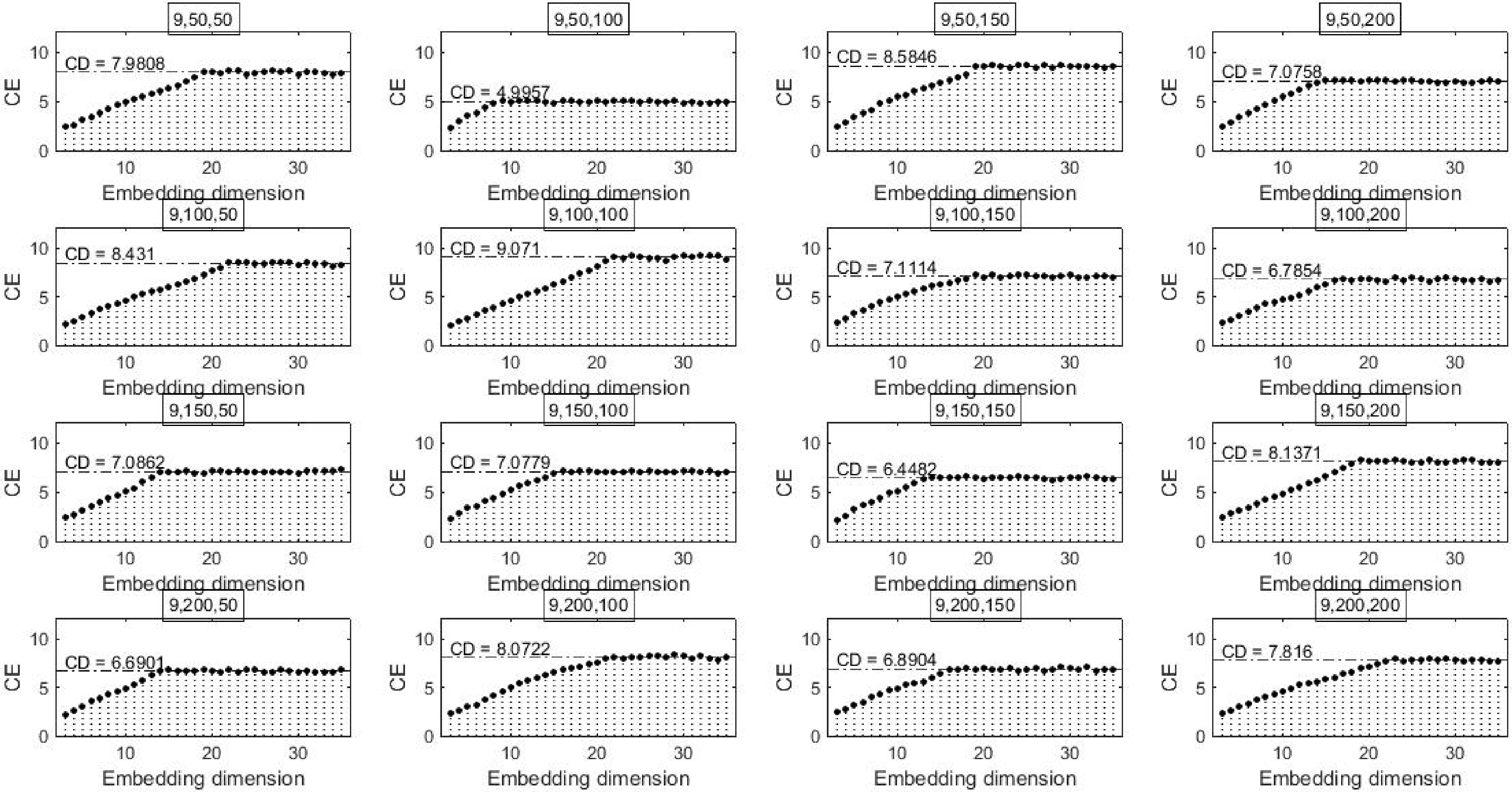

Fig. C.6 Variations of correlation exponents at different combinations of levels of t_{on} and t_{off} at current = 9 A

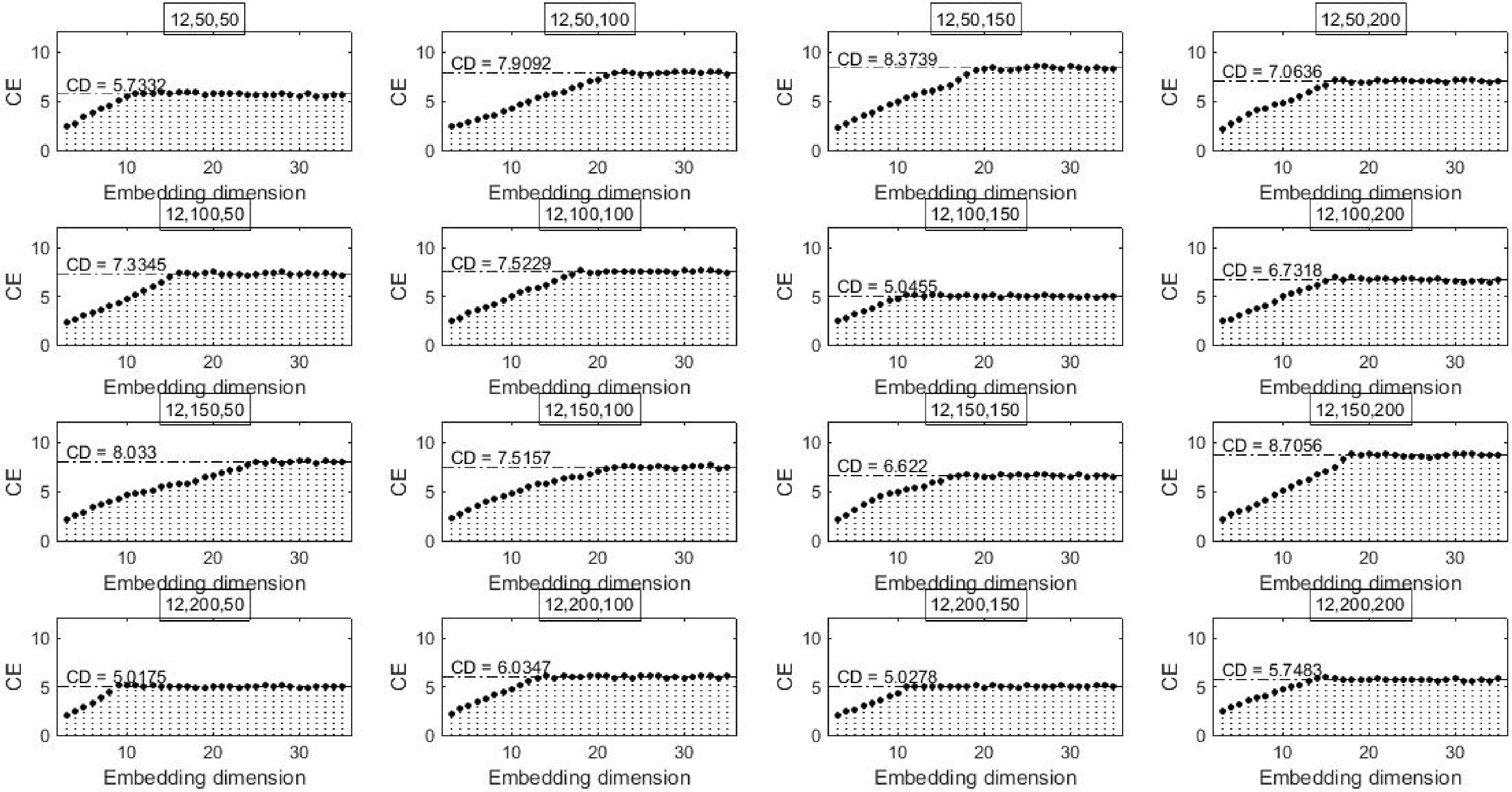

Fig. C.7 Variations of correlation exponents at different combinations of levels of t_{on} and t_{off} at current = 12 A

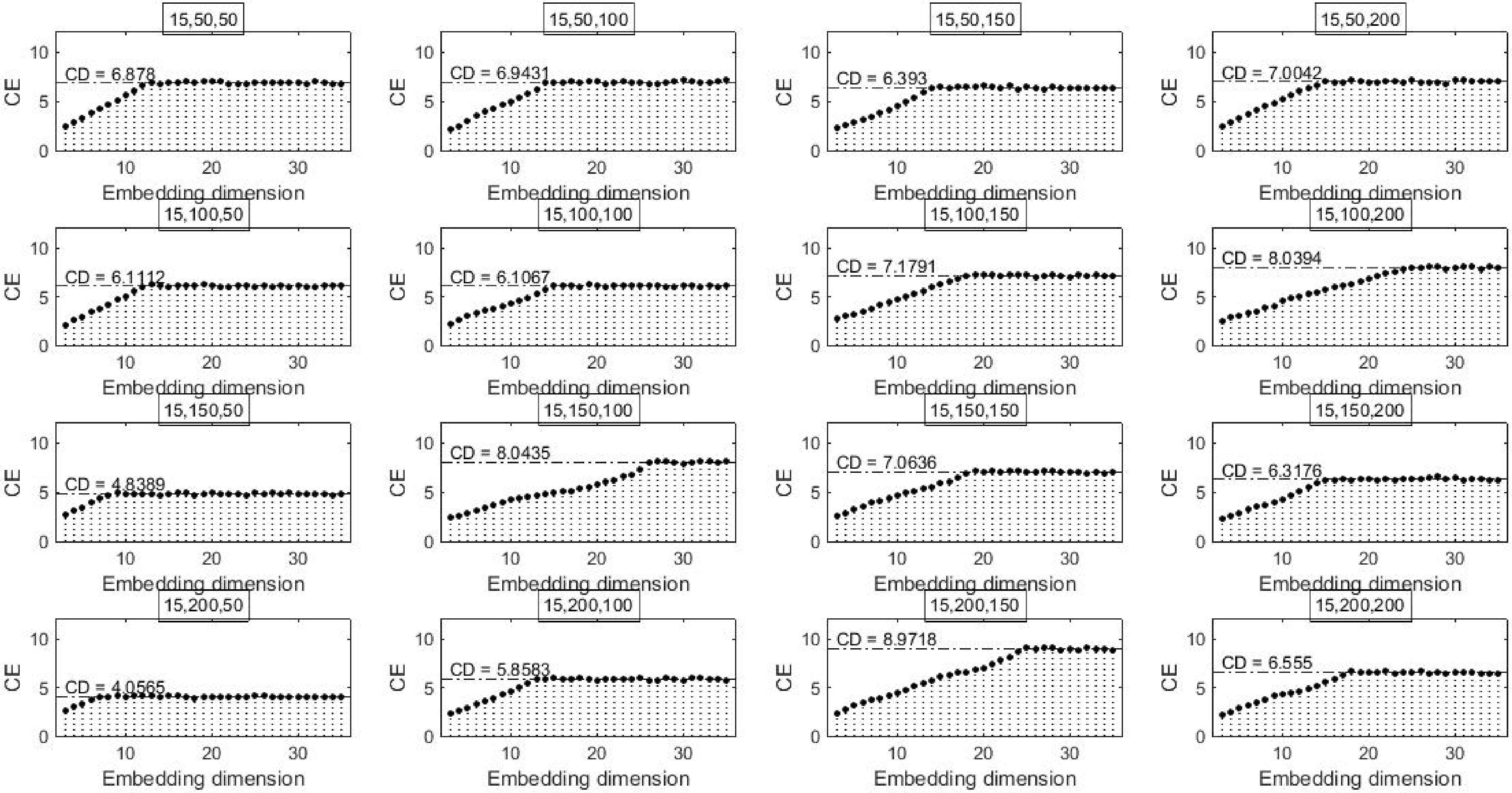

Fig. C.8 Variations of correlation exponents at different combinations of levels of t_{on} and t_{off} at current = 15 A

APPENDIX D

TABLES

Table D.1 Plasma channel characteristics

Sl. no.	Ref. [Year]	Plasma channel characteristics
1	32 [1983]	$R(t) = K Q^m t^n$; $K = \frac{L}{lM+0.5N}$; $m = 0.5N$ and $n = N$ R = spark radius, t = time, Q = discharge power, l = discharge length, m, n, K, M, N = constants
2	61 [1986]	$T_b = \frac{E_0 R}{K\pi^{0.5}} \tan^{-1}\left[\frac{4\alpha t}{R^2}\right]^{0.5}$ T_b = boiling temperature, E_0 = energy density, R = spark radius, α = thermal diffusivity, t = time, K = constants
3	62 [1989]	$R_{plasma}(t) = R_p t^{0.75}$ R_{plasma} = plasma channel radius (μm), t = time (μs), R_p = constant
4	63 [1996]	temperature of the plasma channel varies in the range of 8000-10000 K and decreases slowly with time
5	64 [2000]	$R(t) = 2.85\, I_p^{0.53}\, t^{0.38}$ R = plasma channel radius, I_p = discharge current, t = time
6	65 [2003]	constant plasma channel radius = 0.75 μm
7	66 [2004]	plasma channel diameter = 50-400 μm, temperature = 8100± 1750 K, pressure = 4.5 bar
8	67 [2004]	plasma channel temperature = 5500-7000 K
9	68 [2005]	plasma channel diameter varies in the range of 34-57 μm and temperature is about 7000 K
10	69 [2008]	plasma channel diameter grows to about 250 μm after 1.7 μs of dielectric breakdown
11	70 [2009]	$R_{plasma}(t) = R_p t^{0.2}$ R_{plasma} = plasma channel radius (μm), t = time (μs), R_p = constant
12	71 [2009]	$R_{sp}(t) = K I^m t_{on}^n$ R_{sp} = plasma channel radius (μm), I = discharge current (A), t_{on} = pulse on time, m, n, K = constants
13	72 [2009], 73 [2010]	$R_{sp} = 2040\, I^{0.43}\, t_{on}^{0.44}$ R_{sp} = plasma channel radius (μm), I = discharge current (A), t_{on} = spark duration (μs)
14	21 [2013]	plasma channel radius = 0.2 mm at pulse duration = 105 μs
15	74 [2013]	$R(t) = 0.0249\, t^{0.75}$ R = plasma channel radius (m), t = discharge time (s)
16	75 [2014]	$R_{pc} = K t_e^n$ R_{pc} = plasma channel radius (mm), K, n = constants, t_e = pulse duration (μs), plasma channel radius = 0.11 mm at pulse duration = 52 μs, plasma channel radius = 0.43 mm at pulse duration = 840 μs

Table D.2 Comparison among fundamental thermal models [86]

Ref. [Year] Features	87 [1971]	88 [1974]	89, 90 [1981]	91 [1982], 78 [1983], 61 [1986]	18 [1989]
Main considerations	• Two dimensional heat flow • Semi-infinite cylinder with circular heat source	• Two dimensional heat flow • Finite cylinder with circular heat source on the surface	• Two dimensional heat flow • Semi-infinite cylinder heated over a disk-shaped region	• Two dimensional heat flow • Semi-infinite body with a disk heat source on the surface	• One dimensional heat flow • Point heat source
Assumptions	• Upper part of electrode is adiabatic • Constant thermo-physical properties of the material over the whole temperature range • Erosion takes place in the molten area of electrode • Constant heat flux	• Upper part of electrode is adiabatic • Constant thermo-physical properties of the material over the whole temperature range • Erosion takes place in the molten area of electrode • Constant heat flux	• Surface beyond the disk region is insulated • Constant thermo-physical properties of the material over the whole temperature range • Erosion takes place in the molten area of electrode • Constant heat flux	• Uniform heat flux with constant radius • Constant thermo-physical properties of the material over the whole temperature range • Erosion takes place in the molten area of electrode • Plasma channel is expanding with time	• Heat flux from a point heat source • Average thermo-physical properties of the material over the whole temperature range • Erosion takes place in the molten area of electrode • Plasma radius remains small during the discharge
% of discharge energy	50 %	50 %	50 %	50 %	18 %
Radius of heat flux	Constant	Constant	Constant	Expanding with time	Not applicable
Limitations	• Approximation of heat flux radius is not readily available • Effects of vaporization is neglected • Guideline for the value of outer cylinder radius is not available	• Approximation of heat flux radius is not readily available • The number of terms used highly affect the results • No guideline for the determination of electrode thickness	• Approximation of heat flux radius is not readily available • Effects of vaporization is neglected • Direct application of a disk heat source	• Effects of vaporization is neglected • Guideline for the value of outer cylinder radius is not available	• In small t_{on}, heat flux radius is large compared to crater radius • Effects of melting and vaporization is neglected • The crater profile resulted is hemispherical

Table D.3 Initial position vectors for modeling of MRR and ASR with C, ε and σ tuned by modified PSO

Particle no.	Material removal rate			Average surface roughness		
	C	ε	σ	C	ε	σ
1	2.8692	0.3741	0.6413	7.8464	0.2182	0.6413
2	27.6309	0.3705	0.4735	8.5362	0.6271	0.4735
3	27.3996	0.9601	0.4921	8.7711	0.6377	0.4921
4	10.1175	0.3718	0.7914	4.7648	0.3734	0.7914
5	24.0751	1.0408	0.7303	4.7332	0.4760	0.7303
6	8.1387	0.4240	0.4764	8.9144	0.2271	0.4764
7	25.8437	0.7102	0.7927	7.0968	0.6105	0.7927
8	23.2679	1.0917	0.4666	4.1319	0.2278	0.4666
9	2.6193	1.0371	0.6027	4.2077	0.4283	0.6027
10	3.0346	0.6132	0.7503	8.9040	0.2768	0.7503
11	28.0965	0.9792	0.7616	8.6920	0.2475	0.7616
12	2.2017	0.4416	0.4731	6.1559	0.6164	0.4731
13	21.1043	1.0947	0.7820	8.6928	0.5995	0.7820
14	4.5689	1.1037	0.7528	4.5076	0.3030	0.7528
15	25.3141	0.4255	0.7442	4.0201	0.2226	0.7442
16	3.7709	0.6065	0.7526	3.9201	0.5580	0.7526
17	6.1115	0.3996	0.7766	8.9605	0.4274	0.7766
18	3.2125	0.3955	0.5132	7.5031	0.2547	0.5132
19	22.3486	0.4083	0.4744	8.7844	0.6364	0.4744
20	27.6509	0.7158	0.6943	8.9504	0.6188	0.6943
Initial SR ratio (%)	40.63	40.18	40.45	40.39	40.06	40.45

Table D.4 Initial velocity vectors for modeling of MRR and ASR with C, ε and σ tuned by modified PSO

Particle no.	Material removal rate			Average surface roughness		
	C	ε	σ	C	ε	σ
1	-1.1420	-0.5874	0.2550	-2.6903	0.0859	-0.0538
2	16.1977	-0.4189	0.0710	1.4569	-0.1057	-0.3198
3	-9.5219	0.3831	0.1616	2.4293	0.1356	-0.1096
4	22.1250	0.0540	0.0253	-2.8482	-0.0470	-0.0311
5	26.6057	0.2248	-0.2527	-1.0113	0.0115	-0.0026
6	2.4647	0.5152	0.0114	-1.8713	0.0844	-0.1972
7	22.7751	-0.6845	-0.1259	-4.7858	0.3492	0.0349
8	-15.2420	-0.2692	0.1663	-0.7026	-0.2623	0.1614
9	23.3150	-0.4363	0.1352	5.1228	0.3883	-0.3054
10	-10.9557	-0.1002	-0.0747	-3.2326	-0.2852	0.0649
11	-12.7906	-0.6022	-0.2867	-1.1405	-0.3512	0.3070
12	20.9269	0.3702	0.1573	-3.0261	-0.3518	0.0198
13	-26.1034	-0.6633	0.1473	5.0315	0.4215	0.0467
14	16.6214	0.6079	0.2219	-1.7055	-0.3030	0.0026
15	11.0503	0.5777	0.1754	5.0611	-0.3597	0.0269
16	2.0973	-0.1111	-0.2908	-2.1017	0.1121	0.1956
17	-5.3766	-0.2315	-0.1144	-0.5855	0.0967	-0.0398
18	-1.4190	-0.5537	0.0976	2.4724	-0.0612	-0.0194
19	-22.3169	0.3308	-0.2901	-3.1377	0.3914	0.0463
20	3.8368	-0.2715	-0.0188	1.3004	0.0400	-0.0029

Table D.5 Difference of Lagrange multipliers (α_i, α_i^*) for modeling of MRR and ASR with C, ε and σ tuned by modified PSO
(# and ## indicate support vectors for MRR and ASR respectively)

Sl. no.	Training input vector (cur, t_{on}, t_{off})	Difference of Lagrange multipliers for MRR	Difference of Lagrange multipliers for ASR
1	(6, 50, 50)	0.3284838735#	-0.0000000019
2	(6, 50, 100)	-0.0000000905	5.6135729118##
3	(6, 50, 150)	-0.0000000203	2.0112101327##
4	(6, 50, 200)	-0.0000000711	-1.5737082907##
5	(6, 100, 100)	-14.8346053071#	-8.9977999768##
6	(6, 100, 150)	1.3684640154#	3.8048789847##
7	(6, 150, 50)	6.3557092185#	0.0000002966
8	(6, 150, 100)	4.3634812387#	8.9977998358##
9	(6, 150, 150)	13.4023480957#	-8.9977997524##
10	(6, 150, 200)	-6.2513732208#	-0.4504826345##
11	(6, 200, 50)	-1.0913087391#	0.8200597992##
12	(6, 200, 100)	-0.0000000620	-0.0000000345
13	(6, 200, 200)	-11.2255429582#	2.5978271284##
14	(9, 50, 50)	4.0130967043#	2.9196954829##
15	(9, 50, 100)	14.7045830684#	-0.0000000117
16	(9, 50, 150)	-0.0000000984	-8.9977999552##
17	(9, 50, 200)	0.0000000721	7.8455011954##
18	(9, 100, 50)	-0.0000008126	-1.0069938584##
19	(9, 100, 150)	4.3716848306#	8.9977999651##
20	(9, 100, 200)	-0.0000000198	-2.3436175891##
21	(9, 150, 100)	-11.5410265525#	4.9310973956##
22	(9, 150, 150)	0.0000000681	-4.1265497223##
23	(9, 150, 200)	-4.2034020028#	8.9977999350##
24	(9, 200, 50)	-0.6125952834#	-3.4244267611##
25	(9, 200, 150)	-8.0299868114#	-0.0000000197
26	(9, 200, 200)	28.0968999783#	0.0000000132
27	(12, 50, 100)	-7.5900649457#	-0.0000000104
28	(12, 50, 150)	-22.8724100613#	-0.0000000480
29	(12, 50, 200)	3.0917015612#	0.0000000244
30	(12, 100, 50)	0.0000000608	0.0000000951
31	(12, 100, 100)	-13.1081281553#	-3.7985708088##
32	(12, 100, 150)	28.0968993179#	3.6022598205##
33	(12, 100, 200)	0.0000000134	-7.9241061613##
34	(12, 150, 50)	-2.7063627361#	8.9977999519##
35	(12, 150, 100)	28.0968999258#	-8.9977999123##
36	(12, 150, 150)	-28.0968998613#	-5.3085517713##
37	(12, 200, 50)	17.2811542371#	-4.0032855127##
38	(12, 200, 100)	-28.0968999601#	8.9977999680##
39	(12, 200, 150)	28.0968998943#	-0.0000000573
40	(12, 200, 200)	-16.3297770771#	-0.0000000291
41	(15, 50, 50)	22.6634341946#	8.9977999810##
42	(15, 50, 100)	-28.0968998729#	-7.1733289197##
43	(15, 50, 150)	25.1909322194#	8.9977999835##
44	(15, 50, 200)	-0.0000004244	-0.3260243248##
45	(15, 100, 50)	15.1317773286#	-4.5413407219##
46	(15, 100, 150)	28.0968999745#	4.8724704393##
47	(15, 100, 200)	-28.0968998307#	0.0000000620
48	(15, 150, 100)	-28.0968999703#	8.9977999739##
49	(15, 150, 150)	-16.8305238557#	-8.9977999844##
50	(15, 150, 200)	28.0968997887#	5.8612259452##
51	(15, 200, 50)	23.6216433811#	7.0837013616##
52	(15, 200, 100)	0.0000000330	-8.9977999839##
53	(15, 200, 150)	28.0968999403#	7.2968083326##
54	(15, 200, 200)	-13.5336530969#	3.2731726767##

Table D.6 Initial learner population for modeling of MRR and ASR with C, ε and σ tuned by modified TLBO

Learner no.	Material removal rate			Average surface roughness		
	C	ε	σ	C	ε	σ
1	2.8692	0.3741	0.6413	7.8464	0.2182	0.6413
2	27.6309	0.3705	0.4735	8.5362	0.6271	0.4735
3	27.3996	0.9601	0.4921	8.7711	0.6377	0.4921
4	10.1175	0.3718	0.7914	4.7648	0.3734	0.7914
5	24.0751	1.0408	0.7303	4.7332	0.4760	0.7303
6	8.1387	0.4240	0.4764	8.9144	0.2271	0.4764
7	25.8437	0.7102	0.7927	7.0968	0.6105	0.7927
8	23.2679	1.0917	0.4666	4.1319	0.2278	0.4666
9	2.6193	1.0371	0.6027	4.2077	0.4283	0.6027
10	3.0346	0.6132	0.7503	8.9040	0.2768	0.7503
11	28.0965	0.9792	0.7616	8.6920	0.2475	0.7616
12	2.2017	0.4416	0.4731	6.1559	0.6164	0.4731
13	21.1043	1.0947	0.7820	8.6928	0.5995	0.7820
14	4.5689	1.1037	0.7528	4.5076	0.3030	0.7528
15	25.3141	0.4255	0.7442	4.0201	0.2226	0.7442
16	3.7709	0.6065	0.7526	3.9201	0.5580	0.7526
17	6.1115	0.3996	0.7766	8.9605	0.4274	0.7766
18	3.2125	0.3955	0.5132	7.5031	0.2547	0.5132
19	22.3486	0.4083	0.4744	8.7844	0.6364	0.4744
20	27.6509	0.7158	0.6943	8.9504	0.6188	0.6943
Initial SR ratio (%)	40.63	40.18	40.45	40.39	40.06	40.45

Table D.7 Difference of Lagrange multipliers (α_i, α_i^*) for modeling of MRR and ASR with C, ε and σ tuned by modified TLBO
($^{\#}$ and $^{\#\#}$ indicate support vectors for MRR and ASR respectively)

Sl. no.	Training input vector (cur, t_{on}, t_{off})	Difference of Lagrange multipliers for MRR	Difference of Lagrange multipliers for ASR
1	(6, 50, 50)	0.0985452973$^{\#}$	-0.0000000019
2	(6, 50, 100)	-0.0000000667	5.6148847419$^{\#\#}$
3	(6, 50, 150)	-0.0000000073	2.0106555813$^{\#\#}$
4	(6, 50, 200)	-0.0000000369	-1.5740784925$^{\#\#}$
5	(6, 100, 100)	-13.2983888388$^{\#}$	-8.9999999768$^{\#\#}$
6	(6, 100, 150)	0.8764061745$^{\#}$	3.8069589873$^{\#\#}$
7	(6, 150, 50)	5.7707546754$^{\#}$	0.0000002969
8	(6, 150, 100)	3.4663380899$^{\#}$	8.9999998359$^{\#\#}$
9	(6, 150, 150)	13.4288136957$^{\#}$	-8.9999997512$^{\#\#}$
10	(6, 150, 200)	-5.9293581146$^{\#}$	-0.4502415935$^{\#\#}$
11	(6, 200, 50)	-0.6208954285$^{\#}$	0.8196181922$^{\#\#}$
12	(6, 200, 100)	-0.0000000458	-0.0000000345
13	(6, 200, 200)	-11.3548631890$^{\#}$	2.5976328847$^{\#\#}$
14	(9, 50, 50)	4.2271743808$^{\#}$	2.9196316326$^{\#\#}$
15	(9, 50, 100)	13.8264608164$^{\#}$	-0.0000000117
16	(9, 50, 150)	-0.0000000624	-8.9999999552$^{\#\#}$
17	(9, 50, 200)	0.0000001010	7.8477271070$^{\#\#}$
18	(9, 100, 50)	-0.0000008475	-1.0075169275$^{\#\#}$
19	(9, 100, 150)	4.0131307206$^{\#}$	8.9999999651$^{\#\#}$
20	(9, 100, 200)	-0.0000000104	-2.3467295622$^{\#\#}$
21	(9, 150, 100)	-11.1379333968$^{\#}$	4.9304497329$^{\#\#}$
22	(9, 150, 150)	0.0000000542	-4.1272455872$^{\#\#}$
23	(9, 150, 200)	-4.1045021565$^{\#}$	8.9999999348$^{\#\#}$
24	(9, 200, 50)	-0.3924807537$^{\#}$	-3.4239376413$^{\#\#}$
25	(9, 200, 150)	-7.9335655970$^{\#}$	-0.0000000197
26	(9, 200, 200)	28.0985999775$^{\#}$	0.0000000132
27	(12, 50, 100)	-7.1923780704$^{\#}$	-0.0000000104
28	(12, 50, 150)	-21.9505006369$^{\#}$	-0.0000000481
29	(12, 50, 200)	2.8497760771$^{\#}$	0.0000000244
30	(12, 100, 50)	0.0000000466	0.0000000948
31	(12, 100, 100)	-13.4751603748$^{\#}$	-3.7973615552$^{\#\#}$
32	(12, 100, 150)	28.0984051547$^{\#}$	3.6025617793$^{\#\#}$
33	(12, 100, 200)	0.0000000174	-7.9242297948$^{\#\#}$
34	(12, 150, 50)	-2.2757843274$^{\#}$	8.9999999518$^{\#\#}$
35	(12, 150, 100)	28.0985999195$^{\#}$	-8.9999999123$^{\#\#}$
36	(12, 150, 150)	-28.0985998559$^{\#}$	-5.3091413931$^{\#\#}$
37	(12, 200, 50)	16.5896970704$^{\#}$	-4.0055766596$^{\#\#}$
38	(12, 200, 100)	-28.0985999589$^{\#}$	8.9999999680$^{\#\#}$
39	(12, 200, 150)	28.0985998783$^{\#}$	-0.0000000575
40	(12, 200, 200)	-16.4516089037$^{\#}$	-0.0000000291
41	(15, 50, 50)	22.6528321236$^{\#}$	8.9999999810$^{\#\#}$
42	(15, 50, 100)	-28.0985998561$^{\#}$	-7.1758555468$^{\#\#}$
43	(15, 50, 150)	24.7428877743$^{\#}$	8.9999999835$^{\#\#}$
44	(15, 50, 200)	-0.0000000986	-0.3272010111$^{\#\#}$
45	(15, 100, 50)	14.9719117155$^{\#}$	-4.5434539453$^{\#\#}$
46	(15, 100, 150)	28.0985999740$^{\#}$	4.8727915963$^{\#\#}$
47	(15, 100, 200)	-28.0985997841$^{\#}$	0.0000000620
48	(15, 150, 100)	-28.0985999697$^{\#}$	8.9999999739$^{\#\#}$
49	(15, 150, 150)	-16.7141066250$^{\#}$	-8.9999999844$^{\#\#}$
50	(15, 150, 200)	28.0985997378$^{\#}$	5.8624729960$^{\#\#}$
51	(15, 200, 50)	23.8202712457$^{\#}$	7.0846846713$^{\#\#}$
52	(15, 200, 100)	0.0000000285	-8.9999999839$^{\#\#}$
53	(15, 200, 150)	28.0985999351$^{\#}$	7.2986283281$^{\#\#}$
54	(15, 200, 200)	-13.4986331556$^{\#}$	3.2720348057$^{\#\#}$

Table D.8 Initial learner population for searching of optimum unique set of C, ε and σ by modified TLBO

Learner no.	C	ε	σ
1	0.0562	0.0169	0.6413
2	0.9825	0.0168	0.4735
3	0.9739	0.0329	0.4921
4	0.3274	0.0168	0.7914
5	0.8495	0.0352	0.7303
6	0.2533	0.0182	0.4764
7	0.9156	0.0261	0.7927
8	0.8193	0.0365	0.4666
9	0.0469	0.0351	0.6027
10	0.0624	0.0234	0.7503
11	0.9999	0.0335	0.7616
12	0.0312	0.0187	0.4731
13	0.7384	0.0366	0.7820
14	0.1198	0.0369	0.7528
15	0.8958	0.0183	0.7443
16	0.0899	0.0232	0.7526
17	0.1775	0.0176	0.7766
18	0.0691	0.0175	0.5132
19	0.7849	0.0178	0.4744
20	0.9833	0.0262	0.6943
Initial SR ratio (%)	40.64	40.18	40.45

Table D.9 Difference of Lagrange multipliers (α_i, α_i^*) for normalized MRR and normalized ASR ($^{\#}$ and $^{\#\#}$ indicate support vectors for normalized MRR and normalized ASR respectively)

Sl. no.	Training input vector (cur, t_{on}, t_{off})	Difference of Lagrange multipliers for normalized MRR	Difference of Lagrange multipliers for normalized ASR
1	(6, 50, 50)	-0.000000002796	-0.764554207673$^{\#\#}$
2	(6, 50, 100)	-0.000000009512	0.884361167229$^{\#\#}$
3	(6, 50, 150)	0.000000000122	0.510197961001$^{\#\#}$
4	(6, 50, 200)	-0.000000016877	-0.999999994898$^{\#\#}$
5	(6, 100, 100)	-0.432080569555$^{\#}$	-0.999999998139$^{\#\#}$
6	(6, 100, 150)	0.000000032870	0.154408781906$^{\#\#}$
7	(6, 100, 200)	-0.000000005594	0.710914971657$^{\#\#}$
8	(6, 150, 50)	0.127462045052$^{\#}$	0.037989657879$^{\#\#}$
9	(6, 150, 100)	0.141377784440$^{\#}$	0.999999995288$^{\#\#}$
10	(6, 150, 150)	0.464622968706$^{\#}$	-0.999999995293$^{\#\#}$
11	(6, 150, 200)	-0.217389039837$^{\#}$	-0.551957179210$^{\#\#}$
12	(6, 200, 50)	-0.009938496912$^{\#}$	0.000000001114
13	(6, 200, 100)	-0.000000004138	-0.135215960250$^{\#\#}$
14	(6, 200, 200)	-0.430589900521$^{\#}$	0.077156773467$^{\#\#}$
15	(9, 50, 50)	0.355462431335$^{\#}$	0.999999994509$^{\#\#}$
16	(9, 50, 100)	0.273609069455$^{\#}$	-0.295041059654$^{\#\#}$
17	(9, 50, 150)	-0.000000002954	-0.999999996557$^{\#\#}$
18	(9, 50, 200)	0.000000002403	0.999999996087$^{\#\#}$
19	(9, 100, 50)	-0.000000007705	-0.090219565910$^{\#\#}$
20	(9, 100, 150)	0.217241099393$^{\#}$	0.999999996909$^{\#\#}$
21	(9, 100, 200)	-0.000000001207	-0.289849585477$^{\#\#}$
22	(9, 150, 100)	-0.420062202030$^{\#}$	0.999999997362$^{\#\#}$
23	(9, 150, 150)	0.000000002994	-0.436752900699$^{\#\#}$
24	(9, 150, 200)	-0.138829893909$^{\#}$	0.999999998078$^{\#\#}$
25	(9, 200, 50)	-0.000000029292	-0.875041277073$^{\#\#}$
26	(9, 200, 150)	-0.273962234136$^{\#}$	0.000000001502
27	(9, 200, 200)	0.999999998834$^{\#}$	0.321212248902$^{\#\#}$
28	(12, 50, 50)	-0.332688993668$^{\#}$	-0.301423445472$^{\#\#}$
29	(12, 50, 150)	-0.725705107150$^{\#}$	-0.000000010391
30	(12, 50, 200)	0.071476440548$^{\#}$	0.079249244142$^{\#\#}$
31	(12, 100, 100)	-0.469673124348$^{\#}$	-0.914066753160$^{\#\#}$
32	(12, 100, 150)	0.898274485156$^{\#}$	0.770128415857$^{\#\#}$
33	(12, 100, 200)	0.000000001649	-0.999999996900$^{\#\#}$
34	(12, 150, 50)	-0.000000013432	0.999999998585$^{\#\#}$
35	(12, 150, 100)	0.999999995452$^{\#}$	-0.917033628344$^{\#\#}$
36	(12, 150, 150)	-0.999999992952$^{\#}$	-0.999999996259$^{\#\#}$
37	(12, 200, 50)	0.538360015461$^{\#}$	-0.086447265691$^{\#\#}$
38	(12, 200, 100)	-0.999999998048$^{\#}$	0.999999998030$^{\#\#}$
39	(12, 200, 150)	0.999999993285$^{\#}$	-0.000000009813
40	(12, 200, 200)	-0.574857959601$^{\#}$	-0.094448806725$^{\#\#}$
41	(15, 50, 50)	0.920212678063$^{\#}$	0.999999997745$^{\#\#}$
42	(15, 50, 100)	-0.999999996271$^{\#}$	-0.828828033849$^{\#\#}$
43	(15, 50, 150)	0.776567167323$^{\#}$	0.999999998710$^{\#\#}$
44	(15, 50, 200)	-0.000000001486	-0.451792235691$^{\#\#}$
45	(15, 100, 50)	0.495825151268$^{\#}$	-0.486546465507$^{\#\#}$
46	(15, 100, 150)	0.999999998702$^{\#}$	0.913875910423$^{\#\#}$
47	(15, 100, 200)	-0.969917192846$^{\#}$	0.000000007371
48	(15, 150, 100)	-0.999999998601$^{\#}$	0.999999996940$^{\#\#}$
49	(15, 150, 150)	-0.568482595264$^{\#}$	-0.999999998590$^{\#\#}$
50	(15, 150, 200)	0.999999902894$^{\#}$	0.616622070391$^{\#\#}$
51	(15, 200, 50)	0.846108281196$^{\#}$	0.587529799685$^{\#\#}$
52	(15, 200, 100)	0.000000000960	-0.999999998437$^{\#\#}$
53	(15, 200, 150)	0.999999996666$^{\#}$	0.832877246791$^{\#\#}$
54	(15, 200, 200)	-0.515946613189$^{\#}$	0.417561755751$^{\#\#}$

Table D.10 Initial learner population for pseudo Pareto optimization

Learner no.	Current (A)	Pulse on time (μs)	Pulse off time (μs)
1	6.5059	51.2143	130.6446
2	14.8425	50.4721	54.2352
3	14.7647	170.5833	62.7075
4	8.9462	50.7484	198.9359
5	13.6454	187.0230	171.1407
6	8.2800	61.3682	55.5847
7	14.2408	119.6868	199.5464
8	13.3736	197.3904	51.1178
9	6.4218	186.2756	113.0718
10	6.5616	99.9198	180.2544
11	14.9993	174.4858	185.4086
12	6.2812	64.9521	54.0596
13	12.6452	198.0037	194.6900
14	7.0781	199.8288	181.3827
15	14.0625	61.6875	177.4929
16	6.8095	98.5496	181.3064
17	7.5975	56.3962	192.2230
18	6.6215	55.5727	72.3168
19	13.0641	58.1840	54.6807
20	14.8493	120.8145	154.7704
Initial SR ratio (%)	40.63	40.18	40.45

Table D.11 Different ACF values

Treatment - cur = 12 A, t_{on} = 150 µs and t_{off} = 150 µs
(direction 1, refer figure 6.4)

τ	ACF	$\text{ACF}_{\text{insign}}$	ACF_{sign}	τ	ACF	$\text{ACF}_{\text{insign}}$	ACF_{sign}
1	1.0000	0.0357	0.9643	51	-0.2480	-0.0093	-0.2387
2	0.9545	0.0957	0.8588	52	-0.2626	-0.0115	-0.2512
3	0.8671	0.0840	0.7831	53	-0.2683	-0.0145	-0.2539
4	0.7401	0.0575	0.6826	54	-0.2653	-0.0202	-0.2450
5	0.5997	0.0331	0.5666	55	-0.2482	-0.0244	-0.2239
6	0.4522	0.0089	0.4433	56	-0.2182	-0.0277	-0.1906
7	0.3107	-0.0094	0.3202	57	-0.1722	-0.0257	-0.1466
8	0.1765	-0.0268	0.2033	58	-0.1163	-0.0218	-0.0945
9	0.0617	-0.0355	0.0972	59	-0.0475	-0.0099	-0.0376
10	-0.0346	-0.0383	0.0037	60	0.0227	0.0025	0.0202
11	-0.1101	-0.0332	-0.0769	61	0.0862	0.0111	0.0751
12	-0.1718	-0.0257	-0.1461	62	0.1360	0.0125	0.1235
13	-0.2240	-0.0178	-0.2061	63	0.1705	0.0075	0.1630
14	-0.2699	-0.0106	-0.2593	64	0.1899	-0.0020	0.1920
15	-0.3129	-0.0054	-0.3075	65	0.1964	-0.0135	0.2099
16	-0.3517	-0.0001	-0.3516	66	0.1938	-0.0238	0.2176
17	-0.3868	0.0047	-0.3914	67	0.1828	-0.0335	0.2162
18	-0.4174	0.0081	-0.4255	68	0.1685	-0.0393	0.2078
19	-0.4404	0.0109	-0.4513	69	0.1551	-0.0394	0.1945
20	-0.4536	0.0122	-0.4658	70	0.1448	-0.0333	0.1781
21	-0.4527	0.0134	-0.4661	71	0.1362	-0.0240	0.1602
22	-0.4374	0.0122	-0.4495	72	0.1296	-0.0120	0.1416
23	-0.4074	0.0075	-0.4148	73	0.1203	-0.0024	0.1227
24	-0.3616	0.0005	-0.3621	74	0.1062	0.0031	0.1031
25	-0.2969	-0.0039	-0.2930	75	0.0855	0.0033	0.0822
26	-0.2174	-0.0061	-0.2113	76	0.0593	0.0000	0.0592
27	-0.1268	-0.0051	-0.1217	77	0.0289	-0.0046	0.0335
28	-0.0371	-0.0070	-0.0301	78	-0.0033	-0.0080	0.0048
29	0.0478	-0.0096	0.0574	79	-0.0390	-0.0120	-0.0270
30	0.1202	-0.0150	0.1351	80	-0.0754	-0.0143	-0.0611
31	0.1815	-0.0171	0.1986	81	-0.1128	-0.0167	-0.0961
32	0.2281	-0.0165	0.2446	82	-0.1469	-0.0168	-0.1301
33	0.2581	-0.0136	0.2717	83	-0.1769	-0.0159	-0.1611
34	0.2682	-0.0117	0.2800	84	-0.2012	-0.0146	-0.1866
35	0.2607	-0.0107	0.2714	85	-0.2163	-0.0118	-0.2045
36	0.2394	-0.0095	0.2489	86	-0.2215	-0.0085	-0.2131
37	0.2104	-0.0060	0.2164	87	-0.2171	-0.0061	-0.2110
38	0.1788	0.0012	0.1776	88	-0.2031	-0.0051	-0.1980
39	0.1438	0.0078	0.1361	89	-0.1823	-0.0079	-0.1744
40	0.1067	0.0121	0.0946	90	-0.1498	-0.0085	-0.1413
41	0.0651	0.0100	0.0551	91	-0.1089	-0.0082	-0.1006
42	0.0242	0.0057	0.0185	92	-0.0611	-0.0064	-0.0547
43	-0.0142	0.0011	-0.0153	93	-0.0126	-0.0066	-0.0060
44	-0.0486	-0.0018	-0.0468	94	0.0351	-0.0077	0.0428
45	-0.0846	-0.0076	-0.0769	95	0.0799	-0.0095	0.0894
46	-0.1184	-0.0118	-0.1066	96	0.1217	-0.0100	0.1317
47	-0.1499	-0.0138	-0.1362	97	0.1621	-0.0061	0.1682
48	-0.1795	-0.0141	-0.1655	98	0.1990	0.0011	0.1979
49	-0.2057	-0.0122	-0.1935	99	0.2303	0.0100	0.2204
50	-0.2295	-0.0108	-0.2186	100	0.2527	0.0172	0.2355

Table D.11 (Contd.) Different ACF values

Treatment - cur = 12 A, t_{on} = 150 µs and t_{off} = 150 µs (direction 1, refer figure 6.4)							
τ	ACF	ACF$_{insign}$	ACF$_{sign}$	***τ***	ACF	ACF$_{insign}$	ACF$_{sign}$
101	0.2637	0.0202	0.2435	151	-0.1531	0.0114	-0.1645
102	0.2621	0.0174	0.2447	152	-0.1621	0.0157	-0.1779
103	0.2507	0.0110	0.2397	153	-0.1622	0.0187	-0.1809
104	0.2284	-0.0003	0.2286	154	-0.1538	0.0204	-0.1743
105	0.2011	-0.0107	0.2118	155	-0.1383	0.0210	-0.1593
106	0.1701	-0.0191	0.1892	156	-0.1169	0.0209	-0.1378
107	0.1377	-0.0229	0.1606	157	-0.0917	0.0201	-0.1118
108	0.1022	-0.0239	0.1261	158	-0.0660	0.0172	-0.0831
109	0.0659	-0.0196	0.0855	159	-0.0397	0.0141	-0.0537
110	0.0260	-0.0131	0.0391	160	-0.0161	0.0090	-0.0251
111	-0.0151	-0.0029	-0.0123	161	0.0054	0.0036	0.0017
112	-0.0587	0.0089	-0.0676	162	0.0244	-0.0016	0.0260
113	-0.1050	0.0200	-0.1250	163	0.0413	-0.0062	0.0475
114	-0.1571	0.0251	-0.1823	164	0.0571	-0.0090	0.0661
115	-0.2099	0.0269	-0.2368	165	0.0718	-0.0101	0.0819
116	-0.2599	0.0259	-0.2859	166	0.0842	-0.0108	0.0950
117	-0.3027	0.0239	-0.3266	167	0.0954	-0.0100	0.1055
118	-0.3343	0.0223	-0.3566	168	0.1063	-0.0068	0.1131
119	-0.3558	0.0182	-0.3741	169	0.1189	0.0013	0.1176
120	-0.3655	0.0123	-0.3778	170	0.1268	0.0083	0.1184
121	-0.3628	0.0047	-0.3675	171	0.1300	0.0150	0.1151
122	-0.3463	-0.0025	-0.3437	172	0.1277	0.0207	0.1070
123	-0.3156	-0.0077	-0.3079	173	0.1152	0.0213	0.0940
124	-0.2715	-0.0095	-0.2620	174	0.0975	0.0216	0.0760
125	-0.2161	-0.0076	-0.2085	175	0.0717	0.0182	0.0535
126	-0.1531	-0.0030	-0.1501	176	0.0389	0.0117	0.0272
127	-0.0895	0.0001	-0.0895	177	0.0000	0.0015	-0.0015
128	-0.0253	0.0039	-0.0292	178	-0.0407	-0.0099	-0.0308
129	0.0372	0.0083	0.0289	179	-0.0798	-0.0201	-0.0596
130	0.0954	0.0124	0.0830	180	-0.1110	-0.0250	-0.0861
131	0.1491	0.0171	0.1321	181	-0.1360	-0.0274	-0.1086
132	0.1964	0.0211	0.1753	182	-0.1519	-0.0259	-0.1260
133	0.2344	0.0221	0.2124	183	-0.1609	-0.0236	-0.1373
134	0.2642	0.0213	0.2429	184	-0.1609	-0.0187	-0.1423
135	0.2850	0.0183	0.2667	185	-0.1548	-0.0136	-0.1411
136	0.3019	0.0184	0.2835	186	-0.1415	-0.0070	-0.1345
137	0.3115	0.0185	0.2930	187	-0.1268	-0.0034	-0.1234
138	0.3150	0.0203	0.2947	188	-0.1105	-0.0015	-0.1090
139	0.3080	0.0199	0.2881	189	-0.0947	-0.0020	-0.0926
140	0.2902	0.0172	0.2730	190	-0.0774	-0.0020	-0.0754
141	0.2626	0.0134	0.2492	191	-0.0597	-0.0015	-0.0582
142	0.2255	0.0083	0.2172	192	-0.0424	-0.0006	-0.0418
143	0.1817	0.0039	0.1777	193	-0.0276	-0.0011	-0.0265
144	0.1333	0.0010	0.1323	194	-0.0131	-0.0008	-0.0123
145	0.0817	-0.0010	0.0826	195	-0.0008	-0.0018	0.0010
146	0.0320	0.0008	0.0312	196	0.0095	-0.0042	0.0137
147	-0.0170	0.0024	-0.0194	197	0.0180	-0.0080	0.0261
148	-0.0619	0.0046	-0.0665	198	0.0256	-0.0128	0.0384
149	-0.1017	0.0060	-0.1077	199	0.0320	-0.0188	0.0508
150	-0.1326	0.0083	-0.1409	200	0.0401	-0.0229	0.0630

Table D.11 (Contd.) Different ACF values

Treatment - cur = 12 A, t_{on} = 150 µs and t_{off} = 150 µs (direction 1, refer figure 6.4)							
τ	ACF	ACF_{insign}	ACF_{sign}	τ	ACF	ACF_{insign}	ACF_{sign}
201	0.0492	-0.0255	0.0747	251	0.0086	0.0103	-0.0017
202	0.0591	-0.0261	0.0852	252	-0.0128	0.0098	-0.0226
203	0.0674	-0.0265	0.0939	253	-0.0311	0.0119	-0.0430
204	0.0739	-0.0260	0.0999	254	-0.0479	0.0148	-0.0626
205	0.0769	-0.0257	0.1025	255	-0.0631	0.0180	-0.0811
206	0.0787	-0.0227	0.1014	256	-0.0763	0.0216	-0.0979
207	0.0778	-0.0183	0.0962	257	-0.0901	0.0224	-0.1125
208	0.0750	-0.0119	0.0869	258	-0.1037	0.0205	-0.1242
209	0.0685	-0.0056	0.0740	259	-0.1151	0.0172	-0.1322
210	0.0574	-0.0007	0.0582	260	-0.1247	0.0114	-0.1362
211	0.0437	0.0035	0.0402	261	-0.1288	0.0068	-0.1355
212	0.0275	0.0064	0.0211	262	-0.1273	0.0029	-0.1302
213	0.0089	0.0071	0.0018	263	-0.1187	0.0016	-0.1204
214	-0.0103	0.0065	-0.0167	264	-0.1049	0.0017	-0.1066
215	-0.0289	0.0050	-0.0338	265	-0.0852	0.0044	-0.0896
216	-0.0481	0.0008	-0.0490	266	-0.0641	0.0065	-0.0706
217	-0.0650	-0.0030	-0.0619	267	-0.0397	0.0111	-0.0508
218	-0.0810	-0.0083	-0.0727	268	-0.0177	0.0136	-0.0313
219	-0.0932	-0.0119	-0.0813	269	0.0038	0.0173	-0.0135
220	-0.1027	-0.0146	-0.0881	270	0.0199	0.0180	0.0018
221	-0.1114	-0.0182	-0.0932	271	0.0323	0.0183	0.0140
222	-0.1178	-0.0209	-0.0968	272	0.0383	0.0156	0.0226
223	-0.1210	-0.0220	-0.0989	273	0.0412	0.0134	0.0279
224	-0.1202	-0.0207	-0.0995	274	0.0417	0.0116	0.0300
225	-0.1148	-0.0168	-0.0980	275	0.0417	0.0120	0.0297
226	-0.1068	-0.0125	-0.0943	276	0.0411	0.0134	0.0277
227	-0.0957	-0.0080	-0.0877	277	0.0392	0.0144	0.0248
228	-0.0817	-0.0037	-0.0779	278	0.0347	0.0132	0.0216
229	-0.0650	-0.0003	-0.0647	279	0.0284	0.0098	0.0186
230	-0.0445	0.0034	-0.0479	280	0.0234	0.0070	0.0163
231	-0.0224	0.0052	-0.0277	281	0.0203	0.0055	0.0148
232	0.0018	0.0064	-0.0046	282	0.0192	0.0052	0.0140
233	0.0283	0.0078	0.0205	283	0.0199	0.0063	0.0137
234	0.0558	0.0092	0.0466	284	0.0210	0.0074	0.0136
235	0.0830	0.0105	0.0724	285	0.0233	0.0097	0.0136
236	0.1074	0.0107	0.0967	286	0.0264	0.0129	0.0134
237	0.1287	0.0105	0.1182	287	0.0292	0.0162	0.0131
238	0.1448	0.0090	0.1358	288	0.0300	0.0174	0.0126
239	0.1528	0.0042	0.1487	289	0.0284	0.0161	0.0123
240	0.1552	-0.0010	0.1563	290	0.0237	0.0112	0.0125
241	0.1519	-0.0065	0.1584	291	0.0202	0.0067	0.0135
242	0.1449	-0.0104	0.1553	292	0.0182	0.0026	0.0156
243	0.1364	-0.0109	0.1474	293	0.0189	-0.0002	0.0191
244	0.1262	-0.0092	0.1353	294	0.0214	-0.0025	0.0238
245	0.1134	-0.0066	0.1200	295	0.0237	-0.0059	0.0297
246	0.0998	-0.0023	0.1021	296	0.0281	-0.0081	0.0362
247	0.0850	0.0025	0.0826	297	0.0336	-0.0091	0.0428
248	0.0690	0.0071	0.0619	298	0.0400	-0.0087	0.0487
249	0.0505	0.0097	0.0408	299	0.0450	-0.0083	0.0533
250	0.0298	0.0104	0.0195	300	0.0472	-0.0086	0.0558

Table D.11 (Contd.) Different ACF values

Treatment - cur = 12 A, t_{on} = 150 μs and t_{off} = 150 μs (direction 1, refer figure 6.4)							
τ	ACF	ACF_{insign}	ACF_{sign}	***τ***	ACF	ACF_{insign}	ACF_{sign}
301	0.0450	-0.0108	0.0558	327	-0.0228	-0.0157	-0.0070
302	0.0425	-0.0105	0.0530	328	-0.0187	-0.0169	-0.0018
303	0.0372	-0.0103	0.0475	329	-0.0162	-0.0194	0.0031
304	0.0308	-0.0085	0.0394	330	-0.0143	-0.0219	0.0076
305	0.0213	-0.0079	0.0293	331	-0.0142	-0.0252	0.0110
306	0.0114	-0.0064	0.0179	332	-0.0143	-0.0275	0.0132
307	0.0012	-0.0048	0.0059	333	-0.0151	-0.0291	0.0140
308	-0.0087	-0.0031	-0.0057	334	-0.0144	-0.0277	0.0134
309	-0.0198	-0.0036	-0.0163	335	-0.0129	-0.0244	0.0115
310	-0.0318	-0.0065	-0.0253	336	-0.0099	-0.0185	0.0086
311	-0.0445	-0.0121	-0.0324	337	-0.0070	-0.0123	0.0052
312	-0.0557	-0.0183	-0.0374	338	-0.0048	-0.0067	0.0019
313	-0.0651	-0.0248	-0.0404	339	-0.0031	-0.0022	-0.0009
314	-0.0713	-0.0298	-0.0415	340	-0.0015	0.0012	-0.0027
315	-0.0747	-0.0334	-0.0413	341	-0.0003	0.0028	-0.0031
316	-0.0759	-0.0358	-0.0401	342	0.0015	0.0035	-0.0020
317	-0.0743	-0.0361	-0.0382	343	0.0028	0.0021	0.0007
318	-0.0697	-0.0336	-0.0361	344	0.0039	-0.0008	0.0047
319	-0.0626	-0.0288	-0.0338	345	0.0062	-0.0037	0.0098
320	-0.0549	-0.0233	-0.0316	346	0.0102	-0.0053	0.0155
321	-0.0481	-0.0189	-0.0293	347	0.0147	-0.0065	0.0212
322	-0.0427	-0.0160	-0.0268	348	0.0193	-0.0071	0.0263
323	-0.0380	-0.0141	-0.0239	349	0.0225	-0.0078	0.0303
324	-0.0343	-0.0138	-0.0205	350	0.0249	-0.0079	0.0328
325	-0.0307	-0.0142	-0.0166	351	0.0254	-0.0080	0.0333
326	-0.0266	-0.0145	-0.0120	352	0.0245	-0.0074	0.0319

Table D.12 Singular values of Hankel matrix generated from a typical truncated ACF curve
(Singular values are arranged in columnwise descending order, * corresponding to significant part)

S_{max} = 12.4976							
12.4976 *	0.6430	0.0692	0.0157	0.0084	0.0050	0.0032	0.0013
12.1977 *	0.6061	0.0576	0.0149	0.0084	0.0050	0.0032	0.0013
7.2594 *	0.4984	0.0465	0.0149	0.0083	0.0048	0.0030	0.0012
7.1939 *	0.4866	0.0449	0.0143	0.0083	0.0048	0.0029	0.0012
3.1231 *	0.3298	0.0442	0.0142	0.0082	0.0048	0.0029	0.0012
2.8744 *	0.2960	0.0439	0.0138	0.0079	0.0047	0.0028	0.0011
2.8732 *	0.2946	0.0430	0.0137	0.0079	0.0046	0.0028	0.0011
2.8529 *	0.2538	0.0424	0.0135	0.0078	0.0045	0.0027	0.0011
2.7275 *	0.2441	0.0400	0.0133	0.0077	0.0045	0.0027	0.0010
2.7107 *	0.1761	0.0393	0.0128	0.0076	0.0042	0.0026	0.0009
2.4445 *	0.1756	0.0358	0.0127	0.0073	0.0042	0.0025	0.0009
2.4285 *	0.1569	0.0356	0.0123	0.0071	0.0041	0.0024	0.0009
2.3093 *	0.1450	0.0330	0.0122	0.0067	0.0040	0.0024	0.0007
2.2574 *	0.1231	0.0301	0.0118	0.0064	0.0039	0.0023	0.0006
1.8080 *	0.1227	0.0264	0.0116	0.0064	0.0039	0.0022	0.0005
1.7811 *	0.1127	0.0258	0.0112	0.0061	0.0038	0.0021	0.0005
1.3705 *	0.0926	0.0199	0.0111	0.0060	0.0038	0.0021	0.0004
1.3477 *	0.0851	0.0198	0.0103	0.0058	0.0037	0.0020	0.0004
1.1784 *	0.0847	0.0179	0.0103	0.0058	0.0036	0.0020	0.0004
1.1555 *	0.0832	0.0174	0.0094	0.0057	0.0036	0.0019	0.0003
1.0485	0.0776	0.0172	0.0093	0.0056	0.0035	0.0018	
1.0425	0.0766	0.0170	0.0092	0.0054	0.0035	0.0017	
1.0191	0.0752	0.0168	0.0091	0.0054	0.0035	0.0017	
0.8454	0.0743	0.0167	0.0088	0.0054	0.0033	0.0016	
0.6484	0.0709	0.0158	0.0085	0.0052	0.0033	0.0015	

Table D.13 Roots of equation (6.12) consisting of d_is obtained from a typical ACF_{sign} curve (Complex conjugate roots are not given, * corresponding to the most contributive signal poles)

	Roots			Roots			Roots	
Real	Imaginary	Modulus	Real	Imaginary	Modulus	Real	Imaginary	Modulus
0.9328 *	0.3893 *	1.0108 *	0.4193	0.8860	0.9802	-0.5735	0.7915	0.9774
0.9907 *	0.1861 *	1.0080 *	0.3874	0.9003	0.9801	-0.6012	0.7705	0.9773
1.0039 *	0.0847 *	1.0075 *	0.3550	0.9134	0.9800	-0.6283	0.7486	0.9773
0.9766 *	0.2281 *	1.0029 *	0.3221	0.9254	0.9798	-0.6545	0.7257	0.9773
0.9944 *	0.1299 *	1.0029 *	0.2889	0.9361	0.9797	-0.6799	0.7019	0.9772
0.9858	0.1624	0.9991	0.2554	0.9457	0.9795	-0.7044	0.6772	0.9772
0.9460	0.3032	0.9934	0.2215	0.9541	0.9794	-0.7281	0.6517	0.9771
0.9564	0.2678	0.9932	0.1873	0.9612	0.9793	-0.7508	0.6253	0.9771
0.9304	0.3423	0.9914	0.1529	0.9672	0.9792	-0.7725	0.5982	0.9770
0.8963	0.4210	0.9902	0.1183	0.9719	0.9791	-0.7933	0.5703	0.9770
0.9854	0.0441	0.9864	0.0836	0.9754	0.9789	-0.8131	0.5417	0.9770
0.8554	0.4882	0.9849	0.0488	0.9776	0.9788	-0.8318	0.5123	0.9770
0.8362	0.5191	0.9842	0.0139	0.9786	0.9787	-0.8495	0.4824	0.9769
0.8713	0.4575	0.9841	-0.0209	0.9784	0.9786	-0.8662	0.4518	0.9769
0.7958	0.5785	0.9838	-0.0558	0.9769	0.9785	-0.8817	0.4207	0.9769
0.8161	0.5493	0.9837	-0.0905	0.9742	0.9784	-0.8961	0.3890	0.9769
0.7517	0.6332	0.9828	-0.1251	0.9703	0.9783	-0.9093	0.3568	0.9769
0.7738	0.6059	0.9828	-0.1596	0.9652	0.9783	-0.9215	0.3242	0.9768
0.7282	0.6597	0.9826	-0.1939	0.9588	0.9782	-0.9324	0.2912	0.9768
0.7040	0.6851	0.9823	-0.2279	0.9512	0.9781	-0.9422	0.2578	0.9768
0.6787	0.7097	0.9820	-0.2616	0.9424	0.9780	-0.9508	0.2241	0.9768
0.6528	0.7332	0.9817	-0.2950	0.9324	0.9780	-0.9581	0.1901	0.9768
0.6261	0.7559	0.9815	-0.3280	0.9213	0.9779	-0.9643	0.1559	0.9768
0.5987	0.7776	0.9813	-0.3606	0.9089	0.9778	-0.9692	0.1214	0.9768
0.5703	0.7985	0.9812	-0.3927	0.8954	0.9778	-0.9766	0.0174	0.9768
0.5413	0.8179	0.9808	-0.4243	0.8808	0.9777	-0.9754	0.0522	0.9768
0.5118	0.8366	0.9807	-0.4554	0.8651	0.9776	-0.9729	0.0868	0.9768
0.9807	0.0000	0.9807	-0.4859	0.8483	0.9776	0.9600	0.0000	0.9600
0.4815	0.8542	0.9806	-0.5157	0.8304	0.9775	0.8583	0.3823	0.9396
0.4507	0.8706	0.9803	-0.5449	0.8115	0.9775			

Table D.14 Calculation of PR ratio of each of the FIDs, class average of PR ratios for each of the 10 classes and mean rank for each of the 3 directions

Treatment - cur = 12 A, t_{on} = 150 µs and t_{off} = 150 µs													
Class	Direction 1				Direction 2				Direction 3				Class average of PR ratios
	λ (mm)	**β** (mm)	PR ratio	Rank	**λ** (mm)	**β** (mm)	PR ratio	Rank	**λ** (mm)	**β** (mm)	PR ratio	Rank	
0.0 mm < λ < 0.1 mm (λ$_{class}$ = 0.05 mm)													
0.1 mm ≤ λ < 0.2 mm (λ$_{class}$ = 0.15 mm)	0.1271	1.7184	0.0740	224	0.1194	2.4446	0.0488	437	0.1644	1.5813	0.1040	185	0.0504
									0.1885	2.5750	0.0732	478	
					0.1072	2.6690	0.0402	495	0.1019	3.0043	0.0339	571	
					0.1963	2.9416	0.0667	550	0.1375	3.5434	0.0388	701	
					0.1779	4.4032	0.0404	866	0.1098	4.0390	0.0272	804	
									0.1179	16.5477	0.0071	1308	
0.2 mm ≤ λ < 0.3 mm (λ$_{class}$ = 0.25 mm)	0.2707	2.3161	0.1169	388	0.2422	1.1747	0.2062	96					0.1192
	0.2190	6.3335	0.0346	1079									
0.3 mm ≤ λ < 0.4 mm (λ$_{class}$ = 0.35 mm)	0.3870	6.4457	0.0600	1088	0.3622	2.4174	0.1498	426	0.3675	1.0437	0.3521	77	0.1873
0.4 mm ≤ λ < 0.5 mm (λ$_{class}$ = 0.45 mm)					0.4606	4.2083	0.1095	831					0.1095
0.5 mm ≤ λ < 0.6 mm (λ$_{class}$ = 0.55 mm)	0.5970	2.4655	0.2421	443									0.2421
0.6 mm ≤ λ < 0.7 mm (λ$_{class}$ = 0.65 mm)													
0.7 mm ≤ λ < 0.8 mm (λ$_{class}$ = 0.75 mm)									0.7339	6.1597	0.1191	1066	0.1191
0.8 mm ≤ λ < 0.9 mm (λ$_{class}$ = 0.85 mm)													
0.9 mm ≤ λ < 1.0 mm (λ$_{class}$ = 0.95 mm)													
Mean rank				644.40				528.71				648.75	

Table D.15 Values of PR ratio$_{avg}$

Sl. no.	Machining condition			PR ratio$_{avg}$	Sl. no.	Machining condition			PR ratio$_{avg}$
	Current (A)	Pulse on time (µs)	Pulse off time (µs)			Current (A)	Pulse on time (µs)	Pulse off time (µs)	
1	6	50	50	0.0880	33	12	50	50	0.1188
2	6	50	100	0.0927	34	12	50	100	0.0781
3	6	50	150	0.0653	35	12	50	150	0.0938
4	6	50	200	0.0986	36	12	50	200	0.1090
5	6	100	50	0.0534	37	12	100	50	0.0910
6	6	100	100	0.1203	38	12	100	100	0.0934
7	6	100	150	0.1151	39	12	100	150	0.1105
8	6	100	200	0.1094	40	12	100	200	0.1547
9	6	150	50	0.1093	41	12	150	50	0.0893
10	6	150	100	0.0966	42	12	150	100	0.0966
11	6	150	150	0.0763	43	12	150	150	0.0972
12	6	150	200	0.1133	44	12	150	200	0.0993
13	6	200	50	0.1068	45	12	200	50	0.1105
14	6	200	100	0.1280	46	12	200	100	0.1403
15	6	200	150	0.0834	47	12	200	150	0.1215
16	6	200	200	0.0890	48	12	200	200	0.1118
17	9	50	50	0.0921	49	15	50	50	0.1324
18	9	50	100	0.1501	50	15	50	100	0.1090
19	9	50	150	0.1648	51	15	50	150	0.1499
20	9	50	200	0.0977	52	15	50	200	0.1008
21	9	100	50	0.1126	53	15	100	50	0.1496
22	9	100	100	0.0953	54	15	100	100	0.1093
23	9	100	150	0.1386	55	15	100	150	0.1095
24	9	100	200	0.0851	56	15	100	200	0.1539
25	9	150	50	0.1034	57	15	150	50	0.1797
26	9	150	100	0.1039	58	15	150	100	0.1077
27	9	150	150	0.0908	59	15	150	150	0.1066
28	9	150	200	0.1161	60	15	150	200	0.1141
29	9	200	50	0.1003	61	15	200	50	0.1056
30	9	200	100	0.1039	62	15	200	100	0.1317
31	9	200	150	0.0969	63	15	200	150	0.1677
32	9	200	200	0.1161	64	15	200	200	0.1182

Table D.16 Coefficient $a_{i,j,k}$ of Bezier function

Sl.	i = 0			Sl.	i = 1			Sl.	i = 2			Sl.	i = 3		
no.	j	k	$a_{i,j,k}$	no.	j	k	$a_{i,j,k}$	no.	j	k	$a_{i,j,k}$	no.	j	k	$a_{i,j,k}$
1	0	0	0.0880	17	0	0	0.0121	33	0	0	0.0681	49	0	0	-0.0359
2	0	1	0.0141	18	0	1	0.4798	34	0	1	-1.3682	50	0	1	0.8042
3	0	2	-0.0963	19	0	2	-0.1004	35	0	2	0.9974	51	0	2	-0.6078
4	0	3	0.0928	20	0	3	-0.3942	36	0	3	0.3394	52	0	3	-0.1924
5	1	0	-0.1039	21	1	0	0.4969	37	1	0	-0.9326	53	1	0	0.5912
6	1	1	0.5597	22	1	1	-3.7138	38	1	1	6.9139	54	1	1	-3.9121
7	1	2	-0.3596	23	1	2	3.8839	39	1	2	-7.8166	55	1	2	4.0780
8	1	3	-0.0639	24	1	3	-0.8771	40	1	3	2.5697	56	1	3	-1.1544
9	2	0	0.2716	25	2	0	-1.0830	41	2	0	1.5864	57	2	0	-0.7362
10	2	1	-1.2760	26	2	1	6.3440	42	2	1	-9.8948	58	2	1	4.6935
11	2	2	0.9403	27	2	2	-7.6283	43	2	2	12.9894	59	2	2	-5.8124
12	2	3	0.0435	28	2	3	2.8212	44	2	3	-6.4372	60	2	3	2.8994
13	3	0	-0.1489	29	3	0	0.5542	45	3	0	-0.6713	61	3	0	0.1489
14	3	1	0.7657	30	3	1	-3.2680	46	3	1	4.7419	62	3	1	-1.8060
15	3	2	-0.6816	31	3	2	4.3408	47	3	2	-7.0070	63	3	2	2.9104
16	3	3	0.0434	32	3	3	-1.7868	48	3	3	3.8269	64	3	3	-1.8262